"Bluff Body Flow Simulation using a Vortex Element Method"

Final Technical Report
July 14, 1998
September 30, 2004
Anthony Leonard, Philippe Chatelain, Michael Rubel
October 2008
DE-AC03-98EE50506

Anthony Leonard
California Institute of Technology
1200 E. California Blvd.
Pasadena, CA 91125

Bluff Body Flow Simulation using a Vortex Element Method

Principal Investigator: Anthony Leonard
California Institute of Technology
1200 E. California Blvd
Pasadena CA 91125
(626) 395-4465, fax: (626) 577-9646, tony@galcit.caltech.edu

Department of Energy – Contract No. DE-AC03-98EE50506
Computation of Three-Dimensional, Unsteady Wake Flows Using Vortex Methods »

Technology Development Area Specialist: Sidney Diamond
(202) 586-8032; fax: (202) 586-1600; e-mail: sid.diamond@ee.doe.gov

Participants:
Michael Rubel, Caltech, mrubel@galcit.caltech.edu
Philippe Chatelain, Caltech, philch@galcit.caltech.edu

Introduction

Heavy ground vehicles, especially those involved in long-haul freight transportation, consume a significant part of our nation's energy supply. It is therefore of utmost importance to improve their efficiency, both to reduce emissions and to decrease reliance on imported oil.

At highway speeds, more than half of the power consumed by a typical semi truck goes into overcoming aerodynamic drag, a fraction which increases with speed and crosswind. Thanks to better tools and increased awareness, recent years have seen substantial aerodynamic improvements by the truck industry, such as tractor/trailer height matching, radiator area reduction, and swept fairings. However, there remains substantial room for improvement as understanding of turbulent fluid dynamics grows.

Our group's research effort focused on vortex particle methods, a novel approach for computational fluid dynamics (CFD). Where common CFD methods solve or model the Navier-Stokes equations on a grid which stretches from the truck surface outward, vortex particle methods solve the vorticity equation on a Lagrangian basis of smooth particles and do not require a grid.

We worked to advance the state of the art in vortex particle methods, improving their ability to handle the complicated, high Reynolds number flow around heavy vehicles. Specific challenges that we have addressed include finding strategies to accurately capture vorticity generation and resultant forces at the truck wall, handling the aerodynamics of spinning bodies such as tires, *application of the method to the GTS model*, computation time reduction through improved integration methods, *a closest point transform for particle method in complex geometrics*, and work on large eddy simulation (LES) turbulence modeling.

Near wall vorticity

We developed a representation of near-wall vorticity by means of an attached regularized sheet. This sheet has several roles. It interacts viscously with the rest of the flow, receives contributions of elements close to the wall during a redistribution and helps in capturing the high vorticity gradients near the wall.

This last role is critical if one needs to accurately measure stresses at the wall. In addition, we introduce a correction that takes into account the gradient of vorticity, which can be estimated from the solution of the panel solver. (See Attachment 1)

Spinning boundaries

The flow around spinning objects is of particular interest because it is encountered around the wheels of heavy vehicles and will interact with the rest of the flow. It is also interesting because of its impact on the problem of splash-and-spray.

Because we use a vorticity based formulation along with a computation of velocities by Biot-Savart, we need to account for the vorticity inside any rotating object. This term, a volume integral, is not the best suited for our method which uses a surface mesh to represent boundaries. We thus switch to a surface integral by application of Gauss's theorem.

Results for *three* configurations involving a spinning sphere were accomplished recently. The rotation axis of the sphere was aligned with the stream, set perpendicular to it, *or at 45°. All* cases were computed for Re=300 and a dimensionless spin velocity WR/U_∞ of 0.5, where W is the angular velocity. *(See Attachment 1)*

GTS Model

The flow around the GTS model was computed in collaboration with G Winckelmans' group at the Université Catholique de Louvain (UCL) To make this run affordable, attached vortex elements were used on the front part of the truck and free elements were introduced upstream of the region separation (See Attachment 2)

Timestepping

Because contemporary CFD is limited by the power of available computers, it is of interest to reduce the work necessary to compute a given flow. One major area of inefficiency which remains largely untapped is the time integration process.

In *Figure 1*, one sees a frequency distribution of the strengths of vortex particles from one snapshot of a very low Reynolds number (1000) truck model simulation. By dimensional analysis, the local timescale is inversely proportional to the local strain rate tensor norm, which for the purpose of this illustration is taken to be particle strength (a choice which is approximate in that it neglects the symmetric part of the tensor). In a conventional timestepper–even an adaptive one–the CFL condition limits integration rate according to the strongest gradient in the flow. However, even at this unrealistically small Reynolds number, the mean strength is hundreds or thousands of times smaller than that of the strongest particles, so most of the flow is being over-resolved by the same factor. Performing timesteps which are adaptive per-particle, rather than per-step, could potentially reduce the computational workload by orders of magnitude.

Some multiscale integration techniques are available, but are not suitable for vortex-based fluid flow problems, which operate over a continuous range of scales and involve fairly complicated tree-based right-hand-side evaluation. The goal of this phase of research has been development of a new multiscale time integration scheme which is tailored to vortex particle methods.

Such a method has been developed and refined over the course of several years, and is now beginning to bear fruit. In *Figure 2*, one sees in the left column several snapshots of a simple vortex particle flow developing in two dimensions, with corresponding particle-specific timesteps on the right. The most significant challenge in developing the method was achieving decent scaling for large numbers of particles; the latest incarnation scales linearly with the total number of timesteps across all particles, as required.

Rigorous order-of-accuracy estimates have been derived (the method can be made accurate to any order) and a number of successful tests have been performed, though more will be required.

Fast Closest Point Transform

A new Characteristic / Oct Tree (C/OT) algorithm for the closest point transform, which allows the vortex code to work on arbitrarily complicated boundary geometries, was completed. The algorithm works by separating space into families of characteristic lines of an Eikonal equation, and sorting them according to how they intersect cells of an oct tree. This algorithm is now implemented and used in many areas of the code: generation/redistribution of particles around arbitrary geometries, sampling fields, etc... (See Attachment 3)

Theoretical LES work

There is ongoing debate on the relationship of large eddy simulation (LES) and Reynolds-averaged Navier-Stokes (RANS) solutions to the filtered or time-averaged direct numerical simulations (DNS) they are designed to model. Due to the chaotic nature of turbulence, the modeled solution is not generally the same result one would obtain by applying its simplifying assumption to an exact solution. The problem is not merely an academic one; understanding how a model relates to the flow being modeled is essential for choosing parameters correctly, which in turn is essential for finding and interpreting computed turbulent flows in the context of heavy vehicle aerodynamics.

We are investigating the implications of a new theoretical concept which treats LES as an explicit ensemble averaging procedure. *We also investigated the possibility of representing the large-eddies of turbulence by a set of vortex filaments. The results are given in attachments 4, 5, and 6*

Conclusions

Our Vortex method development *has gone* mostly according to plan; developments i\mean it should now be possible to simulate complicated flows around truck bodies, including those around rotating tires. Time integration techniques have improved, although these improvements are not yet backported into the main code. Work began on *the* development of Large Eddy Simulation ensemble theory, and *a vortex filament approach to LES was explored.*

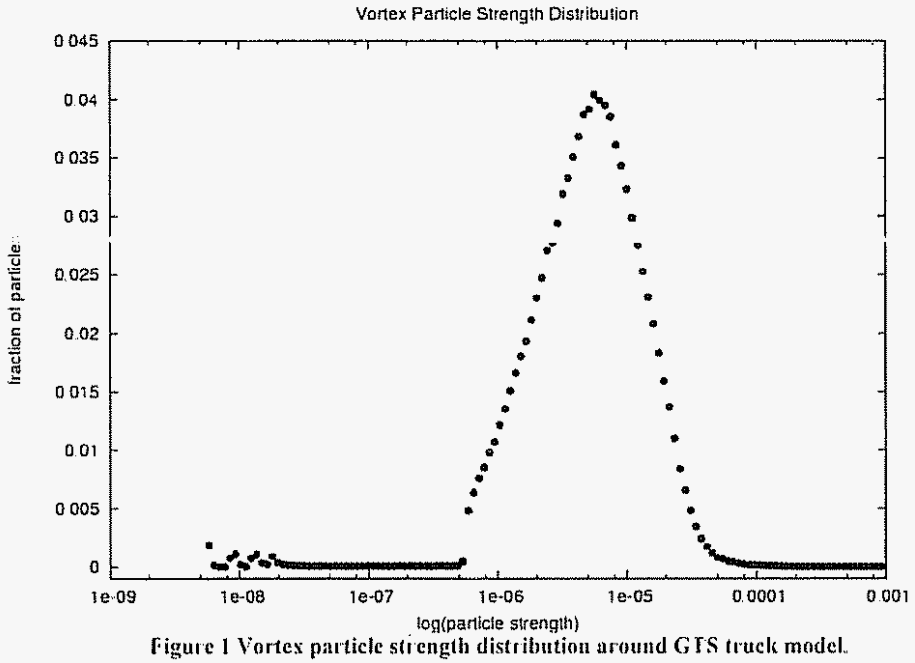

Figure 1 Vortex particle strength distribution around GTS truck model.

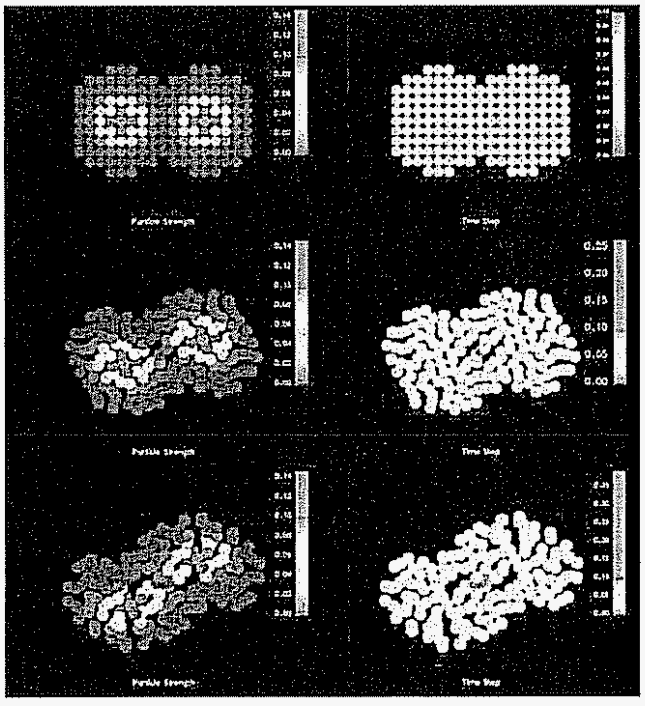

Figure 2 stages in asynchronous time integration of two vortex patches: strengths (left) and timesteps (right

ATTACHMENT NO 1A

JOT JOURNAL OF TURBULENCE

http://jot.iop.org/

Face-centred cubic lattices and particle redistribution in vortex methods†

Philippe Chatelain and Anthony Leonard

Graduate Aeronautical Laboratories, California Institute of Technology, Pasadena, CA 91125, USA
E-mail: philch@galcit.caltech.edu and tony@galcit.caltech.edu

Received 3 October 2002
Published 1 November 2002

Abstract. In vortex particle methods one is concerned with the problem of clustering and depletion of particles in different regions of the flow. The overlap of the vortex blobs is indeed of primary importance for the convergence of the method. In this paper we consider face-centred cubic (FCC) lattices for particle redistribution in three dimensions. This lattice is in fact the most natural way to pack spheres (the FCC is also known as a *closest-sphere packing* lattice). As a consequence, a point has 12 equidistant close neighbours rather than six for the cubic lattice. The FCC lattice thus offers some symmetry properties that should prove useful for a number of reasons, e g., the core overlap issue. A few results for this scheme are presented. The problem of two colliding vortex rings at $Re = 250$ and 500 is studied with both the FCC and cubic lattice schemes. This problem subjects the vortex tubes to a quite strong stretching field and can amply test the quality of the lattice and the remeshing.

PACS numbers: 47 32 Cc, 02 70 Ns

JOT (2002) 3 [1-6]

Contents

† This article was chosen from Selected Proceedings of the 4th International Workshop on Vortex Flows and Related Numerical Methods (UC Santa-Barbara, 17–20 March 2002) ed E Meiburg, G H Cottet, A Ghoniem and P Koumoutsakos

 PII: S1468-5248(02)54440-4 1468-5248/02/000001+6$30 00

1. Introduction

Vortex particle methods are based on the representation of the vorticity by a set of Lagrangian elements. The quality of this representation is critical for the convergence of the method. Because they are Lagrangian, the vortex elements can rapidly cluster along principal axes of compression and form gaps along axes of extension.

Two very different approaches to maintain an approximately uniform distribution stand out. In one, the particles are split or merge depending on the flow locally [1]–[3]. This usually results in a non-controlled growth of the number of particles. Another method consists in redistributing particles onto a regular lattice. A number of schemes have been proposed (see [4] for a review). They are usually designed to conserve the first moments of the particle distribution and/or to distribute the new vorticity field smoothly onto the new points.

These families of schemes are normally based on a regular cubic lattice; they are built in one dimension at first and their extension to two and three dimensions is straightforward by use of a tensor product. These schemes have been used with a spatially varying resolution but even so they are still based on a cubic lattice [5]–[7].

In this work, we introduce a new family of schemes based on the *face-centred cubic* (FCC) lattice. It is also called a *closest-sphere packing* lattice because it is in fact the natural way to pack spheres. The motivation for this work is that this lattice is naturally closer to the spherical nature of the particles. For example, in flows with a boundary, it also may be helpful to have an isotropic cloud of particles near the wall to reduce noise in quantities measured at the wall.

This paper is organized in the following manner: the incompressible flow equations are presented first, with the vortex method, the FCC lattice and particle redistribution, the results and the conclusion following.

2. Three-dimensional incompressible flow

We solve the vorticity equation for an incompressible flow in an unbounded domain:

$$\frac{\mathrm{D}\omega}{\mathrm{D}t} = (\nabla u)\cdot\omega + \nu\nabla^2\omega \tag{1}$$

$$\nabla\cdot u = 0 \tag{2}$$

where $u(x,t)$ is the velocity field, ν is the kinematic viscosity and $\omega = \nabla\times u$ is the vorticity.

A Helmholtz decomposition is used to determine the velocity:

$$u = \nabla\phi + \nabla\times\psi \tag{3}$$

with $\nabla\cdot\psi = 0$. Here ϕ is a scalar potential and the corresponding velocity is irrotational. ψ is the streamfunction which is related to the vorticity by the Poisson equation:

$$\nabla^2\psi = -\omega. \tag{4}$$

3. Vortex method

The vortex method is based on the representation of the vorticity field by a set of N Lagrangian particles:

$$\tilde{\omega}(x,t) = \sum_{i=1}^{N} \zeta_i(x - x_i)\alpha_i. \tag{5}$$

The particles have a position x_i and a strength $\alpha_i = \int \omega \, dx$. The streamfunction, the velocity and its gradient can be computed by means of a Green function. This Green function is associated with the kernel used to represent the particles. One then uses the velocity and its gradient to move the particles and update their strengths, respectively.

The basis used to represent the vorticity field is not necessarily divergence free whereas $\omega = \nabla \times u$ is clearly solenoidal. This second field allows the design of some relaxation methods for $\tilde{\omega}$ [8, 9] and allows the monitoring of the divergence error defined by

$$E_{div} = \int |\tilde{\omega} - \omega|^2 \, dx \tag{6}$$

This divergence problem can be alleviated by a certain choice of the numerical evaluation of the stretching term in equation (1) [4].

4. Particle redistribution

As mentioned above, the vortex particle method is subject to problems of clustering and depletion. A solution consists in creating a new set of particles on a regular lattice. This is called particle redistribution. This process is characterized by the order of the highest conserved moment, the width of the stencil (i.e. how many particles are generated for one particle of the old set) and the smoothness of the interpolation function used.

It is worth noting that the redistribution scheme can also help reduce the divergence error. The particle pattern influences the quality of the particle interactions; these interactions at close range play an important role when one computes the velocity and its gradient and also when a viscous scheme is used.

A more thorough discussion can be found in [4, 7].

4.1. The face-centred cubic lattice

The cubic lattice has been so far the only lattice used for these redistributions. The vortex element method is a grid-free method (with the exception of the redistribution); the geometrical pattern of the particles therefore should not have any influence on the convergence of the method provided the pattern is regular.

The FCC lattice offers such a regularity and also some interesting symmetry properties. This lattice is known as a *closest-sphere packing* lattice; it is one of two lattices that pack the most spheres per unit volume (the other one is the *hexagonal close-packing* (HCP) lattice). We chose the FCC because it is possible to fit a coordinate system that is very helpful in the design of the scheme. A node of this lattice has 12 equidistant direct neighbours against six for a cubic lattice and there are four planes with a mesh parameter h passing through a node (three for a cubic). This lattice is not difficult to generate if one considers it as the superposition of three families of two-dimensional hexagonal lattices, A, B and C in figure 1.

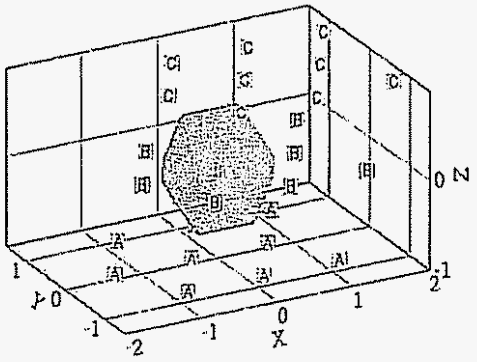

Figure 1. The FCC lattice and the interpolation function: the three families of hexagonal planes used to generate the lattice and the isosurface $W_{FCC_1} = 0.25$

4.2. The interpolation function

The second component of the redistribution is the interpolation rule W one uses to create the new set of particles,

$$\alpha_p^{new} = \sum_q \alpha_q^{old} W\left(\frac{x_p - \bar{x}_q}{h}\right).$$

For the cubic lattice, several families of schemes have been introduced. The great majority of these are based on the tensor product of one-dimensional interpolation functions. For the FCC lattice, such a construction is not possible; the interpolation function has to be built in three dimensions from the start.

We designed a continuous second order interpolation function that is analogous to the three-dimensional *Witches Hat* Λ_1 function for a cubic lattice. This rule redistributes a particle onto the vertices of the containing tetrahedron or octahedron (four or six points respectively). This function is defined by pieces; it is a linear function inside a tetrahedron and a piecewise linear continuous function inside an octahedron. This function was built to conserve circulation and its first moment and to ensure continuity with the linear function inside the tetrahedra of the stencil. This piecewise definition is visible in the isocontour in figure 1. Analytical expressions and C functions are available at [illegible] en.html.

We call this scheme FCC_1. Notice that it is straightforward to generate smoother interpolation functions with a wider stencil. The convolution of our scheme by a *closest-point* distribution function yields a scheme with the same moment conservation but with one more level of continuity. Improving the conservation properties takes more work.

5. Results

Our test consists in two colliding vortex rings. This configuration deforms the set of particles and thus tests the quality of the core overlap through the simulation. There are two sets of results. The first one is a well resolved case at $Re = 250$ where we compare two second order schemes, the Λ_1 in the cubic lattice and our FCC_1 scheme. The second set of results is at $Re = 500$ with a coarser resolution (thus under-resolved) and we consider the two second order schemes along with a third order scheme M_4'. The redistribution frequency (once every ten time steps) was the same in all our tests.

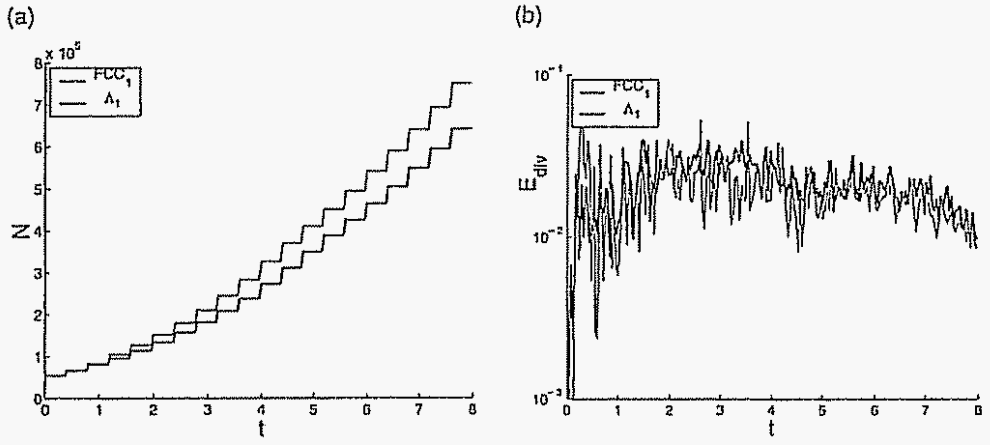

Figure 2. $Re = 250$: number of particles and divergence error

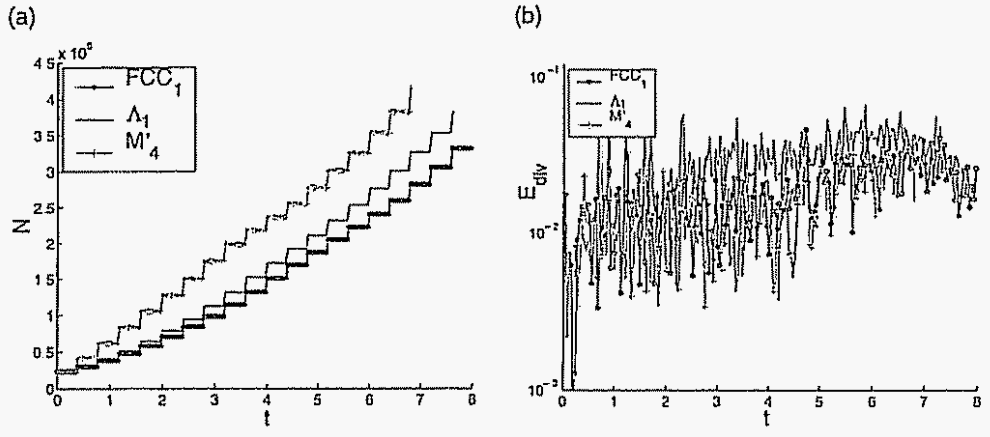

Figure 3. $Re = 500$: number of particles and divergence error

5.1. $Re = 250$

Because of the different lattices used, we define the grid Reynolds number as $Re_h = \frac{UV_p^{1/3}}{\nu}$. It will depend on the actual density of points. The results in this section were obtained at $Re_h \approx 12 \rightarrow 4$. The FCC lattice introduces fewer points than the Λ_1 scheme and shows the same divergence error (figure 2). The error decreases for $t > 6$ as the rings are decaying.

5.2. $Re = 500$

We now consider the under-resolved case, $Re_h \approx 27 \rightarrow 13$. One can now notice a significant difference between the two second order schemes. The error for the FCC_1 scheme stays at the level of the M_4' which introduces far more particles because of its wider stencil (figure 3)

6. Conclusion

We have introduced the first representative of a new family of interpolation schemes based on the FCC lattice. Our scheme has two outstanding features:

(i) Thanks to the many symmetries of the FCC lattice, it is more compact than an equivalent scheme in a cubic lattice. This results in a slower growth of the number of particles because of a tighter *halo* of new particles around the set of old particles.

(ii) Symmetry is also beneficial to the overlap of the particle cores and allows better communications between the particles even under stretching. We have observed a significant effect in the divergence error for high Re_h cases.

Acknowledgment

This research was supported by Department of Energy contract DE-AC03-98EE50506.

References

[1] Leonard A 1980 Vortex methods for flow simulation *J. Comput. Phys.* 37 289–335
[2] Rossi L F 1996 Resurrecting core spreading vortex methods: a new scheme that is both deterministic and convergent *SIAM J. Sci. Comput.* 17 370–97
[3] Rossi L F 1997 Merging computational elements in vortex simulations *SIAM J. Sci. Comput.* 18 1014–27
[4] Cottet G-H and Koumoutsakos P 2000 *Vortex Methods, Theory and Practice* (Cambridge: Cambridge University Press)
[5] Cottet G-H, Koumoutsakos P and Lemine Ould Salihi M 2000 Vortex methods with spatially varying cores *J. Comput. Phys.* 11 164
[6] Cottet G-H, Lemine M and El Hamraoui M 1998 Recent developments in vortex methods for the simulation of unsteady incompressible flows *Electron. Proc. 3rd Int. Workshop on Vortex Flows and Related Numerical Methods (Toulouse, 1998) ESAIM (European Series in Applied and Industrial Mathematics)* http://www.emath.fr/Maths/Proc/Vol.7/
[7] Ploumhans P and Winckelmans G S 2000 Vortex methods for high resolution simulations of viscous flow past bluff-bodies of general geometry *J. Comput. Phys.* 165 354–406
[8] Winckelmans G S and Leonard A 1993 Contributions to vortex particle methods for the computation of three-dimensionnal incompressible unsteady flows *J. Comput. Phys.* 109 247–73
[9] Leonard A, Shiels D, Salmon J K, Winckelmans G S and Ploumhans P 1997 Recent advances in high resolution vortex methods for incompressible flows *Proc. 13th AIAA Computational Fluid Dynamics Conf. (Snowmass Village, CO, 1997)* AIAA 97-2108

ATTACHMENT NO 1B

GRADUATE AERONAUTICAL LABORATORIES

CALIFORNIA INSTITUTE OF TECHNOLOGY

Contributions to the three-dimensional vortex element method and spinning bluff body flows

Thesis by
Philippe Chatelain

Firestone Flight Sciences Laboratory

Guggenheim Aeronautical Laboratory

Karman Laboratory of Fluid Mechanics and Jet Propulsion

Pasadena

Contributions to the Three-Dimensional Vortex Element Method and Spinning Bluff Body Flows

Thesis by
Philippe Chatelain

In Partial Fulfillment of the Requirements
for the Degree of
Doctor of Philosophy

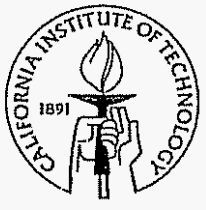

California Institute of Technology
Pasadena, California

2005

(Defended December 3, 2004)

Acknowledgements

I thank my advisor, Anthony Leonard. His open-mindedness, trust and kindness truly shaped this work. None of this would have sbeen possible without my undergraduate advisor, Grégoire Winckelmans, who first introduced me to computational fluid dynamics and vortex methods. Fruitful discussions with Hans Hornung are also acknowledged. My friends and (former) colleagues at the Iris lab, Mark Brady, Gerard O'Reilly, Vincent Wheatley, James Faddy, Nikoo Saber, Paul O'Gorman and Michael Rubel made these five years of work also a fun experience. Michael provided great computing advice and important contributions to this vortex code.

My wife, Caroline gave me her unconditional and invaluable support throughout. Many thanks also go to my parents who always put my education first and never stopped encouraging me. Finally, I do not want to forget my friends, François, Luc and Olivier.

This effort was sponsored by the US Department of Energy under contract No. DE-AC03-98EE50506, and also supported by Caltech discretionary funds. The Master's year was funded by a fellowship of the Belgian American Educational foundation. These contributions are gratefully acknowledged.

Abstract

Several contributions to the three-dimensional vortex element method for incompressible flows are presented. We introduce redistribution schemes based on the hexagonal lattice in two dimensions, and the face-centered cubic lattice in three dimensions. Interpolation properties are studied in the frequency domain and are used to build high-order schemes that are more compact and isotropic than equivalent cubic schemes. We investigate the reconnection of vortex rings at small Reynolds numbers for a variety of configurations. In particular, we trace their dissipative nature to the formation of secondary structures

A method for flows with moving boundaries is implemented. The contributions of rotating or deforming boundaries to the Biot-Savart law are derived in terms of surface integrals. They are implemented for rigid boundaries in a fast multipole algorithm. Near-wall vorticity is discretized with attached panels. The shape function and Biot-Savart contributions of these elements account for the presence of the boundary and its curvature. A conservative strength exchange scheme was designed to compute the viscous flux from these panels to free elements.

The flow past a spinning sphere is studied for a Reynolds number of 300 and a wall velocity that is equal to half the free-stream velocity. Three directions of the angular velocity are considered. Good agreement with previous numerical and experimental measurements of the force coefficients is observed. Topological features such as the separation and critical points are investigated and compared amongst the configurations.

Finally, preliminary results for flapping motions are presented. Simple rigid geometries are used to model a fish swimming in a free-stream and a flapping plate.

Contents

List of Figures

List of Tables

Chapter 1

The Three-Dimensional Vortex Element Method

1.1 Introduction

Vortex element methods have been growing in popularity since the early 1980's. As their name indicates, they are based on the discretization of vorticity–a quantity that has a compact support in many physical problems–thereby making this approach interesting.

The discretization itself comes in various sorts: filaments, sheets or particles. This last family has shown the most dramatic progression. The treatment of the distortion of the elements and the development of deterministic viscous algorithms have allowed for accurate long-time simulations. During the 1990's, wall boundary conditions and faster algorithms were developed to handle high Reynolds number incompressible flows in two and three dimensions. In recent years, we have seen the application to compressible and reacting flows.

The present work brings contributions to several areas of the method. A particular focus is on the development of a framework to handle moving and deforming boundaries. This opens the way to the simulation of spinning bluff body flows and flapping motions, such as those encountered in biological flows.

This first chapter gives a comprehensive review of the vortex element method for

incompressible flows, with emphases on the approaches and problems that we investigate in later chapters. We end this chapter with an overview of our contributions.

1.2 Fundamentals

1.2.1 Hypothesis and Equations

Vorticity

We are studying the three-dimensional incompressible flow of a viscous fluid. Let us start with the Navier-Stokes' equations

$$\begin{aligned} &\nabla \cdot \mathbf{u} = 0, \\ &\frac{\partial \mathbf{u}}{\partial t} + (\nabla \mathbf{u})\,\mathbf{u} + \nabla\left(\frac{p}{\rho}\right) = \nu \nabla^2 \mathbf{u}. \end{aligned} \tag{1.1}$$

The vorticity, ω, is defined as

$$\omega = \nabla \times \mathbf{u}.$$

The term $(\nabla \mathbf{u})\,\mathbf{u}$ in Eq. 1.1 can be rewritten as

$$\begin{aligned} (\nabla \mathbf{u})\,\mathbf{u} &= \nabla \cdot (\mathbf{u}\mathbf{u}) \\ &= \omega \times \mathbf{u} + \nabla\left(\frac{\mathbf{u} \cdot \mathbf{u}}{2}\right) \end{aligned} \tag{1.2}$$

With this last result, the curl of Eq. 1.1 becomes

$$\begin{aligned} \nabla \times \left(\frac{\partial \mathbf{u}}{\partial t} + \omega \times \mathbf{u} + \nabla\left(\frac{\mathbf{u} \cdot \mathbf{u}}{2} + \frac{p}{\rho}\right)\right) &= \nabla \times \nu \nabla^2 \mathbf{u} \\ \frac{\partial \omega}{\partial t} + \nabla \times (\omega \times \mathbf{u}) &= \nu \nabla^2 \omega. \end{aligned} \tag{1.3}$$

Continuing to simplify, we have

$$\frac{\partial \omega}{\partial t} + \nabla \times (\omega \times \mathrm{u}) = \nu \nabla^2 \omega$$

$$\underbrace{\frac{\partial \omega}{\partial t} + (\nabla \omega) \cdot \mathrm{u}}_{=\frac{D\omega}{Dt}} - (\nabla \mathrm{u}) \cdot \omega + \underbrace{\omega (\nabla \cdot \mathrm{u})}_{=0} - \underbrace{\mathrm{u} (\nabla \cdot \omega)}_{=0} = \nu \nabla^2 \omega$$

and finally, we have the evolution equation for vorticity

$$\frac{D\omega}{Dt} = (\nabla \mathrm{u}) \cdot \omega + \nu \nabla^2 \omega \tag{1.4}$$

where the right terms correspond to a stretching effect and a viscous diffusion respectively.

Stream-Function and Velocity

The previous equation allows the computation of the evolution of the vorticity field if the velocity is known. This is made possible through the use of a stream-function ψ. We consider the Helmholtz decomposition of velocity

$$\mathrm{u} = \nabla \varphi + \nabla \times \psi, \tag{1.5}$$

with the gauge of ψ set as $\nabla \cdot \psi = 0$. Taking the curl of Eq. 1.5 yields the following Poisson equation for ψ:

$$\nabla^2 \psi = -\omega \tag{1.6}$$

The computation of the velocity field therefore requires finding ψ and computing its curl.

1.2.2 Discretization

A Lagrangian method considers the evolution of elements which represent small material volumes V_p. An element is carried by the local flow and carries the integral of some intensive physical quantity f, $\alpha_p = \int_{V_p} f \, dV$. We will refer to this integral as

the strength of the element. We can therefore write the following evolution equations for the position $\mathbf{x}_p$ and strength α_p of an element,

$$\frac{d\mathbf{x}_p}{dt} = \mathbf{u}(\mathbf{x}_p) \tag{1.7}$$

$$\frac{d\alpha_p}{dt} = \int_{V_p} \left(\frac{\partial f}{\partial t} + \nabla \cdot (f\mathbf{u}) \right) d\mathbf{x} \tag{1.8}$$

where Leibniz's theorem was used.

In the context of vortex methods, the physical quantity f is the vorticity ω. For an incompressible three-dimensional flow, the use of Eq. 1.4 in Eq. 1.8 yields

$$\frac{d\mathbf{x}_p}{dt} = \mathbf{u}(\mathbf{x}_p) \tag{1.9}$$

$$\frac{d\alpha_p}{dt} = \int_{V_p} \left((\nabla \mathbf{u}) \cdot \omega + \nu \nabla^2 \omega \right) d\mathbf{x} \tag{1.10}$$

$$= (\nabla \mathbf{u}(\mathbf{x}_p)) \cdot \alpha_p + \nu \int_{V_p} \nabla^2 \omega \, d\mathbf{x} \,, \tag{1.11}$$

where we use a center point rule to evaluate the first term.

We note that our problem has now become a system of ordinary differential equations and that we still need to compute its right-hand side.

1.2.3 Field Computations

Two main families of methods have been proposed to compute velocity from Eqs. 1.6 and 1.5. On the one hand, grid-based solvers have given rise to the so-called Vortex-In-Cell–VIC– methods (see Cottet and Koumoutsakos, 2000, sec. 8.2 and references therein) in which vortex strengths are distributed onto a grid and the velocity field is computed using Eqs. 1.5 and 1.6 and interpolated at the particle positions. This kind of approach is effective for periodic problems, but must be modified to enforce far field boundary conditions.

On the other, we use a second approach which is in a sense, grid-less, and implicitly imposes boundary conditions at infinity. We consider volume elements where the

distribution is singular and the strength is concentrated at the particle center,

$$\omega = \sum_p \alpha_p \delta(\mathbf{x} - \mathbf{x}_p)$$

We can then use the fundamental solution of $-\nabla^2$:

$$-\nabla^2 G(\mathbf{x}, \mathbf{x}') = \delta(\mathbf{x} - \mathbf{x}') \tag{1.12}$$

G is also called the free-space Green's function. In three dimensions, it is given by

$$G(\mathbf{x}, \mathbf{x}') = \frac{1}{4\pi} |\mathbf{x} - \mathbf{x}'|^{-1} \tag{1.13}$$

and is a radial function which we will write as $G(|\mathbf{x} - \mathbf{x}'|)$ from here on. In this approach, field computation thus amounts to a summation over the elements

$$\psi(\mathbf{x}) = \sum_p G(|\mathbf{x} - \mathbf{x}_p|)\alpha_p \tag{1.14}$$

$$\mathbf{u}(\mathbf{x}) = \sum_p \nabla \left(G(|\mathbf{x} - \mathbf{x}_p|)\right) \times \alpha_p = \sum_p \mathbf{K}\left(\mathbf{x} - \mathbf{x}_p\right) \times \alpha_p \,, \tag{1.15}$$

where we introduce $\mathbf{K} = \nabla G$.

This approach however can encounter stability problems because of the singularities the velocity field displays (Winckelmans and Leonard, 1993). Instead we employ a regularized distribution for the particles $\omega_\sigma = \sum_p \alpha_p \zeta_\sigma(\mathbf{x} - \mathbf{x}_p)$, where σ is a smoothing radius. ζ_σ induces smooth stream function and velocity contributions G_σ and $\mathbf{K}_\sigma$, respectively.

In our implementation, ζ_σ is a Gaussian,

$$\zeta_\sigma(|\mathrm{x}|) = \frac{1}{(2\pi)^{3/2}\sigma^3} e^{-\frac{r}{2\sigma^2}} \tag{1.16}$$

$$G_\sigma(|\mathrm{x}|) = \frac{1}{4\pi} \frac{\mathrm{erf}\left(\frac{|\mathrm{x}|}{\sqrt{2}\sigma}\right)}{|\mathrm{x}|} \tag{1.17}$$

$$\mathrm{K}_\sigma(\mathrm{x}) = \frac{-\mathrm{x}}{4\pi|\mathrm{x}|^3}\left(\mathrm{erf}\left(\frac{|\mathrm{x}|}{\sqrt{2}\sigma}\right) - \sqrt{\frac{2}{\pi}}\frac{|\mathrm{x}|}{\sigma}e^{-|\mathrm{x}|^2/2\sigma^2}\right) \tag{1.18}$$

One can find more thorough discussions of the topic of this section in Winckelmans (2004) and Cottet and Koumoutsakos (2000).

1.2.4 Viscous Term

The second term in Eq 1.11 still needs to be computed. Several techniques have been proposed. Random-walk methods move the elements in a Brownian motion fashion (Chorin, 1973). Re-sampling methods act on the strengths of the elements by sampling the exact solution of the viscous diffusion of singularities at the particle locations. Our approach follows the method of Degond and Mas-Gallic (1989) which is known as the particle strength exchange (PSE) scheme. It is based on an integral representation of the Laplace operator. In $\mathbb{R}^3$, one can indeed write

$$\nabla^2 f(\mathrm{y}) \simeq \frac{2}{\sigma^2}\int \eta_\sigma(\mathrm{x}-\mathrm{y})\,(f(\mathrm{x})-f(\mathrm{y}))\,d\mathrm{x} + O(\sigma^r)\,, \tag{1.19}$$

which, integrated over the volume of an element, yields

$$\int_{V_p} \nabla^2 f\,d\mathrm{y} \simeq \int \frac{2}{\sigma^2}\int \eta_\sigma(\mathrm{x}-\mathrm{y})\,(f(\mathrm{x})-f(\mathrm{y}))\,d\mathrm{x}\,d\mathrm{y}\,. \tag{1.20}$$

The kernel η_σ has to satisfy moment conditions (Degond and Mas-Gallic, 1989, Cottet and Koumoutsakos, 2000). We have

$$\begin{aligned}
&\int x_i x_j \eta_\sigma(\mathrm{x}) d\mathrm{x} = \delta_{ij} \text{ for } i,\, j = 1,2,3 \\
&\int x_i^{i_1} x_j^{i_2} \eta_\sigma(\mathrm{x}) d\mathrm{x} = 0 \text{ for } i_1 + i_2 = 1 \text{ or } 3 \le i_1 + i_2 \le r+1 \\
&\int |\mathrm{x}|^{r+2} \eta_\sigma(\mathrm{x}) d\mathrm{x} < \infty
\end{aligned} \tag{1.21}$$

One technique to build a kernel η consists in using the function ζ

$$\eta(\rho) = -\frac{1}{\rho}\frac{d}{d\rho}\zeta(\rho)\,, \tag{1.22}$$

which in the case of the Gaussian yields the same Gaussian. If one considers a pair (p,q) of vortex elements, the integral of Eq. 1.20 has a simple expression

$$\left.\frac{d\alpha_p}{dt}\right|_{\text{visc } q} \simeq \frac{2}{\sigma^2}\eta_\sigma(\mathrm{x}_p - \mathrm{x}_q)\left(V_p\,\alpha_q - V_q\,\alpha_p\right)\,, \tag{1.23}$$

which shows that the scheme is conservative. Ploumhans (2001) proved the convergence of the PSE for particles with a smoothly varying core size σ. This result allows the use of coarser particle distributions in the wake of bluff body flows (Chapter 6)

1.2.5 Wall-Bounded Flows

There are many challenges when dealing with boundaries. Koumoutsakos et al (1994) and Koumoutsakos and Leonard (1995) introduced a scheme to account for vorticity creation at the wall. This scheme is based on the model of Lighthill (1963) and consists in the incremental introduction of vorticity in the form of vorticity sheets at the boundaries. At every application, the sheet enforces the no-slip condition. Because this sheet γ appears within a time step δt, the compatibility with a Neumann boundary condition is immediate

$$\nu\frac{\partial\omega}{\partial n} = \frac{\gamma}{\delta t} \tag{1.24}$$

The sheet strength, γ, first has to be found using a boundary element method, and then diffused into the flow. Chapter 4 will cover this topic.

Boundaries also affect the order of the method because the interpolation and integration over the elements assumes an unbounded space. Our spherical test functions let some vorticity leak across the boundary and will require completing the set with images to cancel spurious viscous fluxes through the wall. Chapter 5 introduces attached elements with specific test functions to alleviate this problem.

1.2.6 Vorticity Divergence

One issue that is peculiar to three dimensions is the divergence problem. Vorticity is the curl of the velocity field, and as such, it satisfies

$$\nabla \cdot \omega = \nabla \cdot (\nabla \times \mathbf{u}) = 0 . \tag{1.25}$$

In two dimensions, this condition is met because $\omega = \omega_z(x, y)\, \mathrm{e}_z$. In three dimensions however, the discretized vorticity field will differ slightly from a solenoidal field. This problem is discussed further in Chapters 2 and 6.

1.3 Numerics

1.3.1 Field Computations Acceleration

The summations in Eq. 1.14 and 1.15 imply a $O(N^2)$ cost when one computes the fields at the positions of all the elements, thus making it intractable even for modest problem sizes.

If we consider the sum for a fixed $\mathbf{x}$, we notice that the contribution of a remote cluster of particles can be closely approximated by the influence of one virtual particle located at the center of the group. This is the central idea of multipole expansions and tree codes; the set is sorted geometrically and hierarchically into a tree and a branch cell contains information about the particles it (or its offspring) contains.

One also needs an error control algorithm so to keep the approximation accurate to a prescribed level. The summation now reduces to a tree traversal. For a given branch, the recursion consists in computing the interactions of its offspring if the error criterion is not met or stopping at the branch and using its multipole information otherwise. The loop is initiated by starting with the root cell.

There are evidently variations on this idea. For more information, one may refer to Barnes and Hut (1986), Salmon et al. (1994), Salmon and Warren (1994) and Winckelmans et al. (1995).

1.3.2 Clustering and Depletion

Because vortex elements follow the flow, they tend to cluster along axes of compression and become depleted regions of stretching. This affects the convergence of the method, which is based on integration and interpolation over all space. Historically, the first convergence results for the three-dimensional method were derived by Beale and Majda (1982). One may refer to Cottet and Koumoutsakos (2000) for a recent proof and a complete historical list of references.

A central idea of these convergence results is that the error grows with some power of h/σ and σ^r, where h is the spacing between the particles and r of the highest vanishing moment of the mollifying function. The Gaussian of Eq. 1.16 has $r = 2$. It is therefore important to keep a regular set of overlapping elements. Several techniques have been designed in this regard; we use particle location processing–redistribution which creates a new undistorted set of elements from the old one. This technique was used in all our simulations and will be covered in details in Chapter 2 as we investigate new arrangements for the particles.

1.3.3 Time Integration

Anderson and Greengard (1985) showed that, for an inviscid problem, the time integration stability condition does not affect the convergence of the vortex method, i.e., the convergence rate is $O(\sigma^r + \delta t^s)$ where s is the order of the time integration. In

practice, this theoretical unconditional stability is tempered by other factors such as the divergence problem or the presence of boundaries.

We use a second order Adams-Bashforth (AB2) scheme. A Runge-Kutta 2 (RK2) scheme is used at the start, or when we have to restart the integration after a redistribution. The stability of the PSE integrated with AB2 is constrained by (Koumoutsakos, 2001)

$$r_{\text{PSE}} = \frac{\nu \Delta t}{h^2} < 0.267 \,. \tag{1.26}$$

As mentioned above, there is no Courant-Friedrich-Levy condition, relating the particle size to the time step,

$$\frac{U_{max} \Delta t}{h} < O(1) \,. \tag{1.27}$$

For a bounded flow however, a time-step too large will lead to particles crossing boundaries. This last quantity will therefore be monitored near the walls. Other expressions more suitable for a Lagrangian method have been proposed:

$$\text{CFL} = |\omega|_{\max} \Delta t \text{ or } |\nabla \mathrm{u}|_{\max} \Delta t \tag{1.28}$$

A last condition concerns the mesh Reynolds number

$$Re_h = \frac{U_{max} h}{\nu} \lesssim 2 \tag{1.29}$$

For vortex methods, there is a more appropriate expression,

$$Re_h = \frac{|\omega|_{max} h^2}{\nu} \,. \tag{1.30}$$

It is not independent from the two preceding conditions since

$$\text{CFL} = Re_h r_{\text{PSE}} \,. \tag{1.31}$$

1.4 Overview

Chapter 2 presents an alternative to the existing redistribution schemes based on the face-centered cubic lattices. Compactness and isotropy are benefited from the symmetry properties of this lattice.

Chapter 3 studies the physics of the reconnections of vortex rings from various standpoints and in particular, the energy spectrum.

Chapters 4 to 7 present work that broadens the applicability of the method to moving and deforming geometries. The case of spinning spheres at $Re = 300$ is considered in Chapter 6. Chapter 5 proposes a new element class to represent near-wall vorticity to alleviate regularization problems in those regions. These elements also implement some of the boundary conditions required in flows with deforming and rotating boundaries. Chapter 7 discusses preliminary results for flapping and swimming motions.

Chapter 8 concludes this thesis. It includes a discussion of our results, and directions of future work.

Chapter 2

Face-Centered Cubic Redistributions

2.1 Introduction

As we have seen in Chapter 1, the vortex element method strongly depends on integration and interpolation. In particular, this translates into accuracy degradation when our interpolating elements get too far apart.

One can follow a few different approaches to tackle this problem. One approach consists in progressively introducing new elements in the domain. While elegant, this approach requires a costly algorithm to find the new elements' positions and strengths (see Gharakhani, 2001).

The other approach is to build a whole new set of elements from the old ones. This process must take place every few time steps in order to prevent the particle distribution from getting too distorted. This redistribution process consists in interpolating the new strengths at the nodes of a new non-distorted lattice.

2.2 Redistribution Properties

A redistribution scheme has two components: a lattice and an interpolation function. The term lattice is preferred to mesh because it remains a mathematical object and can span an unbounded region of $\mathbb{R}^3$. Concretely, the lattice nodes are never stored in an array; they are generated on demand.

Ploumhans and Winckelmans (2000) proved the second order accuracy of the particle strength exchange for elements with a smoothly varying size. One can thus use a stretched lattice for problems where it is interesting to vary the resolution. This method will be applied to the simulation of bluff body flows in Chapter 6 and 7

The interpolation rule will be characterized in terms of its smoothness, order of accuracy and support (Fig. 2.1) We will introduce and generalize some results from Cottet and Koumoutsakos (2000). A central result concerns the order of interpolation

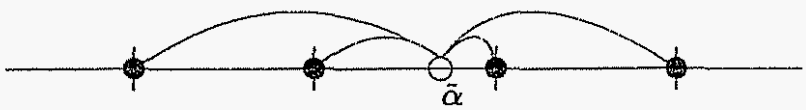

Figure 2.1: Redistribution in one dimension: the strength of a particle of the distorted set (open circle) is redistributed onto four nodes (solid circles)

Let us define the new particles with positions x_p and strengths α_p as

$$\alpha_p = \sum_q \tilde{\alpha}_q W\left(\frac{\mathrm{x}_p - \tilde{\mathrm{x}}_q}{h}\right) \tag{2.1}$$

in terms of the interpolation function W and the old positions and strengths $\tilde{\mathrm{x}}_q$ $\tilde{\alpha}_q$. If we consider an interpolated quantity $\sum_p \alpha_p \phi(\mathrm{x} - \mathrm{x}_p)$ e g vorticity or velocity, the discrepancy we introduce can be written as

$$\begin{aligned} E(\mathrm{x}) &= \sum_p \tilde{\alpha}_p \phi(\mathrm{x} - \tilde{\mathrm{x}}_p) - \sum_p \alpha_p \phi(\mathrm{x} - \mathrm{x}_p) \\ &= \sum_p \tilde{\alpha}_p \left[\phi(\mathrm{x} - \tilde{\mathrm{x}}_p) - \sum_q \phi(\mathrm{x} - \mathrm{x}_q) W\left(\frac{\mathrm{x}_q - \tilde{\mathrm{x}}_p}{h}\right)\right] \end{aligned}$$

The error behavior will thus be dictated by the factor inside the square brackets, which we can express as

$$f(\mathrm{x} - \tilde{\mathrm{x}}_p) = \sum_q \left(\phi(\mathrm{x} - \tilde{\mathrm{x}}_p) - \phi(\mathrm{x} - \mathrm{x}_q)\right) W\left(\frac{\mathrm{x}_q - \tilde{\mathrm{x}}_p}{h}\right) \tag{2.2}$$

To obtain the above expression, we have imposed

$$\sum_q W(\mathrm{x} - \mathrm{x}_q) = 1\,, \tag{2.3}$$

which is physically equivalent to the conservation of circulation. In order to bound f, we expand ϕ about $\mathrm{x} - \mathrm{x}_q$,

$$f(\mathrm{x} - \tilde{\mathrm{x}}_p) = \sum_q \sum_{|\beta|=1}^{\infty} (-1)^{|\beta|} (\mathrm{x}_q - \tilde{\mathrm{x}}_p)^\beta \, \partial_\beta \phi(\mathrm{x} - \mathrm{x}_q) W\left(\frac{\mathrm{x}_q - \tilde{\mathrm{x}}_p}{h}\right)\,, \tag{2.4}$$

where $\beta = \beta_1 \cdots \beta_n$ are n-tuples with $|\beta| = \beta_1 + \cdots + \beta_n$. It is readily seen from this last expression that the moments of W will characterize the error behavior, i.e., if

$$\sum_q \mathrm{x}_q^\beta \, W\left(\frac{\mathrm{x} - \mathrm{x}_q}{h}\right) = \mathrm{x}^\beta \text{ for } 0 \leq |\beta| \leq m - 1 \tag{2.5}$$

then

$$E \sim O\left(h^m\right)\,. \tag{2.6}$$

One may refer to Cottet and Koumoutsakos (2000) for a full proof.

Our work focuses on the development and study of interpolation functions W on a different family of lattices. For this reason, we introduce a notation that reflects the arrangement of the new points $\mathrm{x_n} = h\mathbf{R}\mathbf{n}$, in the fashion of Merserau (1979) and Van De Ville et al. (2004). $\mathbf{R}$ is the matrix whose columns are the principal directions of the lattice. Let us also define the matrix $\hat{\mathbf{R}} = (\mathbf{R}^{-1})^t$ which defines a dual lattice. h is the lattice step and being just a rescaling, it will be dropped from the remainder of this chapter for the sake of clarity.

Let us now consider the properties of the Fourier transform of the interpolation kernel. The switch to Fourier space will indeed facilitate the development of high order schemes. Theorem 7.2.1 from Cottet and Koumoutsakos (2000) and Schoenberg (1973) can be generalized to multi-dimensional cases and any kind of lattice as follows.

Theorem 1. *Consider the interpolation formula*

$$Q(\mathrm{x}) = \sum_{\mathrm{n}} q_{\mathrm{Rn}} W\left(\mathrm{x} - \mathbf{R}\mathrm{n}\right) ,$$

where q_{Rn} is the weight of the point $\mathbf{R}\mathrm{n}$. Let the interpolation function decay fast enough to satisfy the condition

$$|W\left(\mathrm{x}\right)| \leq Ae^{-B|\mathrm{x}|}, \textit{ where } A > 0,\ B > 0.$$

The formula is of degree m if the following two conditions on $g(k) = \int W(\mathrm{x}) e^{-i\mathrm{k}\mathrm{x}}\, d\mathrm{x}$ hold simultaneously:

$$g(\mathrm{k}) - |\mathbf{R}| \textit{ has a zero of order } m \textit{ at } \mathrm{k} = 0\,, \tag{2.7}$$

$$g(\mathrm{k}) \textit{ has zeros of order } m \textit{ or higher at all } \mathrm{k} = 2\pi\hat{\mathbf{R}}\mathrm{n}\ (\mathrm{n} \neq 0). \tag{2.8}$$

Proof Let us consider the interpolation function in lattice coordinates χ; by definition we have for $V(\chi)$

$$\int V(\eta) e^{-i(\kappa + 2\pi\mathrm{n})\,\eta} d\eta = \hat{V}\left(\kappa + 2\pi\mathrm{n}\right) .$$

Following Cottet and Koumoutsakos (2000), we multiply both sides by $e^{2\pi\mathrm{n}\,\chi}$, sum over n, then use the Poisson summation formula on the left-hand side:

$$\sum_{\mathrm{n}} e^{2\pi i\mathrm{n}\,\chi} \int V(\eta) e^{-i(\kappa+2\pi\mathrm{n})\,\eta} d\eta \;=\; \sum_{\mathrm{n}} e^{2\pi\mathrm{n}\,\chi} \hat{V}\left(\kappa + 2\pi\mathrm{n}\right) \tag{2.9}$$

$$\sum_{\mathrm{n}} e^{i\kappa\,(\chi - \mathrm{n})}\, V(\chi - \mathrm{n}) \;=\; \sum_{\mathrm{n}} e^{2\pi\mathrm{n}\,\chi} \hat{V}\left(\kappa + 2\pi\mathrm{n}\right) \tag{2.10}$$

We now reintroduce the physical coordinates $\mathrm{x} = \mathbf{R}\chi$ and define W as $V(\chi) = W(\mathrm{x})$

We have $\hat{V}(\kappa) = \hat{W}(\hat{\mathbf{R}}\kappa)/|\mathbf{R}|$ and

$$\begin{aligned}
\sum_{\mathbf{n}} e^{i\kappa\,\mathbf{n}}\, W(\mathbf{x}-\mathbf{R}\mathbf{n}) &= e^{i\kappa\,\mathbf{x}} \sum_{\mathbf{n}} e^{2\pi\mathbf{n}\,\mathbf{x}} \frac{\hat{W}\left(\hat{\mathbf{R}}\kappa + 2\pi\hat{\mathbf{R}}\mathbf{n}\right)}{|\mathbf{R}|} \\
\sum_{\mathbf{n}} e^{i\mathbf{k}\,\mathbf{R}\mathbf{n}}\, W(\mathbf{x}-\mathbf{R}\mathbf{n}) &= e^{i\mathbf{k}\,\mathbf{x}} \sum_{\mathbf{n}} e^{2\pi\hat{\mathbf{R}}\mathbf{n}\,\mathbf{x}} \frac{\hat{W}\left(\mathbf{k} + 2\pi\hat{\mathbf{R}}\mathbf{n}\right)}{|\mathbf{R}|} \qquad (2\,11)
\end{aligned}$$

where we let $\mathbf{k} = \hat{\mathbf{R}}\kappa$, the physical frequency We then proceed as in Cottet and Koumoutsakos (2000): we develop $e^{i\mathbf{k}\,\mathbf{R}\mathbf{n}}$ about 0 in the left-hand side and use the conditions 2 7 and 2 8 on the right-hand side

$$\begin{aligned}
\sum_{\nu} \frac{i^{|\nu|}\mathbf{k}^{\nu}}{\nu!} \sum_{\mathbf{n}} (\mathbf{R}\mathbf{n})^{\nu}\, W(\mathbf{x}-\mathbf{R}\mathbf{n}) &= e^{i\mathbf{k}\,\mathbf{x}} \frac{\hat{W}(\mathbf{k})}{|\mathbf{R}|} + \mathcal{O}(\mathbf{k}^m) \\
&= \sum_{\nu} \frac{i^{|\nu|}\mathbf{k}^{\nu}}{\nu!}\mathbf{x}^{\nu} + \mathcal{O}(\mathbf{k}^m)
\end{aligned}$$

The identification of the coefficients of k shows that the interpolation is of order m □

2.3 Hexagonal and Face-Centered Cubic Redistributions

2.3.1 Lattice Properties

The face-centered cubic lattice can be introduced in a couple of different ways, through mathematics or crystallography, for example Let us first consider the latter perspective A lattice can be defined in terms of a unit cell It is the simplest repeating unit in the crystal, has parallel opposite faces, and its edges connect equivalent points of the lattice

The face-centered cubic lattice bears its name from the configuration of its unit cell (see Fig 2 2) It is cubic and has additional lattice sites at the center of its faces

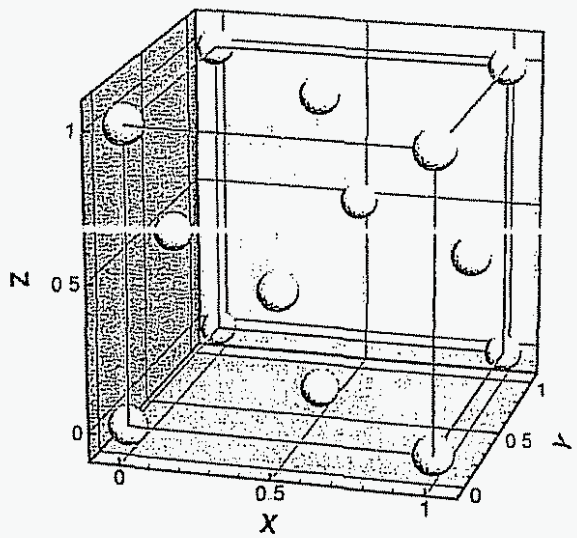

Figure 2.2: Face-centered cubic lattice: unit cell

The FCC lattice can also be constructed as the periodic stack of two-dimensional hexagonal lattices with the spacing between the layers at $\sqrt{6}/3h$ (Fig. 2.3(a)). There are three hexagonal lattices in a period A, B and C; if B lies at the origin of the coordinate system in Fig. 2.3(b), A is shifted by $(-1/2, -\sqrt{3}/6)$ and C, by $(1/2, \sqrt{3}/6)$.

This construction scheme highlights an outstanding feature of this lattice: it corresponds to the packing of spheres. As a matter of fact, the FCC lattice is one of two lattices that pack spheres the most densely. It is also called the Cubic Close Packing lattice. The second lattice to achieve this is the Hexagonal Close Packing lattice which is built from the packing of two families of hexagonal lattices.

On a side note, the question of finding the densest arrangement of spheres is an old and famous problem in mathematics. Kepler (Strena sue de nive sexangula, 1611) conjectured that the CCP— or FCC— and HCP lattices offered the densest arrangements with a density of $\frac{\pi}{\sqrt{18}} \approx 0.74048$. This conjecture was studied for centuries, starting with Gauss (1876) and proved only recently by Hales (1992, 1997a,b).

The equivalent close-packing lattice in two dimensions is obviously the hexagonal

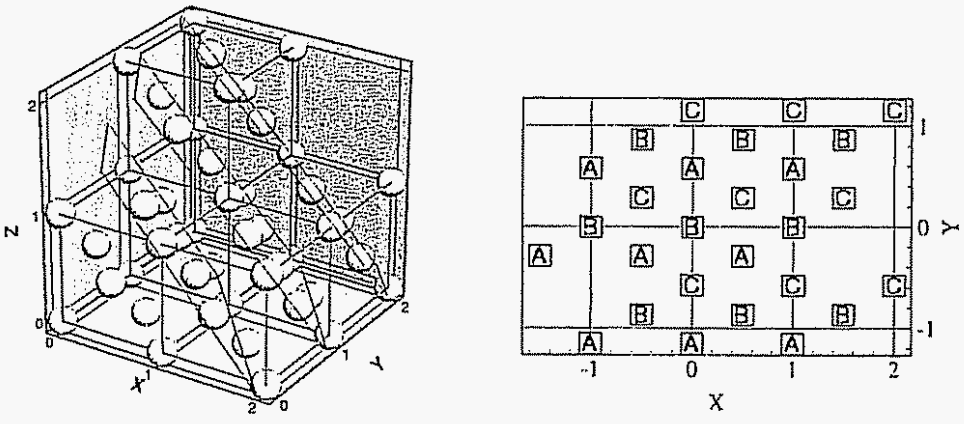

(a) Unit cells and hexagonal planes (b) Hexagonal lattices

Figure 2 3: Face-centered cubic lattice: construction with three families of hexagonal lattices

one which we used in the construction of Fig 2 3(b) This lattice already has the interest of the image treatment community (Merserau (1979) and Van De Ville et al (2004)) On the one hand, it can be the pixel pattern of a sensor that will produce digital images with the same pattern On the other, it can be interesting to resample and work on digitized images of that nature for their treatment because of the properties of the hexagonal lattice, e g edge recognition, etc

The advantages in our frame-work are also abundant The VEM indeed uses test and smoothing functions that have spherical–cylindrical in 2D–symmetry The close packing property is associated with very good symmetry and isotropy; a lattice site is surrounded by 12 equidistant neighbors, compared to 6 for a cubic lattice These natural properties can be beneficial in several ways:

1 The core overlap issue: Vortex elements on a FCC lattice will supposedly display a better behavior when subjected to strain

2 Redistribution functions: The lattice symmetries can be used to design more isotropic and compact schemes

3 The interaction with boundaries: The numerous symmetries will help reduce noise in quantities measured at the wall

Finally, let us mention that the matrices $\mathbf{R}$ and $\hat{\mathbf{R}}$ for the hexagonal and FCC lattices are given in appendix A

2.3.2 Interpolation Functions

Due to the nature of the close-packing lattices, we cannot use the tensor product of known one-dimensional functions to interpolate the particles strengths onto the new sites The use of the lattice coordinates would indeed lead to a non-isotropic redistribution The scheme construction has to be carried out in two and three dimensions from the start We propose two methods to build interpolation functions for the hexagonal and FCC lattices

Splines

In a first approach, one can use the same idea as for one-dimensional splines It consists in starting from the lowest order "closest-point" function and then taking successive convolutions of this function with itself For two or three dimensions such a function is also called the indicator function of the *Voronoi* cell $\mathfrak{C}$(Van De Ville et al , 2004) and is defined as

$$\chi(\mathbf{x}) = \begin{cases} 1 & \mathbf{x} \in \mathfrak{C} \\ 1/m_{\mathbf{x}} & \mathbf{x} \in \partial\mathfrak{C} \\ 0 & \mathbf{x} \notin \mathfrak{C} \end{cases} \tag{2 12}$$

where $m_{\mathbf{x}}$ is number of lattice sites which that position is equidistant to (i e , in 3 dimensions, 2 on a face, 3 or more on an edge, etc) By definition, the tiling of this function over the lattice sites forms a partition of unity and by consequence, the volume of those cells is $\int \chi(\mathbf{x})d\mathbf{x} = |\mathbf{R}|$ We define the functions $\mathfrak{F}_m$ as

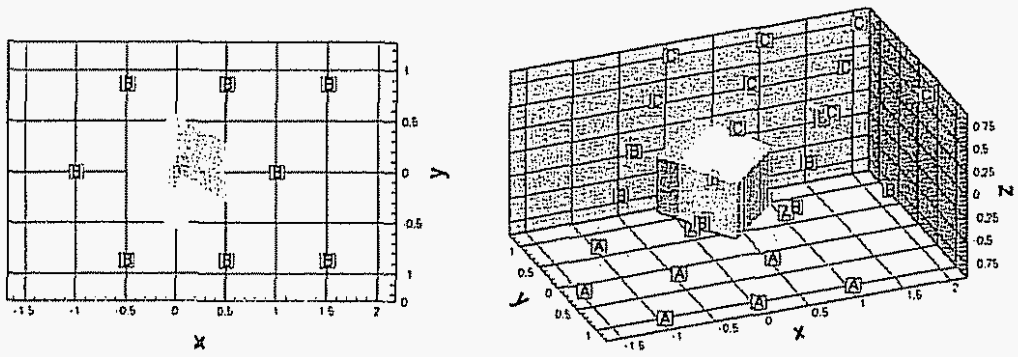

(a) *Hexagonal* (b) *FCC*

Figure 2 4: The hexagonal and face-centered cubic lattices and their Voronoi cells

$$\mathfrak{F}_0 = \chi(\mathbf{x}) \tag{2 13}$$

$$\mathfrak{F}_m = \mathfrak{F}_{m-1} * \mathfrak{F}_0 / \int \mathfrak{F}_0 dx \tag{2 14}$$

where we introduced the following notation for the convolution

$$(f * g)(\mathbf{x}) = \int f(\xi - \mathbf{x})\, g(\xi)\, d\xi$$

One sees that all the $\mathfrak{F}_m$'s will too form a partition of unity Interestingly enough, the functions for $m \geq 1$ show second order accuracy The Fourier transform of $\mathfrak{F}_0$ is a sinc function (see Van De Ville et al , 2004, II B); it vanishes at the dual lattice sites except the origin, $\hat{\mathfrak{F}}_0\left(2\pi\hat{\mathbf{R}}\mathbf{n}\right) = |\det(\mathbf{R})|\,\delta_{\mathbf{n}}$ $\hat{\mathfrak{F}}_1$ and its successors will therefore present the second order roots at the lattice sites necessary for second order interpolation

An analytical construction scheme is described in Van De Ville et al (2004) for the hexagonal lattice but it serves a purpose different from ours It builds increasingly smooth splines with a growing support whereas we are more interested in increasing the order of the redistribution (Eq 2 5) and in keeping the support small, thus preventing the creation of too many new elements

Compact High-Order Schemes

The nature of the FCC and hexagonal lattices allows the design of simple second order schemes, represented by a piecewise linear function In 2D, this yields the simple scheme represented in Fig 2 5(a) In the three-dimensional case, the interpolation construction is a bit more tedious To keep the scheme compact and follow the hexagonal lattice example, we need to consider redistribution inside the tetrahedrons and the octahedrons that constitute the face-centered cubic lattice In a tetrahedron, the function is linear Inside a octahedron, the function is built piecewise linear to be isotropic, second order, and remain continuous across these different regions

These schemes (given in Appendix A) are arguably the most compact second order schemes The hexagonal scheme redistributes onto three points Three degrees of freedom are needed to conserve the first two moments In three dimensions, the FCC scheme redistributes onto four or six points when four degrees of freedom are needed With their small support, good conservation properties, and relatively simple analytical expressions, they constitute an interesting starting point to build smoother and higher order interpolations

As a first step following the method described above for the splines, we take the convolution of these simple schemes by themselves and obtain C^2 schemes (Fig 2 5(b)) In doing so, we increase the support of our interpolation

The second step consists of increasing the order In the fashion of Monaghan (1985), we use the ansatz:

$$\tilde{W}(\mathbf{x}) = AW + B\,\mathbf{x}\cdot\nabla W \tag{2 15}$$

The generalization of this result to several dimensions and any type of lattice will be facilitated in Fourier space Let us assume that the Fourier transform $\hat{W}$ has, as described in theorem 1, a zero of order m at the origin and zeros of order $p \geq m+2$ at the sites of the dual lattice An example of such a function is the second order C^2 hexagonal function, for which $m = 2$ and $p = 4$ (Fig 2 6) We can use this m-order

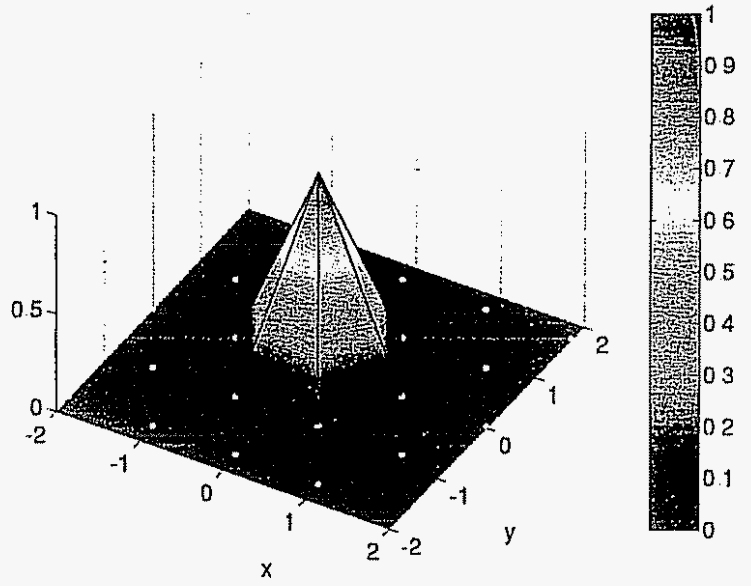

(a) C^0

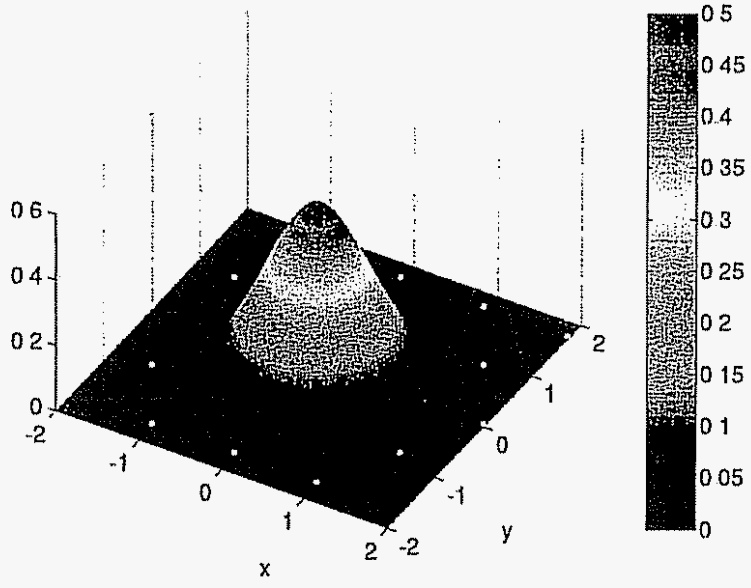

(b) C^2

Figure 2.5: Second order hexagonal schemes

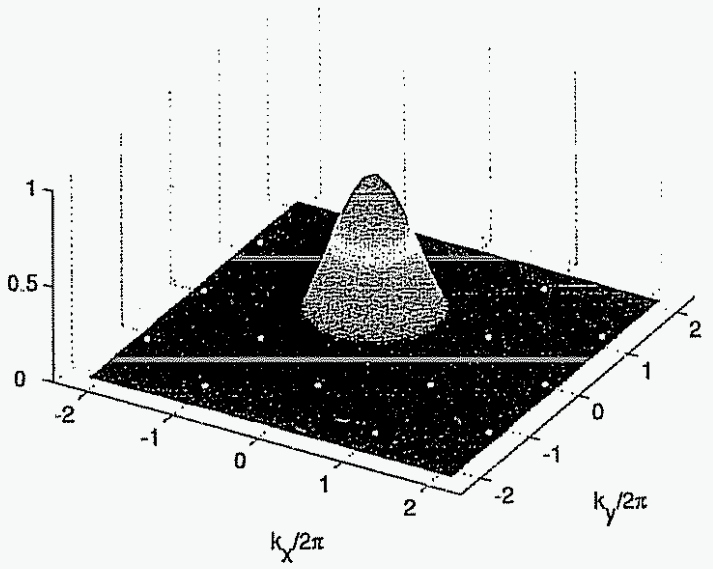

(a) C^0

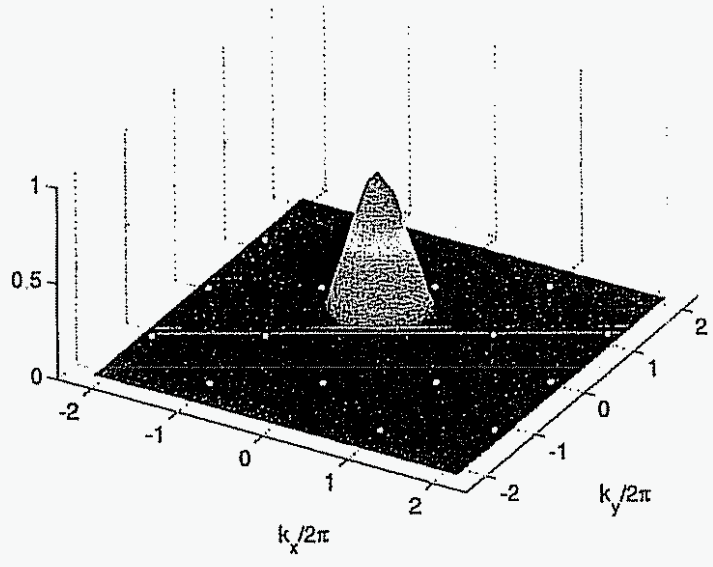

(b) C^2

Figure 2 6: Fourier transforms of the second order hexagonal schemes

scheme to build a $(m+1)$-order scheme:

$$\tilde{W}(\mathbf{x}) = (1 + \frac{n}{m})W + \frac{1}{m}\mathbf{x} \cdot \nabla W \tag{2 16}$$

Proof Let us consider the Fourier transform of $\tilde{W}$,

$$\begin{aligned}
\hat{\tilde{W}} &= \mathcal{F}(AW + B\,\mathbf{x} \cdot \nabla W) \\
&= A\hat{W} + B\,(i\nabla) \cdot \left(i\mathbf{k}\hat{W}\right) \\
&= A\hat{W} - B\,(\nabla \cdot \mathbf{k})\,\hat{W} - B\mathbf{k} \cdot \nabla\hat{W} \\
&= (A - nB)\,\hat{W} - B\mathbf{k} \cdot \nabla\hat{W}
\end{aligned} \tag{2 17}$$

where $n = \nabla \cdot \mathbf{k}$ is the number of dimensions

We will now solve for A and B to meet condition 2 7 $\hat{W} - |\mathbf{R}|$ and $\mathbf{k} \cdot \nabla\hat{W}$ both have a zero of order m at zero In order to have $\hat{\tilde{W}}(0) = |\mathbf{R}|$, we need to impose

$$A - nB = 1 \tag{2 18}$$

We can increase the order of that root Developing Eq 2 17 about 0, we get

$$\begin{aligned}
\hat{\tilde{W}}(\mathbf{k}) &= |\mathbf{R}| + (-1)^m \frac{\mathrm{M}_\nu}{m!}\mathrm{k}^\nu - B\,\mathbf{k} \cdot \nabla\left((-1)^m \frac{\mathrm{M}_\nu}{m!}\mathrm{k}^\nu\right) + \mathcal{O}\left(\mathrm{k}^{m+1}\right) \\
&= |\mathbf{R}| + (-1)^m \frac{\mathrm{M}_\nu}{m!}\mathrm{k}^\nu - B\,(-1)^m \frac{\mathrm{M}_\nu}{(m-1)!}\mathrm{k}^\nu + \mathcal{O}\left(\mathrm{k}^{m+1}\right)
\end{aligned} \tag{2 19}$$

where ν is a m-tuple, $1 < \nu_i < n$, $\mathrm{k}^\nu = k_{\nu_1} k_{\nu_2} \cdots k_{\nu_p}$, and summation over ν_i is implied The symmetry of the mth derivatives tensor was also used If one chooses $B = 1/m$, the extremum at zero will be of order $m+1$

Finally, the condition 2 8 will be satisfied as well because the term, $-B\mathbf{k} \cdot \nabla\hat{W}$ still has zeros of order $p - 1 \geq m + 1$ at all the dual lattice sites $\hat{\mathbf{R}}\mathbf{n}$ □

Using this result for the second order C^2 functions for the hexagonal and FCC lattices, we obtain the schemes shown in Fig 2 7(a) and Fig 2 8(a) We see that along with a more compact support (12 and 40 points, respectively), the Hex and FCC

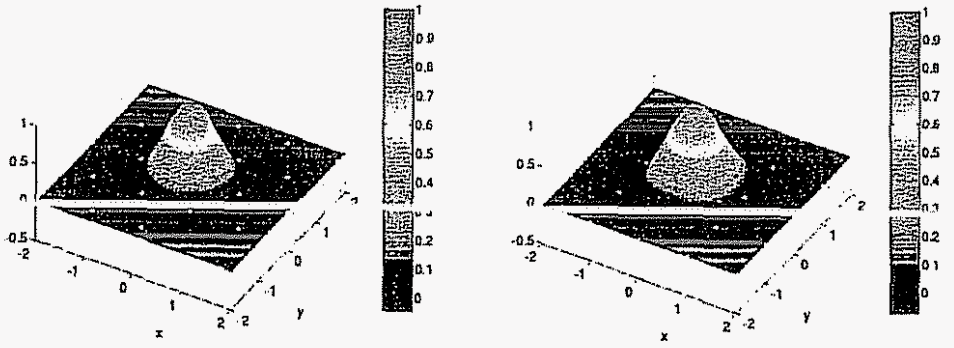

(a) H_3' (b) M_4'

Figure 2.7: Third order schemes in the Hexagonal (H_3') and cubic (M_4') lattices

schemes show better isotropy than their counterparts on a cubic lattice (Fig 2.7(b) and Fig 2.8(b)) built from the tensor product of 1D schemes

It is interesting to realize that this order improvement could also be applied to a second order scheme in a cubic lattice. This will obviously yield a scheme different from a tensor product of third order schemes. Let us consider the M_4' scheme in two dimensions. Built from the tensor product of one-dimensional schemes, it is

$$M_4'(x,y) = \left(\frac{3}{2}M_4(x) + \frac{1}{2}x\frac{dM_4}{dx}(x)\right)\left(\frac{3}{2}M_4(y) + \frac{1}{2}y\frac{dM_4}{dy}(y)\right)$$

Now applying the above construction in 2D to the scheme $M_4(x,y)$, we get

$$\begin{aligned} M_{4\,iso}'(x,y) &= 2M_4(x)M_4(y) + \frac{1}{2}(x,y)\cdot\nabla\left(M_4(x)M_4(y)\right) \\ &= M_4'(x,y) - (M_4'(x) - M_4(x))(M_4'(y) - M_4(y)) \end{aligned} \qquad (2.20)$$

This scheme has the same order and level of continuity as the regular M_4', but as shown in Fig 2.9, the lobes so characteristic of the tensor product have disappeared. One inconvenience though is the behavior of the scheme at the origin. The scheme does not reach the unit value, $M_{4\,iso}'(0,0) = \frac{8}{9}$. This is also true to a lesser degree for

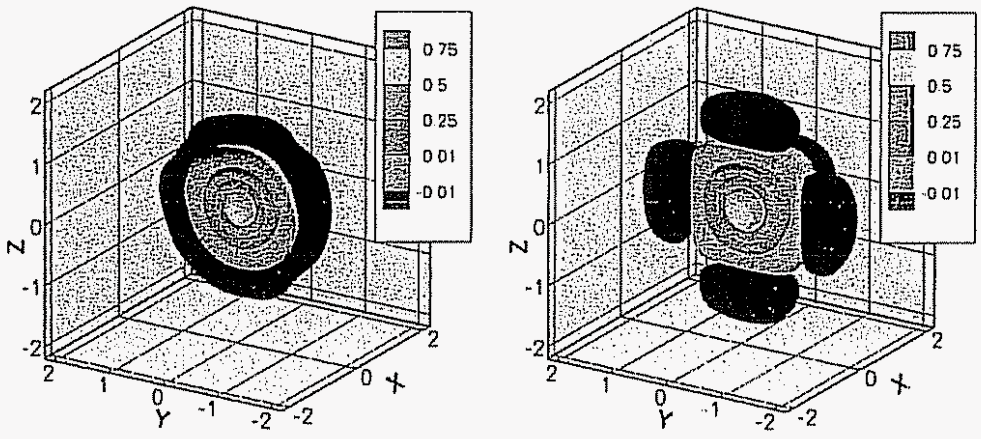

(a) F_3' (b) M_4'

Figure 2 8: Third order schemes in the FCC (F_3') and cubic (M_4') lattices

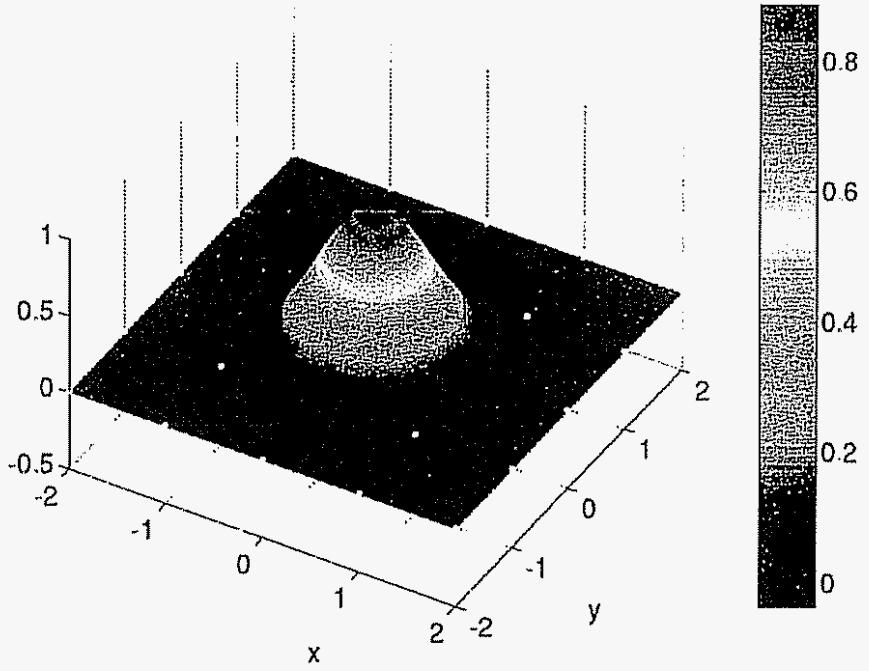

Figure 2 9: Isotropic third order scheme in the cubic lattice $M_{4\,iso}'$

the third order FCC scheme, F_3' The value at 0 is 0 95 The third order hexagonal scheme does reach 1

These two schemes therefore redistribute a particle already at a lattice site onto several sites, creating a slightly weaker particle surrounded by weak particles with positive and negative weights

2.4 Applications

2.4.1 Implementation

While the hexagonal functions could all be derived analytically, the high order FCC functions had to be computed The convolution of the C^0 scheme by itself and the gradient of Eq 2 16 were computed in Fourier space We then switched back to physical space to generate a look-up table

2.4.2 Test Cases

Our test consists in two colliding vortex rings This configuration deforms the set of particles and thus tests the quality of the core overlap through the simulation There are two sets of results The first one is a well resolved case at $Re = 250$ where we compare two second order schemes: the Λ_1 in the cubic lattice and our FCC_1 scheme The second set of results is at $Re = 500$ with a coarser resolution (thus under-resolved) and we consider the two second order schemes along with a third order scheme, M_4' The redistribution frequency (once every ten time steps) was the same in all of our tests

$Re = 250$

Because of the different lattices used, we define the grid Reynolds number as $Re_h = \frac{UV_p^{1/3}}{\nu}$ It will depend on the actual density of points The results in this section were obtained at $Re_h \approx 12 \rightarrow 4$ The FCC lattice introduces fewer points than the Λ_1

scheme and shows the same divergence error (Fig 2 10) The error decreases for $t > 6$ as the rings are decaying

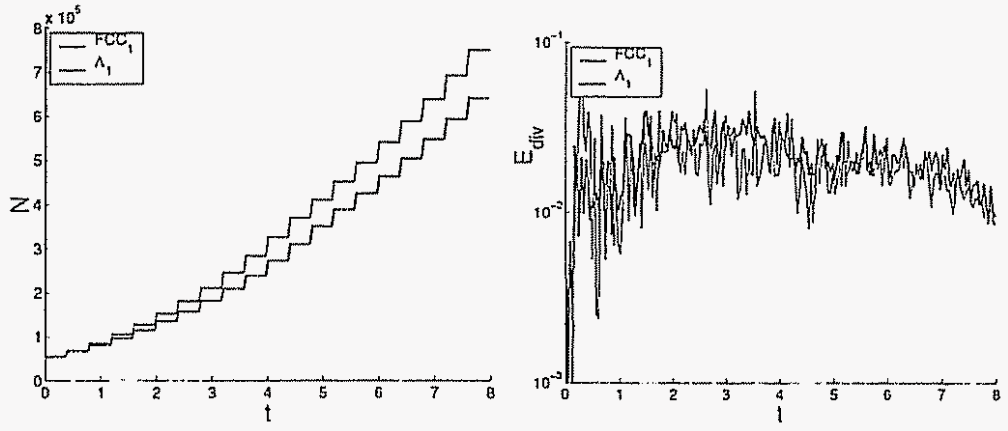

(a) Number of particles

(b) Field error

Figure 2 10: Colliding rings at $Re = 250$

$Re = 500$

We now consider the under-resolved case, $Re_h \approx 27 \rightarrow 13$ One can now notice a significant difference between the two second order schemes The error for the FCC_1 scheme stays at the level of the M_4' which introduces far more particles because of its wider stencil (Fig 2 11)

2.5 Conclusions

We have introduced the first representatives of a new family of interpolation schemes based on the face-centered cubic lattice Our schemes have two outstanding features:

1 Thanks to the many symmetries of the FCC lattice, they are more compact than the equivalent schemes in a cubic lattice This results in a slower growth of the number of particles because of a tighter *halo* of new particles around the

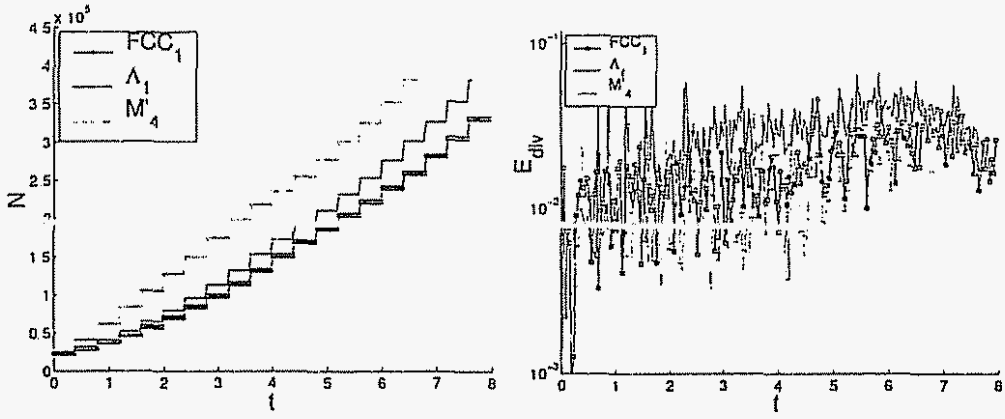

(a) Number of particles

(b) Field error

Figure 2 11: Colliding rings at $Re = 500$

set of old particles At the end of our runs, the number of elements for the FCC lattice was found to be $\sim 15\%$ lower than in the case of the equivalent cubic scheme (Λ_1)

2 Symmetry is also beneficial to the overlap of the particle cores and allows for better communication between the particles, even under stretching We have observed a significant reduction in the divergence error for high Re_h cases

Chapter 3

Reconnection of Vortex Rings

3.1 Introduction

In flow phenomena as diverse as quantum (Kivotides et al , 2002), magnetic (Christensson and Hindmarsh, 1999), and incompressible (Leonard, 1985) fluids, it is useful to study the physics of turbulence by modeling the system as a collection of tubular flux loops which in the case of vortical fields are called vortex filaments. An intrinsic property of such highly structured systems is their ability to dynamically change their topology via reconnection mechanisms. Does this change in topology affect in turn properties of fluid turbulence like intermittency and scalar-mixing (which depend directly on the structure of the flow) or the dynamics of energy in wavenumber space? Or is it the case that reconnection events are not generic and thus, have no direct impact on the mean properties of turbulent flows? The aim of this chapter is to address these issues by fully resolving the Navier-Stokes dynamics of interacting vortex rings for three simple geometries having great potential for illuminating the physics of reconnection. Although the flows considered are not strictly turbulent, the hope is that in a future structural approach to the problem of turbulence, a significant part of the flow complexity could be traced back to the physics of similar vortex interactions

Incompressible vortex reconnections have an extensive bibliography (for a review of the work up to 1994, see Kida and Takaoka (1994) and Kerr and Hussain (1989)). In Pelz (1997), Shelley et al (1993) and Pumir and Kerr (1987), reconnections of vortex tubes were considered with an emphasis on the possibility of singularity formation as $Re \to \infty$. In Winckelmans (1995), the strong interactions between vortex rings were computed with the interest in developing numerical methods and turbulence models rather than in focusing on the physics of reconnection. In Aref and Zawadzki (1991), it is discussed how a linked vortex configuration could be achieved starting from an unlinked initial state, and in Zawadzki and Aref (1991), it is considered how the mixing of a non-diffusing passive scalar is affected during vortex ring collision. The reconnection of two approaching (but not colliding) vortex rings was studied experimentally in Schatzle (1987) and theoretically in Ashurst and Meiron (1987). This chapter extends these studies by considering generic vortex configurations and by capturing more features of vortex reconnections in a turbulent flow.

3.2 Method

We solve the Navier-Stokes equations for an unbounded three-dimensional incompressible viscous flow. We employ the vortex element method introduced in Chapter 1, along with the face-centered cubic redistributions discussed in Chapter 2.

3.2.1 Diagnostics

We calculate the global kinetic energy E and enstrophy Ω defined as

$$E = \frac{1}{2}\int u \cdot u \, dx \,, \tag{3.1}$$

$$\Omega = \int \omega \cdot \omega \, dx \,. \tag{3.2}$$

For unbounded flows, the relation between kinetic energy and enstrophy is

$$\frac{d}{dt}E = -\nu\Omega \,. \tag{3.3}$$

3.2.2 Spectrum

We also compute the evolution of the spectrum of the kinetic energy $E(k)$ which, in terms of the Fourier transform of vorticity

$$\hat{\omega} = \frac{1}{(2\pi)^{3/2}} \int \omega(r)\, e^{-i\, r\, k}\, dr \ , \tag{3 4}$$

is defined as

$$E(k) = \frac{1}{2}(2\pi)^3 \int_{|k|=k} \hat{\omega} \cdot \hat{\omega}^*\, d\Omega_k \ , \tag{3 5}$$

where $d\Omega_k$ denotes $\sin\theta_k\, d\theta_k\, d\phi_k$, the solid angle element in spherical coordinates. The calculation of the spectrum requires a double summation over the vortex elements which results to $O(N^2)$ complexity. Because of this, the calculation of the spectrum is much more costly than the solution of the Biot-Savart law. Since the number of particles grows substantially during our simulations, from around $N = 5\,10^4$ at $t = 0$ to $8\,10^5$ in the end, our computational resources did not allow us to compute the spectra for all times. The details of the derivation and implementation are given in Appendix B.

3.3 Results

3.3.1 Configuration

All calculations were done with the same Reynolds number: $Re = \frac{\Gamma}{\nu} = 250$, where Γ is the circulation of one ring and ν is the kinematic viscosity. This small value of Re was dictated by the computational cost and the need for well-resolved reconnection regions. All the rings have the same initial Γ. All of our conclusions are conditioned upon the relatively small value of Re, as well as on the common initial circulation and should not be extrapolated uncritically to other settings. The initial vorticity distribution in the cross-section of every ring is Gaussian with a cutoff

$$\omega_\theta = \frac{\Gamma}{2\pi\sigma^2} e^{\frac{-r^2}{2\sigma^2}} \tag{3 6}$$

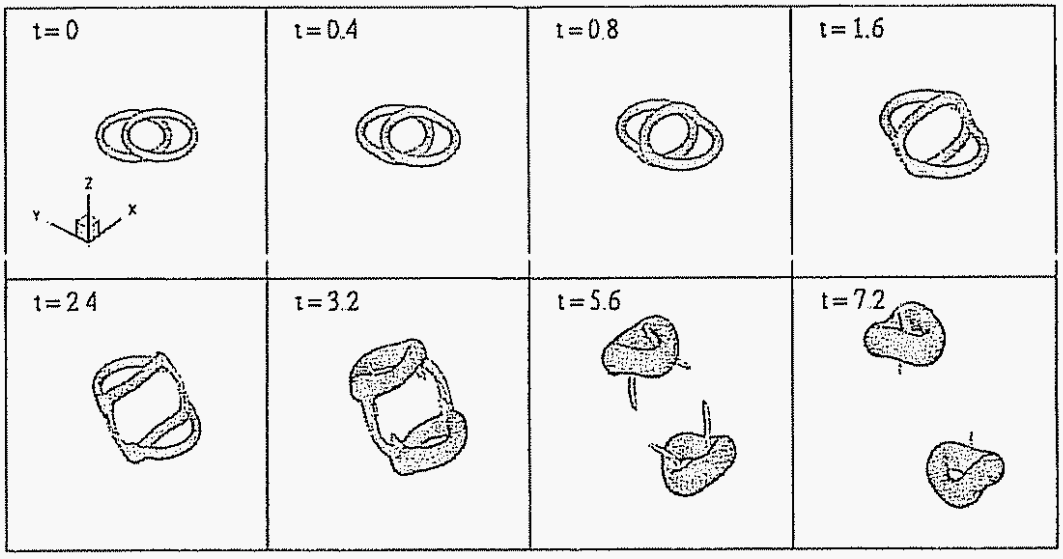

Figure 3.1: Vortex rings in an offset collision: contours of vorticity (from $t = 0$ to 2.4, the contour is $\omega = 0.15\,\omega_{\max}^{t=0}$; for $t > 2.4$, it is $\omega = 0.025\,\omega_{\max}^{t=0}$)

where r is the distance to the core center, σ is the core radius, and ω_θ is the azimuthal vorticity. We chose $\sigma = 0.05\,R$ (where R is the radius of the ring) to ensure that the rings are still thin when reconnections occur. Our results were made dimensionless in the following manner: $t = \frac{\Gamma t'}{R^2}$, $x = \frac{x'}{R}$, $\omega = \frac{R^2\omega'}{\Gamma}$ where t', x', ω' are dimensional.

We studied three configurations. In the first case (Fig. 3.1), the initial rings are placed at a distance of $R/4$ apart in the z direction, offset by R along the y axis and they move in opposite directions along the z axis.

In the second case (Fig. 3.2), two rings of different radii (R and $R/2$) and of initial separation $R/4$ are moving in the same direction along the z axis, with the center of the small ring on a collision course with the circumference of the large one. The small ring has a larger self-induced velocity and catches up with the large ring.

Finally, in the third case (Fig. 3.3), the two rings are linked at 90°, a ring going through the other in its center. One is moving in the positive z direction, the other in the positive y direction.

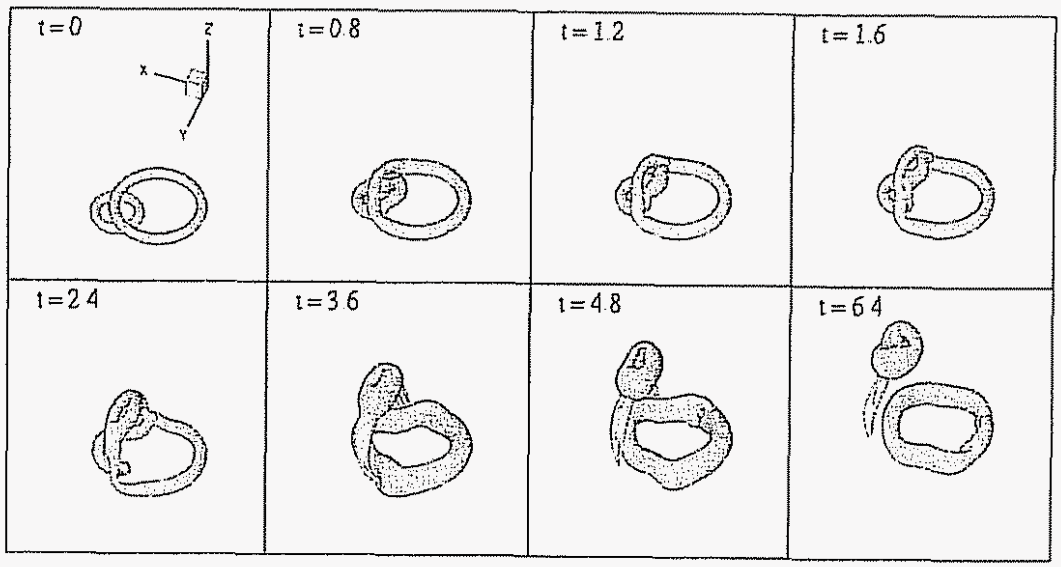

Figure 3.2: Vortex rings of different radii: contours of vorticity (from $t = 0$ to 2.4, the contour is $\omega = 0.15\,\omega_{max}^{t=0}$; for $t > 2.4$, it is $\omega = 0.05\,\omega_{max}^{t=0}$)

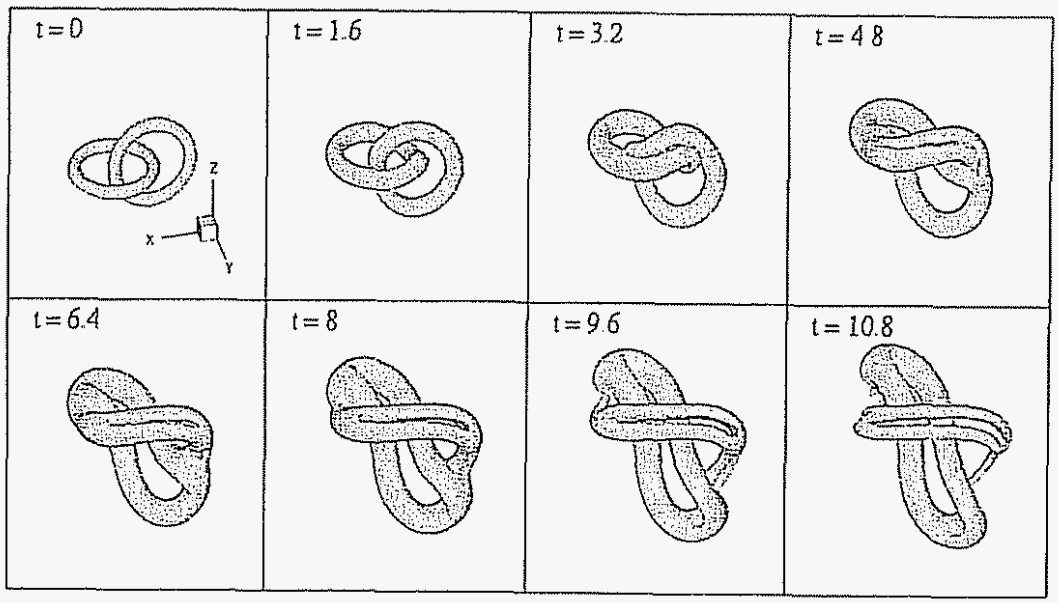

Figure 3.3: Linked vortex rings: contours of vorticity; $\omega = 0.025\,\omega_{max}^{t=0}$

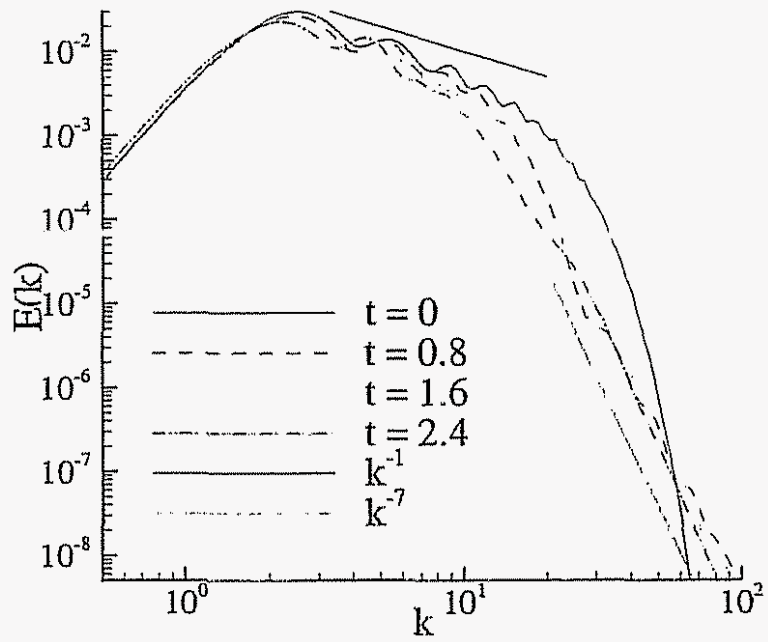

Figure 3.4: Vortex rings in an offset collision: evolution of the energy spectrum

3.3.2 Discussion

All three evolutions lead to ring reconnection (Figs. 3.1, 3.2 and 3.3) and have common features. The latter will be discussed here in the context of the first configuration, observing that the phenomena are the same for the other two cases. The spectrum at $t = 0$ (Fig.3.4) has the characteristic oscillations of the spectrum of isolated vortex rings and a cutoff at the scale of ring core radius $\sigma = 0.05$, $k = 20$. Our results (Figs. 3.1 and 3.5) suggest that the reconnection starts approximately around $t = 0.6$ and ends around $t = 1.75$ with a duration $\Delta t_r = 1.15$. Specifically, as the rings approach each other, they stretch and deform near the collision points so that their respective vorticities become locally anti-parallel. The two ends of this stretching region eventually become reconnection kinks where in the absence of singularities, the strong vorticity gradients are smoothed out by diffusion. This is also seen in the graphs of the global quantities (Fig. 3.5) where the beginning of the reconnection process corresponds to a hump in the graph of Ω and to a steepening of the slope

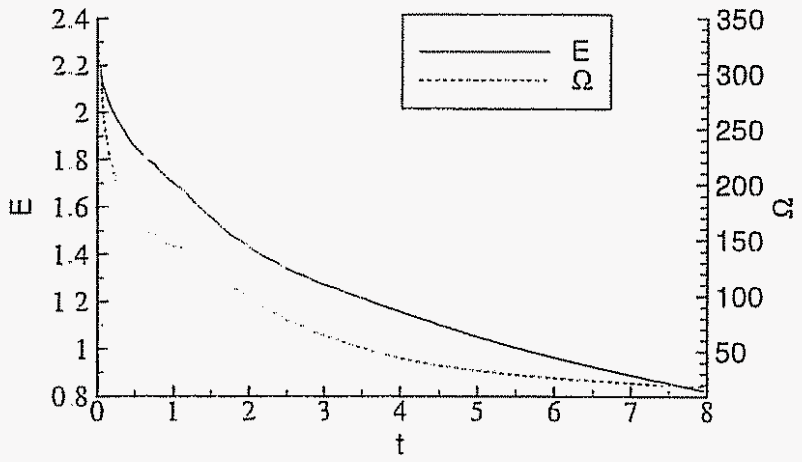

Figure 3.5: Vortex rings in an offset collision: kinetic energy and enstrophy

of $E(t)$ between $t = 0.6$ and $t = 1.4$. Our calculation predicts that the filament core radius increases from the initial value $\sigma_0 = 0.05R$ to the value at reconnection $\sigma_r = 0.12R$ due to diffusion. Using this latter value, we calculate the viscous time scale $t_v = \sigma_r^2/\nu = 0.36$. Scaling the convective ring velocity with $\Gamma/4\pi R$, we estimate the time needed for a ring to traverse σ_r: $t_c = 4\pi R\sigma_r/\Gamma = 1.5$. These times are of the same order as Δt_r; this indicates that both viscous and convective phenomena participate in the reconnection physics. The relative magnitudes of t_v and Δt_r are different from the ones in Schatzle (1987) where the Reynolds number was 1600 and the viscous time scale was therefore much larger than the duration of reconnection.

After some time (Fig. 3.6), we can say that two new rings are formed. The pairs of filaments between the reconnection regions are stretched further as the new rings move apart from each other ($t = 1.6$ to 5.6). These stretched vorticity structures are responsible for a continued transfer of energy to the smallest scales until these structures are dissipated away. This conclusion is supported by the results displayed in Fig. 3.4. The initial exponential cutoff of the spectrum gives way to a non-exponential region (although it still remains very steep) for $t \geq 0.8$. The spectrum still has an exponential cutoff that lies outside the range of Fig. 3.4; this cutoff corresponds to scales close to the particle core size. Between $t = 0.8$ and 2.4 there is a significant

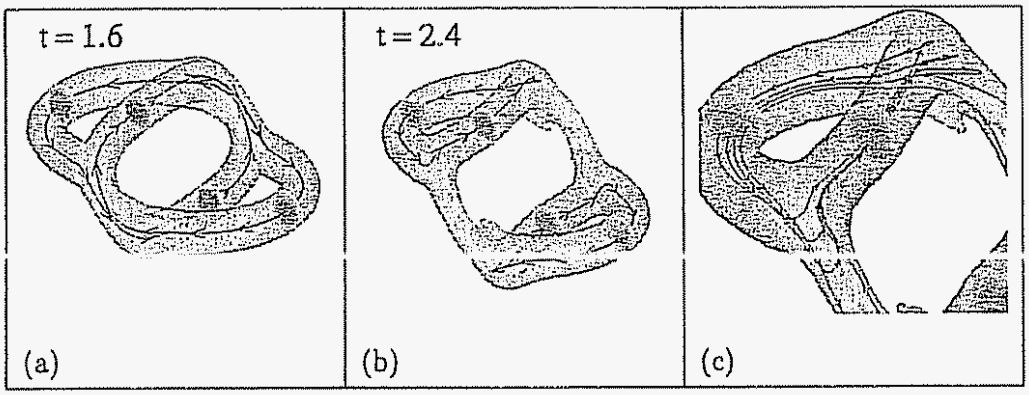

Figure 3.6: Vortex rings in an offset collision: contour of vorticity and vortex lines at $t = 1.6$ and 2.4; the transparent contour is $\omega = 0.025\,\omega_{max}^{t=0}$; the vortex lines in (a) and (b) were chosen to pass through the vortex core center (the maximum value of ω) at a location away from the reconnection kinks; in (c), a few neighboring lines are also shown for $t = 2.4$

decay of the energy spectrum for $k < 20$, but little change for $k > 20$. This last observation indicates that in the small scales of motion, an approximate balance between energy transfer from large scales due to stretching and local energy dissipation due to diffusion is temporarily attained. This conclusion is also consistent with the vorticity structure shown in Fig. 3.7 where it is observed that between $t = 0.8$ and $t = 2.4$ (the time of the last spectrum calculation), the vorticity magnitude in the secondary structures (where the global maximum of vorticity resides) stops increasing and in fact it decays slightly.

It is conceivable that for *Re* numbers higher than 250, an intermediate scaling range that is in between the k^{-1} and k^{-7} regimes could appear with inertial type of scaling. It is also expected that with increasing *Re* number, the hump observed in the global enstrophy during the reconnection could become more pronounced and (according to the previous discussion) shorter in duration

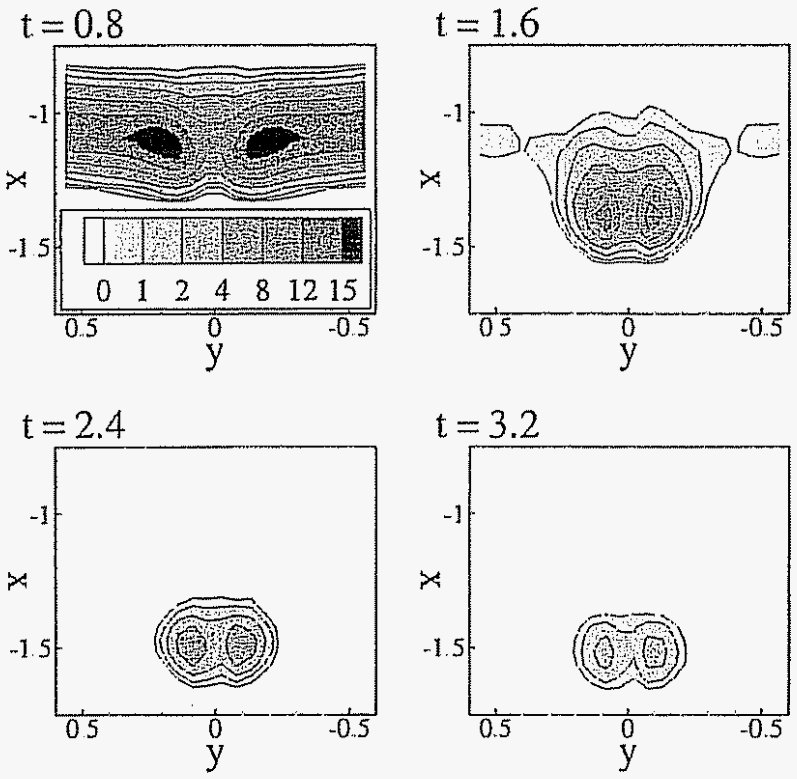

Figure 3.7: Vortex rings in an offset collision: contours of vorticity magnitude in the plane $z = 0$ from $t = 0.8$ to 3.2

3.4 Conclusions

In conclusion, we studied three generic vortex ring configurations and we found that in all cases, the rings reconnect. This suggests that reconnection is a common phenomenon in vortex filament encounters and perhaps also in turbulent flows. In addition, we observe an intensification of dissipation which is local in time and could be a mechanism contributing to turbulence intermittency.

A by-product of reconnection is the formation of stretched structures with antiparallel vorticity which transfer energy to the smallest scales where it is rapidly dissipated. Without this energy redistribution in wavenumber space, the decay of global kinetic energy would have been slower. This important effect depends directly on the details of the initial vortex configuration (compare with experiments in Schatzle (1987)). The observed intensification of small scale motions hints to an enhancement of small scale mixing of passive scalars with $Sc \geq 1$

The excited Kelvin waves represent a fast mechanism for energy transfer, but the small Re number of our calculations is not suitable for understanding their full importance. In particular, they are confined to low wavenumbers in opposition to the Kelvin waves observed in reconnections in quantum fluids (Kivotides et al., 2001). This is because quantum filaments are inviscid and have a very thin core ($\sigma \sim 0.1\,nm$) so that high wavenumber Kelvin waves propagate without damping even for rings with small circulation.

Besides illuminating important physics, the present work will guide future introduction of phenomenological reconnection models into vortex filament computational methods. In this way, the applicability of the latter methods will be extended to flows with complex vorticity configurations.

Chapter 4

Flows Around Rotating and Deforming Boundaries

4.1 Introduction

The Lagrangian nature of the Vortex element method makes it quite appealing for external flows around complex and evolving geometries. The applications are numerous. An obvious one is the family of biological flows which cover a wide range of Reynolds numbers, with insect flight in the medium range of $Re \simeq 100 \rightarrow 300$. This chapter focuses on the additional steps needed in the framework of vortex methods to account for the rotation or deformation of the boundaries. We cover some fundamentals and existence results in Section 4.2; we then study the Biot-Savart boundary terms in Section 4.3. In Section 4.4, we consider the boundary conditions on vorticity. Finally, we discuss the conservation of global quantities for such flows in Section 4.5.

4.2 Kinematics

In a first step, let us consider the flow exterior to a set of bodies $\Omega_i(t)$, i.e. $\mathbb{R}^3 \backslash \cup\{\Omega_i(t)\}$ as our flow domain. We consider the usual Helmholtz decomposition of the velocity

field,

$$\mathbf{u} = \mathbf{u}_\omega + \mathbf{u}_\phi \tag{4.1}$$

$$= \nabla \times \psi + \nabla\phi \tag{4.2}$$

where we fix the gauge of ψ as $\nabla \quad \psi = 0$ We restrict ourselves to the case of incompressible flows. We therefore have

$$\nabla^2\psi = -\nabla \times \mathbf{u} = -\omega\,, \tag{4.3}$$

$$\nabla^2\phi = 0 \tag{4.4}$$

Boundary conditions have to be imposed on the velocity field with the no-slip condition at the solid boundaries

$$\mathbf{u}(\mathbf{x})|_{\mathbf{x}\in\partial\Omega_i(t)} = \mathbf{u}|_{\partial\Omega_i(t)} \tag{4.5}$$

and possibly a free-stream velocity

$$\mathbf{u}|_{\mathbf{x}\to\infty} = \mathbf{u}_\infty\,. \tag{4.6}$$

4.2.1 Extended Domain and Fields

The development of field computations and boundary conditions can quickly become tedious if one considers the domain $\mathbb{R}^3 \setminus \cup\{\Omega_i(t)\}$. The extension of the fields to $\mathbb{R}^3$ facilitates our work, even more so in the case of deforming boundaries. More explicitly, we consider the extensions of ψ, ω and $\mathbf{u}$ to $\mathbb{R}^3$. The extended velocity field may therefore have some divergence inside the immersed bodies since general deformations may involve some dilatation.

If we make the required assumptions about the regularity of the velocity field, we can apply Poincaré's formula (Brard (1973) and Cottet and Koumoutsakos (2000))

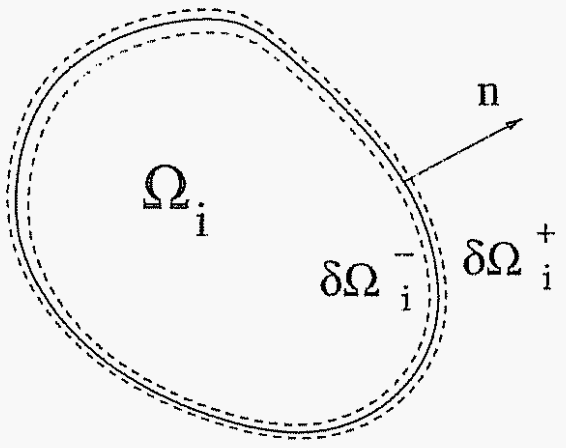

Figure 4.1: Boundaries and sign convention

inside Ω_i

$$\nabla \times \left(\int_{\partial\Omega_i^-} G(\mathbf{x}-\mathbf{x}') \left(-\mathbf{n} \times \mathbf{u}^-(\mathbf{x}')\right) dS + \int_{\Omega_i} G(\mathbf{x}-\mathbf{x}')\, \omega(\mathbf{x}')\, d\mathbf{x}' \right) +$$
$$\nabla \left(\int_{\partial\Omega_i^-} -G(\mathbf{x}-\mathbf{x}') \left(-\mathbf{n} \cdot \mathbf{u}^-(\mathbf{x}')\right) dS + \int_{\Omega_i} -G(\mathbf{x}-\mathbf{x}') \left(\nabla \cdot \mathbf{u}(\mathbf{x}')\right) d\mathbf{x}' \right) \quad (4.7)$$
$$= \begin{cases} \mathbf{u}(\mathbf{x}) & \mathbf{x} \in \Omega_i \\ 0 & \mathbf{x} \in \mathbb{R}^3 \setminus \Omega_i \end{cases}$$

and outside Ω_i

$$\nabla \times \left(\int_{\cup\partial\Omega_i^+} G(\mathbf{x}-\mathbf{x}') \left(\mathbf{n} \times \mathbf{u}^+(\mathbf{x}')\right) dS + \int_{\mathbb{R}^3 \setminus \cup\Omega_i} G(\mathbf{x}-\mathbf{x}')\, \omega(\mathbf{x}')\, d\mathbf{x}' \right) +$$
$$\nabla \left(\int_{\cup\partial\Omega_i^+} -G(\mathbf{x}-\mathbf{x}') \left(\mathbf{n} \cdot \mathbf{u}^+(\mathbf{x}')\right) dS + \int_{\mathbb{R}^3 \setminus \cup\Omega_i} -G(\mathbf{x}-\mathbf{x}') \underbrace{\left(\nabla \cdot \mathbf{u}(\mathbf{x}')\right)}_{=0} d\mathbf{x}' \right) \quad (4.8)$$
$$= \begin{cases} \mathbf{u}(\mathbf{x}) & \mathbf{x} \in \mathbb{R}^3 \setminus \cup\Omega_i \\ 0 & \mathbf{x} \in \cup\Omega_i \end{cases}$$

We assume that there is no through-flow, i.e., $\mathbf{n} \cdot \mathbf{u}^+ = \mathbf{n} \cdot \mathbf{u}^-$. The sum of the two

above equations gives us an expression for the velocity in the extended domain $\mathbb{R}^3$

$$\begin{aligned}\mathbf{u}(\mathbf{x}) = (\mathbf{K}\times) * \omega_{\cup\Omega_i} - \mathbf{K} * \sigma_{\cup\Omega_i} + (\mathbf{K}\times) * \omega_{\mathbb{R}^3\setminus\cup\Omega_i} \\ + \int_{\cup\partial\Omega_i} \mathbf{K}(\mathbf{x}-\mathbf{x}')\times\gamma(\mathbf{x}')dS\,;\end{aligned} \tag{4.9}$$

where $\mathbf{K} = \nabla G$ The different terms on the right-hand side of Eq. 4.9 deserve some attention:

- $\omega_{\cup\Omega_i}$ is the vorticity inside the bodies present in the flow;
- $\sigma_{\cup\Omega_i}$ is the dilatation $\nabla\cdot\mathbf{u}$ inside the bodies;
- $\omega_{\mathbb{R}^3\setminus\cup\Omega_i}$ is the vorticity present in the flow;
- $\gamma = \mathbf{n}\times(\mathbf{u}^+ - \mathbf{u}^-)$ are bound vortex sheets which have to appear in order to enforce the kinematic condition of Eq 4.5.

For boundaries that move as if they were the boundaries of rigid objects, the first two items can be simplified, the vorticity "inside" the bodies reduces to twice their angular velocities $2\mathbf{W}_i$, and the dilatation is null

Before proceeding, we introduce the notations $\mathbf{u}_i$, ω_i and σ_i; these will refer to the known velocity, vorticity and divergence fields inside the deforming object Ω_i, up to and including $\partial\Omega_i^-$.

4.2.2 Boundary Vorticity and Integral Equations

Let us now concentrate on the boundary vorticity term. This term is an unknown that is solved for through the enforcement of the boundary conditions. One can consider either through-flow or slip cancellation at the wall. If we use the latter, we have to consider the limit of the tangential component of Eq. 4.9 for $\mathbf{x}\to\mathbf{x}_{\partial\Omega_i^-}$,

$$\mathbf{u}\cdot\mathbf{t} \to \left(\mathbf{u}_{\text{ext}} - \frac{\gamma\times\mathbf{n}}{2} + \int_{\cup\partial\Omega_i}\mathbf{K}\times\gamma\,dS\right)\cdot\mathbf{t}\,, \tag{4.10}$$

where u_{ext} regroups the first three terms of the right-hand side of Eq 4 9 and the vectors t lie in the local tangent plane If we match this value to the tangential wall velocity, we obtain

$$\left(\frac{\gamma \times n}{2} - \int_{\cup \partial\Omega_i} K \times \gamma \, dS\right) \cdot t = (u_{ext} - u_i) \cdot t \tag{4.11}$$

Well-Posedness

Eq. 4.11 is a Fredholm equation of the second kind which justifies our earlier choice of the no-slip condition; this guarantees well-posedness when we switch to finite dimension spaces for the solution, i.e., we use a panel discretization.

Existence

Brard (1973) considers the existence issue for Eq. 4 11 without the projection into the local tangential plane ($\cdot t$)

$$T\gamma = \left(-\frac{n\times}{2} - \int_{\cup \partial\Omega_i} K \times \, dS\right) \gamma = u_{ext} - u_i \tag{4.12}$$

The existence condition requires that the right-hand side be orthogonal to $\ker(T^*)$, which is formed by the functions $\xi(x') = \text{const}\, n(x')$ The condition is then

$$\int_{\cup \partial\Omega_i^-} n \cdot (u_{ext} - u_i) = 0\,; \tag{4 13}$$

By the divergence theorem, we have

$$\int_{\cup \Omega_i} \nabla \cdot (u_{ext} - u_i) = 0\,; \tag{4 14}$$

which is satisfied because $\nabla \cdot u_i = \nabla \cdot u_{ext} = \sigma_i$ inside Ω_i

Because we use the projection above, this existence condition is implicitly imposed We should however verify that the no through-flow condition will be enforced as well

We have

$$\begin{aligned} \nabla \times (\mathbf{u} - (\mathbf{K}\times) * \omega_{\Omega_i} + \mathbf{K} * \sigma_{\Omega_i}) &= 0 \\ \nabla \cdot (\mathbf{u} - (\mathbf{K}\times) * \omega_{\Omega_i} + \mathbf{K} * \sigma_{\Omega_i}) &= 0 \end{aligned}$$

for $\mathbf{x} \in \Omega_i$ $(\mathbf{u} - (\mathbf{K}\times) * \omega_{\Omega_i} + \mathbf{K} * \sigma_{\Omega_i})$ can therefore be expressed as the gradient of a harmonic field Φ inside the boundary Ω_i

$$(\mathbf{u} - (\mathbf{K}\times) * \omega_{\Omega_i} + \mathbf{K} * \sigma_{\Omega_i}) = \nabla\Phi \text{ with } \Delta\Phi = 0 .$$

Solving Eq 4 11 thus sets Φ to a constant on $\partial\Omega_i^-$ By the maximum principle, Φ is constant in Ω_i, thus implying that $\mathbf{u} \cdot \mathbf{n} = \partial\Phi/\partial n = 0$.

Uniqueness

Uniqueness issues will appear if the operator on the left-hand side of Eq 4.11 has a non-trivial kernel This in turn will depend on the topology of the problem; non-simply-connected $\partial\Omega_i$ will allow non-unique solutions This is the case for any object in two dimensions and for objects with holes in three dimensions.

For such cases, $\dim(\ker[T])$ additional conditions have to be enforced; they are found by applying Kelvin's circulation theorem to irreducible loops in the domain (*Cottet and Koumoutsakos, 2000*) *For the moment, we will restrict ourselves to* simply-connected geometries

4.3 Boundary Contributions

Eq. 4.9 shows that the velocity used in Eq 1.9 and 1 10 must include additional contributions from the objects in addition to the usual Biot-Savart terms $(\mathbf{K}\times) * \omega_{\mathbb{R}^3\setminus\cup\Omega_i}$, and $\int_{\cup\partial\Omega_i} \mathbf{K}(\mathbf{x}-\mathbf{x}') \times \gamma(\mathbf{x}')dS$, if there are bound vortex sheets We proceed

and call these contributions $\mathbf{u}_b$,

$$\mathbf{u}_b = (\mathbf{K}\times) * \omega_{\cup\Omega_i} - \mathbf{K} * \sigma_{\cup\Omega_i} + (\mathbf{K}\times) * \omega_{\mathbb{R}^3\setminus\cup\Omega_i} , \tag{4.15}$$

ψ_b and ϕ_b for the corresponding stream function and potential,

$$\psi_b = G * \omega_{\cup\Omega_i} + G * \omega_{\mathbb{R}^3\setminus\cup\Omega_i} \tag{4.16}$$

$$\phi_b = -G * \sigma_{\cup\Omega_i} \tag{4.17}$$

These terms are volume integrals which may not have a convenient discretization; one might rather have a panel representation of the boundary In addition, these terms involve quantities that are not known in practical problems Indeed, let us consider the swimming motion of a fish where the kinematics are imposed One may not realistically know the velocity field and deformations inside the fish and will only impose the displacement of the skin of the fish Similarly, from a physical point of view, the details of the deformations inside the objects should not have an influence on the velocity field in the flow For these reasons, the present section covers methods to transform those volume integrals into surface integrals

4.3.1 Rigid Objects

In the case of a rigid object, the dilatation sources are null and the vorticity is a constant equal to twice the angular velocity We start from the stream function:

$$\psi_b(\mathbf{x}) = \sum_i 2\mathbf{W}_i \int_{\Omega_i} G(\mathbf{x}-\mathbf{x}')d\mathbf{x}' \tag{4.18}$$

If we rewrite the Green's function

$$G(\mathbf{u}) = \frac{1}{4\pi}|\mathbf{u}|^{-1} = \frac{1}{4\pi}\nabla\cdot\left(\frac{\mathbf{u}}{2|\mathbf{u}|}\right) , \tag{4.19}$$

we obtain, by the divergence theorem

$$\psi_b(\mathbf{x}) = -\sum_i \frac{\mathbf{W}_i}{4\pi} \int_{\partial\Omega_i} \frac{\mathbf{x}-\mathbf{x}'}{|\mathbf{x}-\mathbf{x}'|} \cdot \mathbf{n} dS(\mathbf{x}') \tag{4.20}$$

The velocity field and its gradient can then be obtained by successively taking the curl and the gradient of the above expression:

$$\mathbf{u}_b(\mathbf{x}) = \sum_i \frac{\mathbf{W}_i}{4\pi} \times \int_{\partial\Omega_i} \frac{\mathbf{n}}{|\mathbf{x}-\mathbf{x}'|} - \frac{((\mathbf{x}-\mathbf{x}')\cdot\mathbf{n})(\mathbf{x}-\mathbf{x}')}{|\mathbf{x}-\mathbf{x}'|^3} dS(\mathbf{x}') \tag{4.21}$$

$$\begin{aligned} \nabla\mathbf{u}_b(\mathbf{x}) = \sum_i \frac{\mathbf{W}_i}{4\pi} \times \int_{\partial\Omega_i} & - \frac{\mathbf{n}(\mathbf{x}-\mathbf{x}') + (\mathbf{x}-\mathbf{x}')\mathbf{n} + ((\mathbf{x}-\mathbf{x}')\cdot\mathbf{n})\mathbf{I}}{|\mathbf{x}-\mathbf{x}'|^3} \\ & + \frac{3((\mathbf{x}-\mathbf{x}')\cdot\mathbf{n})(\mathbf{x}-\mathbf{x}')(\mathbf{x}-\mathbf{x}')}{|\mathbf{x}-\mathbf{x}'|^5} dS(\mathbf{x}') \end{aligned} \tag{4.22}$$

Contour Dynamics

One can notice that by taking the curl of Eq. 4.3, we obtain the following expression

$$\nabla^2\mathbf{u} = -\nabla\times\omega \tag{4.23}$$

which is at the basis of contour dynamics (Zabusky et al., 1979) If we consider patches of constant vorticity in three dimensions, $\nabla\times\omega$ is only non-zero and singular at the boundaries of the patches We apply Green's function to obtain an alternative to Eq. 4.21,

$$\mathbf{u}_b = \sum_i \frac{2\mathbf{W}_i}{4\pi} \times \int_{\partial\Omega_i} \frac{\mathbf{n}}{|\mathbf{x}-\mathbf{x}'|} dS(\mathbf{x}') \tag{4.24}$$

This approach, while yielding a simple expression for the velocity, makes no provision for the stream function. Also of interest is that the velocity is not expressed as a curl; the error made in the multipole approximation could therefore have some divergence.

Implementation

The integrals 4 20, 4 21 and 4 22 can be evaluated with a panel description of the boundaries As for the regular Biot-Savart law, we have to accelerate their computation through the use of multipole expansions We detail this procedure in Appendix D along with the development of the error bound

4.3.2 Deforming Objects

In the case of general deformations, it is far more difficult to find a surface-based integral We present some expressions for velocity Using the idea of contour dynamics, we have, for constant volume deformations,

$$\mathrm{u}_b(\mathrm{x}) = \sum_i \int_{\partial\Omega_i} G(\mathrm{x}-\mathrm{x}')\omega_i(\mathrm{x}') \times \mathrm{n}\, dS + \sum_i \int_{\Omega_i} G(\mathrm{x}-\mathrm{x}')\,(\nabla \times \omega_i)\,(\mathrm{x}')\, d\mathrm{x}' \quad (4.25)$$

The second term can be rewritten in terms of velocity, thanks to the identity $\nabla \times \nabla \times \mathrm{u} = \nabla(\nabla \cdot \mathrm{u}) - \nabla^2 \mathrm{u}$ with $\nabla \cdot \mathrm{u} = 0$,

$$\mathrm{u}_b(\mathrm{x}) = \sum_i \int_{\partial\Omega_i} G(\mathrm{x}-\mathrm{x}')\omega_i(\mathrm{x}') \times \mathrm{n}\, dS - \sum_i \int_{\Omega_i} G(\mathrm{x}-\mathrm{x}')\nabla^2 \mathrm{u}_i(\mathrm{x}')\, d\mathrm{x}' \quad (4.26)$$

We can then use Green's second identity

$$\int_V \left(f\nabla^2 g - g\nabla^2 f\right)\, dV = \int \left(f\nabla g - g\nabla f\right) \cdot \mathrm{n}\, dS$$

to obtain

$$\begin{aligned} \mathrm{u}_b(\mathrm{x}) = &\sum_i \int_{\partial\Omega_i} G(\mathrm{x}-\mathrm{x}')\omega_i(\mathrm{x}') \times \mathrm{n}\, dS - \sum_i \int_{\Omega_i} \nabla^2_{\mathrm{x}'}(G(\mathrm{x}-\mathrm{x}'))\mathrm{u}_i(\mathrm{x}')\, d\mathrm{x}' \\ &+ \sum_i \int_{\partial\Omega_i} \left(\mathrm{u}_i \nabla_{\mathrm{x}'}(G(\mathrm{x}-\mathrm{x}')) - G(\mathrm{x}-\mathrm{x}')\nabla_{\mathrm{x}'}\mathrm{u}_i\right) \cdot \mathrm{n}\, dS \end{aligned} \quad (4.27)$$

We see that the second term is null because x lies outside the objects Ω_i

A similar approach can be followed for dilatation. For irrotational flows, one has

$$\nabla^2 \mathrm{u} = \nabla \sigma \,, \tag{4.28}$$

which gives us the expression of velocity

$$\mathrm{u}_b^{\sigma}(\mathrm{x}) = \sum_i \int_{\partial\Omega_i} G(\mathrm{x}-\mathrm{x}')\sigma_i(\mathrm{x}')\mathrm{n}\, dS - \sum_i \int_{\Omega_i} G(\mathrm{x}-\mathrm{x}')\left(\nabla\sigma_i\right)(\mathrm{x}')\, d\mathrm{x}' \tag{4.29}$$

We can use the identity above, this time with $\nabla \times \mathrm{u} = 0$, and the second Green's identity to find

$$\begin{aligned} \mathrm{u}_b^{\sigma}(\mathrm{x}) = &\sum_i \int_{\partial\Omega_i} G(\mathrm{x}-\mathrm{x}')\sigma_i(\mathrm{x}')\mathrm{n}\, dS \\ &+ \sum_i \int_{\partial\Omega_i} \left(\mathrm{u}_i \nabla_{\mathrm{x}'}(G(\mathrm{x}-\mathrm{x}')) - G(\mathrm{x}-\mathrm{x}')\nabla_{\mathrm{x}'}\mathrm{u}_i\right)\cdot \mathrm{n}\, dS \end{aligned} \tag{4.30}$$

One can then combine the results 4.27 and 4.30 for general deformations

$$\begin{aligned} \mathrm{u}_b(\mathrm{x}) = &\sum_i \int_{\partial\Omega_i} G(\mathrm{x}-\mathrm{x}')\left(\omega_i(\mathrm{x}')\times\mathrm{n} + \sigma_i\mathrm{n}\right)\, dS \\ &+ \sum_i \int_{\partial\Omega_i} \left(\mathrm{u}_i \nabla_{\mathrm{x}'}(G(\mathrm{x}-\mathrm{x}')) - G(\mathrm{x}-\mathrm{x}')\nabla_{\mathrm{x}'}\mathrm{u}_i\right)\cdot \mathrm{n}\, dS \end{aligned} \tag{4.31}$$

This expression involves the velocity and components of its gradient at the surface It can be simplified to

$$\begin{aligned} \mathrm{u}_b(\mathrm{x}) = &\sum_i \int_{\partial\Omega_i} G(\mathrm{x}-\mathrm{x}')\left(-(\nabla_{\mathrm{x}'}\mathrm{u}_i)^t\cdot\mathrm{n} + (\nabla_{\mathrm{x}'}\cdot\mathrm{u}_i)\mathrm{n}\right)\, dS \\ &+ \sum_i \int_{\partial\Omega_i} \left(\mathrm{u}_i \nabla_{\mathrm{x}'}(G(\mathrm{x}-\mathrm{x}'))\right)\cdot \mathrm{n}\, dS \,. \end{aligned} \tag{4.32}$$

We then note that the factor involving the gradient and divergence of u_i can be rearranged We decompose the divergence into its components in and out of the plane

$$(\nabla_{\mathrm{x}'}\cdot\mathrm{u}_i)\,\mathrm{n} \equiv \left(\nabla^{\pi}_{\mathrm{x}'}\cdot\mathrm{u}_i + \frac{\partial(\mathrm{u}_i\cdot\mathrm{n})}{\partial n}\right)\mathrm{n}\,, \tag{4.33}$$

where ∇^π is the in-plane gradient. By definition of the surface normal, we have $\partial \mathrm{n}/\partial n = 0$. The second term can then be combined with the term $-(\nabla_{\mathrm{x}'}\mathrm{u}_i)^t \cdot \mathrm{n}$

$$-(\nabla_{\mathrm{x}'}\mathrm{u}_i)^t \cdot \mathrm{n} + \frac{\partial(\mathrm{u}_i \cdot \mathrm{n})}{\partial n}\mathrm{n} = -\left(\nabla_{\mathrm{x}'}\mathrm{u}_i - \frac{\partial \mathrm{u}_i}{\partial n}\mathrm{n}\right)^t \cdot \mathrm{n} \tag{4.34}$$

to cancel the normal derivatives. We can thus write the contributions of general deformations as

$$\begin{aligned}\mathrm{u}_b(\mathrm{x}) = &\sum_i \int_{\partial\Omega_i} G(\mathrm{x}-\mathrm{x}')\left(-(\nabla^\pi_{\mathrm{x}'}\mathrm{u}_i)^t \cdot \mathrm{n} + (\nabla^\pi_{\mathrm{x}'} \cdot \mathrm{u}_i)\mathrm{n}\right) dS \\ &+ \sum_i \int_{\partial\Omega_i} (\mathrm{u}_i \nabla_{\mathrm{x}'}(G(\mathrm{x}-\mathrm{x}'))) \cdot \mathrm{n}\, dS\end{aligned} \tag{4.35}$$

Not surprisingly, this last expression is more complicated than the one for rigid objects. Nevertheless, it meets the physical safeguard mentioned at the beginning of this section; it only involves the surface velocity or its derivatives in the plane of the surface.

4.4 Vorticity Boundary Conditions

The problem of vorticity boundary conditions has two characteristics of note. It involves the introduction of vorticity at the boundaries. We follow Lighthill's model in this respect (see Koumoutsakos et al., 1994) and this approach yields a Neumann boundary condition on the tangential vorticity flux. The second aspect of vorticity boundary conditions is the solenoidal character of vorticity. The vorticity lines in the flow must connect to the ones inside a spinning or deforming object. This translates into a Dirichlet condition on the normal component of vorticity at the wall,

$$\omega \cdot \mathrm{n}|_{\partial\Omega_i} = \omega_i \cdot \mathrm{n}|_{\partial\Omega_i}$$

This section will focus on this last condition, as the other aspects have been covered in Chapter 1. Let us make the assumption that we have a regular set of particles

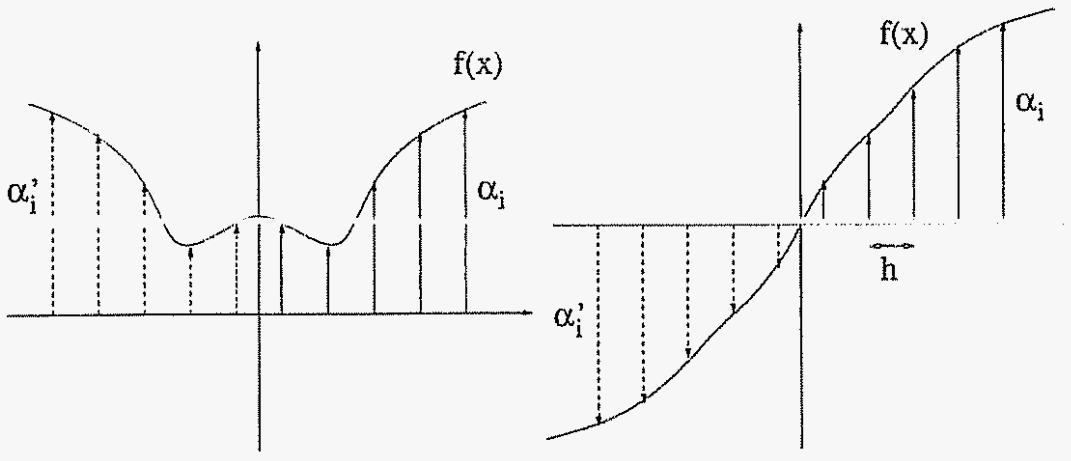

(a) Neumann (b) Dirichlet

Figure 4 2: Method of images: homogeneous boundary conditions

close to the wall. In one dimension, this would correspond to particles located at $x_i = (i + 1/2)h$. One is then confronted with the problem of the inadequacy of the unbounded smoothing functions for elements close to the boundary.

Some elegant solutions using images have been proposed in the context of viscous algorithms. While developing a one-sided test function is possible, it is relatively easy to complete the set of elements next to the wall with images across so that we can still carry out the integration in Eq. 1.19 over $\mathbb{R}^n$. These image particles will be placed across the boundary, symmetrically so that this augmented set of elements constitutes a good interpolation basis. We write for an interpolated quantity

$$f(x) = \sum_{p=0}^{n} \alpha_p \zeta(x - x_p) + \sum_{p=0}^{n} \alpha_p' \zeta(x - x_p') \,,$$

with $x_p' = -x_p$. The strengths of the images can then be chosen accordingly: $\alpha_p' = \alpha_p$ enforces $df/dx(0) = 0$; $\alpha_p' = -\alpha_p$ imposes $f(0) = 0$. One can refer to Ploumhans et al. (2002) for an application in three dimensions where homogeneous Neumann and Dirichlet conditions are respectively imposed on the tangential and normal components of vorticity.

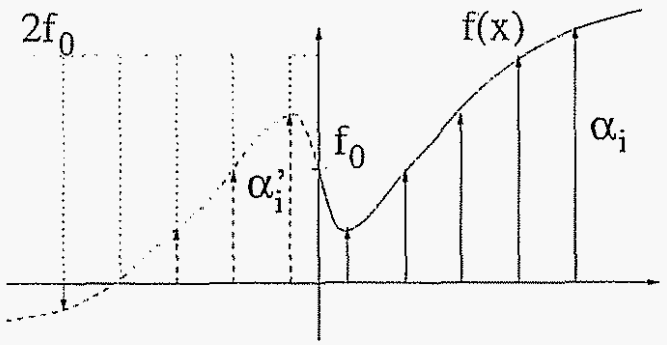

Figure 4 3: Method of images: heterogeneous Dirichlet boundary condition

A heterogeneous Dirichlet condition can be similarly derived Thanks to our images, we have

$$\sum_{p=0}^{n} h\,\zeta(0-x_p) + \sum_{p=0}^{n} h\,\zeta(0-x'_p) = 1$$

and by symmetry,

$$\sum_{p=0}^{n} h\,\zeta(x_p) = \sum_{p=0}^{n} h\,\zeta(x'_p) = \frac{1}{2}$$

The boundary condition $f(0) = f_0$ will thus be set if we set the image strengths to

$$\alpha'_p = 2hf_0 - \alpha_p$$

In three dimensions, the above only applies to the normal component of vorticity; the tangential ones are treated with a zero flux condition (Ploumhans et al., 2002) For surfaces with moderate curvatures, we will therefore build images with a position and a strength given by

$$\mathrm{x}'_p = \mathrm{x}_p - 2d\mathrm{n} \tag{4.36}$$

$$\alpha'_p = \left(2\left(\omega_i \cdot \mathrm{n}\right) V_p - 2\alpha_p \ \ \mathrm{n}\right)\mathrm{n} + \alpha_p\,, \tag{4.37}$$

where n, the local normal, is defined as the direction of the vector joining the closest point on the surface to the particle and d is the norm of that vector

This scheme implicitly assumes a flat surface As a result, its efficiency is contin-

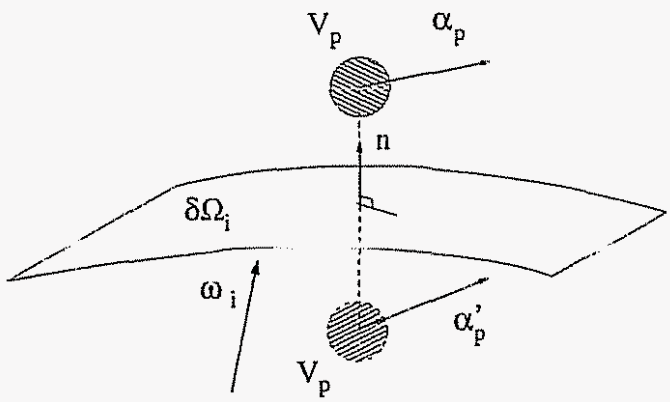

Figure 4 4: Method of images: heterogeneous Dirichlet boundary condition in three dimensions

gent on the smoothness and regularity of the surface. We will see a scheme degradation in regions of high curvature and on sharp edges. A first order correction that accounts for curvature would require a more elaborate image construction.

4.5 Conservation and Diagnostics

4.5.1 Linear Diagnostics

We are considering flows whose vorticity fields have a bounded support. For such flows, we can write (see Batchelor, 1967, 2.9)

$$\int_{\mathbb{R}^3} \omega \, dx = 0 \,. \tag{4.38}$$

This identity holds for inviscid and viscous problems and bounded flows too, if we include vorticity inside the objects We should then have

$$\int_{\mathbb{R}^3 \setminus \cup\Omega_i} \omega \, dx = - \int_{\cup\Omega_i} \omega_i \, dx \,. \tag{4.39}$$

For deforming objects, we can transform this last condition into a surface-based one

$$\int_{\mathbb{R}^3\setminus\cup\Omega_i} \omega \, dx = -\int_{\cup\partial\Omega_i} \mathbf{n}\times\mathbf{u}_i \, dS \tag{4 40}$$

For a set of rigid objects, it reduces to

$$\int_{\mathbb{R}^3\setminus\cup\Omega_i} \omega \, dx = -2\sum_i \mathbf{W}_i \, \mathrm{Vol}(\Omega_i) \tag{4 41}$$

This will be of interest when we solve for the boundary vorticity For a simply-connected geometry, our solver should indeed converge to a solution that satisfies Eq 4 38 In the viscous case, the condition will have to be enforced on the flux of vorticity that enters the domain and will depend on the kinematics of the boundaries

If the vortex sheets are bound to the surface, a local result can be derived Eq 4 38 is indeed based on the identity $\nabla \cdot \omega = 0$; if we consider a small volume at the wall (Fig 4 5), we see that

$$\nabla_\pi \cdot \gamma = \omega_i \cdot \mathbf{n}\,, \tag{4 42}$$

where ∇_π is the divergence in the plane locally tangent to the surface $\partial\Omega_i$

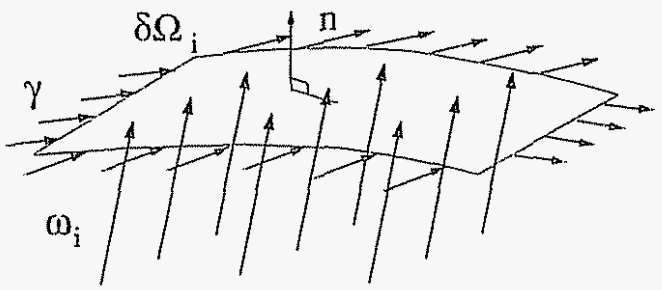

Figure 4 5: Inviscid flow around deforming boundaries: divergence of the bound vortex sheets

Let us now consider the linear impulse The identity

$$\int_V \mathbf{x}\times\nabla\times\mathbf{a}\,dx = (\mathcal{N}-1)\int_V \mathbf{a}\,dx - \int_{\partial V} \mathbf{x}\times(\mathbf{n}\times\mathbf{a})\,dS \tag{4 43}$$

is valid for a simply-connected volume V We apply it to the velocity field $\mathbf{u}$ in $\mathbb{R}^3 \setminus \cup\Omega_i$

$$\int_{\mathbb{R}^3\setminus\cup\Omega_i} \mathbf{u}\, d\mathbf{x} = \frac{1}{2}\int_{\mathbb{R}^3\setminus\cup\Omega_i} \mathbf{x}\times\boldsymbol{\omega}\, d\mathbf{x} + \frac{1}{2}\int_{\partial\cup\Omega_i} \mathbf{x}\times(\mathbf{n}\times\mathbf{u})\, dS\,, \tag{4 44}$$

thereby assuming that the objects Ω_i are simply-connected

4.5.2 Quadratic Diagnostics

The kinetic energy is not conserved for viscous flows We derive an expression for bounded flows

$$\begin{aligned} E &= \frac{1}{2}\int_{\mathbb{R}^3\setminus\cup\Omega_i} \mathbf{u}\cdot\mathbf{u}\, d\mathbf{x} = \frac{1}{2}\int_{\mathbb{R}^3\setminus\cup\Omega_i} (\nabla\times\boldsymbol{\psi})\cdot(\nabla\times\boldsymbol{\psi})\, d\mathbf{x} \\ &= \frac{1}{2}\int_{\mathbb{R}^3\setminus\cup\Omega_i} \boldsymbol{\psi}\ (\nabla\times(\nabla\times\boldsymbol{\psi})) - \nabla\cdot((\nabla\times\boldsymbol{\psi})\times\boldsymbol{\psi})\, d\mathbf{x} \end{aligned}$$

where we used the relation $\mathbf{f}\cdot(\nabla\times\mathbf{g}) = \mathbf{g}\ (\nabla\times\mathbf{f}) - \nabla\cdot(\mathbf{f}\times\mathbf{g})$ We then have

$$E = \frac{1}{2}\int_{\mathbb{R}^3\setminus\cup\Omega_i} \boldsymbol{\psi}\cdot\boldsymbol{\omega}\, d\mathbf{x} + \frac{1}{2}\int_{\partial\setminus\cup\Omega_i} (\mathbf{u}\times\boldsymbol{\psi})\cdot\mathbf{n}\, dS \tag{4 45}$$

This will hold for flows with a fast decaying ω field and for which the velocity goes to 0 at ∞ Logically, flows with an oncoming free stream will have an unbounded surface term at infinity

The helicity $\mathcal{H} = \int \mathbf{u}\cdot\boldsymbol{\omega}\, d\mathbf{x}$ is not conserved for a viscous flow This quantity, which measures the entanglement of vorticity lines, will be particularly interesting for flows around spinning boundaries

4.6 Conclusions

We have introduced a basis for deforming boundaries in the framework of the three dimensional vortex element method We derived the terms due to deforming or rigid rotating objects in the Biot-Savart law and proposed a method to compute them

from a surface integral An image method was designed to enforce the heterogeneous boundary condition on normal vorticity. The terms for rigid rotating objects (Eqs. 4.20, 4.21 and 4.22) and the enforcement of boundary conditions by image particles (Eq. 4.36) will be used in our study of flows around spinning spheres (Chapter 6) and flapping motions (Chapter 7)

Chapter 5

Near-Wall Vorticity

5.1 Introduction

The topological adaptation of vortex elements has been the focus of many efforts. From a computational standpoint, it may be interesting to adapt our discretization to the local character of the vorticity and improve the cost and accuracy of the method. A sheet-like representation of vorticity may be interesting in several flow configurations. In wall-bounded flows, vorticity in the near-wall region is mostly parallel to the wall and its gradients are mostly in a direction normal to the wall. The same can be said in multiphase flows where interfaces are a vorticity source.

5.2 Viscous Vortex Sheets

5.2.1 Definition

In a first step, we consider singular vortex sheets with a strength $\gamma(\mathrm{x}')$. We can regularize the sheet distribution by taking its convolution with a function ζ,

$$\omega(\mathrm{x}) = \int_{\text{sheet}} \zeta_{\sigma(\mathrm{x}')}(\mathrm{x} - \mathrm{x}')\gamma(\mathrm{x}')\, dS(\mathrm{x}')\,.$$

We choose the ζ smoothing function to be a Gaussian, i.e., the same as the one used for the particles. The sheet is discretized with flat panels of constant strength γ; the

above convolution can then be carried out over these panels This can be computed efficiently by means of a two-dimensional lookup table (Appendix E)

5.2.2 Viscous Diffusion

We now need to account for the viscous diffusion of vorticity A straightforward technique in this case is the so called core-spreading technique which progressively increases the smoothing radius σ of the sheet. We will rather treat this problem with a strength exchange approach as it is the one we use for the bulk vorticity.

Particle-Sheet Diffusive Transfer

We define a strength exchange scheme between particles and sheet elements. As discussed in Chapter 1, it is based on the approximation of the diffusion operator by an integral operator Eq. 1.19. However, we will not forget to guarantee the symmetry between the perspectives of the particle and the sheet element. This is essential in order to keep the conservation property of the original scheme. Let us start with the case of a particle. We can compute the transfer from a sheet element onto this particle as

$$\left.\frac{d\alpha_p}{dt}\right|_{\gamma_m} = \int_{V_p} \frac{2\nu}{\sigma^2} \int_{V_m} \eta_\sigma(\mathrm{x}-\mathrm{y})\,(\omega(\mathrm{x})-\omega(\mathrm{y}))\,d\mathrm{x}\,d\mathrm{y} \tag{5.1}$$

where V_p and V_m are the volumes of the particle and sheet element, respectively. We use midpoint quadrature for the integral over the particle volume

$$\left.\frac{d\alpha_p}{dt}\right|_{\gamma_m} = \frac{2\nu}{\sigma^2} \int_{V_{\text{sheet}}} (\omega(\mathrm{x})V_p - \alpha_p)\eta_\sigma(\mathrm{x}-\mathrm{x}_p)\,d\mathrm{x}\,. \tag{5.2}$$

If we now assume that $\omega(\mathrm{x})$ is singular inside the sheet element with a constant finite integral γ across the thickness of the sheet element, the above expression reduces to

$$\left.\frac{d\alpha_p}{dt}\right|_{\gamma_m} = \frac{2\nu}{\sigma^2}(\gamma_m V_p - \alpha_p h) \int_{S_m} \eta_\sigma(\mathrm{x}-\mathrm{x}_p)\,dS(\mathrm{x})\,, \tag{5.3}$$

where we define h as the thickness of the sheet. One technique to build a kernel η consists in using the function ζ (Degond and Mas-Gallic, 1989, Cottet and Koumoutsakos, 2000),

$$\eta(\rho) = -\frac{1}{\rho}\frac{d}{d\rho}\zeta(\rho)\,, \tag{5.4}$$

which in the case of the Gaussian yields the same Gaussian. The last factor in Eq. 5.3 is therefore the same as for the regularization.

In the converse case, the flux from the particle to the sheet element will yield

$$\left.\frac{d(\gamma_m S_m)}{dt}\right|_{\alpha_p} = \frac{2\nu}{\sigma^2}(\alpha_p h - \gamma_m V_p)\int_{S_m}\eta_\sigma(\mathrm{x}-\mathrm{x}_p)\,dS(\mathrm{x}) \tag{5.5}$$

This expression is identical to Eq. 5.3 but for the opposite sign, as it should be to enforce conservation.

Sheet Element to Element Diffusive Transfer

The transfer of vorticity between sheet elements can be handled in a similar fashion. The integration is more difficult to carry out, as it is a double surface integral.

$$\left.\frac{d(\gamma_m S_m)}{dt}\right|_{\gamma_n} = \frac{2\nu}{\sigma^2}\,(h_m\gamma_n - h_n\gamma_m)\int_{S_m}\int_{S_n}\eta_\sigma(\mathrm{x}-\mathrm{y})\,dS_\mathrm{x}\,dS_\mathrm{y} \tag{5.6}$$

We use quadrature for their evaluation while keeping in mind the geometry of our problem. Most of the flux goes out of the plane to the particles and therefore, we will not require the same level of accuracy for this contribution. Sample results for the case of one-sided sheets are provided in Section 5.3.2.

5.2.3 Biot-Savart

We carry out the convolution of the Biot-Savart kernel over a panel. The integrals do not have an analytical expression and have to be tabulated (see Appendix E).

5.3 Wall Vorticity

5.3.1 Regularization Near Boundaries

Let us now go back to our bounded problem. It might be interesting to consider a different set of elements in regions close to the wall for several reasons. These regions are characterized by mostly planar distributions of vorticity—the boundary layers—and the inadequacy of the spherical test function of our particles. The latter evidently affects the accuracy of the method near the wall (see Cottet and Koumoutsakos, 2000, and references therein). If we stay in the framework of regularized elements, the regularization has to be able to deform when close to the boundaries to enforce basic properties such as $\int \zeta dV = 1$.

5.3.2 One-Sided Vortex Sheet

Definition

We consider the limiting case of a vortex sheet situated right at the boundary. We have to modify its mollifier as to satisfy the above condition. We let $\zeta_{\text{one-sided}} = \frac{1}{M}\zeta_{\text{unbounded}}$; M has to be adjusted according to the local geometry (see Appendix E). In the case of a flat surface, we just have $M = 1/2$. We will take M constant over a panel, M_m.

For the same reason, we need to redefine the volume of a panel. For the sake of consistency, we choose to use the same modifier M_m as for the regularization. The volume associated to a one-sided panel is then $S_m\, h\, M_m$.

Conservative Viscous Scheme

Sheet Element to Particle Diffusive Transfer Let us begin with a one-dimensional problem such as the one in Section 4.4. We will now consider a set of elements where the first one lies at $x = 0$. We complete the set with images except for the first element. For a problem with a homogeneous Neumann condition, we can thus write

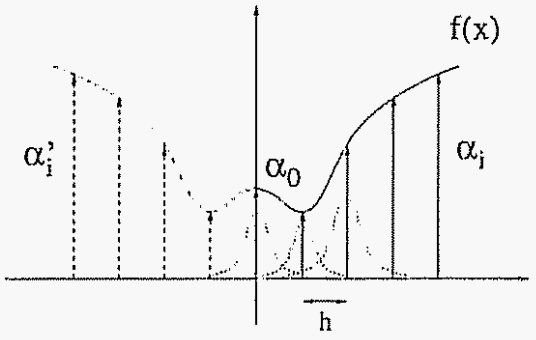

Figure 5 1: Wall element definition

for the element at $x = 0$

$$\frac{d\alpha_0}{dt} = \frac{2\nu}{\sigma^2} \sum_i (\alpha_i h_0 - \alpha_0 h_i)\, 2\eta_\sigma(x_i)$$

where the factor of two is due to the image contributions, $\alpha_i' = \alpha_i$ (Fig 5 1) We consider only the physical part of the central element with its half on the positive side. We define $\gamma = \alpha_0/2$ and $h_\gamma = h_0/2$ We then have

$$\frac{d\gamma}{dt} = \frac{2\nu}{\sigma^2} \sum_i (\alpha_i h_\gamma - \gamma h_i)\, 2\eta_\sigma(x_i)\,.$$

From this last result, we propose the following ansatz for the diffusion flux from a particle onto a wall sheet element

$$\left.\frac{d(\gamma_m S_m)}{dt}\right|_{\alpha_p} = \frac{2\nu}{\sigma^2} (\alpha_p M h - \gamma_m V_p) \int_{S_m} \frac{1}{M} \eta_\sigma(\mathrm{x} - \mathrm{x}_p) dS \qquad (5\ 7)$$

Conversely, if one were to look at the contribution to an element $i > 0$ from the central element,

$$\begin{aligned} \left.\frac{d\alpha_i}{dt}\right|_{\alpha_0} &= \frac{2\nu}{\sigma^2} (\alpha_0 h_i - \alpha_i h_0)\, \eta_\sigma(x_i) \\ &= \frac{2\nu}{\sigma^2} (\gamma h_i - \alpha_i h_0)\, 2\eta_\sigma(x_i)\,; \end{aligned}$$

following the same ansatz, we find that our scheme is consistent

$$\left.\frac{d\alpha_p}{dt}\right|_{\gamma_m} = \frac{2\nu}{\sigma^2}\left(\gamma_m V_p - \alpha_p M h\right)\int_{S_m}\frac{1}{M}\eta_\sigma(\mathbf{x}-\mathbf{x}_p)dS = -\left.\frac{d(\gamma_m S_m)}{dt}\right|_{\alpha_p} \tag{5.8}$$

We can give two interpretations to this approach. In the first place, this scheme tacitly includes contributions from images (as seen in Section 4.4). It can also be considered as a limiting case of one-sided integral operator, such as those described by Eldredge et al. (2002a,b).

Sheet Element to Element Diffusive Transfer In order to treat the diffusion right at the wall, we take some precautions. In convex regions, the unbounded algorithm ignores curvature and allows a spurious flux through the wall. In such cases, we will consider diffusion on a curved surface, which is a popular problem in molecular biology. From Balakrishnan (2000) and Faraudo (2002), we see that a first order solution in geodesic coordinates is identical to the one in a flat Euclidean space; we write

$$\left.\frac{d(\gamma_m S_m)}{dt}\right|_{\gamma_n} = \frac{2\nu}{\sigma^2}\left(M_m h_m \gamma_n - M_n h_n \gamma_m\right)\int_{S_m}\int_{S_n}\eta_\sigma(|\mathbf{x}-\mathbf{y}|')\,dS_\mathbf{x}\,dS_\mathbf{y} \tag{5.9}$$

where we now use $|\mathbf{x}-\mathbf{y}|'$, the distance measured along the surface in the PSE kernel. In a concave region, we use the same approach as in the unbounded case.

Example We consider the diffusion of a quantity f over a sphere of radius $R = 0.5$ with $\nu = 0.01$. The initial condition is a Dirac function at the top of the sphere; the solution can be developed (Balakrishnan, 2000) as

$$f(\mathbf{x},t) = \frac{1}{4\pi\nu t}e^{-\frac{u^2}{4\nu t}}\left(1+\frac{\nu t}{3R^2}+\frac{1}{15}\left(\frac{\nu t}{R^2}\right)^2\frac{4}{315}\left(\frac{\nu t}{R^2}\right)^3+\cdots\right)$$

where $u = R\arcsin(\mathrm{x}_3/R)$ is the geodesic distance to the source and R is the radius of the sphere. The double surface integral is evaluated with a one point quadrature. In Fig. 5.2, we see that our scheme is consistent but its local error exhibits a pattern

that follows the triangular mesh This is clearly due to the one point quadrature and can be improved by increasing the order of quadrature

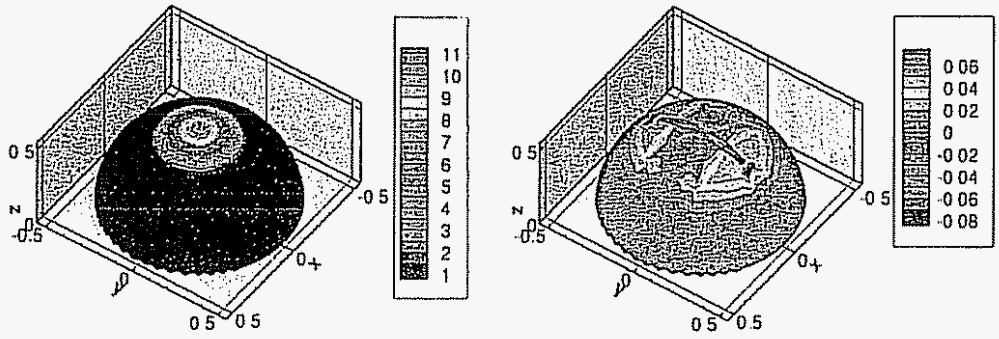

(a) f (b) Error

Figure 5 2: Diffusion on a sphere: solution and error at $t = 4$

Dirichlet Boundary Condition

In Section 4 4, we introduced an image construction to enforce the Dirichlet condition on the normal component of vorticity at the wall Let us consider the one-dimensional example with a central element The evolution equation for α_0 is

$$\frac{d\alpha_0}{dt} = \frac{2\nu}{\sigma^2} \sum_i (\alpha_i h_0 - \alpha_0 h_i)\, \eta_\sigma(x_i) + (\alpha_i' h_0 - \alpha_0 h_i)\, \eta_\sigma(x_i)$$

The image strengths α_i' are set to $2 f_0 h_i - \alpha_i$ We also assume that α_0 is close to the value $f_0 h_0$ and add the term $(f_0 h_0 h_0 - \alpha_0 h_0)\eta(0)$ to the above expression Because $\sum_i h\, \eta(x_i) = \sum_i h\, \zeta(x_i) = 1$, we have

$$\frac{d\alpha_0}{dt} = \frac{2\nu}{\sigma^2} (f_0 h_0 - \alpha_0) \tag{5 10}$$

From the wall element standpoint, the strength exchange scheme therefore amounts to the relaxation of α_0 to the value $f_0 h_0$ We note that the relaxation coefficient is

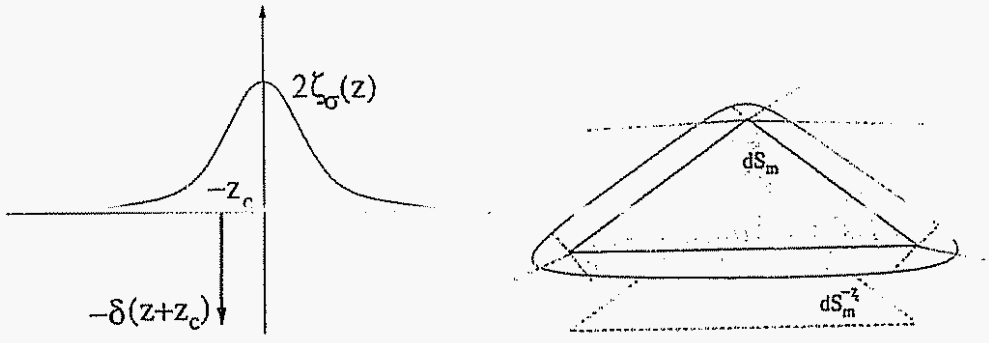

(a) 1D (b) 3D

Figure 5 3: Wall element: Biot-Savart approximation

$2\nu\Delta t/\sigma^2$, which is, up to a constant factor, the stability coefficient of the viscous scheme We again define $\gamma = \alpha_0/2$ and use this approach for the normal component of the wall elements

$$\frac{d((\gamma_m \cdot \mathbf{n})S_m)}{dt} = \frac{2\nu}{\sigma^2}((\mathbf{W} \cdot \mathbf{n})\, h - (\gamma_m \cdot \mathbf{n})) \tag{5 11}$$

to enforce the Dirichlet condition of (Section 4 4)

Biot-Savart

The Biot-Savart integral over the one-sided sheet is computed approximately We consider one surface element For the sake of consistency with its definition, we will compute its stream-function contribution as the sum of the full panel modified by $1/M$, and of a singular panel located underneath it at the centroid of the half-distribution

$$\psi_m = \int_{S_m} \gamma_m \frac{1}{M} G_\sigma(\mathbf{x}-\mathbf{x}')\, dS(\mathbf{x}') + \int_{S_m^{-z_c}} \gamma_m \left(1 - \frac{1}{M}\right) G(\mathbf{x}-\mathbf{x}')\, dS(\mathbf{x}') \tag{5 12}$$

This approach is sketched in Fig 5 3

5.3.3 Convection and Stretching

The vorticity carried by the elements is located at the surface We elect to convect this vorticity at the wall speed as a consequence of the no-slip condition In the case of a rigid object, the effect of the vortex stretching term reduces to the rotation of the vorticity lines For deforming surfaces, stretching will have to be accounted for in a fashion similar to the one for unbounded three dimensional vortex sheets (Brady, 2000, and references therein)

5.3.4 Redistribution

The presence of a buffer layer between the wall and the free elements may also prove useful for redistributions near a boundary Several approaches have been proposed to handle this problem One can adapt the redistribution lattice to the geometry (Koumoutsakos and Leonard, 1995) or design schemes to maintain conservation when close to the boundary (Ploumhans and Winckelmans, 2000, Ploumhans, 2001) We will use the attached elements in a simple scheme to enforce conservation of vorticity near the wall In a first step (Fig. 5.4(a)), the particles are redistributed without any regard to the boundaries Some of the redistributed particles are then inside or too close to the boundaries. They are destroyed and their circulation is transferred to the nearest wall-element (Fig 5.4(b)) This scheme only conserves circulation but the construction of higher order schemes should be straightforward

5.3.5 Corrected Value at the Wall

Our use of specific elements at the wall improves the representation near the wall, thereby ensuring conservation and a correct interpolation However the vorticity at the wall requires a specific treatment It is a result of the balance between its source at the wall and the diffusion into the flow, both of which are large on most of the

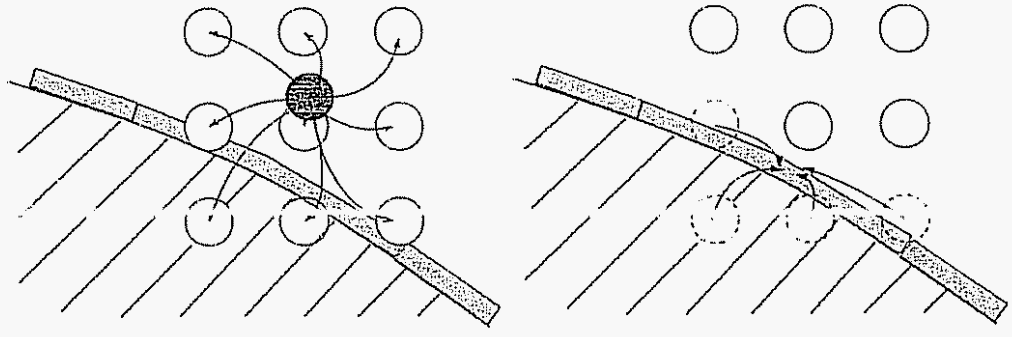

(a) Unbounded step (b) Correction

Figure 5.4: Wall element: redistribution scheme

surface. We introduce a local expression which takes the vorticity flux into account

$$\omega(\mathrm{x}_{\mathrm{wall}}) = \sum_p \left(\alpha_p \zeta(\mathrm{x}_{\mathrm{wall}} - \mathrm{x}_p) + \alpha'_p \zeta(\mathrm{x}_{\mathrm{wall}} - \mathrm{x}'_p)\right) + \sum_m \gamma_m \int_{S_m} \frac{1}{M_m} \zeta_\sigma(\mathrm{x}_{\mathrm{wall}} - \mathrm{x}') \gamma_m \, dS(\mathrm{x}') - \frac{\partial \omega}{\partial n}(\mathrm{x}_{\mathrm{wall}}) 2\sqrt{\frac{\nu \delta t}{\pi}} \tag{5.13}$$

If we consider the tangential components of vorticity, the contributions of the particles, their images, and the wall element only account for the zero flux condition during the time step. The last term of Eq. 5.13 is the solution at the wall at $t = \delta t$ of the one-dimensional diffusion problem

$$\begin{aligned} \frac{\partial \omega}{\partial t} &= \nu \nabla^2 \omega \text{ for } x > 0 \\ \omega &= 0 \text{ for } t = 0, x > 0 \\ \frac{\partial \omega}{\partial n} &= \text{constant} \end{aligned}$$

One could object that the flux is not known with great accuracy and affected by numerical noise. This point is addressed at the end of this section.

Example

We consider a one dimensional example that is somewhat reminiscent of our physical problem Our domain is the positive x-axis We discretize a function f with a set of Gaussian particles for which we take $\eta = \zeta$, $h = \sigma$ We use a wall element The elements are therefore positioned at $x_i = ih$

A Neumann boundary condition is imposed at $x = 0$, $-\nu\,\partial f/\partial n = g(t)$ During the first part of the time-step, we use our particles and their images to cancel the flux at $x = 0$ We then integrate the contribution of a constant flux onto the elements during the time step $\partial\alpha|_W = \int_{V_i} \partial f/\partial t dx$ (Koumoutsakos et al , 1994, Ploumhans et al , 2002)

In the case of a sinusoidal flux $g(t) = \sin(2\pi t/T)$, there exists an analytical expression for the wall value

$$f(0,t) = -\sqrt{\frac{T}{\pi\nu}}\left(S\left(2\sqrt{t/T}\right)\cos(2\pi t/T) - C\left(2\sqrt{t/T}\right)\sin(2\pi t/T)\right) ,$$

where $S(u)$ and $C(u)$ are the Fresnel integrals, $S(u) = \int_0^u \sin(\pi t^2/2)\,dt$ and $C(u) = \int_0^u \cos(\pi t^2/2)\,dt$ In Fig 5 5, we investigate the behavior of the expression with respect to the resolution (h,δt) and the PSE stability parameter r_{PSE} Eq 5 13 does provide a better estimate than the straight summation of the shape functions and its effectiveness is fairly constant between the two values of r_{PSE}

A last point that we have already alluded to is the use of the vorticity flux in our correction In practice, this quantity is indeed solved for at every time step and is noisy in time and space The space noisiness can be imputed to the interactions of the particles with the boundary In general, the boundary will not be aligned with any of the lattice planes causing the particle coverage to be irregular near the wall This issue was a rationale for the development of isotropic distributions (Chapter 2) and of near wall elements

The time issue can be addressed by not including the boundary condition enforcement in the time integration We use a second order Adams-Bashforth like Ploumhans et al (2002), but treat the wall boundary condition as a correction that is already

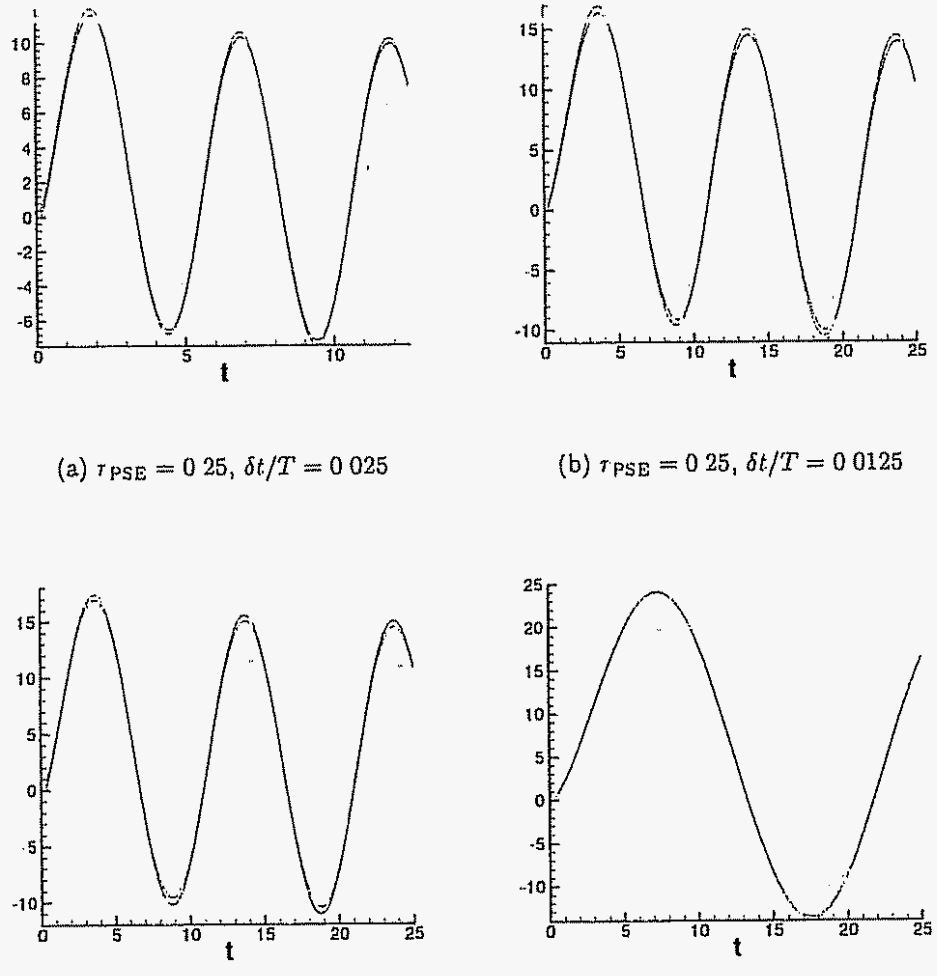

(a) $\tau_{PSE} = 0\ 25$, $\delta t/T = 0\ 025$

(b) $\tau_{PSE} = 0\ 25$, $\delta t/T = 0\ 0125$

(c) $\tau_{PSE} = 0\ 5$, $\delta t/T = 0\ 025$

(d) $\tau_{PSE} = 0\ 5$, $\delta t/T = 0\ 0125$

Figure 5 5: One-dimensional example with sinusoidal flux, wall value: analytical (red), simple summation of blobs and images (green), summation with correction (blue) for two values of the PSE stability parameter $\tau_{PSE} = \nu\,\delta t/h^2$ and $\delta t/T$

integrated in time As can be seen from its stability region, AB 2 does not damp purely oscillatory modes and probably leads to a cycle of over-correcting fluxes from one time step to another.

5.4 Conclusions

The vortex element method with regularized particles and Biot-Savart summation is in difficulty near the boundaries where the interpolation and integration accuracy are degraded. We introduce wall elements which have one-sided shape functions built to be conservative. These elements interact viscously with the free elements and stay attached to the wall, thus enforcing tacitly the no-slip condition for vorticity at the wall. They also allow the free elements to stand further away from the wall, thereby lowering the chances of an element to enter the boundaries and alleviating the need for images in the viscous scheme. The closest image is now at roughly 2 σ; for a Gaussian smoothing, this represents $\exp -\frac{4\sigma^2}{2\sigma^2} < \exp -\frac{\sigma^2}{2\sigma^2}$. Finally, we introduced a correction to provide an improved estimation of wall quantities by accounting for the flux at the wall.

Chapter 6

Flows Past Spinning Spheres

6.1 Introduction

Flow around spinning spheres are met in a wide array of domains, from sports to suspension problems in chemical or environmental engineering. Despite this ubiquity, studies of this problem are scarce in the literature

In the case of the transverse rotation, the first observations are attributed to Robins (1805). However, the discovered lift effect will be named after Magnus (1853) Barkla and Auchterlonie (1971) discuss these early works with more depth and provide some measurements of the lift by using an experimental setup in direct continuation of Robins's work. Their results cover Reynolds numbers of $1.5\,10^3$ to 10^5. There are analytical results by Rubinow and Keller (1961) for very low Reynolds numbers using Stokes and Oseen expansions Until recently, results were particularly rare for intermediate Re ranges (Tsuji et al , 1985, Oesterlé and Bui Dinh, 1998)

For an axial rotation, even fewer results are available A couple of numerical studies were carried out recently (Kim and Choi, 2002, Pregnalato et al , 2002).

6.2 Configuration

We are considering the impulsively started flow around a spinning sphere at $Re = U_\infty D/\nu = 300$ and a spin rate $WD/2U_\infty = 0\,5$, where D is the sphere diameter, U_∞ is

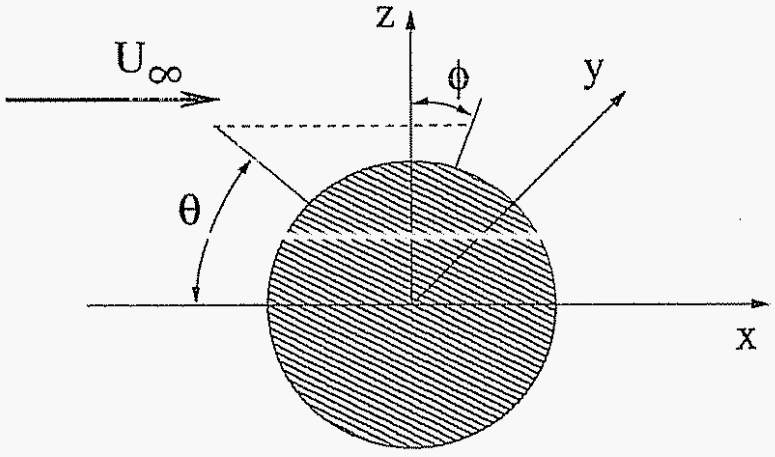

Figure 6.1: Configuration and coordinate system

the free stream velocity and W is the angular velocity of the sphere. The free-stream is in the direction of e_x. Three configurations are studied, one per direction of the angular velocity vector: e_x, e_y and $\sqrt{2}/2e_x + \sqrt{2}/2e_y$. Both the free-stream and the rotation are impulsively started at $t = 0$

Fig. 6.1 shows the coordinate systems used in this chapter and the orientation of the free-stream. Cylindrical coordinates, in particular, will be used for the localization of critical points on the sphere or in its neighborhood. All the results of this chapter are non-dimensionalized

$$t = \frac{U_\infty t^*}{D}$$
$$x = \frac{x^*}{D}$$

where * denotes the corresponding dimensional quantities.

6.3 Stream-Wise Rotation

We start with $W = e_x$. This first case is interesting for several reasons. Previous numerical results by Kim and Choi (2002) show that, for certain ranges of Re and WR/U_∞, the wake may be fully unsteady, steady, or steady in a rotating frame

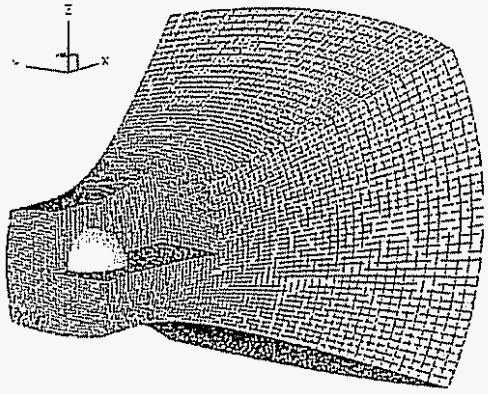

Figure 6 2: Trumpet mapping shape and position: the mapping is cut in the neighborhood of the sphere to provide a better view

We will refer to this last configuration as frozen as in our reference. Our values of $Re = 300$ and of the spin rate $WR/U_\infty = 0\,5$ correspond to a frozen configuration A perturbation is applied to the free-stream

$$\mathbf{u}_{\text{perturb}} = \mathbf{e}_z \cos(2\pi(t-2)) \; for \; t \in [2;3]$$

in order to accelerate the transition to the unsteady asymmetric wake

6.3.1 Numerics

The sphere was discretized with 20480 triangles; it was generated by recursively dividing the faces of a icosahedron The time step was set to 0 0125. Particles were redistributed every 5 time steps onto a face-centered cubic lattice by using the F_3' scheme of Chapter 2. The redistribution lattice was stretched using a trumpet-shaped mapping (Daeninck et al., 2004) which progressively reduces the resolution as one moves downstream (Fig. 6 2) The parameters of Table 6 1 were chosen to guarantee a roughly constant resolution in the sphere neighborhood where the particle spacing is 0 015

Fig 6 3 shows the evolution of numerical diagnostics. While the problem size

R_0	2
m	600
center	0 0 0

Table 6.1. Trumpet mapping parameters

(Fig. 6.3(a)) reaches a plateau, thanks to the anisotropic redistribution, the mesh Reynolds number (Fig. 6.3(b)) exhibits a growth from $t = 15$. For $t < 15$, this maximum is achieved in the boundary layers. For $t > 15$, the wake (Fig. 6.4, 6.7) contains stronger vorticity structures which are transported into coarser regions of the lattice ($x > 8$).

A quantity that is often useful in three dimensional vortex methods is $\int |\omega_\sigma - \omega|^2 dx$; it measures the difference between vorticity represented by our elements $\sum_p \alpha_p \zeta_{\sigma_p}(\mathrm{x}-\mathrm{x}_p)$ and the curl of the velocity given by the Biot-Savart law $\sum_p \mathrm{K}\sigma_p(\mathrm{x}-\mathrm{x}_p) \times \alpha_p$. Because the second field is divergence-free by definition, this quantity is often referred to as the divergence error. Our results (Fig. 6.3(c)) show that this quantity is roughly constant throughout the simulation.

The last diagnostic is the Courant number (Fig. 6.3(d)). Because we use a Lagrangian method, the classical formulation in terms of the velocity, $C_u = |\mathrm{u}|_{\max} \delta t/h$, is not the most appropriate. Rather, one can consider a figure based on vorticity $C_\omega = |\omega|_{\max} \delta t$ or even the velocity gradient $C_{|\nabla \mathrm{u}|} = |\nabla \mathrm{u}|_{\max} \delta t$, which tracks the largest relative displacement of material elements over a time step. Let us add some nuance here: in a bounded flow, C_u still has importance as we do not want elements to cross the boundaries.

The computational time was approximately 300 hours on six processors. This includes the computation and sampling of fields for visualization purposes.

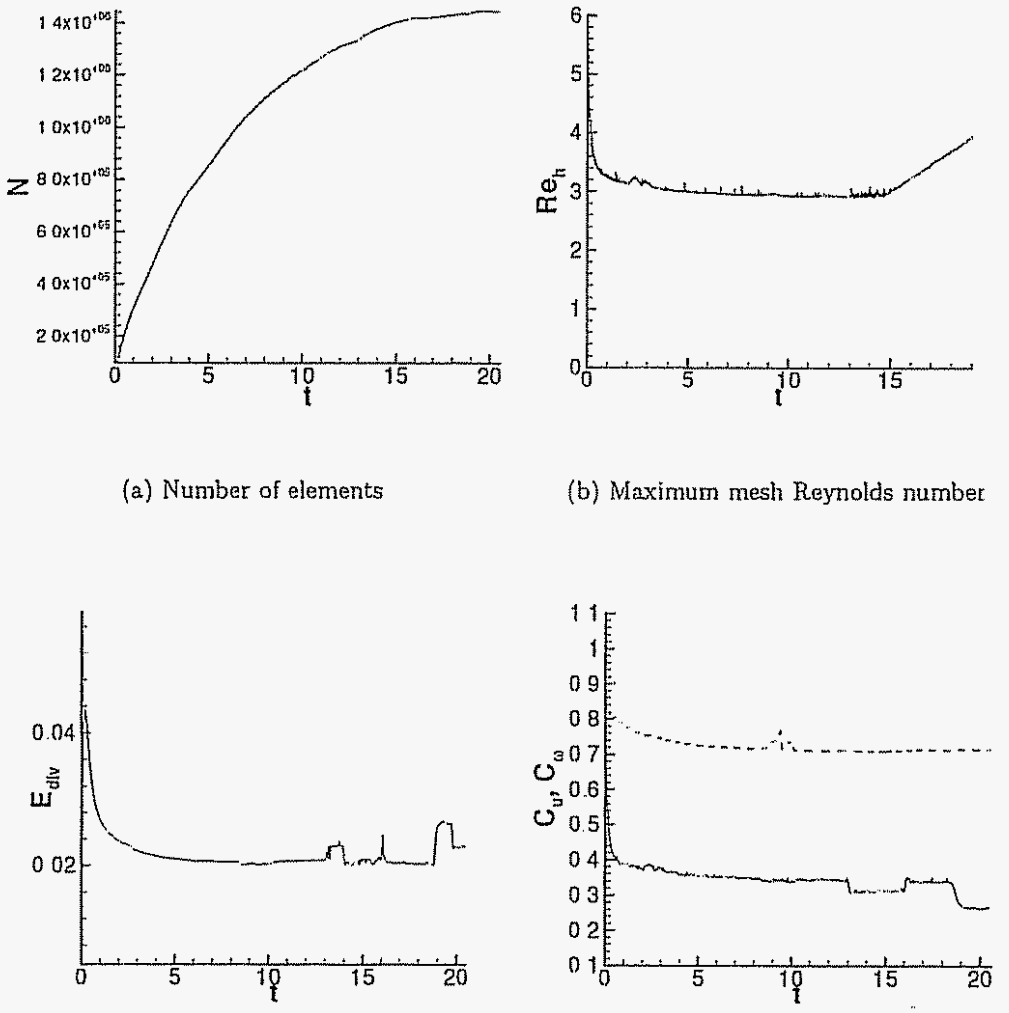

(a) Number of elements

(b) Maximum mesh Reynolds number

(c) Divergence error

(d) Courant number, vorticity expression (solid) and velocity expression (dashed)

Figure 6 3: Spinning sphere at $Re = 300$, stream-wise rotation: numerical diagnostics

6.3.2 Wake

We begin our analysis of the physics of this flow by considering its wake. We first consider the vorticity structures using the Q-criterion (Hunt et al , 1988) where Q is the second invariant of the the $\nabla \mathbf{u}$ tensor

$$Q = \frac{1}{2}\left(\Omega_{ij}\Omega_{ij} - S_{ij}S_{ij}\right) . \tag{6.1}$$

In the case of an incompressible flow, it can be rewritten as

$$Q = -\frac{1}{2}Tr(\nabla \mathbf{u}_{ij} \nabla \mathbf{u}_{ij}) \tag{6.2}$$

$Q > 0$ regions are characterized by the preponderance of the rotation rate over the strain rate and the likelihood of a minimum in pressure since $Q = \frac{\nabla^2 p}{2\rho}$ (Jeong and Hussain, 1995, Dubief and Delcayre, 2000). The evolution of the surfaces $Q = 0$ in Fig. 6.4 shows the growth of a nearly axis-symmetric wake and its transition to the aforementioned frozen configuration. As Fig. 6.5 suggests, the wake consists of a central vortex filament whose vorticity is pointing downstream–$\omega_x > 0$ like the sphere angular velocity–, and recirculations which also have some stream-wise vorticity pointing upstream–$\omega_x < 0$–(Fig. 6.5). This configuration is evidently a consequence of the solenoidal character of vorticity, as vortex lines originating in the back of the sphere have to make their way to the front.

The $\omega_x < 0$ structures grow in size until late into the simulation, $t \simeq 10$, at which point the oscillation of the center filament brings regions with vorticity of opposite signs closer. The viscous cancellation of oppositely signed vorticity is then locally enhanced, which brings even more asymmetry to the azimuthal velocity. For this reason, the $\omega_x < 0$ corona that was somewhat diffuse for $t < 10$ gives way to more localized structures that are wrapped around the $\omega_x > 0$ filament (Fig. 6.6 and 6.7). These structures eventually form a steady helical strand that rotates at its own rate (Fig. 6.4)

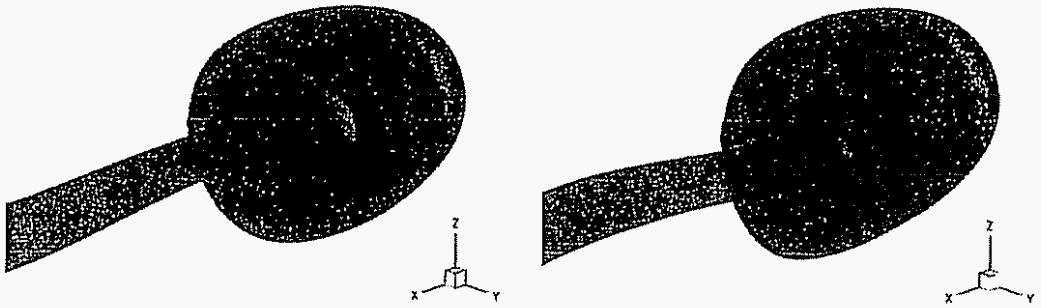

(a) $t = 10$ (b) $t = 12$

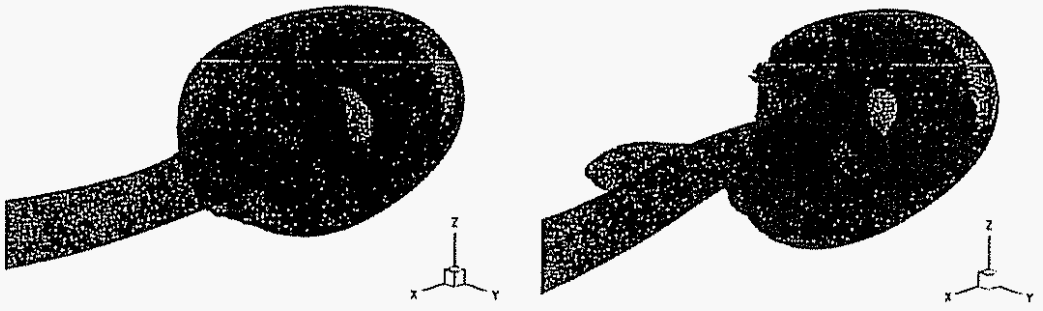

(c) $t = 14$ (d) $t = 16$

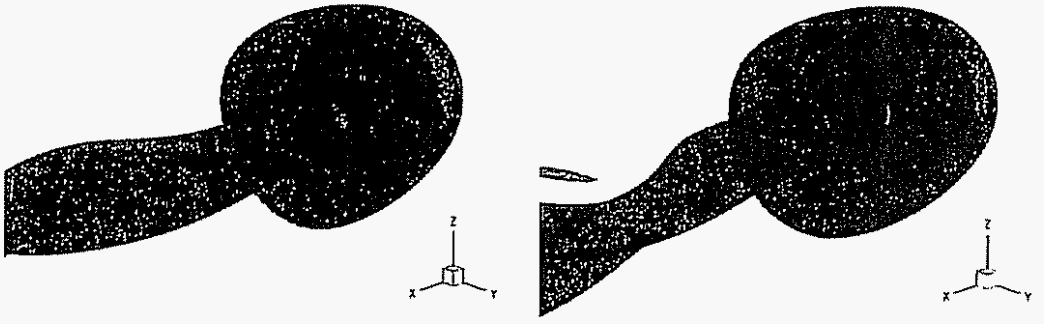

(e) $t = 18$ (f) $t = 20$

Figure 6 4: Spinning sphere at $Re = 300$, stream-wise rotation: vorticity structures identified by the iso-surface $Q = 0$; partial transparency of the iso-surfaces and the dashed lines help localizing the sphere

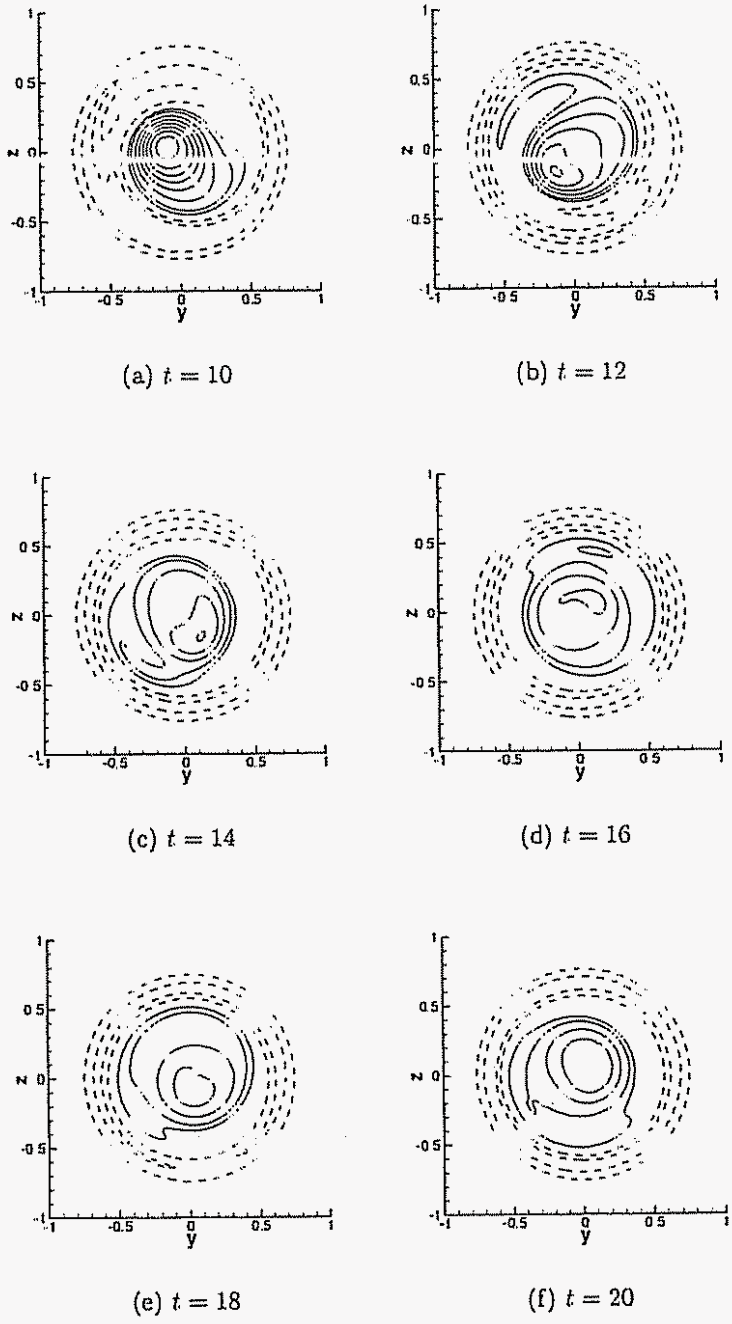

(a) $t = 10$ (b) $t = 12$

(c) $t = 14$ (d) $t = 16$

(e) $t = 18$ (f) $t = 20$

Figure 6 5: Spinning sphere at $Re = 300$, stream-wise rotation: stream-wise vorticity at $x = 1$; contours values are in the interval $[-4; 4]$ by steps of 0 5, 0 is omitted and ± 0 25 were added Positive values are solid; negatives ones, dashed

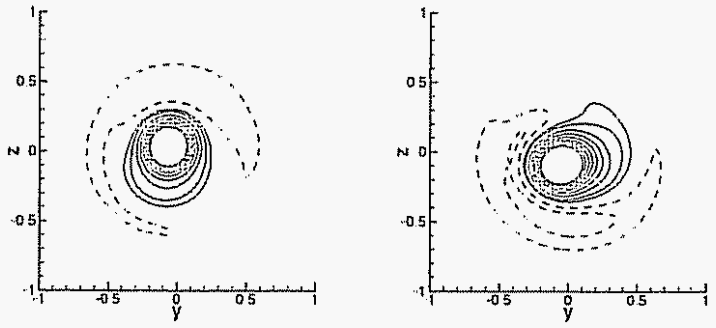

(a) $t = 10$ (b) $t = 12$

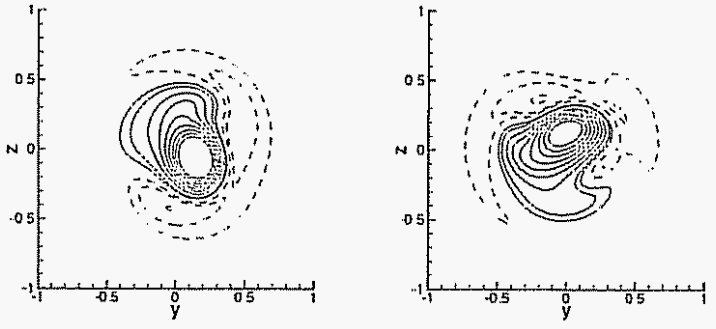

(c) $t = 14$ (d) $t = 16$

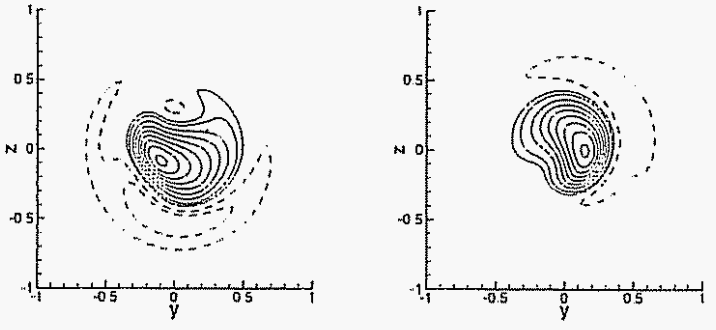

(e) $t = 18$ (f) $t = 20$

Figure 6.6: Spinning sphere at $Re = 300$, stream-wise rotation: stream-wise vorticity at $x = 2$; contours values are the same as in Fig 6.5

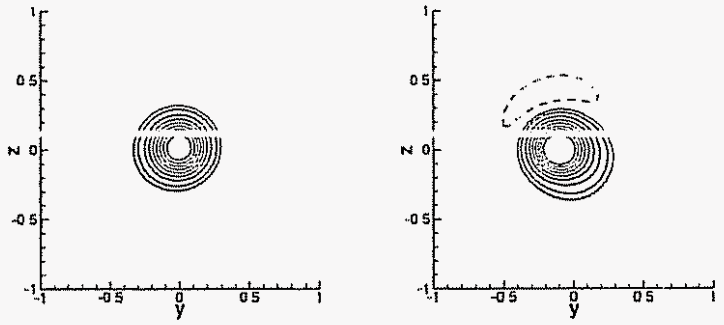

(a) $t = 10$ (b) $t = 12$

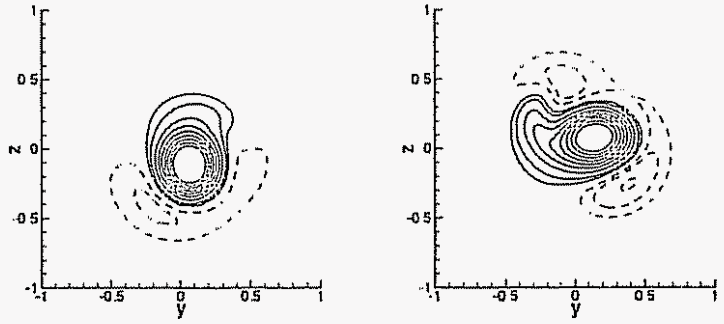

(c) $t = 14$ (d) $t = 16$

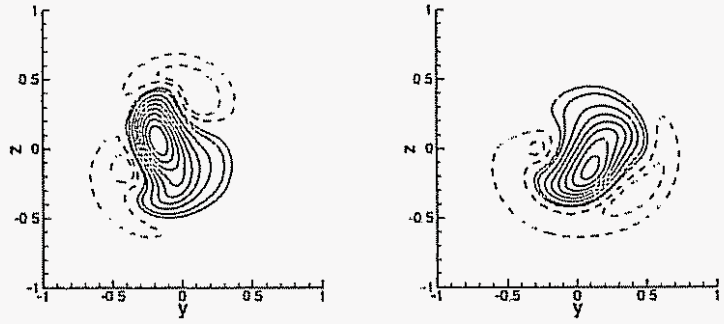

(e) $t = 18$ (f) $t = 20$

Figure 6.7: Spinning sphere at $Re = 300$, stream-wise rotation: stream-wise vorticity at $x = 3$; contours values are the same as in Fig. 6.5

6.3.3 Forces

The force $\mathbf{F}$ acting on a body can be computed with several methods We present results generated by two of them The first one, based on global impulse, is given by

$$\mathbf{F} = -\frac{d}{dt}\int_{\mathbb{R}^3\setminus\cup\Omega_i} \mathbf{u}\, dx \tag{6.3}$$

A formulation based on vorticity was derived in Section 4.5. We will note that the integral above is unbounded for a flow with a free stream This can be easily fixed by rather considering the momentum deficit in the flow

$$\mathbf{F} = \frac{d}{dt}\int_{\mathbb{R}^3\setminus\Omega} (U_\infty \mathbf{e}_x - \mathbf{u})\, dx \tag{6.4}$$

The integral, once re-written in terms of vorticity, is similar to Eq 4.44

$$\int_{\mathbb{R}^3\setminus\Omega} (U_\infty \mathbf{e}_x - \mathbf{u})\, dx = -\frac{1}{2}\int_{\mathbb{R}^3\setminus\cup\Omega_i} \mathbf{x}\times\omega\, dx + \frac{1}{2}\int_{\partial\cup\Omega_i} \mathbf{x}\times(\mathbf{n}\times(U_\infty \mathbf{e}_x - \mathbf{u}))\, dS\,, \tag{6.5}$$

except for a constant term, which will not have any effect because of the time differentiation

The second method considers the balance of momentum over a control volume (Noca et al , 1999); it was applied to the flow around a sphere by Ploumhans et al. (2002). As in this last reference, we use a spherical control volume with a radius twice that of the sphere.

Ploumhans et al (2002) found the control volume approach to be more reliable The other approach is based on the computation of the moments of vorticity in the whole flow and as one adds the contribution of vorticity far downstream, one uses vorticity from under-resolved regions Moreover, this vorticity appears in differences of large terms

Fig 6.8 shows the drag coefficient $C_d = \frac{F_x}{\frac{1}{2}U_\infty \frac{\pi R^2}{4}}$ computed with both methods. The method based on the global impulse yields a noisier result which was filtered in our chart and tends to drift off Past the initial transients, the control volume method

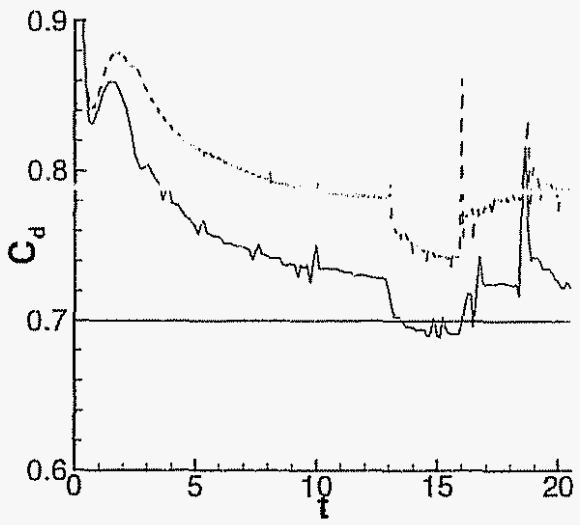

Figure 6.8: Spinning sphere at $Re = 300$, stream-wise rotation: drag coefficient C_d by the control volume (solid) and global impulse (dashed)

yields a value of ~ 0.725 for the drag coefficient; it is in agreement with the value 0.70 of Kim and Choi (2002)

The transversal force coefficients C_y and C_z (Fig. 6.9(a)) are smaller in magnitude and appear to approach a periodic behavior. Kim and Choi (2002) find that they follow the rotation of the wake structures and their norm $C_l = \sqrt{C_y^2 + C_z^2}$ is constant $= 0.025$. Our results show that we have not reached this periodic regime just yet, or that we are reaching a slightly different flow state than theirs

6.3.4 Attachment and Separation

Fig. 6.10 shows the magnitude of wall vorticity at $t = 20$ as defined in Eq. 5.13. The quantity $\tau/\mu = \mathrm{n} \times (\omega - 2\mathrm{W})$ (Fig. 6.11) is perhaps more interesting as it is the actual shear up to a constant factor μ. We observe some spatial pattern in those wall quantities; its origin is the vorticity flux in the correction term of Eq. 5.13. This flux is the solution given by a panel method.

Fig. 6.11 also shows friction lines, lines tangent to the local shear; the lines were

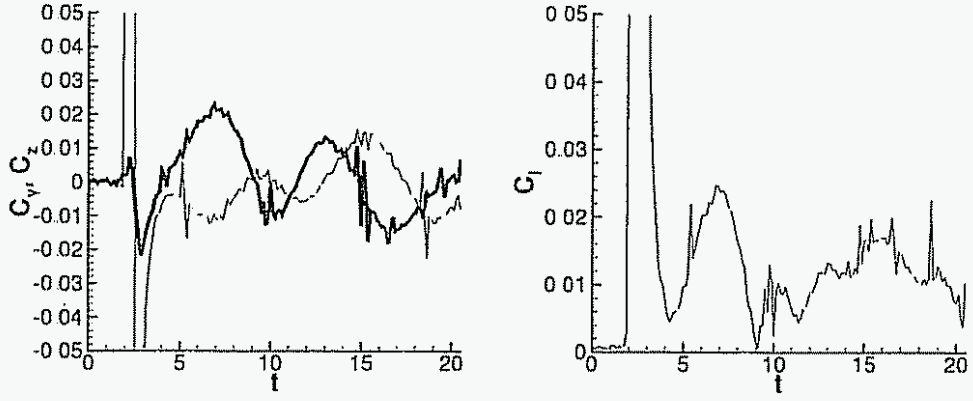

(a) C_y (bold) and C_z (plain) (b) C_l

Figure 6 9: Spinning sphere at $Re = 300$, stream-wise rotation: transversal force coefficients

seeded in the front and back of the sphere There are two nodal points of attachment (Lighthill, 1963) One is the upstream stagnation point; the other, the reattachment point The lines emerging from these converge to a roughly axis-symmetric separation line that we locate at $\theta \simeq 108^o$, a value close to the one of Kim and Choi (2002), 110^o We can decompose the shear into its azimuthal and axial components

$$\tau_\phi = \tau_y \sin(\phi) - \tau_z \cos(\phi) \quad (6\ 6)$$

$$\tau_\theta = \tau_x \sin(\theta) - \cos(\theta)(\tau_y \cos(\phi) + \tau_z \sin(\phi)) \quad (6\ 7)$$

Both components (Fig 6 12 and 6 13) exhibit a difference in magnitude between the front and the back of the sphere The flow in the recirculation region is slower and has acquired a certain amount of swirl (azimuthal velocity), thus reducing the corresponding shear component

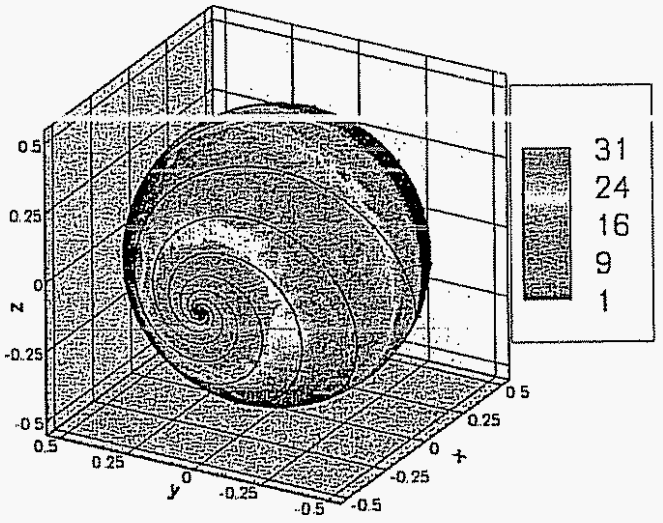

(a) Front

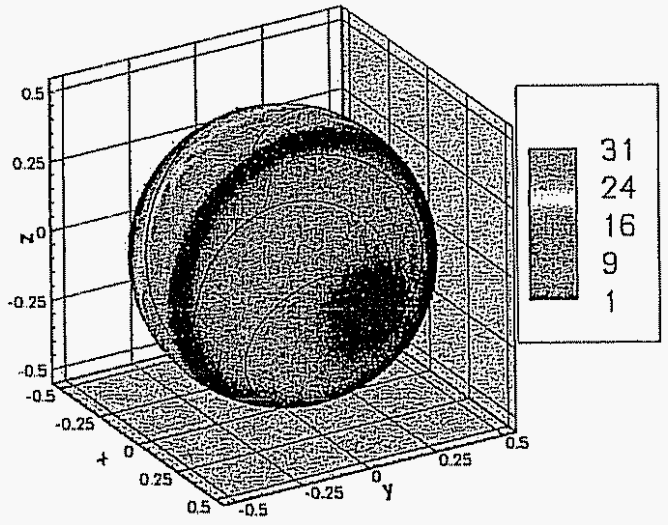

(b) Back

Figure 6 10: Spinning sphere at $Re = 300$, stream-wise rotation: wall vorticity and lines at $t = 20$

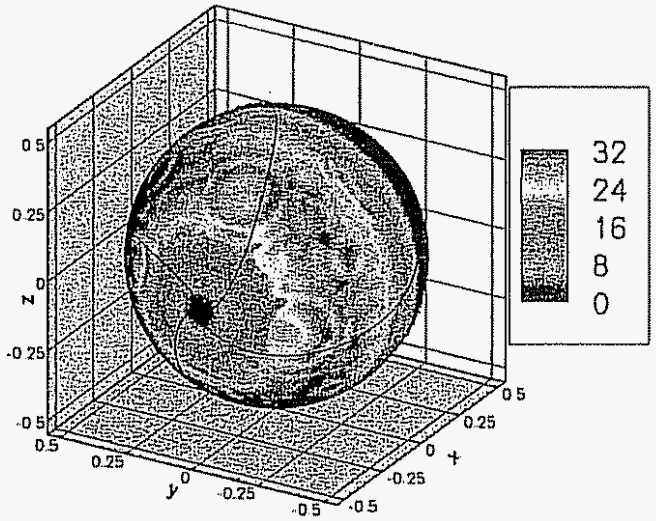

(a) Front

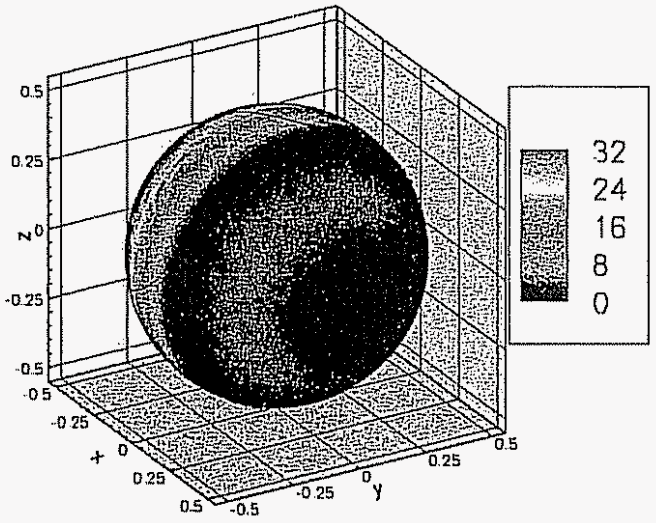

(b) Back

Figure 6 11: Spinning sphere at $Re = 300$, stream-wise rotation: shear and lines at $t = 20$

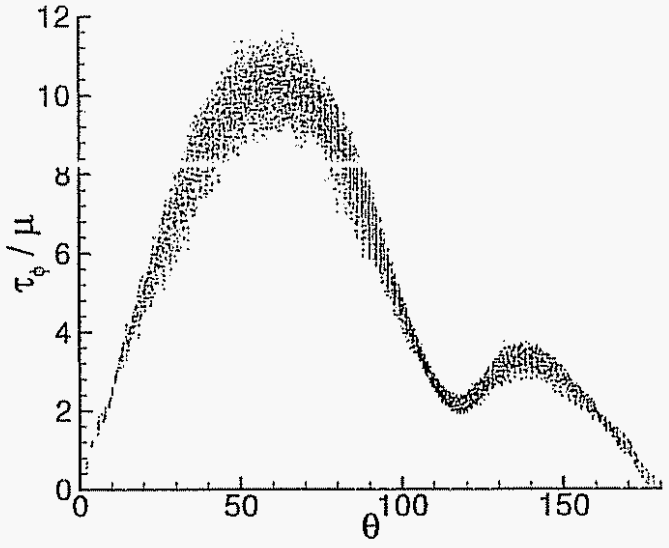

Figure 6 12: Spinning sphere at $Re = 300$, stream-wise rotation: azimuthal shear magnitude at $t = 20$

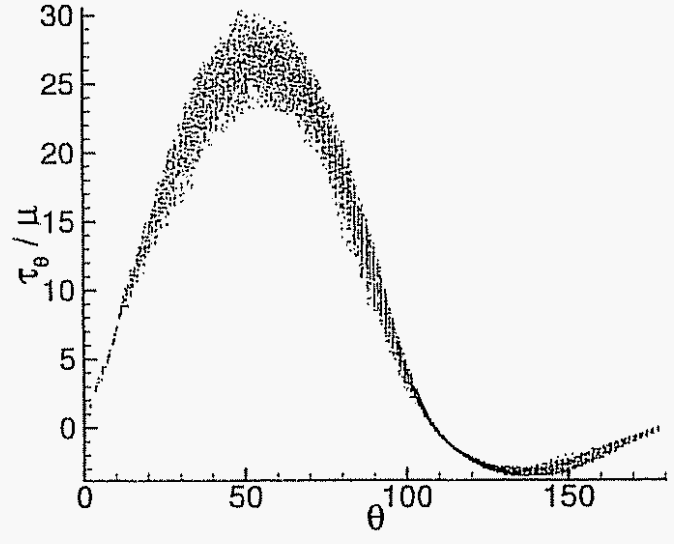

Figure 6 13: Spinning sphere at $Re = 300$, stream-wise rotation: axial shear magnitude at $t = 20$

R_0	0 5
m	700
center	−2 0 0

Table 6.2: Spherical mapping parameters

6.4 Transverse Rotation

In this case, $\mathbf{W} = \mathbf{e}_y$. The wall thus moves in the direction of the free-stream for $z > 0$ and against it for $z < 0$.

6.4.1 Numerics

This simulation was started using the same geometry and numerical parameters as in Section 6.4. At $t = 9.5$, the simulation was stopped and a spherical mapping was used for the redistributions from then on. This is the same mapping as in Ploumhans et al. (2002); its parameters are reproduced in Table 6.2. The resolution of the spherical mapping decreases rapidly with distance from the sphere. This made the simulation more affordable for longer times (Fig. 6.14). The mesh Reynolds number (Fig. 6.14(b)) jumps from 2.7 to 5 because the wake vorticity structures are re-sampled onto a coarser lattice.

6.4.2 Wake

The wake of a non-spinning sphere at $Re = 300$ is unsteady and asymmetric (Johnson and Patel, 1999, Ploumhans et al., 2002, Kim and Choi, 2002). The sphere indeed starts to sustain a small amount of lift and the shed periodic hairpin structures show a bias in the direction of this lift. Because of its rotation, the present configuration develops more lift and increases the bias. The $Q = 0$ surfaces in Fig. 6.15 and 6.16 give a overview of the shedding cycle of this flow. We will refer to the downwash-inducing vortex pair as the main pair since it corresponds to the lift. We will call the upwash-inducing one the secondary pair.

The period of this flow is $T \simeq 4.5$ and the Strouhal frequency $St_{\omega^*=0.5} \simeq \frac{2R}{U_\infty T} = 0.22$. Those are values to compare to the frequency of a non-spinning sphere $St^{\perp}_{\omega^*=0} = 0.136 \pm 0.002$ (Johnson and Patel, 1999, Ploumhans et al , 2002, Kim and Choi, 2002) and the rotation frequency $\frac{W}{2\pi} = 0.159$.

Fig. 6.17 and 6.18 give a closer view of the shedding of those structures. We plot transparent surfaces of $Q = 0$ and vortex lines in a $y > 0$ region near the sphere. We seed vortex lines on the surface at locations that follow the sphere rotation; more precisely,

$$x_i = R\cos(\pi/4)\cos(\psi(t) + i\pi/3)$$
$$y_i = R\sin(\pi/4)$$
$$z_i = R\cos(\pi/4)\sin(\psi(t) + i\pi/3)$$

where $i = 0 \cdots 5$ and $\psi(t) = -Wt$. Vorticity is subjected to diffusion; the vortex lines are therefore not material lines. The lines appear to be redirected abruptly; some of those events actually correspond to vortex reconnections and pinch-off which is crucial during vortex shedding.

The bottom separation (discussed below) feeds a large vorticity structure over the shedding cycle. If we consider the section of this structure in the longitudinal plane, we see that a kink appears between 0 and $T/3$ and is the early sign of the pinch off ($5T/6$). The shed structure can be seen to be the tip of a newly formed downwash-inducing hairpin vortex. The vortex lines inside the tails of the hairpin are seen to be originating from the sides of the sphere ($T/2 \rightarrow 5T/6$). As the tip is convected downstream, the tails are stretched and brought close to each other and to the next hairpin tip. Viscous diffusion eventually connects the tails to each other and to the hairpin structure of the following cycle ($0 \rightarrow T/4$, bottom right corner).

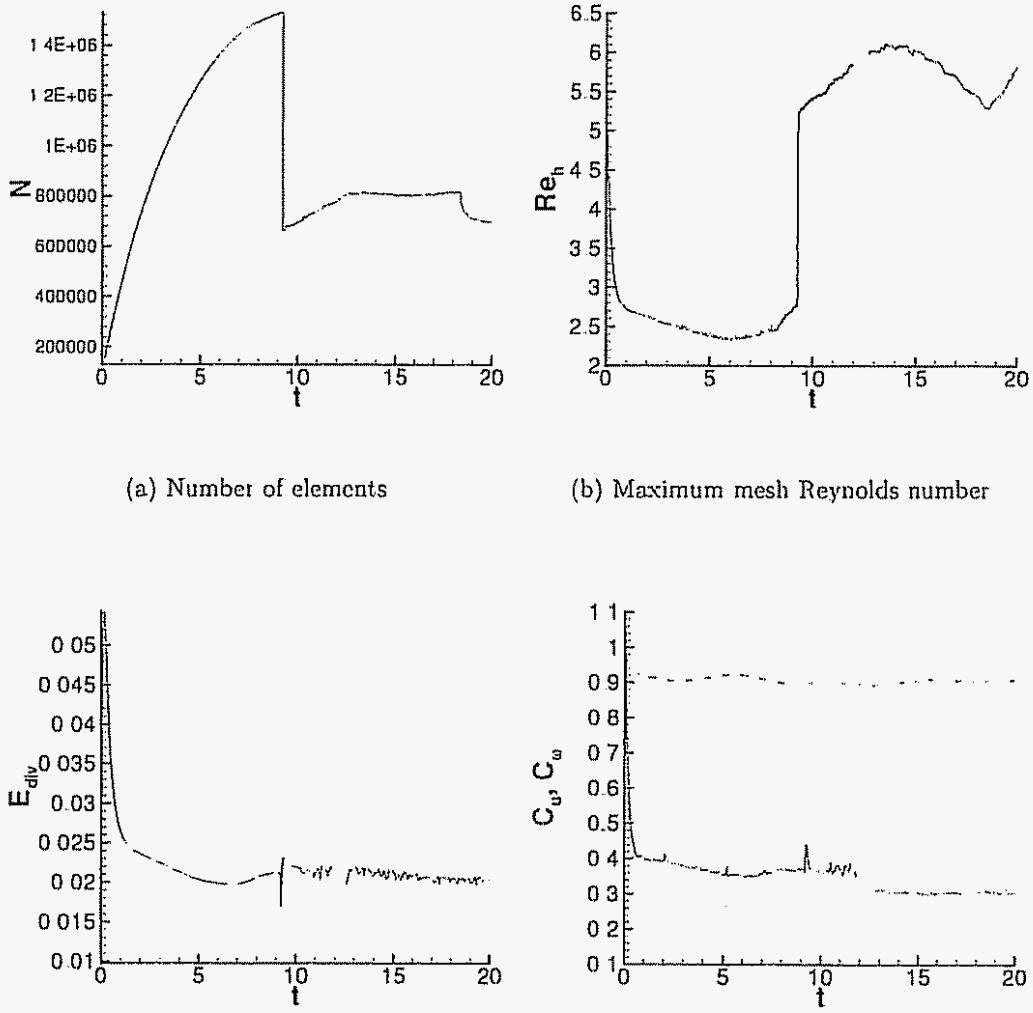

(a) Number of elements

(b) Maximum mesh Reynolds number

(c) Divergence error

(d) Courant number, vorticity expression (solid) and velocity expression (dashed)

Figure 6 14: Spinning sphere at $Re = 300$, transverse rotation: numerical diagnostics

(a) 0

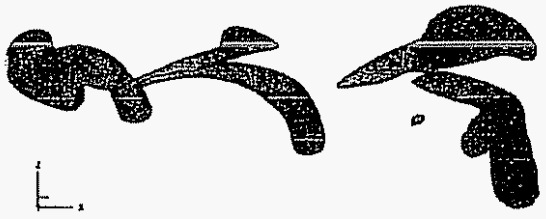

(b) $T/4$

(c) $T/2$

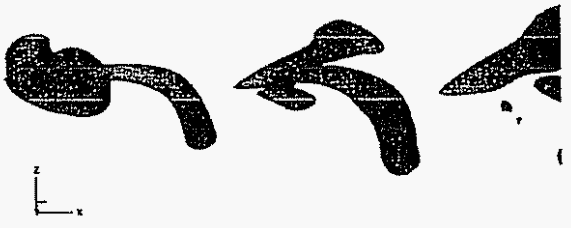

(d) $3T/4$

Figure 6 15: Spinning sphere at $Re = 300$, transverse rotation: shedding cycle, $Q = 0$ iso-surface, side view

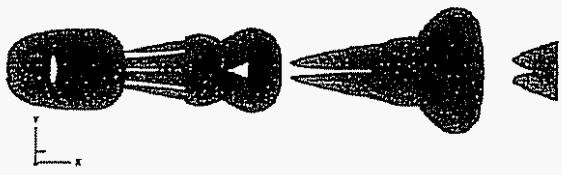

(a) 0

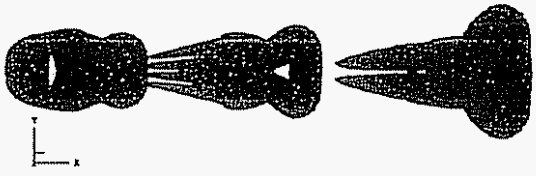

(b) $T/4$

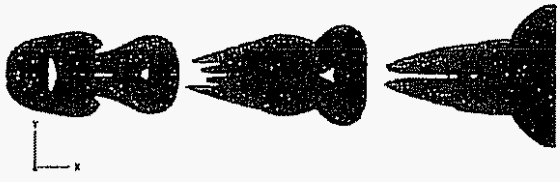

(c) $T/2$

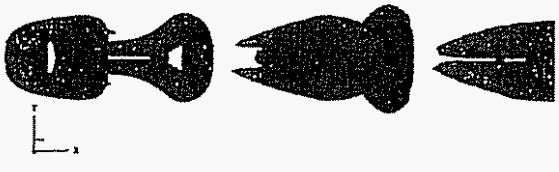

(d) $3T/4$

Figure 6 16: Spinning sphere at $Re = 300$, transverse rotation: shedding cycle, $Q = 0$ iso-surface, top view

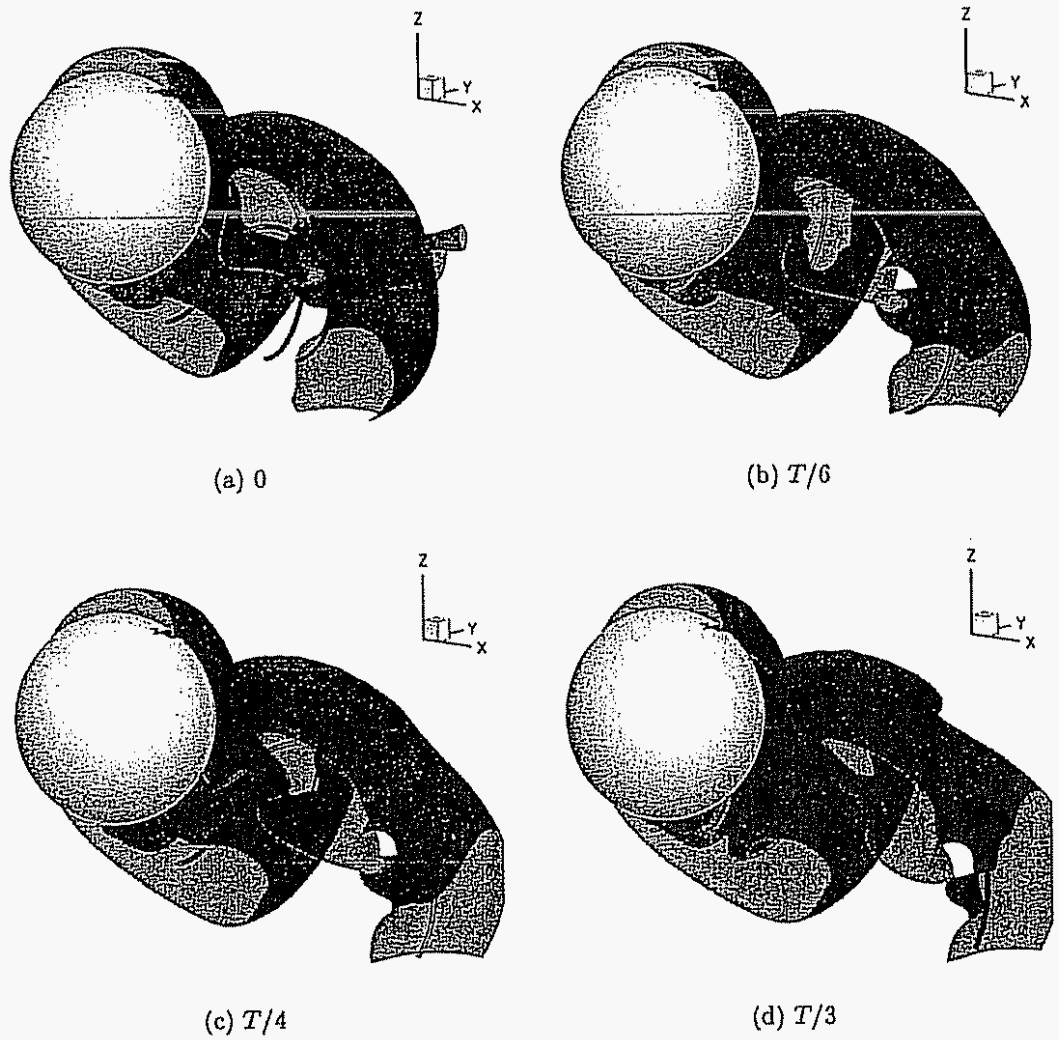

(a) 0 (b) $T/6$

(c) $T/4$ (d) $T/3$

Figure 6 17: Spinning sphere at $Re = 300$, transverse rotation: shedding cycle, $Q = 0$ iso-surface and vorticity lines

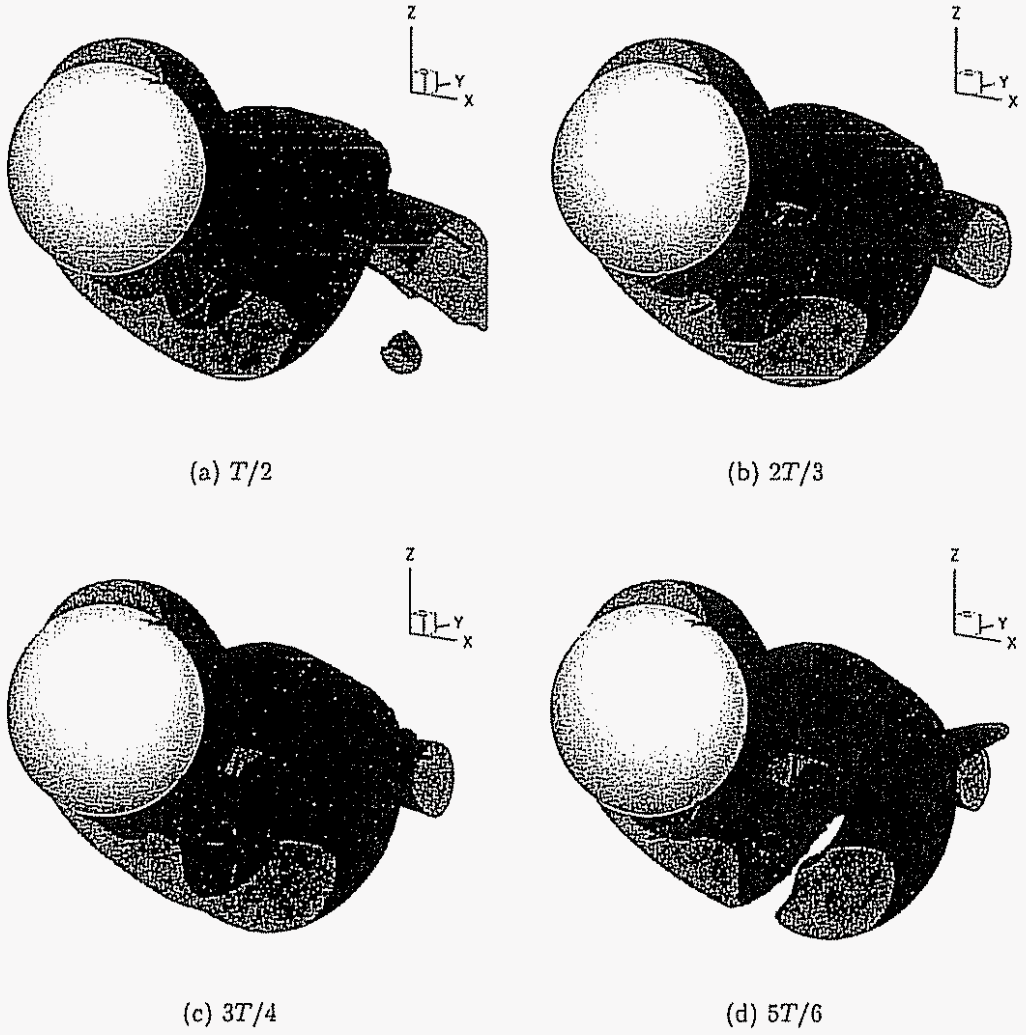

(a) $T/2$ (b) $2T/3$

(c) $3T/4$ (d) $5T/6$

Figure 6 18: Spinning sphere at $Re = 300$, transverse rotation: shedding cycle, $Q = 0$ iso-surface and vorticity lines (continued)

6.4.3 Forces

The history of the force coefficients is plotted in Fig 6 19 They were computed using the control volume approach We do note an abrupt transition around the time we changed the redistribution lattice

The force coefficients are not yet showing periodicity in time If indeed the flow and the forces remain periodic for large times, the average force coefficients can be computed for the last cycle of the simulation between $t \simeq 15.5$ and 20 We obtain $\overline{C_d} = 0\ 81$ and $\overline{C_l} = 0\ 4$; the ratio of these coefficients is then $\overline{C_l}/\overline{C_d} = 0\ 49$

We can compare those values to previous correlations or analytical results that cover a wide range of conditions For small Reynolds numbers first, Rubinow and Keller (1961) considered a Stokes expansion and found that

$$\begin{aligned} C_l &\simeq 2\omega^*(1 + O(Re)) \\ C_d &\simeq 12\,Re^{-1}(1 + \frac{3}{8}Re + o(Re)) , \end{aligned}$$

which in our case would yield $C_l = 1$ and $C_d = 4\ 54$ This is not unexpected as we are quite far from $Re < 1$

The work of Bearman and Harvey (1976), Barkla and Auchterlonie (1971), Maccoll (1928) concerned flows where $10^3 < Re < 10^5$ and involved, in some cases, not spheres but actual golf balls We will not try to use their results, but rather, consider more recent work which focused on intermediate Re Tsuji et al (1985) proposed

$$\begin{aligned} C_l &\simeq (0\ 4 \pm 0\ 1)\omega^* \\ C_d &\simeq K_1 + \frac{K_2}{Re} + \frac{K_3}{Re^2} \end{aligned}$$

The second expression assumes no effect of the rotation rate and showed good agreement over their experimental range, $550 < Re < 1600$ and $\omega^* < 0\ 7$; the constants K_1, K_2 and K_3 are adjusted according to the Reynolds number In our case, this yields $C_l \simeq 0\ 2 \pm 0\ 05$ and $C_d \simeq 0\ 66$ More recently, Oesterlé and Bui Dinh (1998)

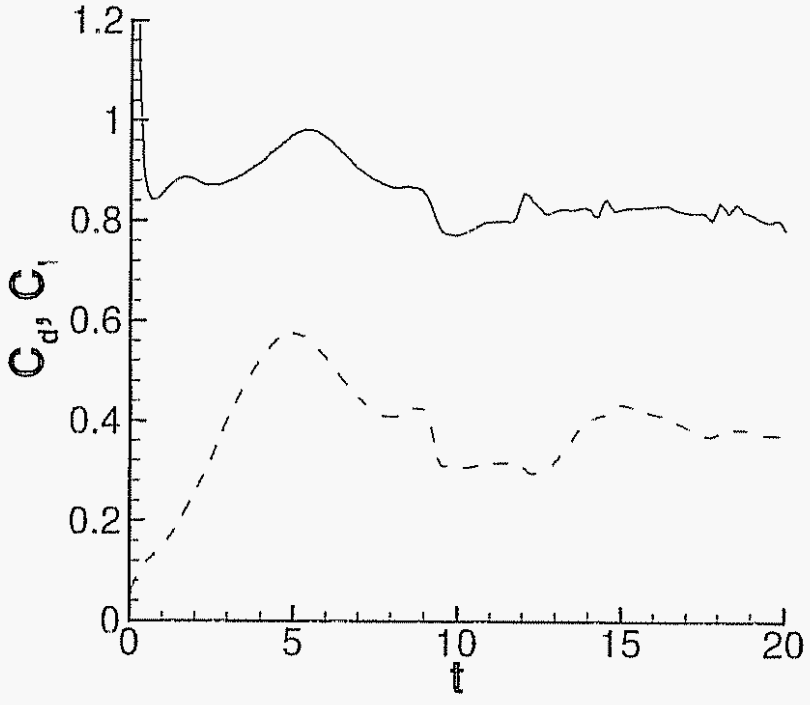

Figure 6.19: Spinning sphere at $Re = 300$, transverse rotation: drag coefficient C_d (solid) and lift coefficient C_l (dashed)

proposed

$$C_l \simeq 0.45 + (2\omega^* - 0.45)e^{-0.075\omega^{*0.4}Re^{0.7}}$$

for the ranges, $10 < Re < 140$ and $1 < \omega^* < 6$ This expression gives $C_l \simeq 0.475$ for the present case

6.4.4 Attachment and Separation

Fig. 6.20 and 6.21 show the magnitude of the skin friction along with skin friction lines for several instants during a shedding cycle. The lines emerge from a first node which remains located at $\phi = 0^o$, $\theta = 14^o$. At all times during a cycle, the lines converge into a second node on the top of the sphere which does move by a few degrees around its average position at $\phi = 0$, $\theta = 110^o$.

The skin friction lines describe the velocity field relative to the wall at a small distance above it. The two skin friction nodes therefore correspond to stagnation points in a frame rotating with the sphere (Fig. 6.23). Moreover, because these two points are stationary in the laboratory frame, they must be moving in the rotating frame. In effect, from the perspective of the sphere, there is one attachment point and one separation point, both moving at a velocity WR in the $y = 0$ plane of the sphere.

In the laboratory frame, the flow does, however, have a separation near the bottom of the sphere (Fig. 6.22). The separation line stands some distance from the wall; Fig. 6.25 shows the region of its intersection with the $y = 0$ plane. It is relatively difficult to locate accurately the separation point. It is a saddle point, and moreover its eigenvectors form a very narrow angle (Fig. 6.24). If we take this into consideration, we can give a rough estimate of the position of this point which moves very little over a shedding period, $x \simeq -0.55R$, $y \simeq -0.87R$, and corresponds to a distance from the center of the sphere $r = 1.03R$, and angles $\theta \simeq 56^o$, $\phi = 180^o$. An estimation of the rest of the line is given in Appendix F.2.

Similarly, the stagnation point does not lie on the surface of the sphere. Fig. 6.26 gives an estimation of its position by considering the streamlines in a $y = 0$ plane (Fig. 6.26(a)) and projected streamlines in an oblique slice (Fig. 6.26(b)).

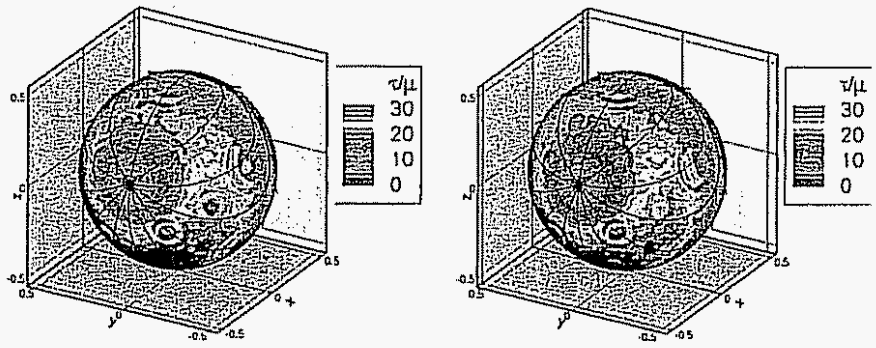

(a) $t = 15$ (b) $t = 16$

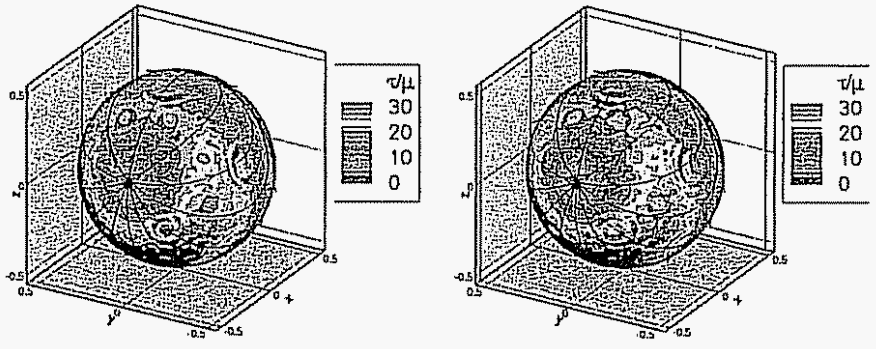

(c) $t = 17$ (d) $t = 18$

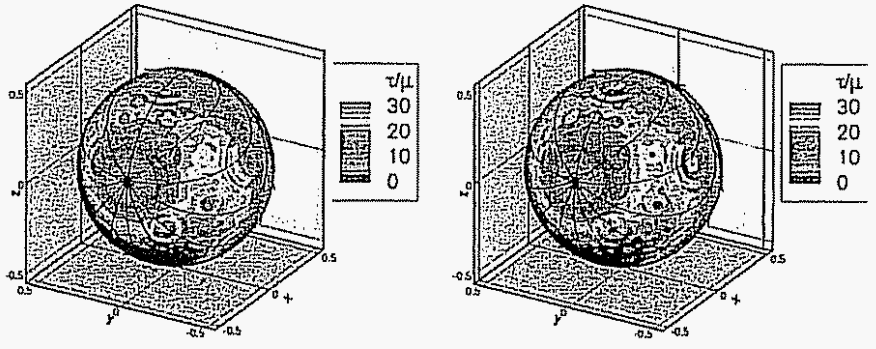

(e) $t = 19$ (f) $t = 20$

Figure 6 20: Spinning sphere at $Re = 300$, transverse rotation: skin friction magnitude and lines, front view

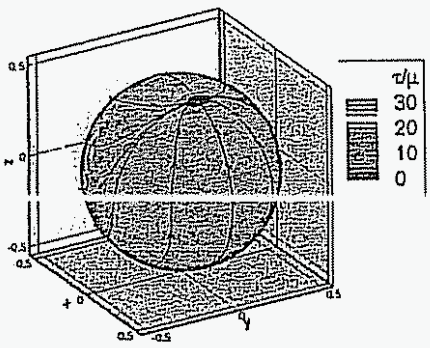

(a) $t = 15$

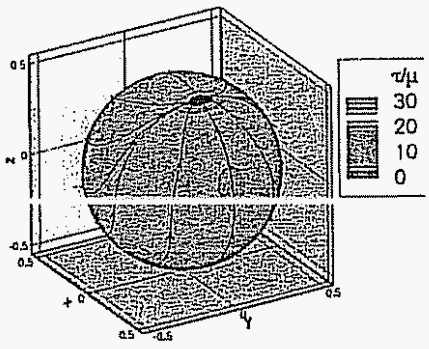

(b) $t = 16$

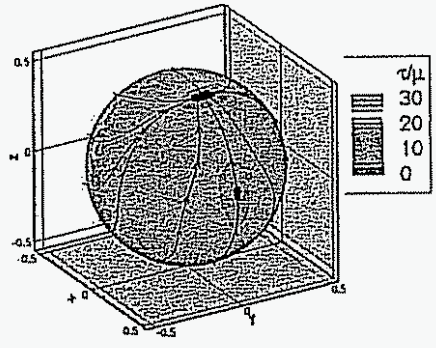

(c) $t = 17$

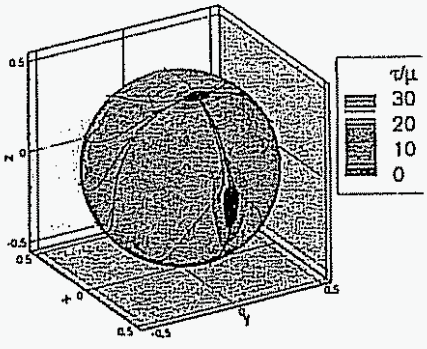

(d) $t = 18$

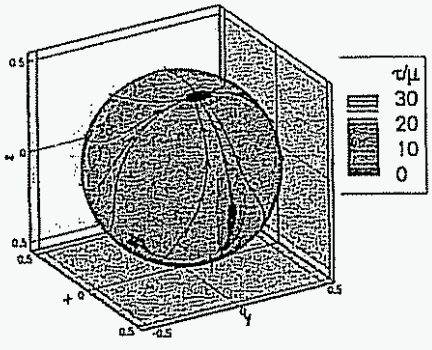

(e) $t = 19$

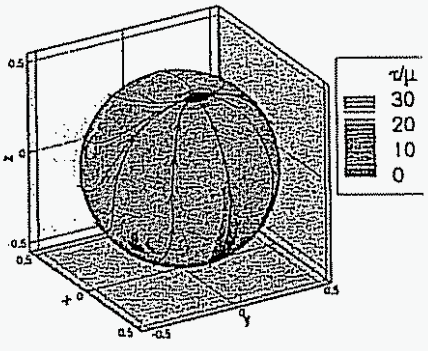

(f) $t = 20$

Figure 6 21: Spinning sphere at $Re = 300$, transverse rotation: skin friction magnitude and lines, back view

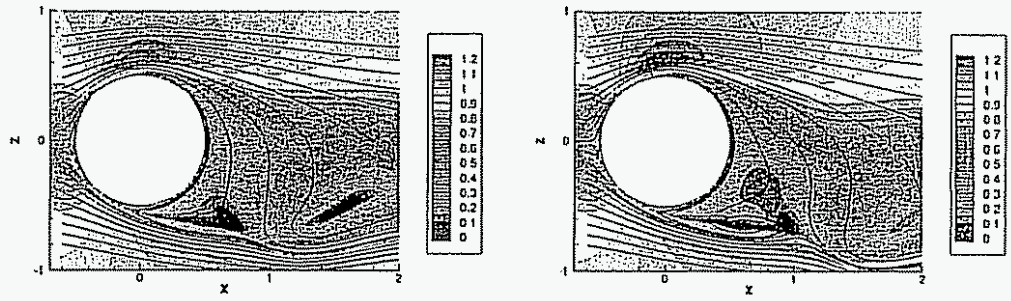

(a) $t = 15$ (b) $t = 16$

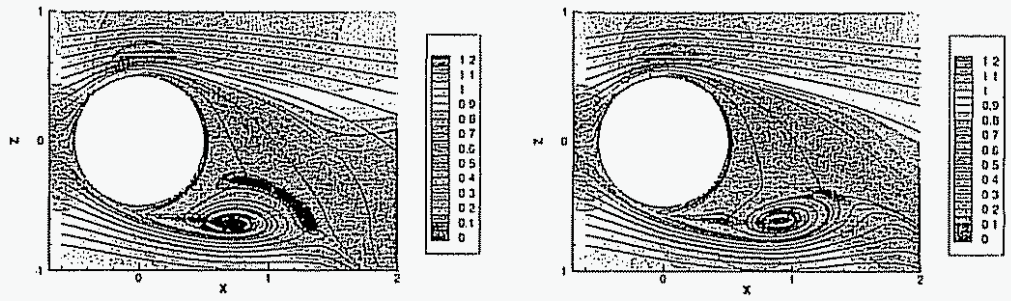

(c) $t = 17$ (d) $t = 18$

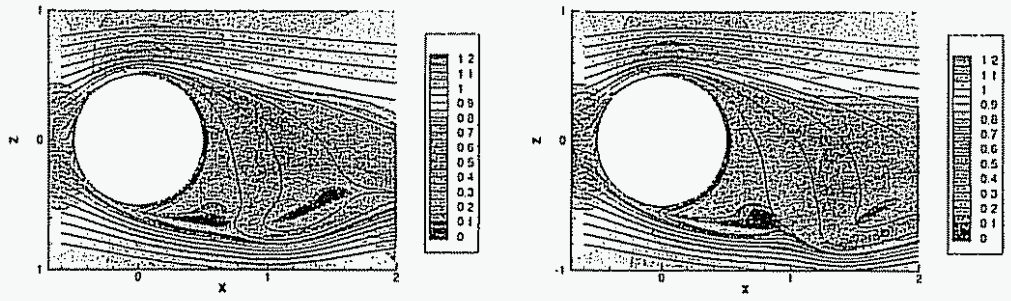

(e) $t = 19$ (f) $t = 20$

Figure 6 22: Spinning sphere at $Re = 300$, transverse rotation: velocity magnitude and streamlines in the $y = 0$ plane

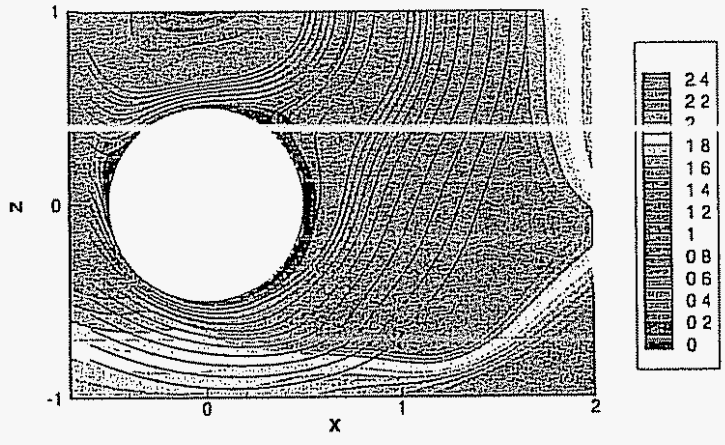

Figure 6 23: Spinning sphere at $Re = 300$, transverse rotation: velocity magnitude and streamlines in a frame rotating with the sphere, in the $y = 0$ plane at $t = 20$

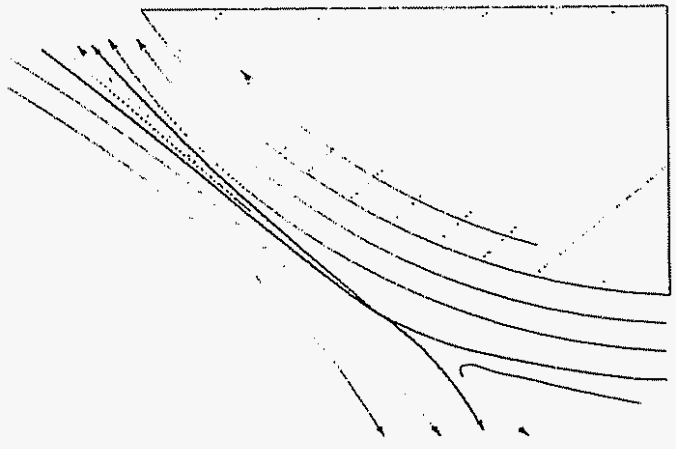

Figure 6 24: Spinning sphere at $Re = 300$, transverse rotation, bottom separation: localization of the saddle point

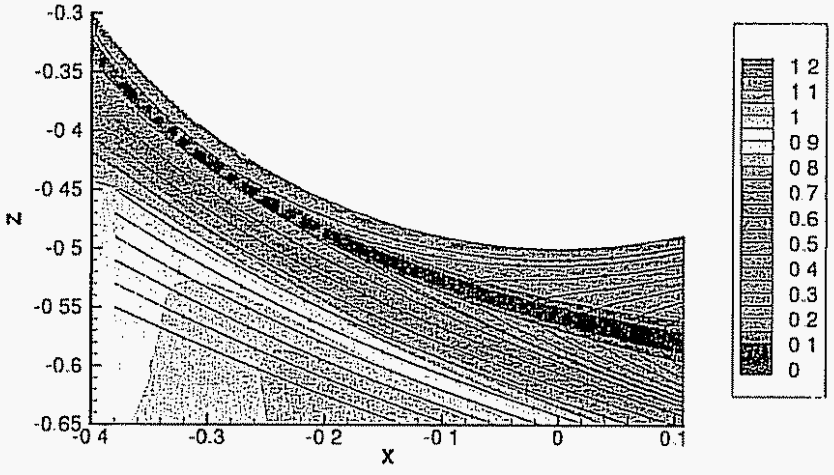

Figure 6.25: Spinning sphere at $Re = 300$, transverse rotation: velocity magnitude and streamlines in the $y = 0$ plane at $t = 20$, separation region

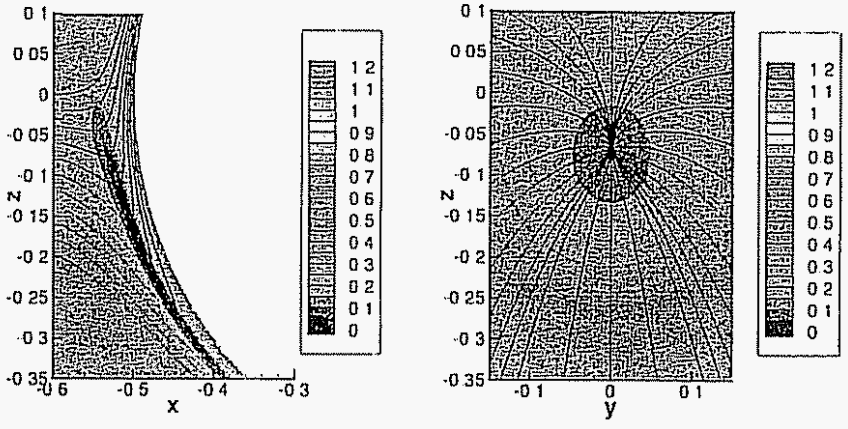

(a) velocity magnitude and streamlines in the $y = 0$ plane

(b) velocity magnitude and projected streamlines in the $0.98x + 0.18z = -0.56$ plane

Figure 6.26: Spinning sphere at $Re = 300$, transverse rotation: stagnation region at $t = 20$

6.5 Oblique Rotation

In this last case, the angular velocity is set to $\mathbf{W} = W\frac{\sqrt{2}}{2}(\mathbf{e}_x + \mathbf{e}_y)$ It loses most symmetries of the previous configurations As a result, it is more difficult to investigate

6.5.1 Numerics

This simulation used a spherical mapping from the start The parameters are identical to those of Section 6 4 It also used a coarser mesh for the representation of the sphere (5120 triangles) As seen in Fig 6 27, the only outstanding features are in the number of particles and the mesh Reynolds number plots At $t = 12\,5$, a more aggressive approach was adopted for the elimination of the weak elements in the wake This had no or little repercussion on the other diagnostics As in the previous cases, Re_h exhibits a growth by stages, as structures are convected into coarser regions of the redistribution lattice

6.5.2 Wake

Fig 6 28 and 6 29 show the different stages of a shedding cycle The wake shares some features with the one of Section 6 4 One recognizes in particular the hairpin structures, which are this time wrapped around each other

The shedding appears to have a period of $T \simeq 5$, which corresponds to a Strouhal frequency $St^{\measuredangle}_{\omega^*=0\,5} \simeq 0\,2$ Fig 6 30 and 6 31 offer a closer perspective on the periodic shedding of this flow As in the transverse case, we seed vorticity lines from points that rotate with the sphere In this case, we added a point on the axis of rotation at $\theta = 135^o$, $\phi = 90^o$ Because the flow is not symmetric, we only hide the region $y < -0\,4R$ A striking feature of the near wake is its similarity to the stream-wise rotation case of Section 6 3 It indeed consists in a main $\omega_x > 0$ filament which interacts with peripheral $\omega_x < 0$ structures

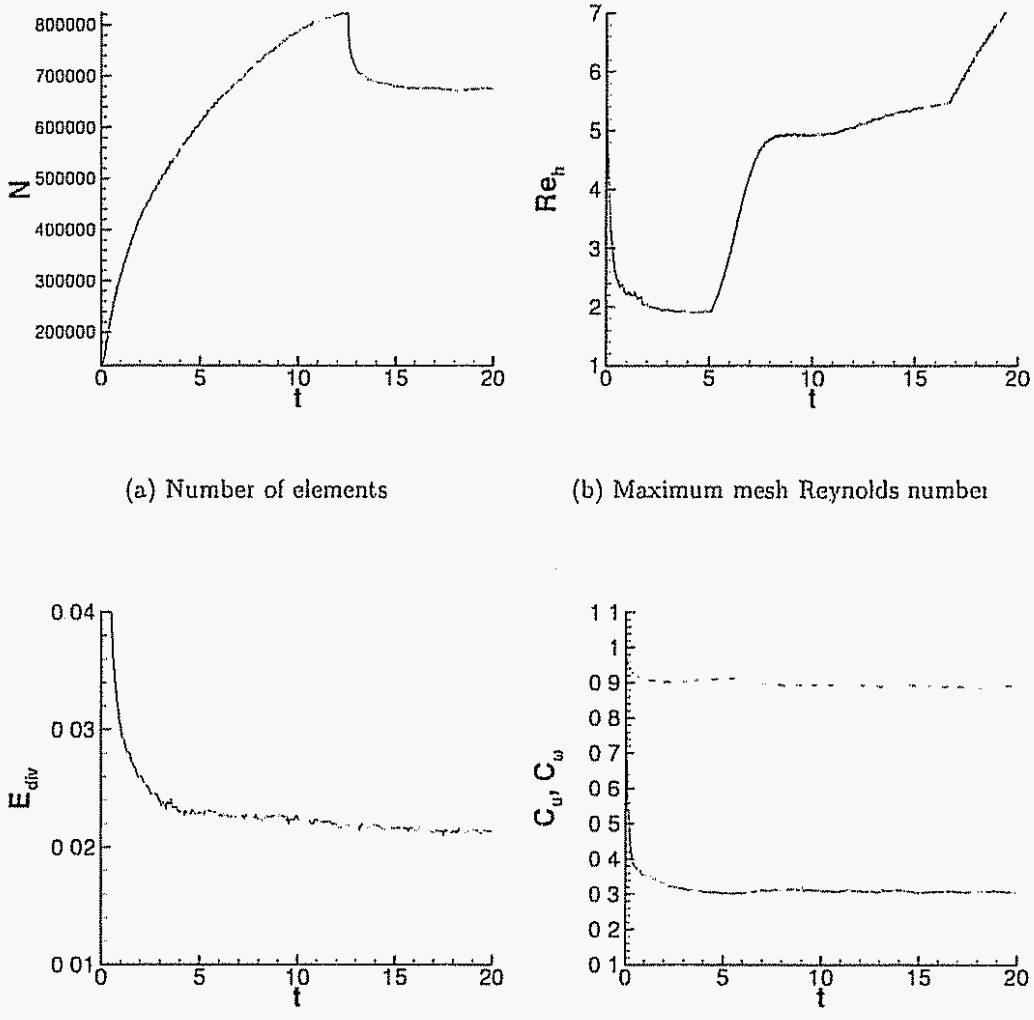

(a) Number of elements

(b) Maximum mesh Reynolds number

(c) Divergence error

(d) Courant number, vorticity expression (solid) and velocity expression (dashed)

Figure 6.27: Spinning sphere at $Re = 300$, oblique rotation: numerical diagnostics

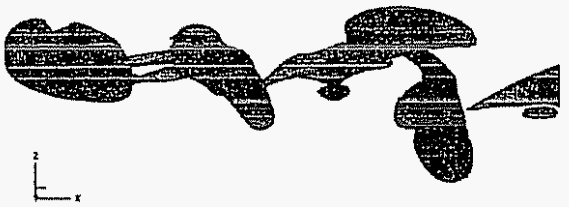

(a) 0

(b) $T/4$

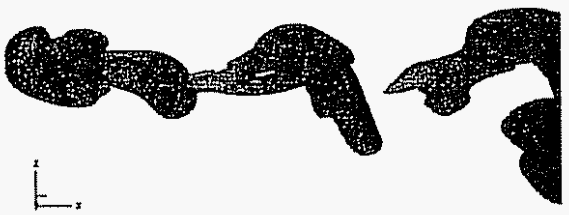

(c) $T/2$

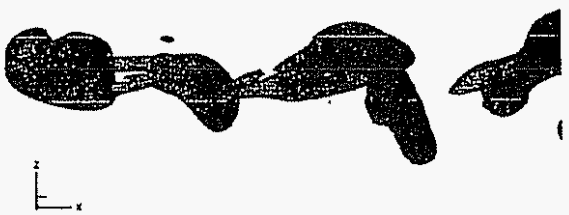

(d) $3T/4$

Figure 6 28: Spinning sphere at $Re = 300$, oblique rotation: shedding cycle, $Q = 0$ iso-surface, side view

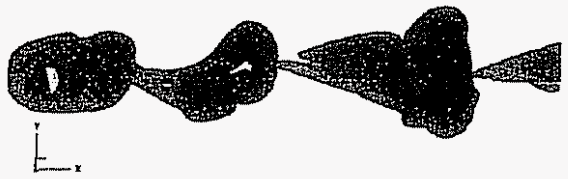

(a) 0

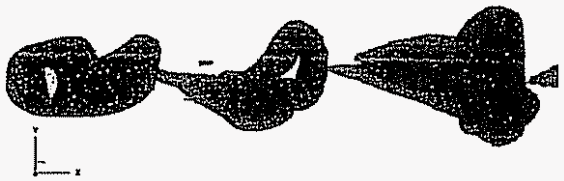

(b) $T/4$

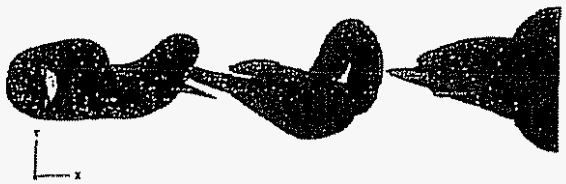

(c) $T/2$

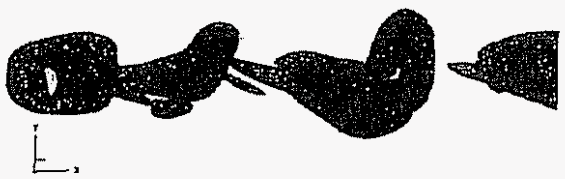

(d) $3T/4$

Figure 6 29: Spinning sphere at $Re = 300$, oblique rotation: shedding cycle, $Q = 0$ iso-surface, top view

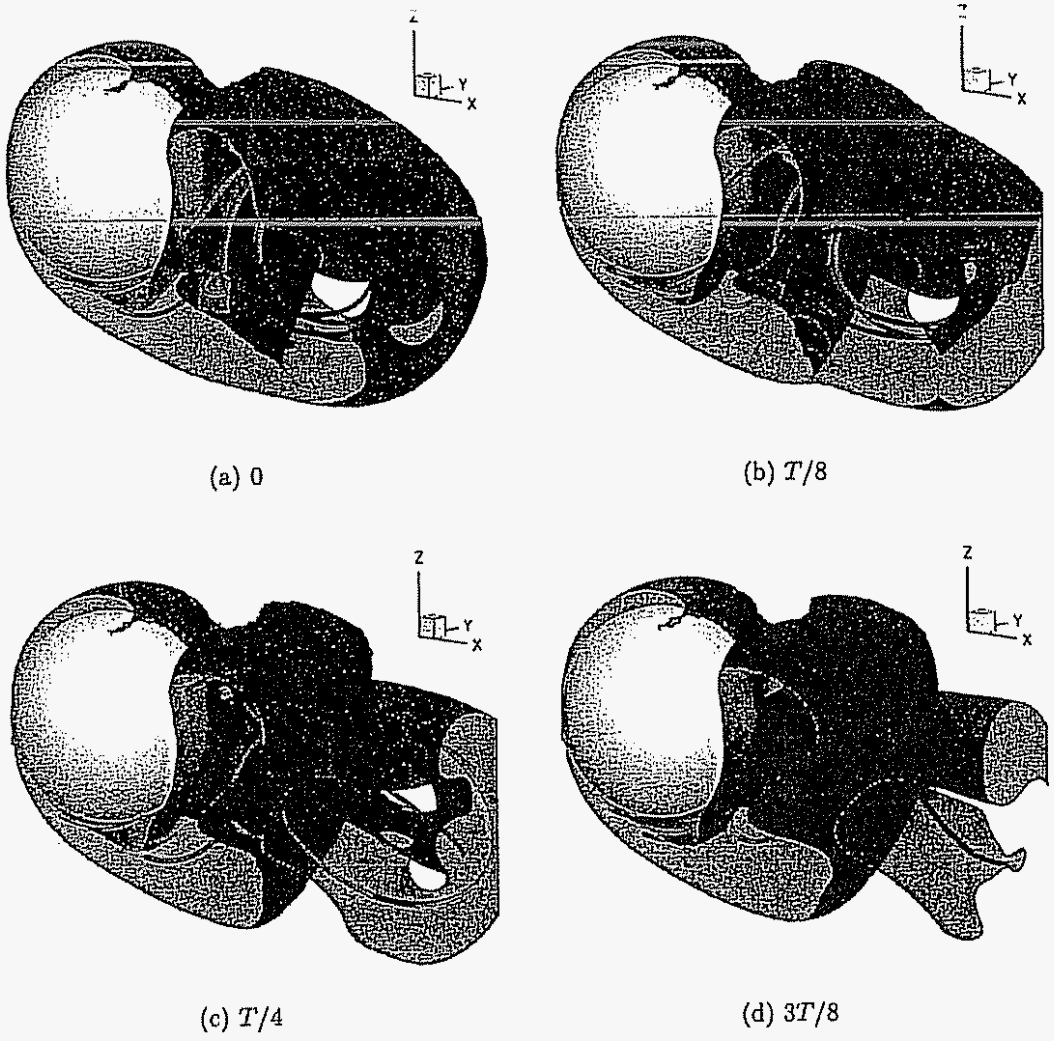

(a) 0

(b) $T/8$

(c) $T/4$

(d) $3T/8$

Figure 6 30: Spinning sphere at $Re = 300$, oblique rotation: shedding cycle, $Q = 0$ iso-surface and vorticity lines

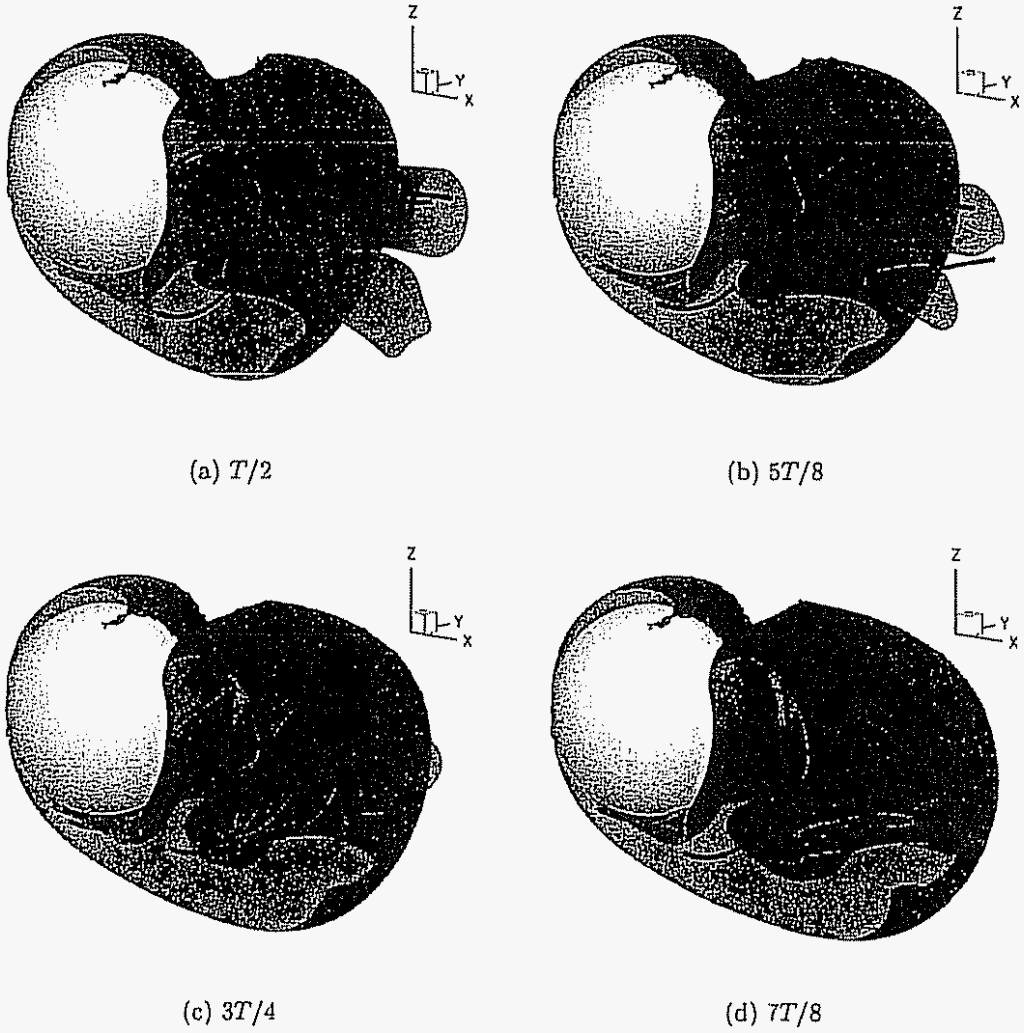

(a) $T/2$ (b) $5T/8$

(c) $3T/4$ (d) $7T/8$

Figure 6 31: Spinning sphere at $Re = 300$, oblique rotation: shedding cycle, $Q = 0$ iso-surface and vorticity lines (continued)

6.5.3 Forces

The force coefficients are plotted in Fig 6 32 During the last shedding cycle of our simulation, the drag coefficients have nearly adopted a periodic behavior around the average values $\overline{C_d} \simeq 0\,76$, $\overline{C_z} \simeq 0\,26$ and $\overline{C_y} \simeq -0\,165$ We note that the drag coefficient is between the stream-wise and transverse values and that interestingly enough, lift has been decreased proportionally to the amount of transverse angular velocity, $C_z^{\swarrow} \simeq \frac{\sqrt{2}}{2} C_z^{\perp} = 0\,28$

There is a non-zero transverse force C_y This component manifests itself in our plot of the wake (Fig 6 29), where the structures appear to have a positive y self-induced velocity

The ratio between the lateral force and the drag is $\sqrt{\overline{C_y}^2 + \overline{C_z}^2}/\overline{C_d} = 0\,41$ This value is lower than in the case of the transverse rotation; the decrease in drag, C_d and the transverse force, C_y are not large enough to compensate for the drop in C_z

6.5.4 Attachment and Separation

The skin friction lines have four critical points in this configuration. There is one attachment node in the front of the sphere Its location is fairly constant during a cycle, $\phi \simeq -14^o$, $\theta \simeq 9\,5^o$ All the friction lines converge into a separation node at $\phi \simeq 14\,5^o$, $\theta \simeq 106^o$. The last two points were not present on the transverse case There is an attachment node at $\phi \simeq 133^o$, $\theta \simeq 113^o$ which does move by a few degrees during a cycle, and a saddle which remains at $\phi \simeq 103^o$, $\theta \simeq 106^o$

As discussed in Section 6 4 4, all of these critical points do not lie on the axis of rotation of the sphere and correspond to attachments and separations in a rotating frame The critical points and lines for the laboratory frame are at some distance in the flow Appendix F 3 presents some additional results for the separation line

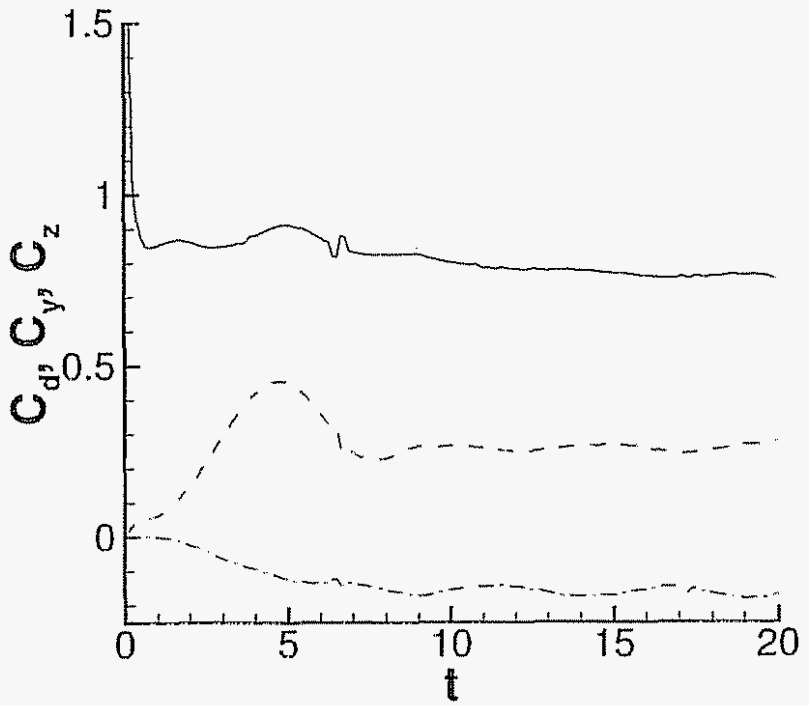

Figure 6 32: Spinning sphere at $Re = 300$, oblique rotation: drag coefficient C_d (solid), lift coefficient C_z (dashed) and transverse force coefficient C_y (dash-dotted)

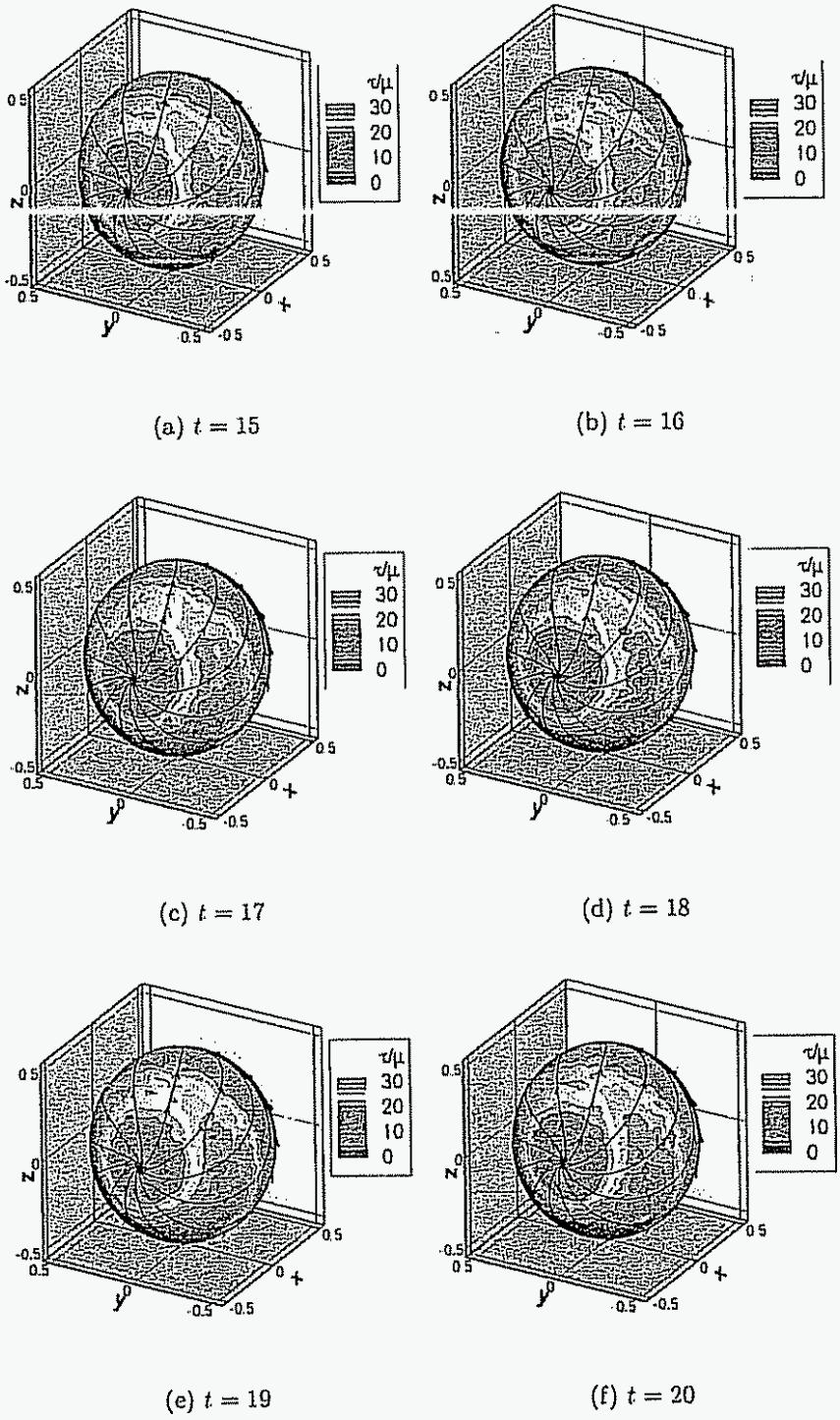

(a) $t = 15$ (b) $t = 16$

(c) $t = 17$ (d) $t = 18$

(e) $t = 19$ (f) $t = 20$

Figure 6 33: Spinning sphere at $Re = 300$, oblique rotation: skin friction magnitude and lines, front view

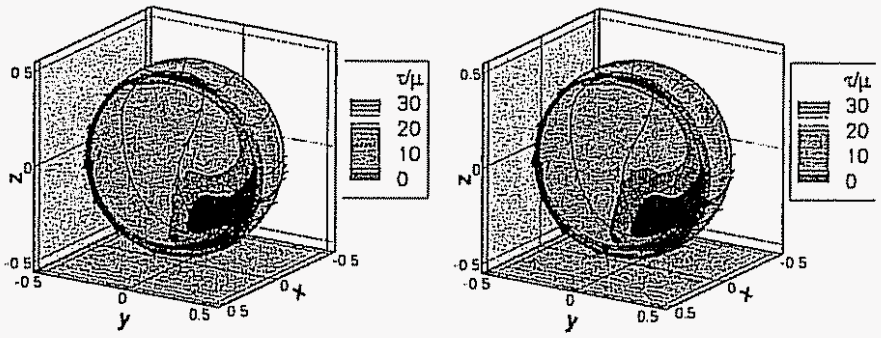

(a) $t = 15$ (b) $t = 16$

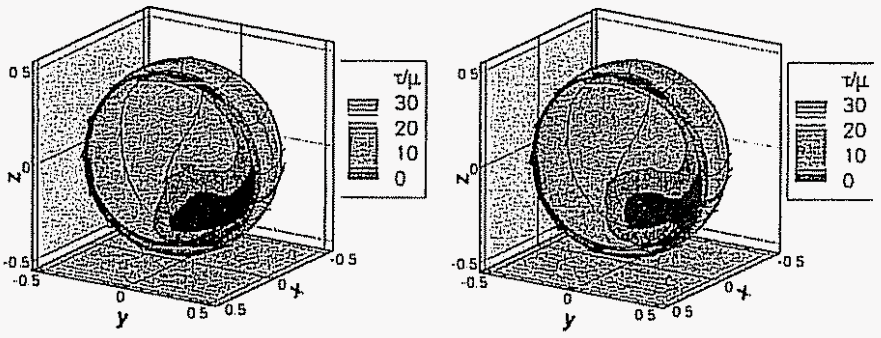

(c) $t = 17$ (d) $t = 18$

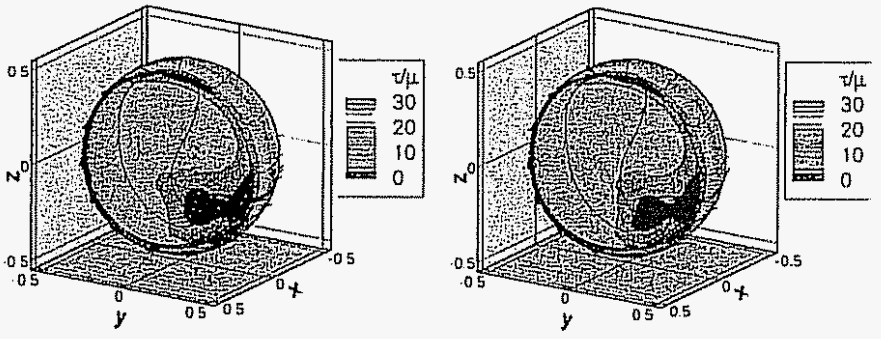

(e) $t = 19$ (f) $t = 20$

Figure 6 34: Spinning sphere at $Re = 300$, oblique rotation: skin friction magnitude and lines, back view

6.6 Conclusions

The first objective of this chapter was the validation of the approaches discussed in Chapter 4 and 5. Our results for the first configuration were found to be in agreement with recent numerical results. Our force measurements for the transverse rotation appear to be sound as they are inside the bounds given by experimental correlations for $Re \simeq 300$.

Wall vorticity measurements still display some spatial noise. The oscillations can be tracked to the solution of the boundary element method. This issue can be mitigated by increasing the size of the panels relative to the particles, as is done in Section 6.5. Beyond those numerical considerations, the present work brings new results for the spinning sphere flow at moderate Reynolds number.

Chapter 7

Flapping Motions

7.1 Introduction

The developments of Chapter 4 allow the study of flows with motions more complicated than the spinning sphere (Chapter 6) This chapter presents preliminary results for flows that involve the flapping motions of rigid objects. We consider the flow around a simplified fish in the presence of a free-stream and the swimming motion of an isolated plate.

7.2 Fish

We model a fish in a free-stream with two ellipsoids, one for the body, the other for the fin Each ellipsoid is generated from a sphere made of 1280 triangles which is then stretched into an ellipsoid The body is centered at the origin; its major axes are 2, 0.5 and 1 (Fig 7 1). The fin is located at $x = 1.6$; its major axes are 1, 0 3 and 1 5 The Reynolds number based on the free-stream is $Re = U_\infty L/\nu = 100$ where L is the length of the fin.

The geometry and the results are made dimensionless by the change of variables

$$t = \frac{U_\infty t^*}{L}$$
$$\mathrm{x} = \frac{\mathrm{x}^*}{L}.$$

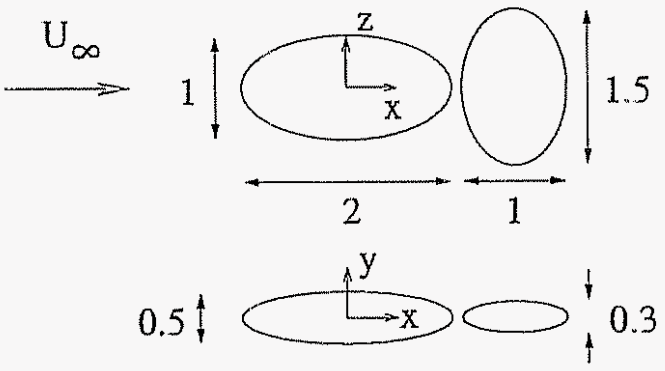

Figure 7.1: Swimming fish: geometry

The center of the fin is in a periodic translation

$$x = 1.6 \tag{7.1}$$

$$y = 0.2588 \sin(2\pi f t + \phi_t) \tag{7.2}$$

$$z = 0\ ; \tag{7.3}$$

its angle with the flow is also periodic

$$\theta_z = 0.2618 \sin(2\pi f t + \phi_r)$$

7.2.1 Low Frequency

The motion frequency is chosen as 0.25. The phase shift angles ϕ_t and ϕ_r are set to 0. The time step δt is 0.02 and the redistribution used a trumpet mapping ($R_0 = 2$, $m = 400$, $\mathrm{x_0} = [0\,0\,0]$). The numerical diagnostics of this simulation are shown in Fig. 7.2.

From the momentum plot (Fig. 7.3), we see that the wake is not momentum-less, i.e., I_x is not reaching a steady value. The fish is thus not overcoming drag. Fig. 7.4 and 7.5 show the vorticity structures shed by this configuration in terms of the sign

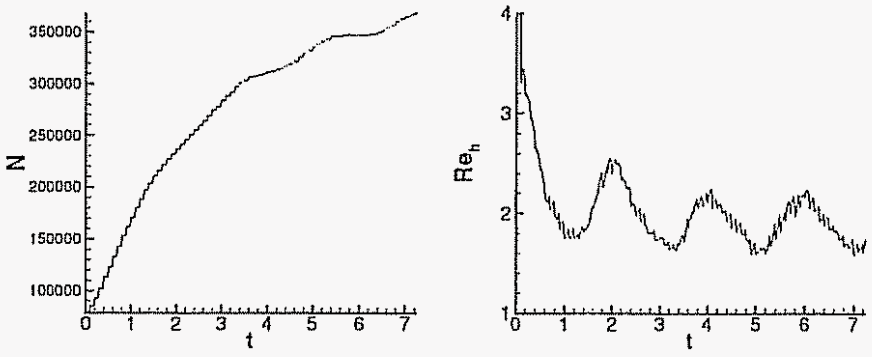

(a) Number of elements

(b) Maximum mesh Reynolds number

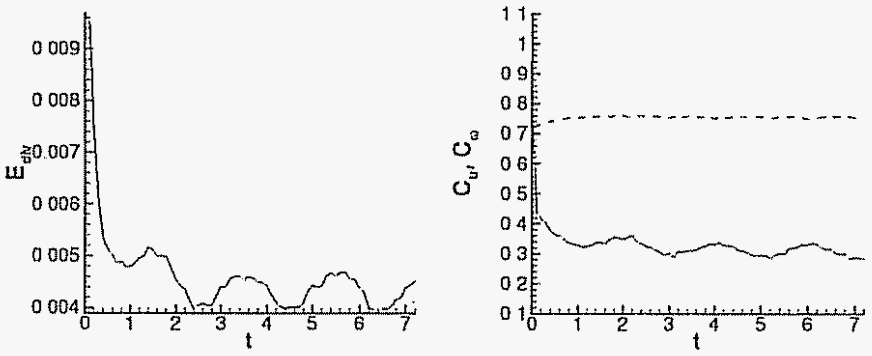

(c) Divergence error

(d) Courant number, vorticity expression (solid) and velocity expression (dashed)

Figure 7 2: Swimming fish at $Re_{U_\infty} = 100$, $f = 0\ 25$: numerical diagnostics

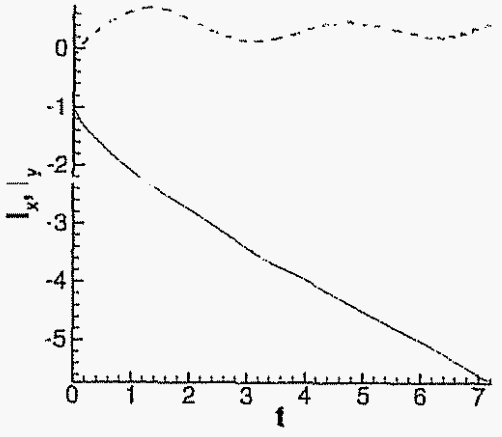

Figure 7.3: Swimming fish at $Re_{U_\infty} = 100$, $f = 0.25$: flow momentum; stream-wise momentum I_x is solid, transverse I_y is dashed

of ω_z in the symmetry plane and $Q = 0$ surfaces

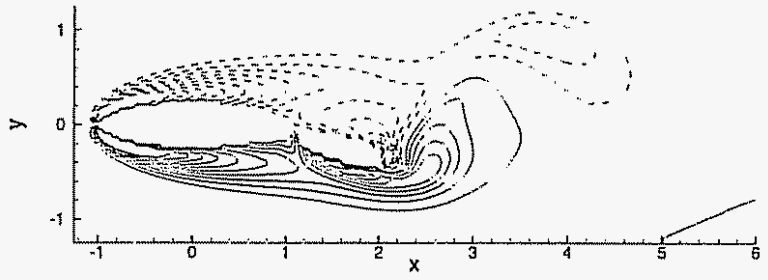

Figure 7 4: Swimming fish at $Re_{U_\infty} = 100$, $f = 0\ 25$: ω_z in the $z = 0$ plane at $t = 7\ 6$, contours in the interval $[-5; 5]$ by step of 0 5, the value 0 is omitted Positive contours are solid; negative ones, dashed

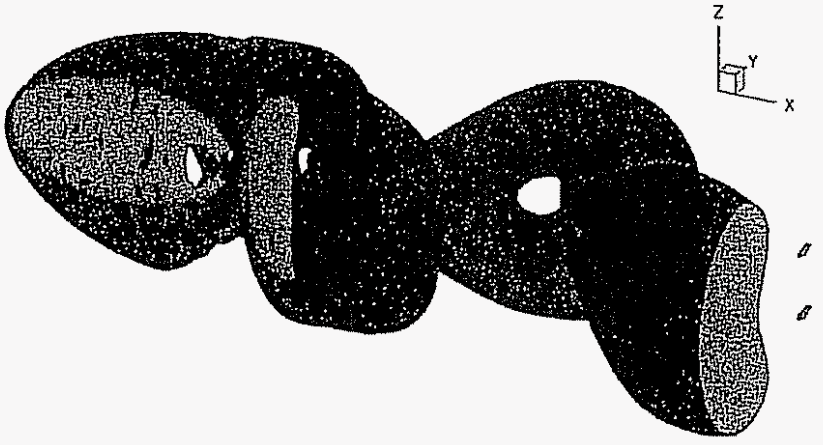

Figure 7 5: Swimming fish at $Re_{U_\infty} = 100$, $f = 0\ 25$: $Q = 0$ surfaces at $t = 7\ 6$

7.2.2 High Frequency

With the intent to produce more thrust, we increase the flapping frequency to 1 The time step δt is 0 01 and the redistribution used a trumpet mapping ($R_0 = 2$, $m = 600$, $x_0 = [1\,0\,0]$) This simulation covers three periods of the flapping motion

We see from the diagnostics in Fig 7 6, and in particular, C_ω (Fig 7 6(d)), that high values of vorticity are reached during this simulation It is explained by the faster flapping and the shedding of a vortex sheet at the back end of the fin This localized peak of vorticity evidently affects the vorticity divergence (Fig 7 6(c)) From the momentum plot (Fig 7 7), we note that the transverse component exhibits noise related to the vortex sheet shedding mentioned earlier No positive thrust was achieved Contours of ω_z and $Q = 0$ iso-surfaces are shown in Fig 7 8 and 7 9 respectively

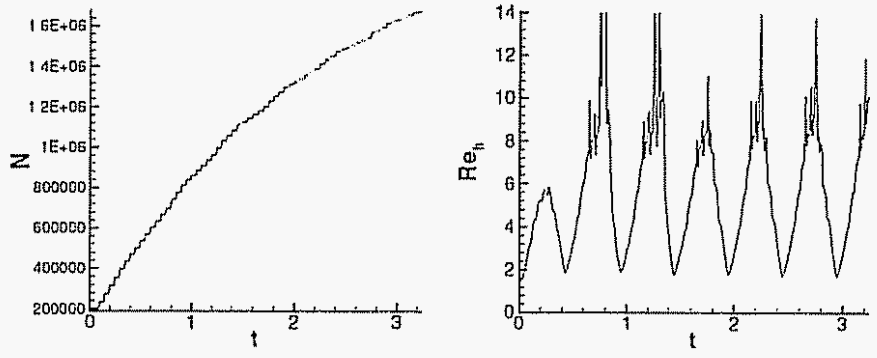

(a) Number of elements

(b) Maximum mesh Reynolds number

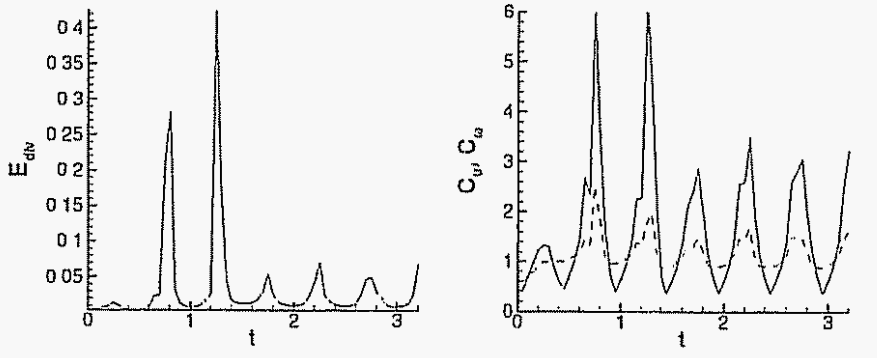

(c) Divergence error

(d) Courant number, vorticity expression (solid) and velocity expression (dashed)

Figure 7 6: Swimming fish at $Re_{U_\infty} = 100$, $f = 1$: numerical diagnostics

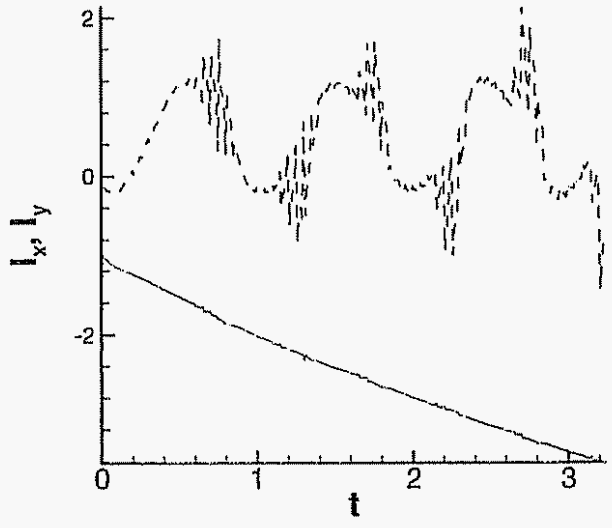

Figure 7.7: Swimming fish at $Re_{U_\infty} = 100$, $f = 1$: flow momentum; stream-wise momentum I_x is solid, transverse I_y is dashed.

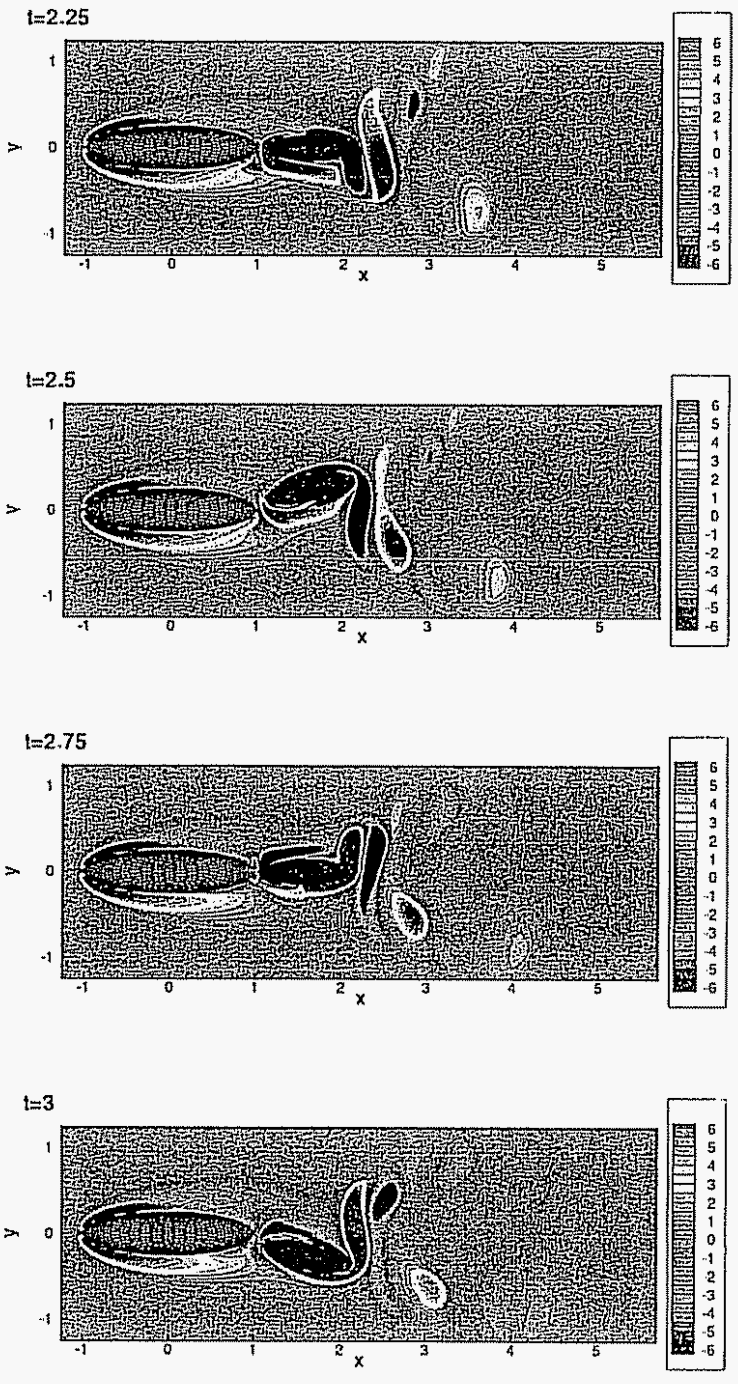

Figure 7 8: Swimming fish at $Re_{U_\infty} = 100$, $f = 1$: ω_z in the $z = 0$ plane at four stages of a stroke

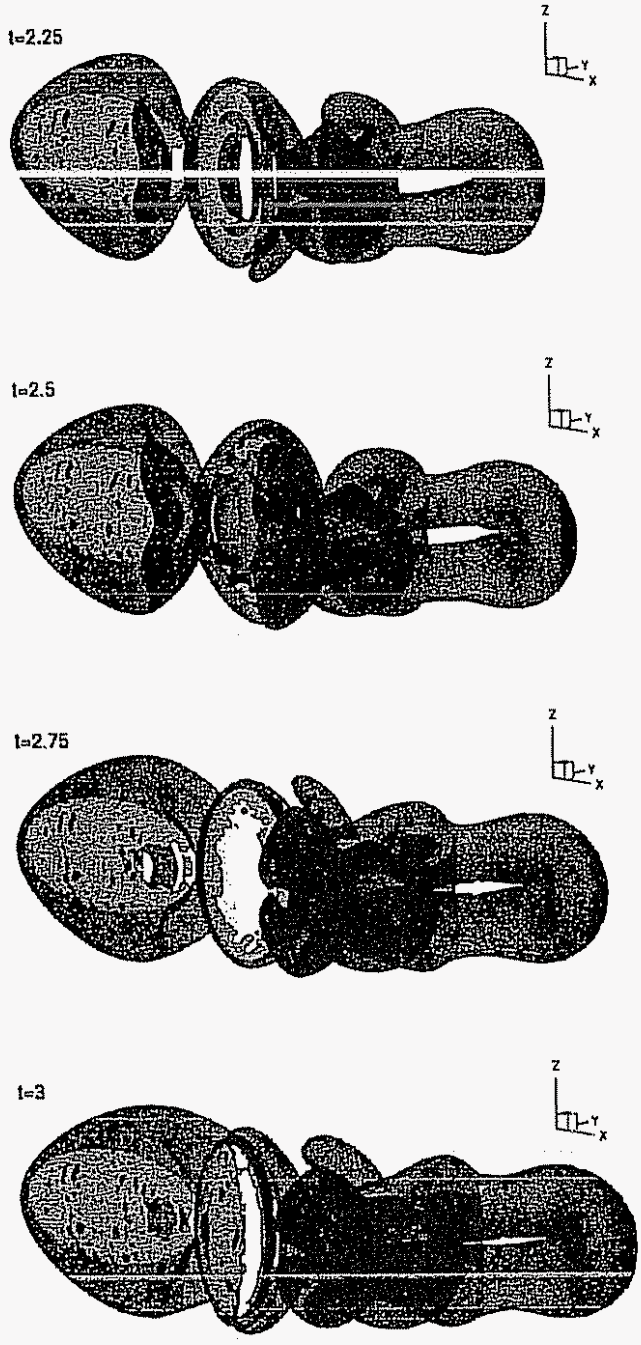

Figure 7 9: Swimming fish at $Re_{U_\infty} = 100$, $f = 1$: $Q = 0$ transparent surfaces at four stages of a stroke

7.3 Flapping Plate

Let us consider a simpler geometry with no free-stream It is a single flat ellipsoid with major axes [1, 0.25, 2] As for the fish, the geometry and the periodic motion are defined with respect to the first major axis of the ellipsoid L, $\mathrm{x} = \mathrm{x}'/L$ The motion is described as follows,

$$x = 0 \tag{7.4}$$

$$y = 1 \sin(2\pi f t + \phi_t) \tag{7.5}$$

$$z = 0\,, \tag{7.6}$$

and

$$\theta_z = \pi/4 \sin(2\pi f t + \phi_r)\,,$$

where $f = 0\ 25$, $\phi_t = -\pi/2$ and $\phi_r = -\pi$ The phase difference between the translation and the rotation is such that the plate is perpendicular to the axis of translation at its extreme positions and reaches an angle of attack of 45° when it is at $y = 0$
If we call A the amplitude of the translation, a Reynolds number of this flow can be defined as

$$Re = \frac{2\pi f A L}{\nu} = 157$$

We used a trumpet mapping with $R_0 = 4$, $m = 4$ and $\mathrm{x}_0 = [-0\ 500]$ The time step was set to 0 02

This configuration exhibits the same numerical problems as the high frequency fish; the plate sheds a vortex sheet during a part of its stroke We can see from the momentum history (Fig 7.11) that we increase the x component We have been through roughly two cycles and can already observe periodic features The slope of I_x is the largest when the plate is in the middle of its translation and going through $y = 0$ (at $t = 1$, 3 and 5) As the plate goes through the extrema of the motion (at $t = 2$, 4 and 6), I_x exhibits some noise and a slight dip We also note that the evolution of I_y displays more important slopes than I_x; this means that our flapping

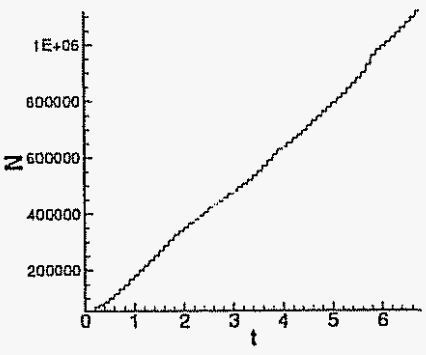

(a) Number of elements

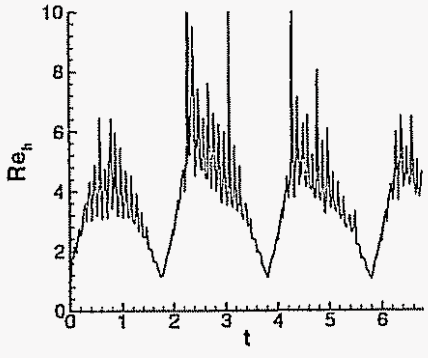

(b) Maximum mesh Reynolds number

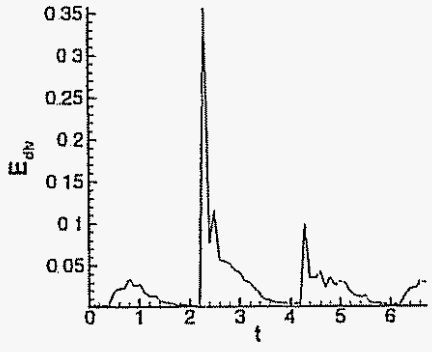

(c) Divergence error

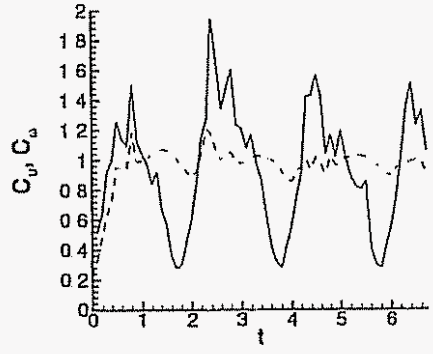

(d) Courant number, vorticity expression (solid) and velocity expression (dashed)

Figure 7.10: Flapping plate at $Re = 157$: numerical diagnostics

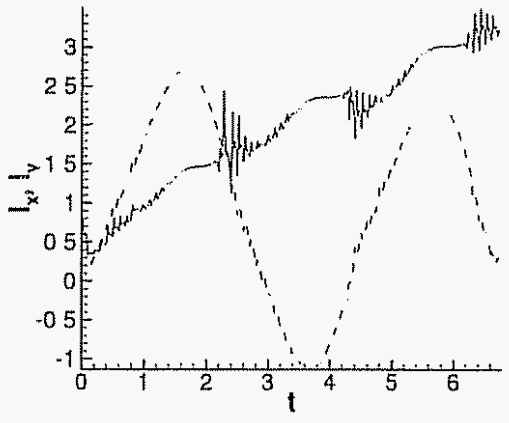

Figure 7 11: Flapping plate at $Re = 157$: flow momentum; the component I_x is solid, the transverse one I_y is dashed

motion probably induces an important flow in the transverse direction It may thus require significant power ($\propto F_y y_{\text{plate}}$) and not be very efficient in this respect

Fig 7 12 shows the vortex structures of this flow after two periods, at $t = 8$ The plate sheds trailing vortices which, logically, have the same induced velocity for strokes in both directions The structures shed at the extreme positions are relatively large and have moved a fair distance in the y direction, which is in agreement with our earlier interpretation of I_y

7.4 Conclusions

From a numerical perspective, the results of this chapter show that our method can handle complex moving geometries and that it is therefore well adapted for flapping and swimming motions However, they point to some shortcomings too; our method does not adapt its resolution in an efficient manner for this family of flows and may fail to resolve very fine scales, e g , in the case of a separation at an edge Our results also give us a preview of the complex physics of such flows; we see that the kinematics, in particular, will require a lot of care if we want to develop thrust efficiently

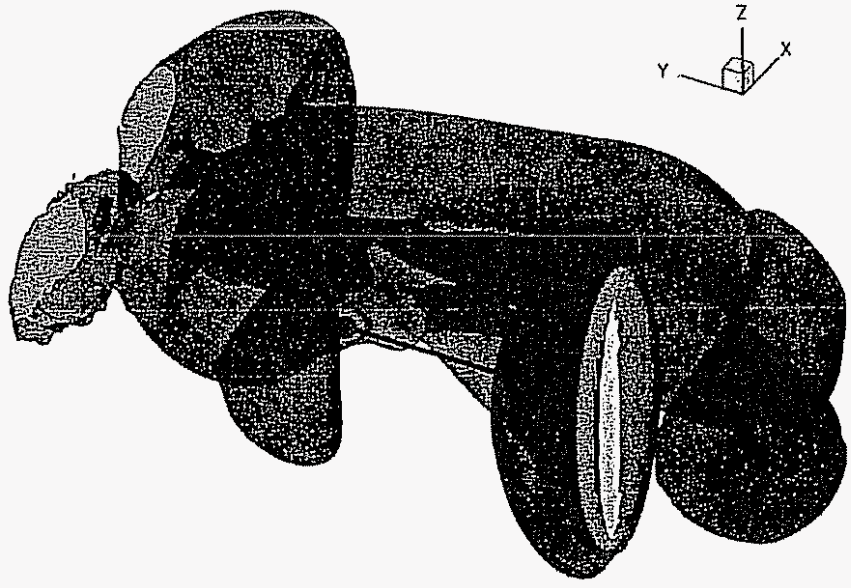

Figure 7 12: Flapping plate at $Re = 157$: transparent $Q = 0$ surfaces at $t = 8$; the black line represents the trajectory of the center of the plate

Chapter 8

Discussion and Outlook

To recapitulate, our work covered a broad range of issues for the three-dimensional vortex element method. Our first area of work was the construction and implementation of redistribution schemes based on the face-centered cubic lattice. These schemes introduce fewer new elements and display better isotropy than their counterparts in a cubic lattice. Our code was then used to investigate the physics of vortex ring reconnections. An algorithm to compute the vorticity autocorrelation and the energy spectrum was implemented, however its complexity in $O(N^2)$ restricts it to small problems

The second part of our work concerned bounded flows. We derived the contributions for spinning or deforming boundaries in the framework of the Biot-Savart law and introduced a method to compute them from a surface integral. While the kernel for spinning rigid boundaries is quite simple and based on the angular velocity, the expression for general deformations is naturally more complex. We introduced attached elements to represent near-wall vorticity. These elements have a shape function and a velocity kernel that accounts for the surface curvature. A hybrid strength exchange scheme was developed for the viscous interaction between these attached elements and free elements. They are used to enforce the wall normal vorticity boundary condition and mitigate the need for image particles across the wall

These tools were used to compute the flow past a spinning sphere at $Re = 300$. Three configurations were studied, one per orientation of the angular velocity. The

dimensionless spin rate was kept constant at 0.5. For stream-wise rotation, we obtained good quantitative agreement with previous work for the forces and separation position. There are very few experimental or numerical results in the case of the transverse rotation at our Reynolds number. We could only verify that our force coefficients are bounded by correlations for smaller and larger Re. Results are even scarcer if we consider an oblique rotation.

Preliminary results for more complex flows were presented in Chapter 7. We considered the swimming motion of a simplified fish at $Re_{U_\infty} = 100$ at two different frequencies and the flapping motion of a plate with no free-stream.

Future Work

In its current state, our code is able to handle rigid geometries that are more complicated than the sphere. It includes a version of Rubel (2002)'s closest point transform code to handle the computation of the distances relative to the boundaries. To reduce the memory requirements, our version includes a threshold beyond which the computed distance is approximated.

The simulation of more realistic swimming or insect flight motions at moderate Re will require the development of the boundary terms for deforming boundaries. However, in many cases, the flapping limb is thin enough to be considered a membrane. Because its volume is small, its deformations do not induce a contribution to Biot-Savart. Nevertheless, infinitely thin surfaces will need additional treatment in our code.

One other possible field of application is tumbling motions. This application will need additional work because forces must be computed efficiently at every time step.

Finally, as the results in Chapter 7 suggest, fine scales may appear rapidly for arbitrary flapping motions. A smoothly varying particle size can thus become impractical. In the long term, we will need a more flexible adaptation of the vortex element size if we want to treat complex deforming geometries at high Reynolds numbers. The answer may be in a combined Vortex-in-cell and Biot-Savart method where the latter

generates the boundary conditions of the former

Appendix A

Face-Centered Cubic and Hexagonal Redistributions

This section present the development and analytical expressions of the schemes presented in Chapter 2.

A.1 Hexagonal Lattice

The sites of the hexagonal lattice are described as $\mathbf{x_n} = \mathbf{Rn}$, where the matrix $\mathbf{R}$'s columns contain the lattice directions

$$\mathbf{R} = \begin{pmatrix} 1 & 1/2 \\ 0 & \sqrt{3}/2 \end{pmatrix}$$

There is a dual lattice, defined by the matrix

$$\dot{\mathbf{R}} = \left(\mathbf{R}^{-1}\right)^t = \begin{pmatrix} 1 & 0 \\ -\sqrt{3}/3 & 2\sqrt{3}/3 \end{pmatrix}$$

These two lattices and their coordinate systems are presented in Fig. A.1

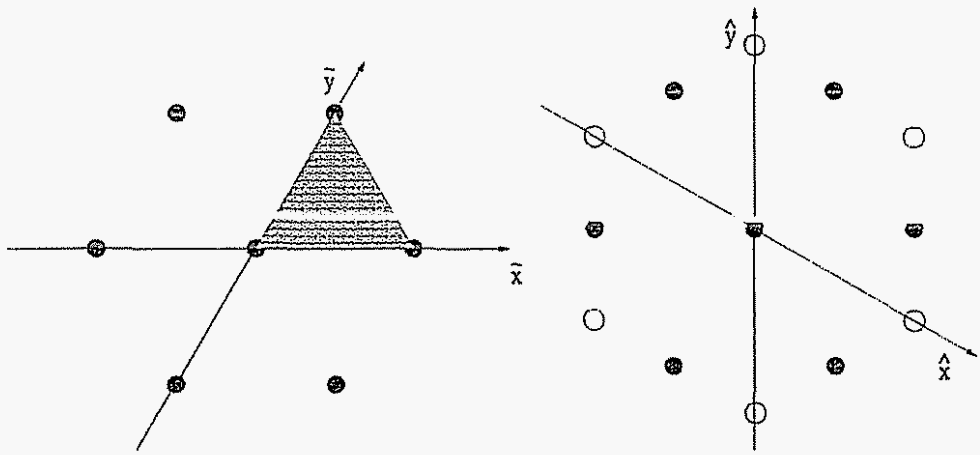

(a) Lattice coordinates (b) Dual lattice coordinates

Figure A.1: The hexagonal lattice, its dual lattice and their coordinate systems

A.1.1 Splines

The family of splines are built from the indicator function of the Voronoi cell

$$\mathfrak{F}_0 = \begin{cases} 1 & \text{if } |\hat{x}| < 0.5 \text{ and } |\hat{y}| < 0.5 \text{ and } |\hat{x} - \hat{y}| < 0.5 \\ 0 & \text{otherwise} \end{cases} \tag{A.1}$$

where $\hat{x}$ and $\hat{y}$ are dual lattice coordinates We then take successive convolutions of $\mathfrak{F}_0$ with itself; we get for $\mathfrak{F}_1$

$$\mathfrak{F}_1 = \frac{4}{3} \begin{cases} (1 - \hat{x}')(1 - \hat{x}' - \hat{y}') & \text{if } |\hat{x}' + \hat{y}'| < 1 \text{ and } |\hat{x}'| > 0.5 \\ (1 - \hat{y}')(1 - \hat{x}' - \hat{y}') & \text{if } |\hat{x}' + \hat{y}'| < 1 \text{ and } |\hat{y}'| > 0.5 \\ ((1 - \hat{y}')(1 - \hat{x}' - \hat{y}') - (0.5 - \hat{y}')^2) & \text{if } |\hat{x}'| \leq 0.5 \text{ and } |\hat{y}'| \leq 0.5 \\ 0 & \text{otherwise} \end{cases} \tag{A.2}$$

For conciseness, we use variables $\hat{x}'$, $\hat{y}'$ that map all the sextant onto the first one

$$\hat{x}' = \begin{cases} |\hat{x} - \hat{y}| & \text{if } \hat{x}\hat{y} > 0 \text{ and } |\hat{x}| > |\hat{y}| \\ |\hat{x}| & \text{otherwise} \end{cases} \tag{A.3}$$

$$\hat{y}' = \begin{cases} |\hat{x} - \hat{y}| & \text{if } \hat{x}\hat{y} > 0 \text{ and } |\hat{x}| <= |\hat{y}| \\ |\hat{y}| & \text{otherwise} \end{cases} \tag{A.4}$$

A.1.2 Compact Schemes

The compact schemes are expressed in the lattice coordinate system For the C^0 scheme, we have

$$\mathfrak{H}_{C^0} = \begin{cases} 1 - \tilde{x}' - \tilde{y}' & \text{if } |\tilde{x}' + \tilde{y}'| < 1 \\ 0 & \text{otherwise} \end{cases} \tag{A.5}$$

where once again we use a mapping to work in the first sextant–the first quarter in the hexagonal lattice coordinate system–

$$\tilde{x}' = \begin{cases} |\tilde{x}| & \text{if } \tilde{x}\tilde{y} > 0 \\ |\tilde{x} + \tilde{y}| & \text{otherwise} \end{cases} \tag{A.6}$$

$$\tilde{y}' = \begin{cases} |\tilde{y}| & \text{if } \tilde{x}\tilde{y} > 0 \\ \min(|\tilde{x}|, |\tilde{y}|) & \text{otherwise} \end{cases} \tag{A.7}$$

The C^2 scheme is found by convolution of the C^0 scheme by itself

$$\mathcal{H}_{C^2} = \frac{1}{12}\begin{cases} (\tilde{x}' - \tilde{y}' - 2)(\tilde{x}' + \tilde{y}' - 2)^3 & \text{if } |\tilde{x}' + \tilde{y}'| < 2 \text{ and } \tilde{x}' > 1 \\ (\tilde{y}' - \tilde{x}' - 2)(\tilde{x}' + \tilde{y}' - 2)^3 & \text{if } |\tilde{x}' + \tilde{y}'| < 2 \text{ and } \tilde{y}' > 1 \\ (6 + 12\tilde{x}'\tilde{y}'(\tilde{x}' + \tilde{y}' - 1) & \\ \quad - (\tilde{x}'^2 + \tilde{y}'^2)(12 + 2\tilde{x}'\tilde{y}') & \text{if } |\tilde{x}' + \tilde{y}'| < 2 \text{ and } \tilde{x}' + \tilde{y}' < 1 \\ \quad +8(\tilde{x}'^3 + \tilde{y}'^3) - \tilde{x}'^4 - \tilde{y}'^4) & \\ (10 - 12(\tilde{x}' + \tilde{y}') + 12\tilde{x}'\tilde{y}' & \\ \quad - 2\tilde{x}'\tilde{y}'(\tilde{x}'^2 + \tilde{y}'^2) & \text{if } |\tilde{x}' + \tilde{y}'| < 2 \text{ and } \tilde{x}' + \tilde{y}' \geq 1 \\ \quad +4(\tilde{x}'^3 + \tilde{y}'^3) - \tilde{x}'^4 - \tilde{y}'^4) & \\ 0 & \text{otherwise} \end{cases} \tag{A.8}$$

The third order scheme can then be written as

$$\mathcal{H}^3_{C^1} = \mathcal{H}^2_{C^2} + \frac{1}{12}\begin{cases} (2(\tilde{x}'^2 - \tilde{y}'^2) - 4\tilde{x}' - 2\tilde{y}') & \\ \qquad (\tilde{x}' + \tilde{y}' - 2)^2 & \text{if } |\tilde{x}' + \tilde{y}'| < 2 \text{ and } \tilde{x}' > 1 \\ (2(\tilde{y}'^2 - \tilde{x}'^2) - 4\tilde{y}' - 2\tilde{x}') & \\ \qquad (\tilde{x}' + \tilde{y}' - 2)^2 & \text{if } |\tilde{x}' + \tilde{y}'| < 2 \text{ and } \tilde{y}' > 1 \\ -\tilde{x}|\tilde{x}^2(12 - 3\tilde{y} - 2\tilde{x}) + 12\tilde{x}(\tilde{y} - 1) & \\ \quad - \tilde{y}(6 - 6\tilde{y} + \tilde{y}^2)| & \text{if } |\tilde{x}' + \tilde{y}'| < 1 \\ -\tilde{y}|\tilde{y}^2(12 - 3\tilde{x} - 2\tilde{y}) + 12\tilde{y}(\tilde{x} - 1) & \\ \quad - \tilde{x}(6 - 6\tilde{x} + \tilde{x}^2)| & \\ -\tilde{x}| - 6 + 6\tilde{x}^2 - 2\tilde{x}^3 & \\ \quad + 6\tilde{y} - 3\tilde{x}^2\tilde{y} - \tilde{y}^3| & \text{if } |\tilde{x}' + \tilde{y}'| < 2 \text{ and } \tilde{x}' + \tilde{y}' > 1 \\ -\tilde{y}| - 6 + 6\tilde{y}^2 - 2\tilde{y}^3 & \\ \quad + 6\tilde{x} - 3\tilde{y}^2\tilde{x} - \tilde{x}^3| & \\ 0 & \text{otherwise} \end{cases} \tag{A.9}$$

A.2 Face-Centered Cubic Lattice

The directions of the FCC lattice and its dual counterpart are given by

$$\mathbf{R} = \begin{pmatrix} 1 & 1/2 & 1/2 \\ 0 & \sqrt{3}/2 & \sqrt{3}/6 \\ 0 & 0 & \sqrt{6}/3 \end{pmatrix}, \hat{\mathbf{R}} = \begin{pmatrix} 1 & 0 & 0 \\ -\sqrt{3}/3 & 2\sqrt{3}/3 & 0 \\ -\sqrt{6}/6 & -\sqrt{6}/6 & \sqrt{6}/2 \end{pmatrix} \tag{A.10}$$

A.2.1 Splines

The first spline is given by

$$\mathfrak{F}_0 = \begin{cases} 1 & \text{if } |\hat{x}| < 0.5 \text{ and } |\hat{y}| < 0.5 \text{ and } |\hat{z}| < 0.5 \\ & \text{and } |\hat{x} - \hat{y}| < 0.5 \text{ and } |\hat{x} - \hat{z}| < 0.5 \text{ and } |\hat{z} - \hat{y}| < 0.5 \\ 0 & \text{otherwise} \end{cases} \tag{A.11}$$

We then get by convolution

$$\mathcal{F}_1 = \begin{cases} (1-\hat{x}')(1-\hat{y}')(1-\hat{z}') & \text{if } |\hat{x}'| \geq 0.5 \text{ and } |\hat{y}'| \geq 0.5 \\ & \text{and } |\hat{z}'| \geq 0.5 \\ (1-\hat{x}')(1-\hat{y}')\hat{z}' + (0.5-A)(B-\hat{y}'+0.5)^2 & \\ \quad + (2/3)(C-\hat{z}')^3 & \text{if } |\hat{x}'| \geq 0.5 \text{ and } |\hat{y}'| \geq 0.5 \\ \quad + 2(0.5-A)(0.5-B)(C-\hat{z}') & \text{and } |\hat{z}'| < 0.5 \\ \quad + (0.5-B)(A-\hat{x}'+0.5)^2 & \\ (1-\hat{x}')\hat{y}'\hat{z}' + (1.5-2\hat{x}'+\hat{y}')(0.5-\hat{y}')\hat{z}' & \\ \quad + 2(0.5-\hat{x}'+\hat{z}')(0.5-\hat{y}'+\hat{z}')(0.5-\hat{z}') & \\ \quad + (0.5-\hat{x}'+\hat{y}')(0.5-\hat{z}')^2 + 0.5(0.5-\hat{z}')^2 & \text{if } |\hat{x}'| < 0.5 \\ \quad - 2(0.5-\hat{z}'-(\hat{y}'-\hat{z}')/3)(\hat{y}'-\hat{z}')^2 & \\ & \text{if } |\hat{x}'| \geq 0.5 \text{ and } |\hat{y}'| < 0.5 \\ C\,D\,(1-\hat{x}') & \text{and } |\hat{z}'| < 0.5 \\ & \text{and } (\hat{y}'-\hat{x}') \leq -0.5 \\ (1-\hat{x}')\hat{y}'\hat{z}' & \\ \quad + (1.5-2\hat{x}'+\hat{y}')(0.5-\hat{y}')\hat{z}' & \text{if } |\hat{x}'| \geq 0.5 \text{ and } |\hat{y}'| < 0.5 \\ \quad + 2(0.5-A)(0.5-B)(C-\hat{z}') & \text{and } |\hat{z}'| < 0.5 \\ \quad + (0.5-\hat{x}'+\hat{y}')(C-\hat{z}')^2 + 0.5(C-\hat{z}')^2 & \text{and } (\hat{y}'-\hat{x}') > -0.5 \\ \quad - 2(C-\hat{z}'-B/3)B^2)); & \\ 0 & \text{otherwise} \end{cases} \tag{A.12}$$

where the variables $\hat{x}'$, $\hat{y}'$, $\hat{z}'$ are the dual lattice variables reordered in decreasing order $\hat{x}' \geq \hat{y}' \geq \hat{z}'$ and the variables A, B and C are defined as

$$A = \hat{x}' + C - \hat{z}' - 0.5 \tag{A.13}$$

$$B = \hat{x}' + C - \hat{z}' - 0.5 \tag{A.14}$$

$$C = \min(1 + \hat{z}' - \hat{y}', 1 + \hat{z}' - \hat{x}', 0.5) \tag{A.15}$$

$$D = \min(1 + \hat{y}' - \hat{x}', 0.5) \tag{A.16}$$

A.2.2 Compact Schemes

We switch back to the lattice coordinates $\tilde{x}$, $\tilde{y}$, $\tilde{z}$

$$FCC_1 = \begin{cases} 1 - 0.5(|\tilde{x}' + \tilde{y}'| + |\tilde{y}' + \tilde{x}'| + |\tilde{x}' + \tilde{z}'|) & \text{if } \tilde{x}\tilde{y}\tilde{z}(\tilde{x} + \tilde{y} + \tilde{z}) > 0 \\ \frac{1}{6}(1 + 3(1 - (|\hat{y}'| + |\hat{z}'|)) & \\ \quad + 2|1 - (|\hat{y}'| + |\hat{z}'|)| & \text{if } \tilde{x}\tilde{y}\tilde{z}(\tilde{x} + \tilde{y} + \tilde{z}) < 0 \text{ and } \tilde{y}\tilde{z} > 0 \\ \quad - |\hat{x}' + \hat{z}'| - |\hat{x}' + \hat{y}'|) & \\ \frac{1}{6}(1 + 3(1 - (|\hat{z}'| + |\hat{x}'|)) & \\ \quad + 2|1 - (|\hat{z}'| + |\hat{x}'|)| & \text{if } \tilde{x}\tilde{y}\tilde{z}(\tilde{x} + \tilde{y} + \tilde{z}) < 0 \text{ and } \tilde{x}\tilde{z} > 0 \\ \quad - |\hat{y}' + \hat{x}'| - |\hat{y}' + \hat{z}'|) & \\ \frac{1}{6}(1 + 3(1 - (|\hat{x}'| + |\hat{y}'|)) & \\ \quad + 2|1 - (|\hat{x}'| + |\hat{y}'|)| & \text{if } \tilde{x}\tilde{y}\tilde{z}(\tilde{x} + \tilde{y} + \tilde{z}) < 0 \text{ and } \tilde{x}\tilde{y} > 0 \\ \quad - |\hat{z}' + \hat{y}'| - |\hat{z}' + \hat{x}'|) & \\ 0 & \text{otherwise} \end{cases} \tag{A.17}$$

FCC_3 was obtained numerically by the convolution of FCC_1 by itself The high order FCC_3' was then computed from the combination of FCC_3 with its gradient These two operations were carried out in Fourier space

Appendix B

Energy Spectrum

B.1 Definitions

We define the Fourier transform of a field f as

$$\hat{f}(\mathrm{k}) = \frac{1}{(2\pi)^{3/2}} \int f(\mathrm{x}) e^{-i\mathrm{x}\,\mathrm{k}}\, d\mathrm{x}\,; \tag{B 1}$$

the inverse transform is

$$f(\mathrm{x}) = \frac{1}{(2\pi)^{3/2}} \int \hat{f}(\mathrm{k}) e^{i\mathrm{x}\,\mathrm{k}}\, d\mathrm{k}\,. \tag{B 2}$$

From these definitions, we have for the gradient operator

$$\mathrm{f} = \nabla g \leftrightarrow \hat{\mathrm{f}} = -i\mathrm{k}\hat{g}\,; \tag{B 3}$$

it follows that

$$\mathrm{f} = \nabla \times \mathrm{g} \leftrightarrow \hat{\mathrm{f}} = -i\mathrm{k} \times \hat{\mathrm{g}}\,,$$

$$f = \nabla \cdot \mathrm{g} \leftrightarrow \hat{f} = -i\mathrm{k} \cdot \hat{\mathrm{g}}$$

$$f = \nabla^2 g \leftrightarrow \hat{f} = -|\mathrm{k}|^2 \hat{g}$$

The energy is defined in the physical and Fourier spaces by Parseval's identity,

$$E = \frac{1}{2}\int \mathbf{u}^2\, d\mathbf{x} = \frac{(2\pi)^3}{2}\int \hat{\mathbf{u}}\cdot\hat{\mathbf{u}}^*\, d\mathbf{k}. \tag{B.4}$$

The energy spectrum is then defined as the integral on the spherical shell $|\mathbf{k}| = k$

$$E(k) = \frac{(2\pi)^3}{2}\int \hat{\mathbf{u}}\cdot\hat{\mathbf{u}}^*\, k^2 d\Omega_k \tag{B.5}$$

where Ω_k is a solid angle measured from the origin.

B.2 Vorticity Formulation

We derive an equivalent expression based on vorticity. From the relations $\mathbf{u} = \nabla\times\boldsymbol{\psi}$ and $\nabla^2\boldsymbol{\psi} = -\boldsymbol{\omega}$, the transforms of velocity and vorticity are related by

$$\hat{\mathbf{u}} = -i\mathbf{k}\times\hat{\boldsymbol{\psi}} = i\mathbf{k}\times\frac{\hat{\boldsymbol{\omega}}}{|\mathbf{k}|^2}. \tag{B.6}$$

One thus has

$$\begin{aligned} E(k) &= \frac{(2\pi)^3}{2}\int\left(i\mathbf{k}\times\frac{\hat{\boldsymbol{\omega}}}{|\mathbf{k}|^2}\right)\cdot\left(-i\mathbf{k}\times\frac{\hat{\boldsymbol{\omega}}^*}{|\mathbf{k}|^2}\right)k^2 d\Omega_k \\ &= \frac{(2\pi)^3}{2}\int\left[(\mathbf{k}\cdot\mathbf{k})\left(\frac{\hat{\boldsymbol{\omega}}\cdot\hat{\boldsymbol{\omega}}^*}{|\mathbf{k}|^4}\right) - \left(\frac{\mathbf{k}\cdot\hat{\boldsymbol{\omega}}}{|\mathbf{k}|^2}\right)\left(\frac{\mathbf{k}\cdot\hat{\boldsymbol{\omega}}^*}{|\mathbf{k}|^2}\right)\right]k^2 d\Omega_k \end{aligned}$$

where the second term is nil because $\boldsymbol{\omega}$ is solenoidal,

$$E(k) = \frac{(2\pi)^3}{2}\int \hat{\boldsymbol{\omega}}\cdot\hat{\boldsymbol{\omega}}^*\, d\Omega_k. \tag{B.7}$$

We wish to rewrite this expression in terms of quantities in physical space. By the definition of the Fourier transform,

$$E(k) = \frac{1}{2}\int\int_{\mathbf{x}}\int_{\mathbf{x}'}\boldsymbol{\omega}(\mathbf{x})e^{-i\mathbf{x}\,\mathbf{k}}\,\boldsymbol{\omega}(\mathbf{x}')e^{i\mathbf{x}'\,\mathbf{k}}\, d\mathbf{x}\, d\mathbf{x}' d\Omega_k.$$

We let $\rho = x' - x$ and rewrite the triple integral as

$$E(k) = \frac{1}{2} \int \int_x \int_\rho \int \omega(x)\omega(x+\rho) e^{i\rho\, k}\, dx\, \rho^2\, d\rho\, d\Omega_\rho\, d\Omega_k\,;$$

the integral over Ω_k can be carried out to finally obtain

$$E(k) = 2\pi \int_0^\infty R_\omega(r) \frac{\sin(kr)}{kr}\, dr \tag{B 8}$$

where $R_\omega(r)$ is the vorticity autocorrelation

$$R_\omega(r) = \int_{|r|=r} \omega(x) \cdot \omega(x+r)\, dx\, r^2 d\Omega_r \tag{B 9}$$

B.3 Particle Implementation

If one disposes of R_ω, computing the whole energy spectrum is relatively immediate. We will use our vortex particle discretization to sample R_ω. The sample resolution conditions the maximum wavenumber for which we can compute the energy spectrum, the integrand in Eq. B.8 being oscillatory.

The discrete form is

$$R_\omega(r) = \sum_p \sum_q \alpha_p \cdot \alpha_q \int_{|r|=r} \int \zeta_{\sigma_p}(x - x_p)\zeta_{\sigma_q}(x + r - x_q)\, dx\, r^2 d\Omega_r\,;$$

in the case of the Gaussian smoothing, we have to compute the term

$$\begin{aligned} &\int_{|r|=r} \left(\zeta_{\sigma_p} * \zeta_{\sigma_q}\right)(r - (x_q - x_p))\, r^2 d\Omega_r \\ &= \int \zeta_{\sqrt{\sigma_p^2+\sigma_q^2}}(r - (x_q - x_p))\, r^2 d\Omega_r\,. \end{aligned}$$

Integration is straightforward; the following two definitions ensue

$$\chi(\rho,\lambda) = \frac{1}{\sqrt{2\pi}}\frac{\rho}{\lambda}\left(e^{-(\rho-\lambda)^2} - e^{-(\rho+\lambda)^2}\right) \tag{B.10}$$

$$\chi_\epsilon(\tau,l) = \frac{1}{\epsilon}\chi\left(\tau/\epsilon, l/\epsilon\right) \tag{B.11}$$

and allow us to write

$$R_\omega(\tau) = \sum_p \sum_q \alpha_p \cdot \alpha_q \chi_{\sqrt{\sigma_p^2+\sigma_q^2}}\left(\tau, |\mathbf{x}_p - \mathbf{x}_q|\right) . \tag{B.12}$$

This is a double summation over the elements. Every pair (p,q) contributes to a few sample points τ_i of R_ω. Their number will depend on the maximum frequency of the computed spectrum, e.g., one can set $\Delta\tau = 2\pi/(8k_{\max})$ so to have 8 sampling points per period of $\sin(k_{\max}\tau)$.

Appendix C

Sources of Vorticity

C.1 Solid Boundaries

This section presents the details of the implementation of wall diffusion We have to evaluate the contribution of the viscous flux at a wall onto the nearby free elements and the attached elements In the vicinity of a flat wall, one may use the Green's function for three-dimensional diffusion and write

$$\Delta\omega_{\Delta t,\,dS} = \int_0^{\Delta t} \sigma dS\, 2\, G_{\text{diff}}\left(\mathrm{x}, \Delta t, \mathrm{x}', \tau\right) d\tau \tag{C 1}$$

$$= \int_0^{\Delta t} \frac{\Delta\gamma}{\Delta t}\, 2\, \frac{H\left(\Delta t - \tau\right) e^{-\frac{|\mathrm{x}-\mathrm{x}'|^2}{4\nu(\Delta t-\tau)}}}{\left(4\pi\nu(\Delta t-\tau)\right)^{3/2}}\, d\tau \tag{C.2}$$

where H is the Heavyside function and the factor 2 accounts for the half-space geometry This expression has to be integrated over the particle volume,

$$\Delta\alpha_{\Delta t,\,dS} = \int_{V_p}\int_0^{\Delta t} \sigma\, 2\, \frac{e^{-\frac{|\mathrm{x}-\mathrm{x}'|^2}{4\nu(\Delta t-\tau)}}}{\left(4\pi\nu(\Delta t-\tau)\right)^{3/2}}\, d\tau \tag{C.3}$$

where we substituted the flux σ by its value $\Delta\gamma/\Delta t$ that is constant over the time step and noted that the Heavyside function is always unity inside the integral

We elect to perform the volume integral first and over spherical volumes. This is justified by the type of redistribution lattice (Face-Centered Cubic) we are using and

by the fewer evaluations of erf that will be required.

$$\int_{V_p} 2\,G_{\text{diff}}\,dV = \int_0^{2\pi}\int_0^{R_p}\int_0^{\pi} \frac{2\,e^{-\frac{r^2+\rho^2+2r\rho\cos(\theta)}{4\nu(\Delta t-\tau)}}}{(4\pi\nu(\Delta t-\tau))^{3/2}}\rho^2\sin\theta\,d\theta d\rho d\phi \tag{C.4}$$

$$= \frac{2}{r}\int_0^{R_p} \frac{e^{-\frac{(\rho-r)^2}{4\nu(\Delta t-\tau)}} - e^{-\frac{(\rho+r)^2}{4\nu(\Delta t-\tau)}}}{(4\pi\nu(\Delta t-\tau))^{1/2}}\rho d\rho \tag{C.5}$$

The reader will note the bound R_p which we define as $4\pi/3\,R_p^3 = V_p$, making it different from the lattice step size h, be it in a FCC or cubic lattice. For convenience, we define $\theta = \Delta t - \tau$,

$$\int_{V_p} 2\,G_{\text{diff}}\,dV = \frac{2\,\tau^{-1}}{(4\pi\nu\theta)^{1/2}}\left[\int_{-\tau/\sqrt{4\nu\theta}}^{(R_p-\tau)/\sqrt{4\nu\theta}} \sqrt{4\nu\theta}(\sqrt{4\nu\theta}u-\tau)e^{-u^2}du + \int_{\tau/\sqrt{4\nu\theta}}^{(R_p+\tau)/\sqrt{4\nu\theta}} \sqrt{4\nu\theta}(-\sqrt{4\nu\theta}u+\tau)e^{-u^2}du\right] \tag{C.6}$$

The integration yields

$$\int_{V_p} 2\,G_{\text{diff}}\,dV = \frac{(4\pi\nu\theta)^{1/2}}{\pi\,r}\left(e^{-\frac{(R_p+r)^2}{4\nu\theta}} - e^{-\frac{(R_p-r)^2}{4\nu\theta}}\right) + \text{erf}\left(\frac{r+R_p}{\sqrt{4\nu\theta}}\right) - \text{erf}\left(\frac{r-R_p}{\sqrt{4\nu\theta}}\right) \tag{C.7}$$

This expression can then be integrated in time,

$$\Delta\alpha_{\Delta t,dS} = \Delta\gamma\,dS\,\left(F(\rho,\rho^+) - F(\rho,\rho^-)\right) \tag{C.8}$$

where we introduced the dimensionless variables $\rho = r/\sqrt{2\nu\Delta t}$, $\rho^+ = (r+R_p)/\sqrt{2\nu\Delta t}$ and $\rho^- = (r-R_p)/\sqrt{2\nu\Delta t}$ and the function F,

$$F(\alpha,\beta) = \sqrt{\frac{2}{\pi}}e^{-\beta^2/2}\left(\beta - \frac{2}{3}\frac{\beta^2-1}{\alpha}\right) + \text{erf}\left(\beta/\sqrt{2}\right)\left(\beta^2+1-\frac{2}{3}\frac{\beta^3}{\alpha}\right) + \beta\left(-|\beta| + \frac{2}{3}\frac{\beta^2}{\alpha}\right) \tag{C.9}$$

Finally, the surface integration is performed by means of quadrature on the panels.

This approach is somewhat different from Ploumhans and Winckelmans (2000). We indeed wanted to use the spherical nature of our elements here, too. As such, our scheme is not conservative. First, our integration is not exact and depends highly on the regularity of the elements' positions. Second, our integral does not cover the near-wall region where our attached elements are. One can then use this region to make the scheme conservative and give it what is left of γ after transferring contributions to particles.

Appendix D

Rotation Kernel

D.1 Multipole Approximation Error

In this section, we will follow the development from Salmon and Warren (1994) to obtain an error bound on multipole expansions for the rotation kernel. We have for the stream function

$$\psi(\mathbf{x}) = -\sum_i \frac{\mathbf{W}_i}{4\pi} \int_{\partial\Omega_i} \frac{\mathbf{x}-\mathbf{x}'}{|\mathbf{x}-\mathbf{x}'|} \ \mathbf{n}\, dS(\mathbf{x}')$$

and for velocity

$$\mathbf{u} = \sum_i \frac{\mathbf{W}_i}{4\pi} \times \int_{\partial\Omega_i} \frac{\mathbf{n}}{|\mathbf{x}-\mathbf{x}'|} - \frac{((\mathbf{x}-\mathbf{x}')\cdot\mathbf{n})\,(\mathbf{x}-\mathbf{x}')}{|\mathbf{x}-\mathbf{x}'|^3}\, dS(\mathbf{x}')$$

Equivalently, we can consider the function ϕ_i individually

$$\phi_i(\mathbf{x}) = \int_{\partial\Omega_i} \mathbf{H}(\mathbf{x}-\mathbf{x}')\cdot\mathbf{n}\, dS(\mathbf{x}')$$

with $\mathbf{H} = \frac{\mathbf{x}-\mathbf{x}'}{|\mathbf{x}-\mathbf{x}'|}$. We then have

$$\psi(\mathbf{x}) = -\sum_i \frac{\mathbf{W}_i}{4\pi}\phi_i(\mathbf{x}) \tag{D.1}$$

and

$$\mathrm{u}(\mathrm{x}) = \sum_i \frac{\mathbf{W}_i}{4\pi} \times \nabla\phi_i(\mathrm{x}) \tag{D 2}$$

One can write the multipole approximations for ϕ_i and $\nabla\phi_i$ as

$$\phi_i(\mathrm{x}) = \sum_{n=0}^{\bar{r}} \Phi_{(n)}(\mathrm{x}) + \Delta\Phi_{(p)}(\mathrm{x})$$

where

$$\Phi_{(n)}(\mathrm{x}) = \frac{(-1)^n}{n!} \partial_{i_1 \ \ i_n} \mathbf{H}(\mathrm{x} - \mathrm{x}_0) \cdot \mathbf{M}_{(n)}^{i_1 \ \ i_n}$$

The successive multipole moments are defined as

$$\mathbf{M}_{(n)}^{i_1 \ \ i_n} = \int_S (\mathrm{x} - \mathrm{x}_0)^{i_1} (\mathrm{x} - \mathrm{x}_0)^{i_2} \cdots (\mathrm{x} - \mathrm{x}_0)^{i_n} \mathrm{n} dS \,.$$

We want to bound the error in the approximation of the gradient of ϕ_i which appears in the velocity expression

$$\nabla\phi_i(\mathrm{x}) = \sum_{n=0}^{p} (\nabla\Phi)_{(n)}(\mathrm{x}) + \Delta\,(\nabla\Phi)_{(p)}(\mathrm{x})$$

where

$$(\nabla\Phi)_{(n)}(\mathrm{x}) = \frac{(-1)^n}{n!} \partial_{i_1 \ \ i_n} \nabla\mathbf{H}(\mathrm{x} - \mathrm{x}_0) \cdot \mathbf{M}_{(n)}^{i_1 \ \ i_n} \,.$$

We have

$$\Delta\,(\nabla\Phi)_{(p)}(\mathrm{x}) = \int_S (\nabla\Phi)_{(p)}(\mathrm{x}, \mathrm{x}') \ \ \mathrm{n} dS \tag{D 3}$$

where

$$(\nabla\Phi)_{(p)}(\mathrm{x}, \mathrm{x}') = \frac{(-1)^{p+1}}{p!} (\mathrm{x} - \mathrm{x}_0)^{i_1} (\mathrm{x} - \mathrm{x}_0)^{i_2} \cdots (\mathrm{x} - \mathrm{x}_0)^{i_{p+1}} \int_0^1 (1-t)^p \partial_{i_1 \ \ i_{p+1}} \nabla\mathbf{H}(\mathrm{x} - \mathrm{x}_0 - t(\mathrm{x}' - \mathrm{x}_0)) \,. \tag{D 4}$$

We can then bound this expression (see Salmon and Warren, 1994, appendix B) with the expansion centered about the origin,

$$\left|\left(\nabla\Phi\right)_{(p)}\left(\mathrm{x},\mathrm{x}'\right)\right| \leq \frac{1}{r}\frac{\alpha^{p+1}}{1-\alpha}$$

with $r = |x|$ and $\alpha = \frac{|x'|}{r}$. If we use this evaluation in Eq. D 3 and carry out the integration, we find

$$\left|\Delta\left(\nabla\Phi\right)_{(p)}\left(\mathrm{x}\right)\right| \leq \frac{1}{r}\frac{1}{1-\frac{b_{\max}}{r}}\frac{B_{(p+1)}}{r^{p+1}} \tag{D 5}$$

where we bounded $(1-\alpha)^{-1}$ by $(1-\alpha_{\max})^{-1}$ and defined the moment $B_p = \int_S |\mathrm{x}-\mathrm{x}_0|^p \, dS$

If we use the multipoles up to order $p = 2$, this yields the following bound for the velocity

$$\begin{aligned} |\Delta\mathrm{u}|_{(p)} &\leq \frac{|\mathrm{W}_i|}{4\pi}\frac{1}{r}\frac{1}{1-\frac{b_{\max}}{r}}\frac{B_{(3)}}{r^3} && \text{(D 6)} \\ &\leq \frac{|\mathrm{W}_i|}{4\pi}\frac{B_{(2)}}{b_{\max}^3}\frac{1}{1-\frac{b_{\max}}{r}}\left(\frac{b_{\max}}{r}\right)^4, && \text{(D.7)} \end{aligned}$$

where we used the inequality $B_{(3)} < b_{\max}B_{(2)}$; $B_{(2)}$ is indeed a moment that is cheaper to compute and already used in our error bounds for the normal Biot-Savart interactions.

D.2 Kernel and Derivatives

For the sake of completeness, we list here the first few derivatives of $\mathbf{H}$:

$$\mathrm{H}_i(\mathrm{u}) = \frac{\mathrm{u}_i}{|\mathrm{u}|} \tag{D 8}$$

$$\partial_j \mathrm{H}_i = \frac{\delta_{ij}}{|\mathrm{u}|} - \frac{\mathrm{u}_i\mathrm{u}_j}{|\mathrm{u}|^3} \tag{D 9}$$

$$\partial_j\partial_k \mathrm{H}_i = -\frac{\delta_{ij}\mathrm{u}_k + \delta_{ik}\mathrm{u}_j + \delta_{jk}\mathrm{u}_i}{|\mathrm{u}|^3} + 3\frac{\mathrm{u}_i\mathrm{u}_j\mathrm{u}_k}{|\mathrm{u}|^5} \tag{D 10}$$

$$\begin{aligned}\partial_j\partial_k\partial_l \mathbf{H}_i = &- \frac{\delta_{ij}\delta_{kl} + \delta_{ik}\delta_{jl} + \delta_{jk}\delta_{il}}{|\mathbf{u}|^3} \\ &+ 3\frac{\delta_{ij}\mathbf{u}_k\mathbf{u}_l + \delta_{ik}\mathbf{u}_j\mathbf{u}_l + \delta_{jk}\mathbf{u}_i\mathbf{u}_l + \delta_{il}\mathbf{u}_j\mathbf{u}_k + \delta_{jl}\mathbf{u}_i\mathbf{u}_k + \delta_{kl}\mathbf{u}_i\mathbf{u}_j}{|\mathbf{u}|^5} \\ &- 5\frac{\mathbf{u}_i\mathbf{u}_j\mathbf{u}_k\mathbf{u}_l}{|\mathbf{u}|^7}.\end{aligned} \tag{D.11}$$

Appendix E

Near-Wall Vorticity

E.1 Viscous Vortex Sheets

E.1.1 Regularization

We have to carry out the convolution

$$\omega(\mathrm{x}) = \int_{\text{sheet}} \zeta_{\sigma(\mathrm{x}')}(\mathrm{x}-\mathrm{x}')\,\gamma(\mathrm{x}')\,dS(\mathrm{x}')$$

The sheet is discretized with flat panels with a constant strength γ The Gaussian can be rewritten as a divergence in cylindrical coordinates attached to the panel and centered at the evaluation point We have, in coordinates made dimensionless with respect to σ,

$$\zeta(\rho, w) = e^{-\frac{w^2+\rho^2}{2}} = e^{-\frac{w^2}{2}} \frac{1}{\rho}\frac{\partial}{\partial\rho}\left(1 - e^{-\frac{\rho^2}{2}}\right)$$

We can then use the 2D divergence theorem along the perimeter of the panel m

$$\begin{aligned}
\omega(\mathrm{x})|_m &= \int_{S_m} \frac{1}{\sigma^3}\zeta\left(\frac{\mathrm{x}-\mathrm{x}'}{\sigma}\right)\gamma_m\,dS(\mathrm{x}') \\
&= \int_{S_m^{\mathrm{u}}} \frac{1}{\sigma}\zeta\left(\mathrm{u}-\mathrm{u}'\right)\gamma_m\,dS^u = \frac{\gamma_m}{(2\pi)^{3/2}\sigma} e^{-\frac{z^2}{2\sigma^2}} \int_{S_m^{\mathrm{u}}} e^{-\frac{\rho^2}{2}}\,dS^u \\
&= \frac{\gamma_m}{(2\pi)^{3/2}\sigma} e^{-\frac{z^2}{2\sigma^2}} \int_{\Gamma_m^{\mathrm{u}}} \frac{1-e^{-\frac{\rho^2}{2}}}{\rho}\hat{\rho}\cdot\left(d\mathrm{l}^u \times \mathrm{n}\right),
\end{aligned}$$

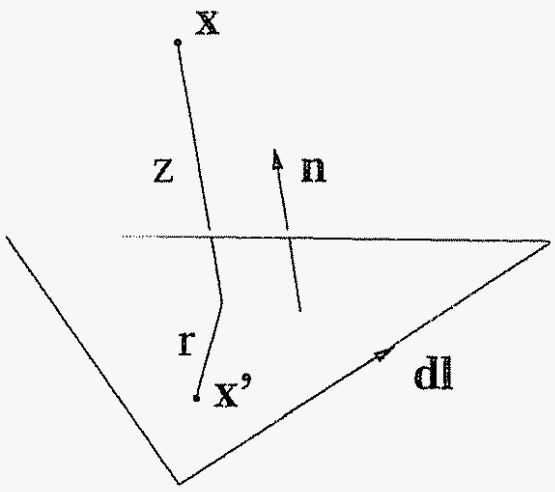

Figure E.1: Sheet regularization: coordinate system

where we have introduced several notations: $\mathbf{u} = \mathbf{x}/\sigma$ are dimensionless coordinates, ρ is the dimensionless radius in the plane of the panel, $\hat{\boldsymbol{\rho}}$ is the radial vector, dS^u and dl^u are respectively a surface and contour element in the dimensionless coordinate system. The integral we are left with can be decomposed in contributions from each segment of the polygon which can be written as

$$\int_{u_1}^{u_2} \frac{1 - e^{-\frac{u^2+v^2}{2}}}{u^2+v^2} v\, du$$

where we defined u as the coordinate parallel to the segment and v, the perpendicular one. This last expression shows that we have to tabulate the primitive $I_\zeta(u,v) = \int_0^u \cdots du$ for values of u and v within the the kernel cutoff (typically 5). For values of u or v beyond the cutoff, we have an analytical form

$$\left[\arctan\left(\frac{u}{v}\right)\right]_{u_1}^{u_2}$$

E.1.2 Kernel

We here give the development of the contribution to the stream-function ψ. Contributions to the velocity and velocity gradients are similar or in direct continuation of

the present calculation We need to compute

$$\psi(\mathrm{x}) = \int_{\text{sheet}} G_{\sigma(\mathrm{x}')}(\mathrm{x}-\mathrm{x}')\gamma(\mathrm{x}')\, dS(\mathrm{x}')\,.$$

As for the regularization, we consider the contribution of a single panel and switch to dimensionless coordinates We first have

$$G(\rho, w) = \frac{1}{4\pi}\frac{\mathrm{erf}(\sqrt{\frac{w^2+\rho^2}{2}})}{\sqrt{w^2+\rho^2}} \tag{E.1}$$

The contribution of a panel can then be written as

$$\begin{aligned}\psi(\mathrm{x})|_m &= \int_{S_m} \frac{1}{\sigma} G\left(\frac{\mathrm{x}-\mathrm{x}'}{\sigma}\right)\gamma_m\, dS(\mathrm{x}') \\ &= \sigma\gamma_m \int_{S_m^u} G\left(\mathrm{u}-\mathrm{u}'\right)\, dS^u = \frac{\sigma\gamma_m}{4\pi}\int_{S_m^u}\frac{\mathrm{erf}(\sqrt{\frac{w^2+\rho^2}{2}})}{\sqrt{w^2+\rho^2}}\, dS^u\end{aligned}$$

We then re-write G as a divergence in the plane of the panel

$$\begin{aligned}G(\rho, w) = \frac{1}{4\pi}\frac{1}{\rho}\frac{\partial}{\partial\rho}\Bigg(&\sqrt{\rho^2+w^2}\,\mathrm{erf}\left(\sqrt{\frac{\rho^2+w^2}{2}}\right) - \sqrt{w^2}\,\mathrm{erf}\left(\sqrt{\frac{w^2}{2}}\right) \\ &-\sqrt{\frac{2}{\pi}}e^{-\frac{w^2}{2}}\left(1-e^{-\frac{\rho^2}{2}}\right)\Bigg)\,;\end{aligned} \tag{E.2}$$

we then use the divergence theorem and integrate along the sides of the panel The integral does not have an analytical form and has to be tabulated in three dimensions

E.2 Near-Wall Elements

E.2.1 Regularization

We need to re-normalize the unbounded smoothing function by some function $M(\mathbf{x})$ that will depend on the geometry. We have

$$M(\mathbf{x}) = \int_{\mathbb{R}\setminus\Omega_i} \zeta_\sigma(\mathbf{x}-\mathbf{x}')d\mathbf{x}' \tag{E.3}$$

where $\mathbf{x} \in \partial\Omega_i$. If we assume that the boundary is locally spherical–within ζ_σ support–, with a roughly constant curvature radius R, the above integral can be written more explicitly as a function of the local curvature R. In the concave case, we have $R < 0$

$$\begin{aligned} M(R) &= \int_0^{2\pi}\int_0^{\pi/2}\int_0^{2|R|/\sigma\cos(\theta)} \zeta(\rho)\rho^2\sin\theta\, d\rho\, d\theta\, d\phi & \text{(E.4)}\\ &= 2\pi\int_0^{\pi/2} q(2|R|/\sigma\cos(\theta))\sin(\theta)d\theta & \text{(E.5)}\\ &= \frac{\pi\sigma}{|R|}\int_0^{2|R|/\sigma} q(u)\,du & \text{(E.6)} \end{aligned}$$

where $q(\rho) = \int_0^\rho \zeta(t)t^2dt$. For the Gaussian, we have

$$q(\rho) = \frac{1}{4\pi}\left(\mathrm{erf}(\rho/\sqrt{2}) - \sqrt{2/\pi}\rho e^{-\rho^2/2}\right),$$

to finally obtain

$$M(R) = \frac{1}{2}\mathrm{erf}(\sqrt{2}|R|/\sigma) - \frac{1}{2}\sqrt{2/\pi}\frac{1-e^{-2|R|^2/\sigma^2}}{|R|/\sigma} \tag{E.7}$$

In the convex case, $R > 0$, we just have the complementary relation

$$M(R) = 1 - \frac{1}{2}\mathrm{erf}(\sqrt{2}R/\sigma) + \frac{1}{2}\sqrt{2/\pi}\frac{1-e^{-2R^2/\sigma^2}}{R/\sigma} \tag{E.8}$$

We will assume that curvature is constant across a panel. In three dimensions,

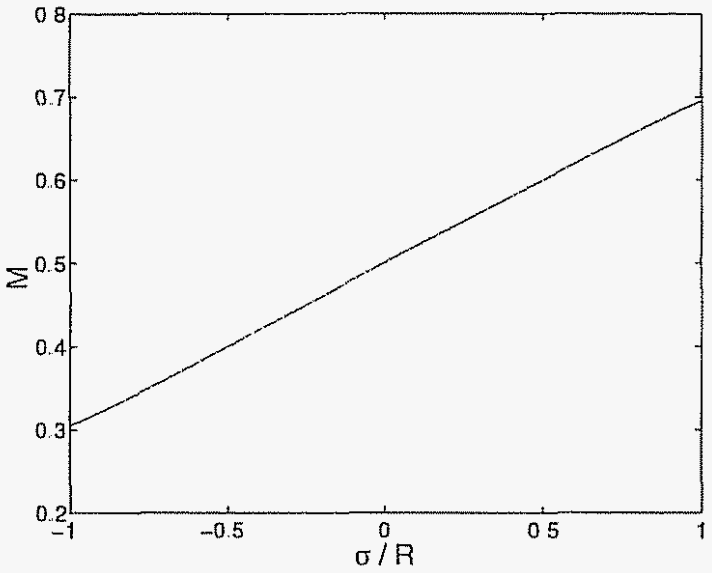

Figure E.2: One-sided panels: Regularization modifier function

it will be taken as the mean curvature which is the average of the two principal curvatures of the surface. This is a good approximation. In the case of a saddle, where the curvatures have opposite signs, the volumes lost and gained in the two main directions should be evened out with this average.

Appendix F

Additional Results for the Flows Past Spinning Spheres

F.1 Stream-Wise Rotation

F.1.1 Helicity

Helicity is a quantity defined by

$$\mathcal{H} = \int \mathbf{u} \cdot \boldsymbol{\omega} \, d\mathbf{x}$$

It measures the entanglement of vortex lines

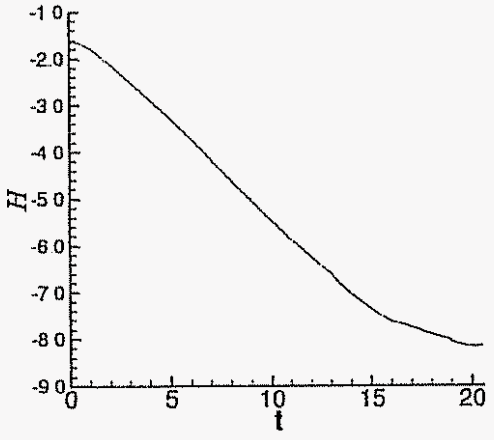

Figure F 1: Spinning sphere at $Re = 300$, stream-wise rotation: helicity

F.2 Transverse Rotation

F.2.1 Helicity

This configuration remains symmetric with respect to the $y = 0$ plane

$$u_x(\cdot, y, \cdot) = u_x(\cdot, -y, \cdot) \qquad \omega_x(\cdot, y, \cdot) = -\omega_x(\cdot, -y, \cdot)$$
$$u_y(\cdot, y, \cdot) = -u_y(\cdot, -y, \cdot) \qquad \omega_y(\cdot, y, \cdot) = \omega_y(\cdot, -y, \cdot)$$
$$u_z(\cdot, y, \cdot) = u_z(\cdot, -y, \cdot) \qquad \omega_z(\cdot, y, \cdot) = -\omega_z(\cdot, -y, \cdot)$$

if one neglects slight numerical deviations As a consequence, $\mathcal{H} \simeq 0$

F.2.2 Stream-Wise Vorticity

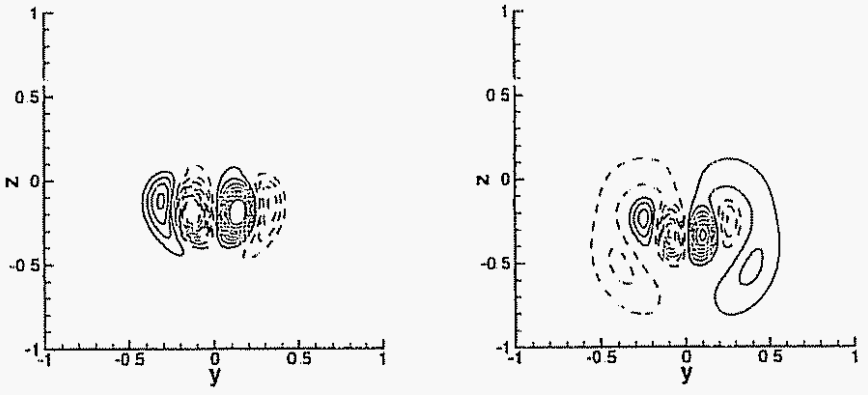

(a) 0 (b) $T/6$

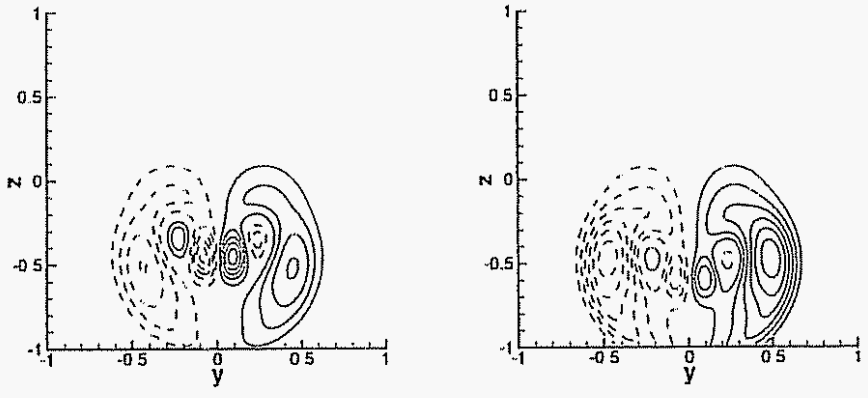

(c) $T/4$ (d) $T/3$

Figure F.2: Spinning sphere at $Re = 300$, transverse rotation: shedding cycle, stream-wise vorticity in the $x = 2$ plane; contours values are in the interval $[-4; 4]$ by steps of 0.5, 0 is omitted

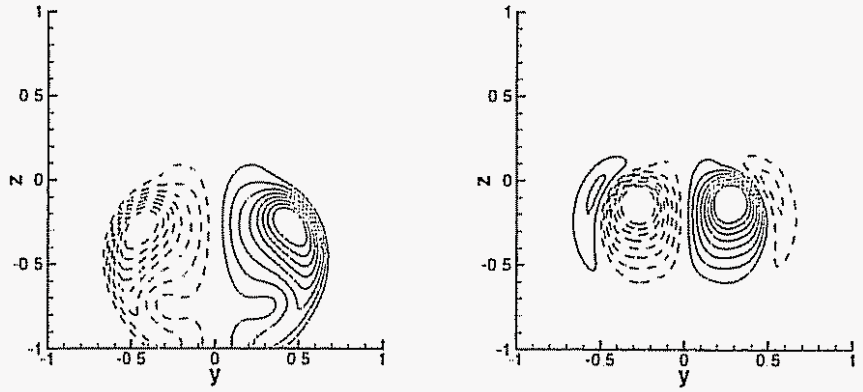

(a) $T/2$ (b) $2T/3$

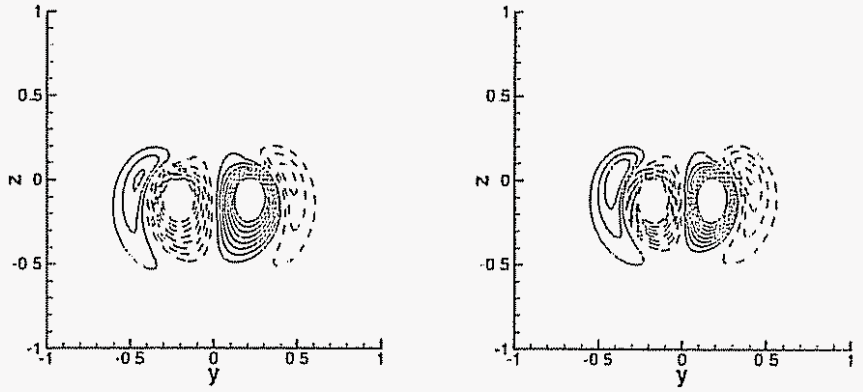

(c) $3T/4$ (d) $5T/6$

Figure F 3: Spinning sphere at $Re = 300$, transverse rotation: shedding cycle, streamwise vorticity contours in the $x = 2$ plane (continued)

F.2.3 Bottom Separation

We consider constant ϕ planes and the projection of the velocity field in those planes. For each ϕ, we estimate the position of the saddle

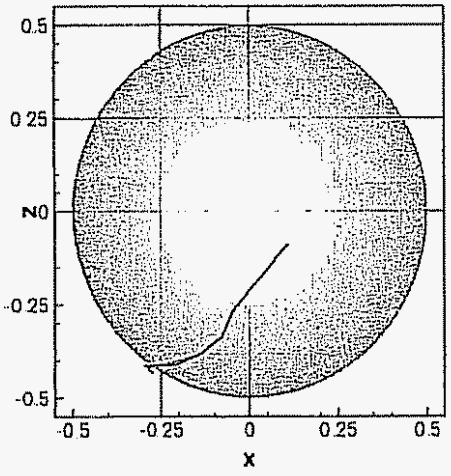

(a) Location with respect to the sphere

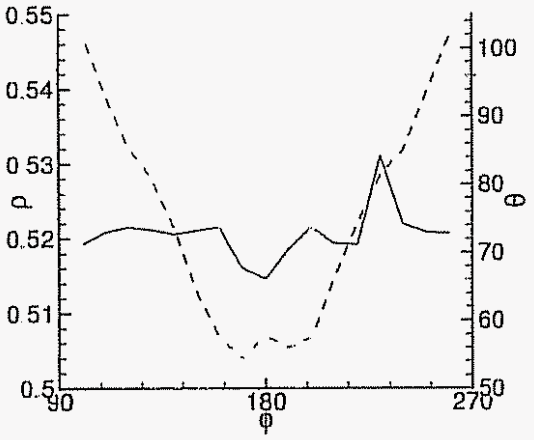

(b) Cylindrical coordinates as a function of ϕ: radius $\rho = r/D$ (solid), angle θ (dashed)

Figure F.4: Spinning sphere at $Re = 300$, transverse rotation: separation line

F.3 Oblique Rotation

F.3.1 Helicity

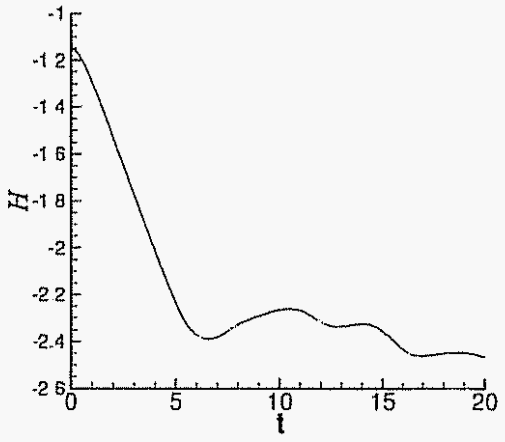

Figure F.5: Spinning sphere at $Re = 300$, oblique rotation: helicity

F.3.2 Stream-Wise Vorticity

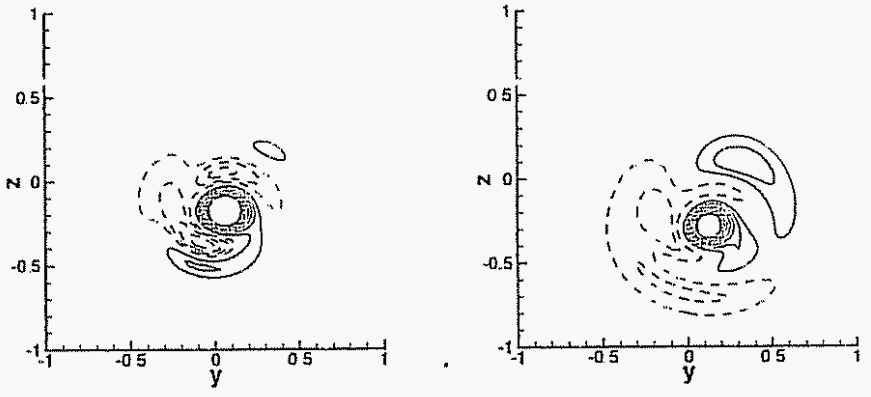

(a) 0 (b) $T/8$

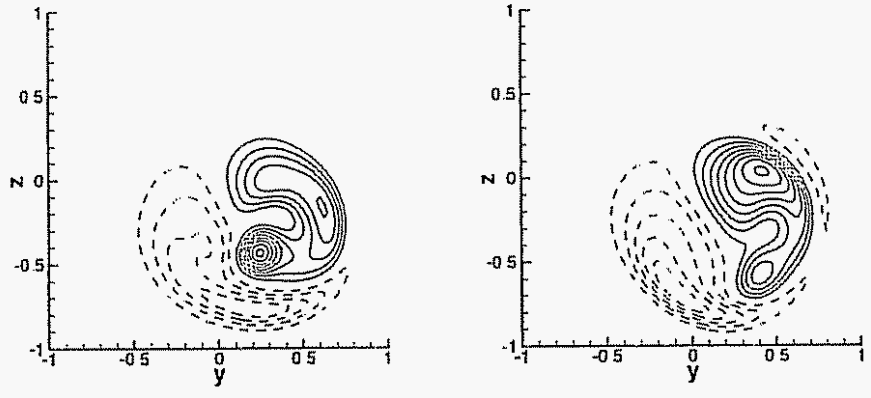

(c) $T/4$ (d) $3T/8$

Figure F.6: Spinning sphere at $Re = 300$, transverse rotation: shedding cycle, stream-wise vorticity in the $x = 2$ plane; contours values are in the interval $[-4; 4]$ by steps of 0.5, 0 is omitted

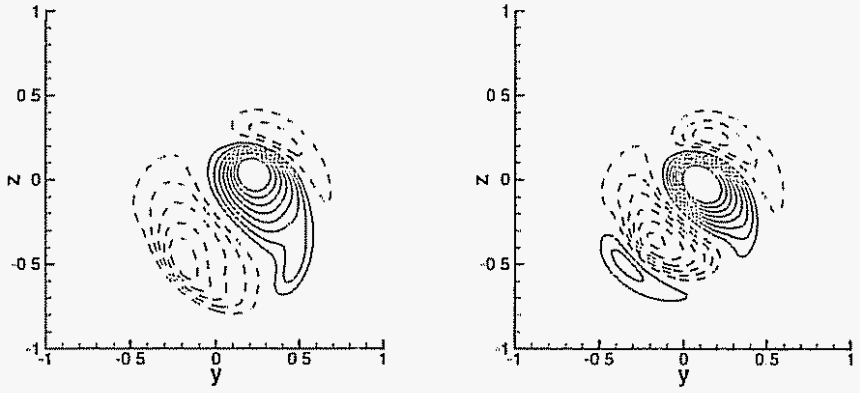

(a) $T/2$ (b) $5T/8$

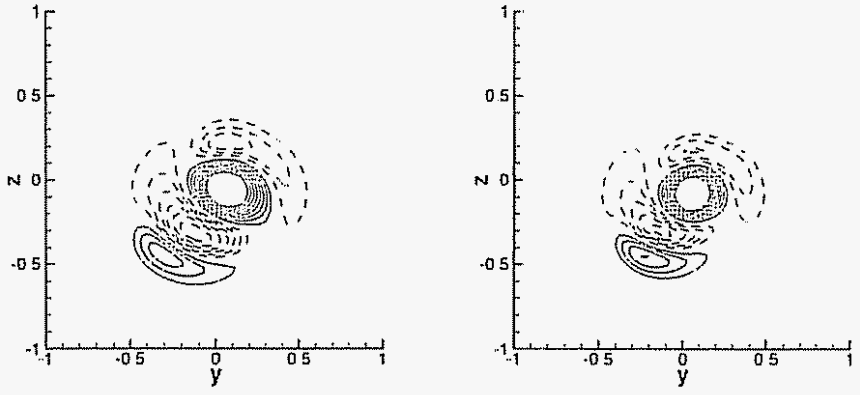

(c) $3T/4$ (d) $7T/8$

Figure F.7: Spinning sphere at $Re = 300$, oblique rotation: shedding cycle, streamwise vorticity in the $x = 2$ plane (continued)

F.3.3 Bottom Separation

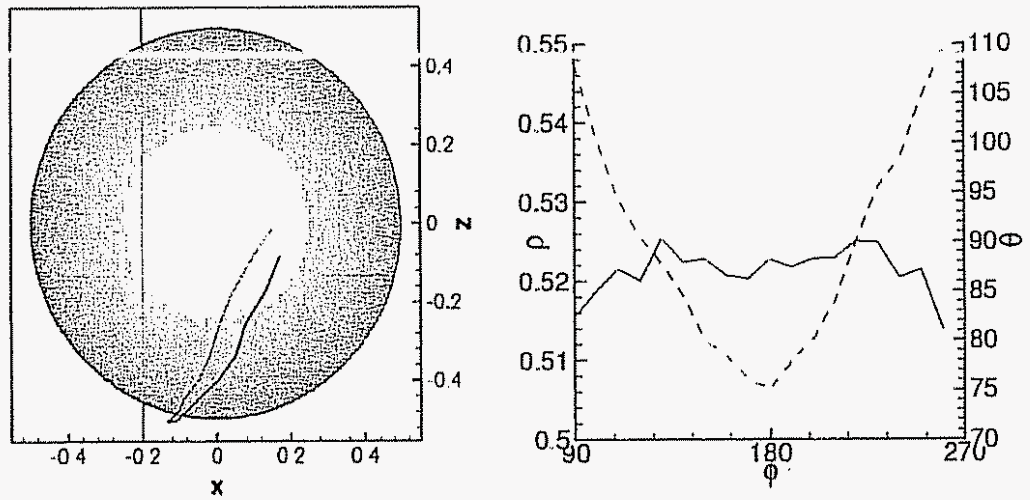

(a) Location with respect to the sphere

(b) Cylindrical coordinates as a function of ϕ: radius $\rho = r/D$ (solid), angle θ (dashed)

Figure F.8: Spinning sphere at $Re = 300$, oblique rotation: separation line

Bibliography

C. Anderson and C Greengard. On vortex methods. *SIAM J Num. Anal.*, 22: 413–440, 1985.

H. Aref and I. Zawadzki. Linking of vortex rings. *Nature*, 354(6348):50–53, 1991.

W T. Ashurst and D I Meiron. Numerical study of vortex reconnection. *Phys. Rev Lett* , 58(16):1632–1635, 1987.

J. Balakrishnan. Spatial curvature effects on molecular transport by diffusion. *Phys Rev. E*, 61(4):4648–4651, 2000.

H.M Barkla and L.J. Auchterlonie. The magnus or robins effect on rotating spheres. *J. Fluid Mech* , 47(3):437–447, 1971.

J. Barnes and P Hut. A hierarchical O(N log N) force calculation algorithm. *Nature*, 324, 1986.

G K Batchelor. *An Introduction to Fluid Dynamics*. Cambridge Univ Press, London, 1967.

J. T. Beale and A. Majda. Vortex methods ii: high order accuracy in two and three dimensions. *Math. Comput* , 32:29–52, 1982.

P W. Bearman and J K Harvey. Golf ball aerodynamics. *Aeronaut Q.*, 27:112–122, 1976.

M Brady. *Regularized vortex sheet evolution in three dimensions*. Ph D. thesis, California Institute of Technology, 2000.

R Brard A vortex theory for bodies moving in water In R Brard and A Castera, editors, *Proc 9th Symposium on Naval Hydrodynamics*, pages 1187–1284, 1973

P Chatelain, D Kivotides, and A Leonard Reconnection of colliding vortex rings *Phys Rev Lett.*, 90(5):054501, 2003

A J Chorin Numerical study of slightly viscous flows *J Fluid Mech.*, 57:785–796, 1973

M Christensson and M Hindmarsh Magnetic fields in the early universe in the string approach to MHD *Phys Rev D*, 60(063001), 1999

G.-H Cottet and P Koumoutsakos *Vortex Methods, Theory and Practice* Cambridge University Press, 2000

G Daeninck, P Chatelain, M Rubel, G S Winckelmans, and A Leonard Simulation of vehicle aerodynamics using a vortex element method In Springer, editor, *The aerodynamics of heavy vehicles: trucks, buses and trains, Lecture notes in applied and computational mechanics*, 2004

P Degond and S Mas-Gallic The weighted particle method for convection-diffusion equations part 1: The case of an isotropic viscosity *Math Comput.*, 53(188): 485–507, October 1989

Y Dubief and F Delcayre On coherent-vortex identification in turbulence *J Turbulence*, 1, 2000

J D Eldredge, T Colonius, and A Leonard A vortex particle method for two dimensional compressible flow *J Comp Phys.*, 179:371–399, 2002a

J D Eldredge, A Leonard, and T Colonius A general deterministic treatment of derivatives in particle methods *J Comp Phys.*, 180:686–709, 2002b

J Faraudo Diffusion equation on curved surfaces i theory and application to biological membranes *J Chem Phys.*, 116(13):5831–5841, 2002

C F Gauss Besprechung des buchs von l a seeber: Intersuchungen ber die eigenschaften der positiven ternren quadratischen formen usw *Göttingsche Gelehrte Anzeigen (1831, July 9)*, 2:188–196, 1876

A Gharakhani Grid-free simulation of 3d vorticity diffusion by a high-order vorticity redistribution method In *15th AIAA Comp Fluid Dyn Conf (Anaheim, CA, 2001)* AIAA, 2001

T C Hales The sphere packing problem *J Comput Appl Math*, 44:41–76, 1992

T C Hales Sphere packings i *Discrete & Computational Geometry*, 17:1–51, 1997a

T C Hales Sphere packings ii *Discrete & Computational Geometry*, 18:135–149, 1997b

J C R Hunt, A A Wray, and P Moin Eddies, stream and convergence zones in turbulent flows Report CTR-S88, Center For Turbulence Research, 1988

J Jeong and F Hussain On the identification of a vortex *J Fluid Mech*, 285:69–94, 1995

T A Johnson and V C Patel Flow past a sphere up to a reynolds number of 300 *J Fluid Mech*, 378:19–70, 1999

R M Kerr and F Hussain simulation of vortex reconnection *Physica D*, 37:474–484, 1989

S Kida and M Takaoka Vortex reconnection *Annu Rev Fluid Mech*, 26:169–189, 1994

D Kim and H Choi Laminar flow past a sphere rotating in the streamwise direction *J Fluid Mech*, 461:365–386, 2002

D Kivotides, J C Vassilicos, D C Samuels, and C F Barenghi Kelvin waves cascade in superfluid turbulence *Phys Rev Lett*, 86(14):3080–3083, 2001

D Kivotides, J. C. Vassilicos, D. C. Samuels, and C F. Barenghi. Velocity spectra of superfluid turbulence. *Europhys Lett.*, 57(6):845–851, 2002.

P. Koumoutsakos and A. Leonard. High resolution simulation of the flow around an impulsively started cylinder using vortex methods. *J. Fluid Mech.*, 296(1), 1995

P. Koumoutsakos, A. Leonard, and F. Pépin. Boundary conditions for viscous vortex methods. *J. Comput. Phys*, 113:52–61, 1994.

A. Leonard. Computing three-dimensional incompressible flows with vortex elements. *Annu. Rev. Fluid Mech.*, 17:523–559, 1985.

J. Lighthill. *Laminar boundary layers*, chapter Attachment and separation in three-dimensional flow Oxford Univ. Press, 1963.

J. H. Maccoll. Aerodynamics of a spinning sphere. *J. Roy. Aero. Soc*, 32:777–798, 1928.

G. Magnus. Ueber die abweichung der geschosse, und ueber: eine auffallende erscheinung bei rotirenden körpern *Poggendorfs Annalen der Physik und Chemie*, 88:1, 1853.

R. M. Merserau The processing of hexagonally sampled two-dimensional signals *Proceedings of the IEEE*, 1979.

J. J. Monaghan Extrapolating b-splines for interpolation *J. Comput Phys.*, 60: 253–262, 1985.

F. Noca, D. Shiels, and D Jeon. A comparison of methods for evaluating time-dependent fluid dynamic forces on bodies, using only velocity fields and their derivatives. *J. Fluids and Structures*, 13:551–578, 1999.

B Oesterlé and T. Bui Dinh Experiments on the lift of a spinning sphere in a range of intermediate reynolds numbers. *Exps Fluids*, 25:16–22, 1998.

R. B. Pelz. Locally self-similar, finite-time collapse in a high-symmetry vortex filament model. *Phys. Rev. E*, 55(2):1617–1626, 1997.

P. Ploumhans. *Simulation of high Reynolds number flows past bluff bodies using vortex and boundary element method*. Ph.D. thesis, Université Catholique de Louvain, Faculté des Sciences Appliquées, 2001.

P. Ploumhans, G. S. Winckelmans, J. K. Salmon, A. Leonard, and M. S. Warren. Vortex methods for direct numerical simulation of three-dimensional bluff body flows: application to the sphere at $re = 300$, 500, and 1000. *J. Comput. Phys.*, 178, 2002.

P. Ploumhans and G. S. Winckelmans. Vortex methods for high resolution simulations of viscous flow past bluff-bodies of general geometry. *J. Comput. Phys.*, 165:354–406, 2000.

C. J. Pregnalato, M. C. Thompson, and K. Hourigan. Flow transitions in the wake of a streamwise-rotating sphere. Conference on bluff body wakes and vortex-induced vibrations, Port Douglas, Australia, December 2002.

A. Pumir and R. M. Kerr. Numerical simulation of interacting vortex tubes. *Phys. Rev. Lett.*, 58(16):1636–1639, 1987.

B. Robins. *New principles of gunnery*. ed. Hutton, 1805. first printed in 1742.

M. Rubel. Octree algorithms for the implicit closest point transform. To be submitted, 2002.

S. I. Rubinow and J. B. Keller. The transverse force on a spinning sphere moving in a viscous fluid. *J. Fluid Mech.*, 11:447–459, 1961.

J. K. Salmon and M. S. Warren. Skeletons from the treecode closet. *J. Comput. Phys.*, 111:136–155, 1994.

J. K. Salmon, M. S. Warren, and G. S. Winckelmans. Fast parallel tree codes for gravitational and fluid dynamical N-body problems. *The International Journal of Supercomputer Applications*, 8(2):129–142, Summer 1994. ISSN 0890-2720.

P. R. Schatzle. *An Experimental Study of Fusion of Vortex Rings*. Ph.D. thesis, California Institute of Technology, 1987.

I. J. Schoenberg. *Cardinal spline interpolation*. Society for Industrial and Applied Mathematics, Philadelphia, PA, 1973.

M. J. Shelley, D. I. Meiron, and S. A. Orszag. Dynamic aspects of vortex reconnection of perturbed anti-parallel vortex tubes. *J. Fluid. Mech.*, 246:613–652, 1993.

Y. Tsuji, Y. Morikawa, and O. Mizuno. Experimental mesaurement of the magnus force on a rotating sphere at low reynolds numbers. *J. Fluids Eng. – Trans. A S.M.E.*, 107:484–488, 1985.

D. Van De Ville, T. Blu, M. Unser, W. Philips, I. Lemahieu, and R. Van de Walle. Hex-splines: a novel spline family for hexagonal lattices. *IEEE Transactions on Image Processing*, 2004.

G. S. Winckelmans. Annual Research Briefs, C.T.R. Stanford, 1995.

G. S. Winckelmans. *Encyclopedia of Computational Mechanics*, chapter Vortex Methods. John Wiley and Sons, 2004.

G. S. Winckelmans and A. Leonard. Contributions to vortex particle methods for the computation of three-dimensionnal incompressible unsteady flows. *J. Comput. Phys.*, 109(2):247–273, December 1993.

G. S. Winckelmans, J. K. Salmon, M. S. Warren, and A. Leonard. Application of fast parallel and sequential tree codes to computing three-dimensional flows with the vortex element and boundary element methods. *Second International Workshop on Vortex Flows and Related Numerical Methods*, Montréal, August 1995.

N J. Zabusky, M.H Hugues, and K.V Roberts. Contour dynamics for the Euler equations in two dimensions *J. Comput. Phys.*, 1979.

I Zawadzki and H Aref Mixing during vortex ring collision. *Phys Fluids A*, 3(5): 1405–1410, 1991

ATTACHMENT NO. 2

Simulation of vehicle aerodynamics using a vortex element method

Goéric Daeninck[1], Philippe Chatelain[2], Michael Rubel[2], Grégoire Winckelmans[1], and Anthony Leonard[2]

[1] Mechanical Engineering Dept.
Université catholique de Louvain
Place du Levant 2, Louvain-la-Neuve, 1348, Belgium
daeninck@term.ucl.ac.be

[2] Graduate Aeronautical Laboratories
California Institute of Technology
Pasadena, CA 91125, USA
philch@galcit.caltech.edu

1 Introduction

The numerical method used here is a combination of a Lagrangian vortex element method (VEM) and a boundary element method (BEM). Vortex methods are based on the vorticity formulation of the Navier-Stokes equations and on the fact that, for incompressible flows, it is sufficient to follow the evolution of the vorticity field (the velocity can be recovered from the vorticity).

For bluff body flows, the vorticity is only present in the boundary layers and in the wake. As vortex methods only require particles to carry the vorticity, they require much less computational elements than grid-based methods

It was only recently that direct numerical simulations (DNS) of 3-D bluff body flows were performed using a vortex method (Ploumhans *et al* [4]) Such simulations were made possible because of the important advances made by the "vortex methods community" in the past ten to fifteen years.

We present some recent developments on going aimed at the extension of the vortex method as a tool for Large Eddy Simulations of bluff body flows First, we review the modifications that we introduced for computing 3-D flows where the attached boundary layer regions are modeled using infinitely thin vortex sheets while the separation regions and the wake are modeled using vortex blobs. We then present some results using this approach applied to the flow past the Ground Transportation System (GTS). Finally, a new hybrid Eulerian-Lagrangian approach is briefly presented: the near-wall regions are resolved using a grid based method while the vortex element method is used for the convection-dominated part of the flow.

2 VEM and BEM with infinitely thin boundary layers

As the contributions presented here are based on the vortex and boundary element methods developed in the frame of DNS for 3-D bluff body flows, please refer to [4] and references therein for more details on the these methods. Also, notice that performing simulations of 3-D flows using a vortex method requires fast N-body solvers based on multipole expansions running efficiently on parallel computers ([5, 6]). Finally, an excellent general overview of Lagrangian vortex methods can be found in Cottet and Koumoutsakos [1].

2.1 Infinitely thin boundary layers

We here consider simulations where the thin attached boundary layer regions are modeled using infinitely thin vortex sheet panels, while the vorticity in regions where separation is allowed is captured using vortex particles In practice, the body surface mesh is tagged in order to define the "attached" regions and the "separation" regions

Let us consider a set of M panels, discretizing the body surface, and N vortex particles Let P_{att} be the subset of "attached"-tagged vortex panels and P_{diff} the "diffusing"-tagged panels (i e. where separation is allowed).

One time step then goes as follows:

1 Compute the velocity field, u, and its gradient, ∇u, at particle locations from ω, the vorticity carried by the vortex particles and P_{att}, the subset of attached vortex panels
2 Update the particles' position and strength, for the time step, Δt,

$$\frac{\mathrm{d}x_i}{\mathrm{d}t} = \mathrm{u}\big|_i \,, \quad \frac{\mathrm{d}\alpha_i}{\mathrm{d}t} = \nabla\mathrm{u}\big|_i \cdot \alpha_i + \mathrm{PSE}\big|_i \,, \tag{1}$$

where the Particle Strength Exchange (PSE) scheme is used to treat the viscous diffusion.
3 Enforce the no slip boundary condition at the wall:
   a) Compute the slip velocity, u_{slip}, underneath all vortex panels ($P_{\text{att}} \cup P_{\text{diff}}$) from the vorticity carried by the vortex particles and P_{att}.
   b) Compute the vortex sheet, $\Delta\gamma$, that cancels the slip velocity at the solid boundary.
   c) For panels belonging to P_{att}, the new panel strength is set to $\gamma_i + \Delta\gamma_i$ For panels in P_{diff}, the vortex sheet is equivalent to a vorticity flux that must be emitted into the flow for the time Δt: $\nu \frac{\partial\omega}{\partial n} = \frac{\Delta\gamma}{\Delta t}$ This amounts to modifying the strength of the particles close to these panels as in [4].
4 Redistribute the particles (when necessary): the old set of particles is replaced by a new one, in which the particles are on a regular lattice

2.2 Progressively diffusing panels

When using "attached" panels, it is obvious that the flow experiences an abrupt transition as it goes from the "attached" vorticity region to the "separation" region In this transition region, the boundary layer thickness varies from zero to a finite value (magnitude of the local particle size) over a very short distance

In order to ensure a smooth transition zone, "partial" diffusing panels are used: a diffusion ratio, r, is attributed to each of these panels. The idea is to ensure that a fraction r of the total boundary layer vorticity, γ_{tot}, is carried by the vortex particles while the remaining fraction $(1 - r)$ is still attached to the vortex panels The diffusion fraction is chosen such that there is a smooth transition from non-diffusing panels ($r = 0$) to totally diffusing panels ($r = 1$)

First, let's define γ_{tot} as the total boundary layer strength after the no-slip enforcement:

$$\gamma_{\text{tot}} = \gamma_{\text{panel}} + \gamma_{\text{part}} + \Delta\gamma, \tag{2}$$

where γ_{panel} is the current panel strength, γ_{part} the current strength of the boundary layer fraction discretized by vortex particles (see below) and $\Delta\gamma$ the vortex sheet that cancels the slip velocity at the solid boundary (Step 1b, Section 2 1).

We can then compute $\Delta\gamma_{\text{part}}$ and $\Delta\gamma_{\text{panel}}$, respectively the variation of the vortex panel strength and the vorticity flux to be emitted onto the vortex particles, such that, for each panel:

$$\gamma_{\text{part}} + \Delta\gamma_{\text{part}} = r\ \gamma_{\text{tot}} \tag{3}$$

$$\gamma_{\text{panel}} + \Delta\gamma_{\text{panel}} = (1 - r)\ \gamma_{\text{tot}} \tag{4}$$

Notice that these equations are solved in the local panel coordinate system for the tangential vorticity components only (as the panel's strength normal component must be equal to zero)

For progressive diffusing panels, Step 3c (Section 2 1) is modified as follows: the new panel strength is set to $\gamma_{panel} + \Delta\gamma_{panel}$; the vortex sheet $\Delta\gamma_{part}$ is the vorticity flux that must be emitted into the flow for the time Δt: $\nu \frac{\partial\omega}{\partial n} = \frac{\Delta\gamma_{part}}{\Delta t}$

Even if γ_{part}, the boundary layer strength carried by the vortex particles above a given panel, is well defined conceptually: $\gamma_{part} = \int_0^\delta \omega_{part}\, dz$, its evaluation is somewhat arbitrary (Fig. 1) First, lets redefine γ_{part} as the averaged boundary layer strength (carried by the vortex particles) over a surface S (ideally the panel's surface):

$$\gamma_{part} = \frac{\int_S \int_0^\delta \omega_{part}\, dz\, dS}{S}$$

For each panel, we approximate this quantity as the discrete integral of ω_{part} over an hemisphere of radius R centered on the panel divided by an "equivalent" surface S_{eq}:

$$\gamma_{part} \sim \frac{\sum_{d_i<R} \alpha_i}{S_{eq}}$$

where d_i is the distance of a particle to the panel center, α_i is its strength, and S_{eq} was chosen equal to πR^2. It is clear that R should be greater than the local boundary layer thickness, but also remain fairly low in order to obtain a good approximation of the local boundary layer strength

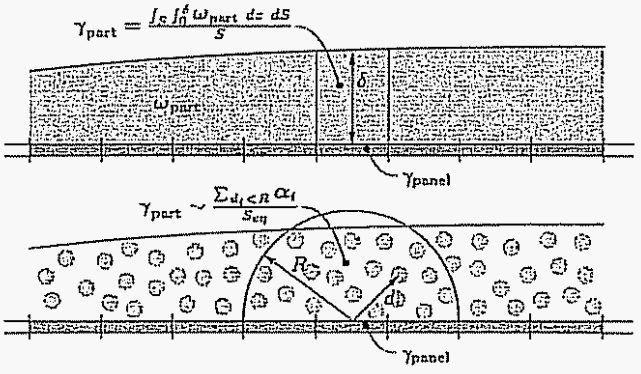

Fig. 1. Boundary layer strength carried by the vortex particles (γ_{part}) and attached to the vortex panels (γ_{panel})

2.3 Auto diffusing panels

If one wants to perform simulations where ground effects are taken into account, ground panels are necessary in order to enforce the no-slip boundary condition there Furthermore, the wake vorticity has to interact in a viscous way with the ground This is true even if one is not interested in the wake-ground effect (as in the far wake for example), due to the fact that the interaction of wake vorticity with a non-viscous ground rapidly leads to numerical blowup This observation leads to the conclusion that it is necessary to use "diffusing" ground panels over the whole wake region.

In order to avoid the extra cost of ensuring a few layers of particles above the whole wake region at all times (to capture the diffused panel vorticity), we introduce "automatic"

diffusing panels: as soon as vortex particles travel above these panels, their vorticity is diffused onto them (they act as "diffusing panels"); otherwise the panel vorticity remains attached

2.4 Improved panel solver

The vortex sheet $\Delta\gamma$, necessary on the body surface in order to cancel the slip velocity, is found as the solution of a boundary integral equation The discretization of this boundary integral equation results in a system of $2M$ linear equations for the vortex panels (i.e. find $\Delta\gamma_i$ for each panel) which is solved iteratively. The use of multipole expansions for vortex panels reduces the cost of each iteration to $\mathcal{O}(M \log M)$ The efficiency of this iterative "multipole-based" solver was improved as follows:

- Choice of a good initial guess: the use of $\Delta\gamma_i = -2\,\mathbf{n}_i \times \mathbf{u}_i^{\text{slip}}$ (exact solution for coplanar panels) has proved to lead to faster convergence compared to the former method where the previous time step solution is used This is mainly because the vortex sheet is only a small correction at each time step dominated by high frequency variations as vortex particles come locally close to panels or not. These high frequency variations call for local corrections which are well estimated by the exact solution for coplanar panels
- Let $\Delta\gamma^r$ be the corrective vortex sheet at iteration r In order to evaluate $\Delta\gamma^{r+1}$ one must compute the slip velocity, $\mathbf{u}^{\text{slip}^r}$, induced by $\Delta\gamma^r$ Now, instead of computing the slip velocity induced by the whole vortex sheet $\Delta\gamma^r$ at each iteration we can compute the slip velocity induced by $(\Delta\gamma^r - \Delta\gamma^{r-1})$ and simply add it to $\mathbf{u}^{\text{slip}^{r-1}}$ (linear problem) This is advantageous because of the use of multipole expansions: as we converge to the solution, $(\Delta\gamma_i^r - \Delta\gamma_i^{r-1})$ gets smaller and thus each iteration takes less time to compute as we can make a more extensive use of multipole expansions
- When using "attached" panels, compute the vortex sheet correction $\Delta\gamma$ only, even for "attached" panels (instead of solving the system for γ) This correction is much smaller compared to γ (panel's attached vorticity) which, again, is advantageous because of the use of multipole expansions

These modifications reduced the global computational time for the panel solver by a factor 2 (up to 5 in some cases)

2.5 Total circulation

For a physical flow, one must ensure that the total vorticity remains equal to zero for all times. As the global time integration scheme is not conservative, the sum of the particle strengths is set back to zero at each time step, by distributing the difference over all particles

However, when "attached" vortex panels are used, this simple scheme cannot be used anymore as one must take the "attached" vorticity into account Several approaches for enforcing the total vorticity where investigated.

- Our first approach was based on the fact that the vortex flux at the wall must be divergence free At a global level, this leads to the following constraint :

$$\int_{S_{\text{body}}} \Delta\gamma \, dS = 0$$

  We track the total amount of circulation diffused onto the vortex particles (Γ_{shed}) over time The particle strengths are then adjusted to Γ_{shed} at each time step
  Despite the sound physical foundation of this approach, it performs very poorly in time Actually, the basic hypothesis, $\int_{S_{\text{body}}} \Delta\gamma \, dS = 0$, is true only for a divergence free vorticity field, which is not the case in practice. Practically, as we modify $\Delta\gamma$ in order to satisfy the total vorticity constraint, the vortex sheet no longer cancels the slip velocity and particles soon penetrate inside the body which finally leads to numerical blowup.

- In the second approach we do not place any constraint on the vortex sheet We simply ensure, at each time step, that the total vorticity remains equal to zero by setting the sum of the particle strengths to minus the total "attached" vorticity, $-\int_{S_{body}} \gamma_{attached}\, dS$ (carried by the "attached" vortex panels)
  This approach produces good results, even for long time simulations

2.6 Vorticity flux at the wall for under resolved boundary layers

When performing simulations where the boundary layers are no longer well resolved, the characteristic diffusion distance becomes small compared to the local particle size This can become critical as the panel diffusion step must ensure that the total flux of vorticity is distributed to neighbor vortex particles The use of the classical diffusion scheme with the correction for conservation leads to a very noisy distribution of the vorticity on the neighbor particles. This situation degrades even further for simulations with ground effect where a decreasing resolution is used in the wake

Actually, in these under-resolved computations, one "simply" wants to transfer the whole vorticity flux to the first layer of particles above the wall We therefore "relax" the local Reynolds number at the wall with respect to the local grid size to ensure that the vorticity flux can be "sufficiently well" captured This scheme gives produces results because of its diffusive nature which helps to remove the high-frequency noise present in the computed vorticity flux.

2.7 Redistribution schemes, relaxation of the particle field divergence and subgrid-scale modeling

The vortex particle method has no built-in control for keeping the vorticity field divergence-free as time evolves When the computation is well resolved (as it has been shown in various DNS results for the flow past a sphere), the divergence of the vorticity field appears to be kept "naturally" to a fairly low value, even for long time simulations. However, as soon as one wants to push the resolution towards its limits, the divergence problem becomes a major issue.

In fact, one can state that an increasing divergence of vorticity field is the sign that the computation is not well resolved locally and that energy is accumulating in small scales of the flow: subgrid-scale stress modeling becomes necessary.

It is clear that the redistribution step plays a major role here, as it is essential to keep a good representation of the vorticity field. One can go even one step further by using the redistribution scheme as a form of subgrid-scale model: it can easily be shown that the low order Λ_1 scheme (which only conserves moments of order zero and order one of the vorticity field) has a viscous-like behavior. The diffusion effect introduced by a Λ_1 redistribution scheme applied every n time steps is roughly equivalent to an effective viscosity given by:

$$\nu_{\text{redist}} \simeq \frac{h^2}{12\, n\, \Delta t}\,, \tag{5}$$

where h is the local grid size and Δt the time step.

Although quite crude, the method enabled us to perform long time simulations for the flow past a hemisphere ($T = 75$) with a relatively low number of particles (Fig. 2) Let's mention that, in the vicinity of the body, the resolution is twice coarser compared to the resolution used for the DNS past a sphere at $Re = 300$ used in ??. These results show that the vortex method is able to capture the dynamics of the complex vortex structures with a reduced number of computational elements and to reproduce the qualitative behavior of a turbulent flow past the hemisphere

However, due to its highly diffusive nature which is only controlled by the local grid size, the redistribution interval and the time step, one cannot rely on a low order Λ_1 redistribution scheme to perform satisfactory subgrid scale modeling Furthermore, the effect

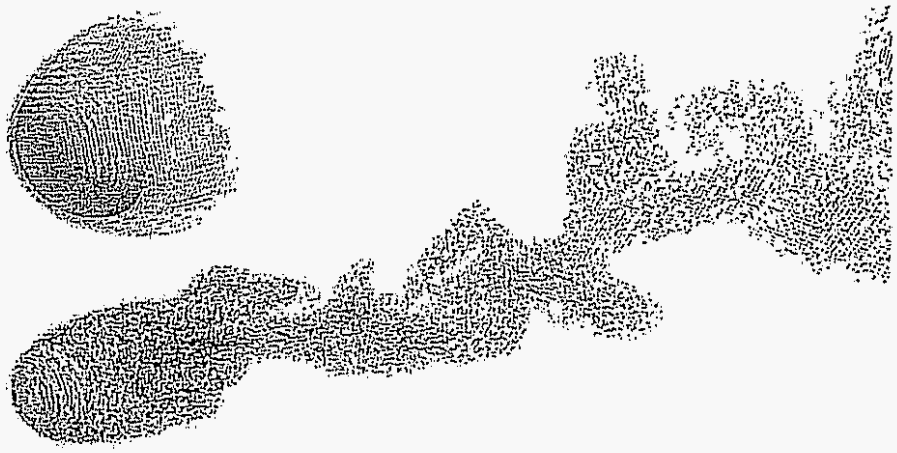

Fig. 2 Flow past a hemisphere using the Λ_1 redistribution scheme Only particles with $|\alpha_i|$ above an arbitrary threshold are shown Top: view of the vortex particles and their strength at an early stage of the flow ($T = 6$) One can see the vortex ring behind the body becoming unstable Bottom: view of the developed turbulent flow at $T = 75$

of any additional model would by far be exceeded by the highly diffusive behavior of the redistribution scheme

From this arises the need for high order redistribution schemes such as the Λ_3 scheme, which is classically used in DNS computations This scheme conserves up to the third moments of the vorticity distribution and acts as hyper-viscosity As the Λ_3 scheme does not have a viscous behavior, there also is no longer enough dissipation of the small-scale energy: this translates into a rapid increase of the vorticity field's divergence and finally leads to numerical blowup

Before introducing more advanced subgrid-scale models, we wanted to assess the capability of the vortex method combined with a high-order redistribution scheme to capture small flow structures compared to the local particle size In order to deal with the divergence problem, we introduced a "relaxation scheme" where the particle strengths are set back to the curl of the velocity field computed at particle locations (this field is necessarily divergence free) This relaxation procedure is, again, a diffusive operation However, when it is applied sufficiently scarcely, the global diffusive effect remains fairly low The particle reset can be seen as a periodic filter which eliminates the energy that gets accumulated in the small scales captured by the computation

Very promising results were obtained using this approach for the flow past the GTS (see Section 3) The next step will be to introduce a subgrid-scale model (a Smagorinsky model to start with), as it would no longer be annihilated by the effect of the redistribution scheme The periodic relaxation scheme should then become less necessary as the energy dissipation at small scales will be taken into account We however think that some active control on the divergence-free property of the flow should still be maintained

3 Flow past the GTS

All the recent developments presented in the previous sections where tested on the flow past the GTS This simple geometry was used because modeling the flow using infinitely thin attached boundary layers along the truck and allowing separation on the backface is a good approximation of the physical flow (at a zero degree yaw angle) The "real" ground effect was also taken into account in this simulation: the truck is traveling above a fixed ground

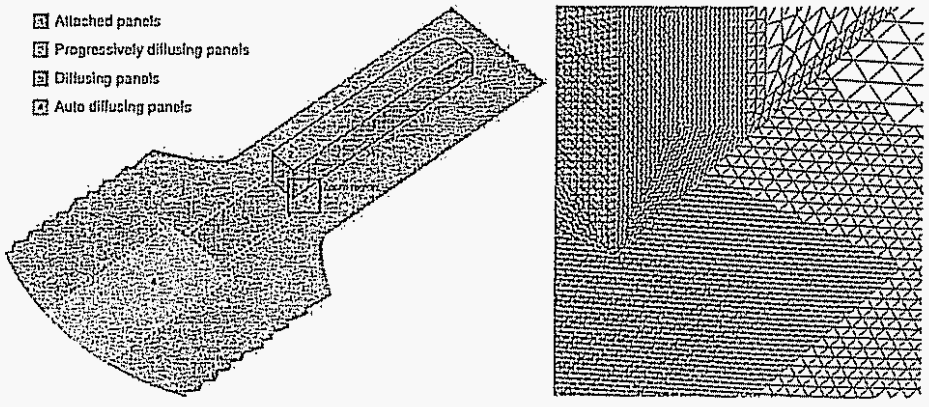

Fig. 3. Left: "Numerical setup" for the flow past the GTS Right: Zoom on body surface discretization (vortex sheet panels); panels are colored by diffusion ratio

As can be seen in Fig 3, the whole front part of the truck was tagged as an attached boundary layer region. Then progressively diffusing panels are used in order to ensure a smooth transition from the infinitely thin boundary layers to the region where diffusing panels are used. A close up view of the panel discretization is shown in Fig ?? One can see that a variable panel size is used for computational efficiency: coarse panels can be used in the attached regions, whereas the diffusing (and progressively diffusing) panels' size is chosen equal to the local particle size On the ground, the panels were tagged as attached except for the wake region: the near wake region uses diffusive panels (with a transition region), and the far wake uses auto-diffusing panels.

We use a redistribution mapping which smoothly goes from a constant lattice (in the near body region) to an exponentially growing lattice (in the far wake) At each redistribution, the center of the mapping is "displaced" randomly around its nominal position: this reduces the influence of the arbitrary intersection between the redistribution lattice and the body. In the near body region, the particle size is $h = 0.023\ W$ (W is the width of the truck) The time step is $\Delta T = 0.01\ W/U_{\mathrm{GTS}}$. Redistribution is performed every 5 steps (Λ_3 scheme) The relaxation scheme for the divergence of the vorticity field is applied every 50 steps. The simulation was carried out up to $T = 16$, at that time the number of particles was $\sim 1\,000\,000$ The computation ran 50 hours on 8 Pentium 4 processors at 2.4 GHz (Beowulf linux cluster)

Defining a Reynolds number for these under-resolved computations has little meaning (no quantified subgrid scale modeling, infinitely thin boundary layers) We can however mention that the viscosity coefficient used for the PSE scheme was $\nu_{\mathrm{PSE}}/(U_{\mathrm{GTS}}W) = 10^{-4}$

In Fig 5 one can see the vorticity field in a slice behind the GTS: it clearly shows the development of a truly turbulent flow in the wake. These results feature much more small structures when compared (qualitatively) to simulations where the Λ_1 redistribution scheme was used

4 A hybrid Eulerian-Lagrangian vortex method for flows with massive separation

In the previous section, an "over-simplified" approach was used for the boundary layers: they were modeled by infinitely thin vortex sheets in *a priori* defined regions It is clear that this approach can only provide physical results in simple cases In more general situations, the evolution of the boundary layer has to be simulated in order to determine where the separation dynamically occurs

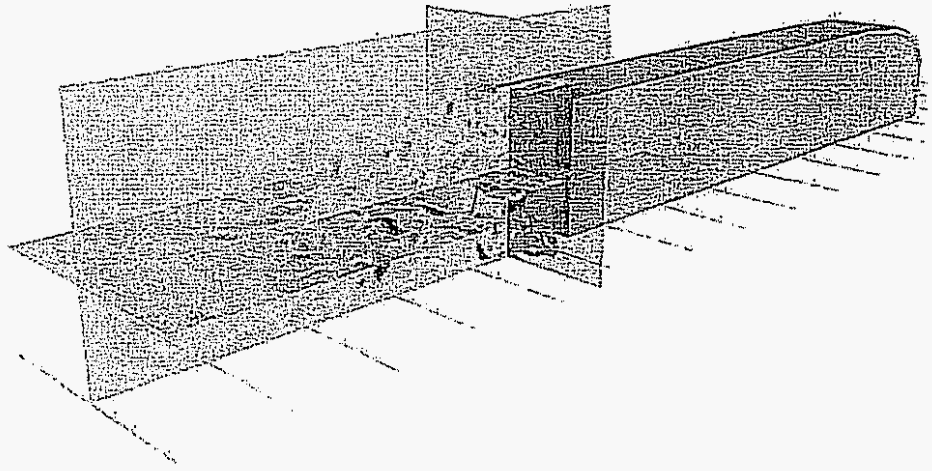

Fig. 4. Flow past the GTS with viscous ground effect in the wake The regions of non zero vorticity are shown in three slices behind the truck: each slice is colored by the y-component of vorticity

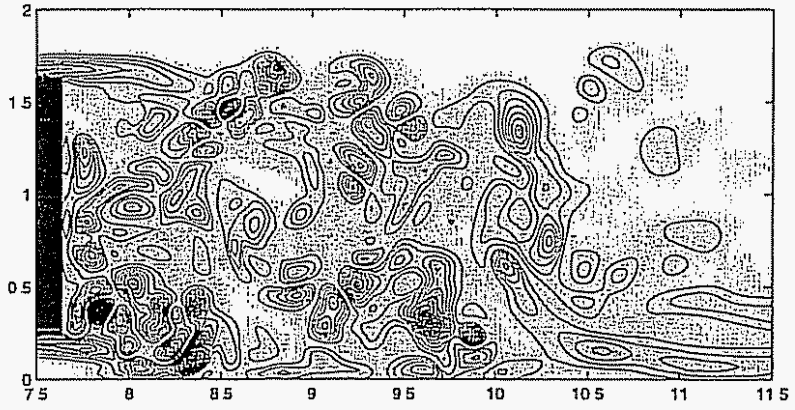

Fig. 5. Zoom on the vertical midplane slice behind the truck: regions of non zero vorticity are shown, it is colored by the vorticity y-component of vorticity (normal to the plane)

The VEM suffers from two drawbacks in the boundary layer regions which prevent it from working efficiently in these regions:

- The VEM uses isotropic computational elements whereas, in the boundary layer regions, the strong gradients in the direction normal to the wall would allow highly anisotropic elements for computational efficiency.
- Altough the VEM performs particularly well for flows dominated by convection (due to the implicit treatment of the convective term), it is less suited to flexible and accurate treatment of the no-slip boundary condition.

These drawbacks currently limit the applicability of the VEM to relatively low Reynolds number flows or flows where an excessive degree of modeling must be introduced in the boundary layer regions. Approaches along the lines of Detached-Eddy Simulation (DES), combining RANS methods (boundary layer regions) and LES methods (separated regions), are required in order to perform simulations at much higher Reynolds numbers

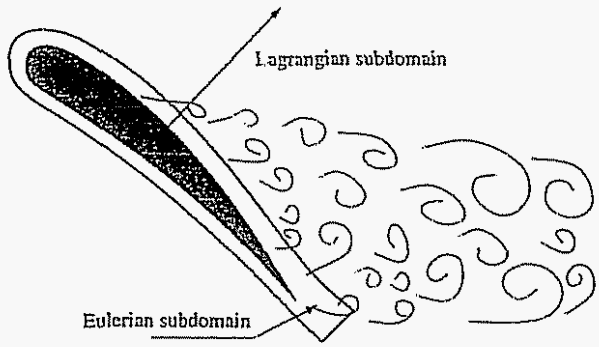

Fig. 6. Example of Eulerian and Lagrangian subdomains The Eulerian subdomain covers only the near-wall region in order to capture the thin boundary layers and the separation regions The Lagrangian subdomain covers whole computational domain and captures well the wake dynamics

This leads naturally to the observation that Eulerian grid-based methods should be used to resolve the near-wall regions, where viscous effects are important, while using the Lagrangian VEM for the convection-dominated part of the flow The strengths and the weaknesses of both methods are indeed complementary in such a hybrid approach.

Hybrid Eulerian-Lagrangian vortex based methods are not new. A great challenge for these methods is to ensure consistant boundary conditions on each subdomain (Eulerian and Lagrangian) and to allow an accurate transfer of information between these subdomains Previous approaches (e g. Cottet *et al.* [3]) required complex and expensive iterative methods in order to determine the boundary conditions on each domain

We propose a new approach where the Lagrangian subdomain covers the entire computational domain (altough under-resolved in the near-wall region), while the Eulerian subdomain is limited to the near-wall region and resolves well that region (Fig. 6) This allows to obtain the boundary conditions on the Eulerian domain directly from the information in the Lagrangian domain (no need for iterative methods) On the other hand, the evolution of the Lagrangian field in the near-wall region is corrected by the Eulerian information which is well resolved there

Preliminary results where obtained for the 2-D simulation of the flow past a cylinder at $Re = 3000$ (Fig 7) In this simulation, a finite difference method based on the velocity-vorticity formulation was used in the Eulerian subdomain. A coarse resolution was chosen for the Lagrangian subdomain, while the Eulerian subdomain uses a fine grid in order to capture well the detailed dynamics in the near-wall region. A good behavior of the algorithm was observed in terms of robustness and information transfer between subdomains. Further investigations will focus on quantitative validations of the method. The next steps will be to extend the method to 3-D, to introduce a DES approach in the Eulerian subdomain, and a LES model in the Lagrangian subdomain

References

1 G.-H Cottet and P Koumoutsakos, *Vortex Methods: Theory and Applications* (Cambridge Univ. Press, Cambridge, UK), January 2000.

2 A Leonard, D Shiels, J K Salmon, G S Winckelmans and P Ploumhans, Recent Advances in High Resolution Vortex Methods for Incompressible Flows, In *Proc. 13th AIAA Computational Fluid Dynamics Conf.*, Snowmass Village, CO, June 29 – July 2, 1997, AIAA #97-2108

3 M Ould-Salihi, G.-H. Cottet and M El Hamraoui, Blending finite-difference and vortex methods for incompressible flow computations , *SIAM J Sci Comp.*, 22, 1655-1674 (2000)

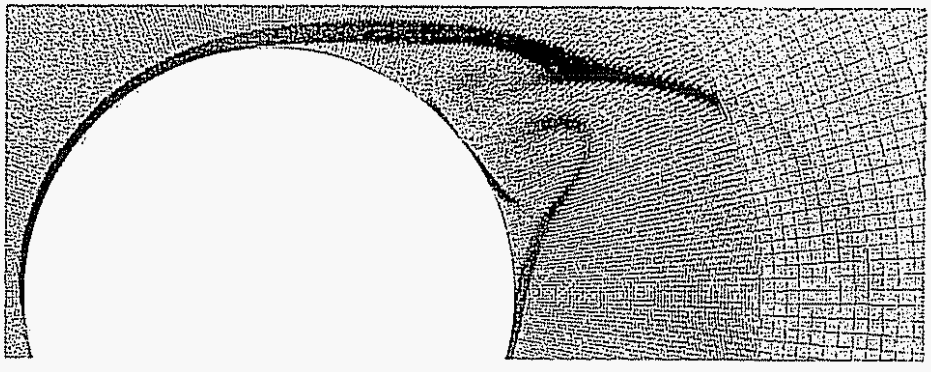

Fig. 7. Vorticity field for the flow past cylinder at $Re = 3000$ One can see the Eulerian subdomain covering the near-body region with the fine grid, and the coarse Lagrangian subdomain covering the whole computational domain (the near wall-region is hidden by the Eulerian subdomain)

4. P Ploumhans, G S Winckelmans, J K Salmon, A Leonard and M S Warren, Vortex methods for high-resolution simulation of three-dimensional bluff body flows; application to the sphere at Re=300, 500 and 1000, *J. Comput. Phys.* 178 (1), 427 (2002)
5 J K Salmon and M. S Warren, Skeletons from the Treecode Closet, *J Comput Phys* 111 (1), 136 (1994).
6 G S Winckelmans, J K Salmon, A Leonard, and M. S Warren, Three-dimensional vortex particle and panels methods: Fast tree-code solvers with active error control for arbitrary distributions/geometries, in *Proc. Forum on Vortex Methods for Engineering Applications, Albuquerque, NM, February 22–24, 1995*, p 25

ATTACHMENT NO. 3

OCTREE ALGORITHMS FOR THE IMPLICIT CLOSEST POINT TRANSFORM

M RUBEL*

Abstract. Two new algorithms which find the Implicit Closest Point Transform are presented. Given a 2-D polygonal surface in 3-D space and a test point, the algorithms identify the location on the surface which is closest to the test point. Both algorithms give results which are exact to machine precision, and can operate efficiently without requiring that the points lie on a regular lattice or belong to a set whose positions are known in advance. Operating time per test point is constant in both cases; the algorithms differ in their initial setup times and memory consumption.

Key words. closest point transform, implicit closest point transform, distance transform, euclidean distance transform, octree, level set

AMS subject classifications. 65D18, 51N20, 51N05, 68U05

1. Terminology.

surface	One contiguous 2-D surface in Euclidean 3-D space
boundary	A set of one or more surfaces
feature	Any single vertex, edge, or face in a discretized boundary
EDT	Euclidean Distance Transform
CPT	Closest Point Transform
FMM	Fast Marching Method
C/SC	Characteristic / Scan Conversion Algorithm (Mauch)
C/OT	Characteristic / Octree Algorithm
LUB/OT	Least Upper Bound / Octree Algorithm

2. Background. When modeling a physical process with a complicated boundary, it is often necessary to find how points in space are oriented relative to it. For example, one might wish to identify all points that fall within some distance of the boundary, to classify each point as inside or outside, or to measure the first arrival traveltime (the shortest distance) to each point.

The precise way to ask these questions is to apply the Euclidean Distance Transform (EDT), which maps each test point to its shortest distance from the boundary, or more generally the Closest Point Transform (CPT), which maps each test point to its closest point on the boundary.

Among algorithms developed to perform the CPT or EDT efficiently, the most successful ones have approached it from the point of view of finding viscosity solutions to the Eikonal problem:

$$|\nabla \vec{u}| = 1 \qquad \vec{u}_{\text{boundary}} = 0 \tag{2.1}$$

Equation 2.1 works here because its characteristic curves are normal to the boundary and measure distance from it, following the natural definition of distance from a surface. Readers seeking a more detailed account of the theory are referred to Sethian's [5] review of Fast Marching Methods, which includes an extensive discussion.

*GALCIT, California Institute of Technology, 205-45 Caltech, Pasadena, CA 91125 USA, *mrubel@galcit.caltech.edu*

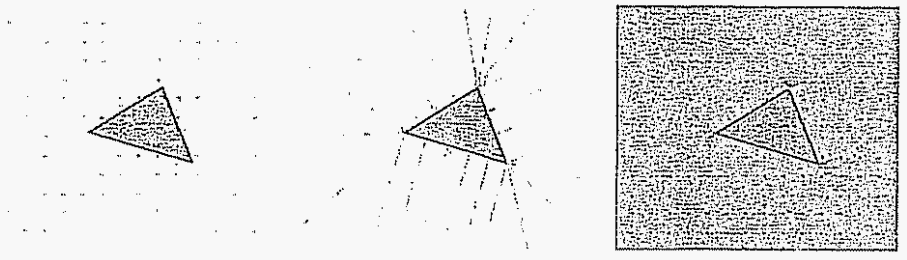

FIG 2.1 *Illustration of Mauch's C/SC algorithm applied outside a triangle in 2-D (a) Triangle and grid of test points (b) Characteristics (c) Test points set over six external characteristic regions*

For numerical reasons, most grid-based Eikonal solvers, such as [8], [3] use some form of upwind finite differencing. The Fast Marching Method [7], [4] is an approximate algorithm which combines upwind finite differencing with a priority queue strategy like the one in Dijkstra's shortest-path or Dial's shortest-forest. The FMM, which is log-linear or linear in the number of test points, has been adapted to a variety of applications [5], and in particular can be applied to find the EDT [6]. Kim's newer Group Marching Method [1], works similarly but arrives at its answer in linear time.

An alternative strategy is to solve Equation (2.1) by the method of characteristics In formulating his Characteristic / Scan Conversion (C/SC) algorithm, Mauch [2] observed that for a boundary geometry composed of simple features, such as polygons, edges, and vertices, the space filled by all characteristic lines originating from each feature is an open polyhedron (Figure 2.1). The polyhedra may overlap At a given test point, the characteristic line corresponding to the closest point belongs to one of the polyhedra it falls inside.

Mauch loops over the characteristic regions and selects test points by scan conversion (Algorithm 1), finding the exact CPT to machine precision in linear time (linear in both the number of test points and the number of boundary elements) Furthermore, for boundaries with a sensible inside and outside, the algorithm can be extended to provide inside/outside information as well, by following the negative branch of the solution inside the boundary (note that if $\vec{u}$ solves Equation (2.1), then so does $-\vec{u}$)

Because Mauch's algorithm uses scan conversion, it is currently limited to problems where all of the test points lie on a regular grid However, Mauch has proposed the use of Orthogonal Range Queries to extend the method to irregularly-spaced test points [2]

3. **Explicit vs. Implicit.** All algorithms discussed in the previous section find the CPT or EDT explicitly. That is, each transform could have been written:

$$\text{result} = F(\text{boundary geometry; test point locations}) \tag{3.1}$$

The test point locations needed be known in advance for the algorithms to perform efficiently. We require an algorithm that remains efficient even when test point locations are unknown beforehand; that is, when the CPT must be written as an implicit function:

$$G(\text{result; boundary geometry; test point locations}) = 0 \tag{3.2}$$

The algorithm must be capable of computing to the CPT to each test point individually in constant time

Algorithm 1 Mauch's Characteristic / Scan Conversion Algorithm Computes the shortest distance δ_s^i which separates each test point $\vec{x}^i$ from its closest point $\vec{x}_{\text{cp}}^i$ on feature F_{cp}^i.

```
for all test points i do
  δ_s^i ⇐ ∞
end for
for all features F_j on boundary do
  find characteristic region R_j of feature F_j
  using scan conversion, select test points x^i which lie within R_j
  for all points x^i thus selected do
    δ ⇐ signed distance from x^i to F_j
    if |δ| < |δ_s^i| then
      δ_s^i ⇐ δ
      F_cp^i ⇐ F_j
      x_cp^i ⇐ closest point on F_j to x^i
    end if
  end for
end for
```

4. Broad Strategy. Since no *a-priori* assumptions may be made about where test points will be located, we formulate the following broad strategy to ensure that total work will be linear in the number of test points

Divide the region of interest into small cells in manner which yields the following properties:

- It should be easy to find which cell contains a given test point
- Each cell should have a pre-computed list of features which could contain the closest point
- The length of each list should be no more than a constant which is independent from the number of boundary features

Once the region of interest has been divided and the closest-feature lists computed for each cell, Algorithm (2) may be applied to find the CPT to a test point

Algorithm 2 General algorithm for computing the shortest distance δ_s, which separates the test point at $\vec{x}$ from its closest point $\vec{x}_{\text{cp}}$ on feature F_{cp}

```
δ_s ⇐ ∞
C ⇐ cell that contains x
for all features F_j listed in C do
  if x inside characteristic region R_j of feature F_j then
    δ ⇐ signed distance to F_j
    if |δ| < |δ_s| then
      δ_s ⇐ δ
      F_cp ⇐ F_j
      x_cp ⇐ closest point on F_j to x
    end if
  end if
end for
```

Two approaches for finding the Implicit CPT will be presented shortly. Both follow the above strategy, differing only in how they choose which features to include in a given cell's F_i list. But first, a brief note is in order about how space will be divided into cells.

5. The Octree. One could simply divide space into uniform cells on a regular grid. The grid spacing would have to be small enough to bound the number of features in any one cell by a constant, so a more complicated boundary would naturally lead to a finer grid.

Although simple, the uniform grid strategy would be inefficient when applied to the commonly interesting case where regions of sharp detail are strongly localized in an otherwise coarse surface. Instead, we employ the octree data structure, in which a cube is divided recursively, perpendicular to its coordinate axes, until the desired level of detail (or local cell size) is attained. A quadtree, the octree's two-dimensional analogue, is illustrated in Figure 5.1.

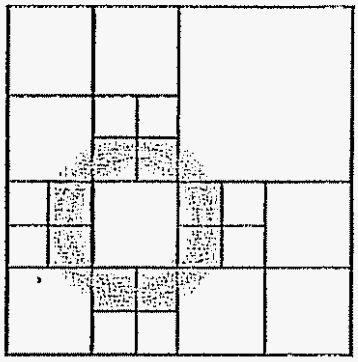

FIG. 5.1. *Illustration of a quadtree which has been refined in the neighborhood of an annulus*

In both of the schemes described below, an octree is formed by recursively dividing an initial octree (starting with a single "root" cell, in the simplest case) until the number of features associated with each "leaf" cell is bounded by some constant.

6. Least-Upper Bound Approach.

6.1. Theory. In this first strategy to decide which features might be closest to any test point in a given cell, we temporarily set aside Equation 2.1 and instead make use of the triangle inequality.

Suppose we compute the shortest distances from all boundary features to the cell centerpoint, calling these distances $\delta_i, i = 1 \ldots N$ where N is the number of boundary features. Further suppose that the cell radius is r (that is, no point in the cell is more than r units away from the center). Let δ_s be the distance from a test point within the cell to its closest point on the boundary. It follows from the triangle inequality and definition of shortest distance that:

$$\delta_s \leq \min_{i=1 \ldots N}(\delta_i) + r \tag{6.1}$$

Further suppose that the closest point is on feature k, which has minimum distance δ_k away from the center of the cell. Again from the triangle inequality, we conclude

that:

$$\delta_s \geq \delta_k - r \tag{6 2}$$

Combining the two,

$$\delta_k \leq \min_{i=1}^{N}(\delta_i) + 2r \tag{6 3}$$

Thus, when building a list of features which might contain the closest point to any test point in a given cell, one need only include those features for which Property 6 3 is satisfied (Figure 6 1)

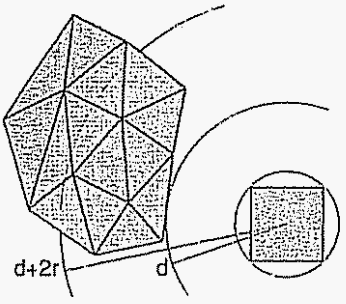

FIG 6 1. *Illustration of Least Upper Bound criterion. Only faces whose shortest distance from the cell center is less than or equal to $d_{min} + 2r$ need be considered; the outer three triangles can be safely ignored*

6.2. Analysis. Because the number of features per cell is bounded by a constant, the work to find the closest point to a given test point is constant. Thus the total work to perform the Implicit CPT, once the octree is built, is linear in the number of test points.

It is less obvious how much work and memory are required for octree construction. We now attempt a rough analysis.

Rather than dealing directly with boundary features in our analysis, which would preclude us from treating the problem in a general way, we consider $\alpha(\vec{x}, s)$, the fraction of boundary area which needs to be considered when computing the transform at a point $\vec{x}$ in the center of a cell of size s. By construction, $0 < \alpha \leq 1$, and it is inversely proportional to the number of boundary features.

For LUB/OT to one or more polygonal faces (and perhaps in more general cases, though we have not yet proven so), $\alpha_{\text{lub}}(\vec{x}, s)$ may be expanded locally about $s = 0$, except at discontinuities:

$$\alpha_{\text{lub}}(\vec{x}, s) = a_0(\vec{x})s + \mathcal{O}(s^2) \tag{6 4}$$

where $a_0 > 0$. Equation (6 4) can also be inverted; that is, there exists some constant b_0 for which:

$$s(\vec{x}, \alpha_{\text{lub}}) = b_0\alpha_{\text{lub}} + \mathcal{O}(\alpha_{\text{lub}}^2) \tag{6 5}$$

Suppose we are building an octree according to the LUB criterion. Let the tree have N_L leaf cells, of volume v_i, $i = 1 \ldots N_L$. Let $\overline{v}$ be the average (arithmetic mean)

of these volumes. By definition, we may write:

$$\overline{v} = \frac{1}{N_L} \sum_{i=1}^{N_L} v_i \tag{6.6}$$

The sum of leaf volumes is a constant: the volume of the octree. Substituting and rearranging,

$$N_L \propto \frac{1}{\overline{v}} \tag{6.7}$$

The volume of the cell centered at $\vec{x}$ is s^3. As $\max_{\text{cells}}(\alpha_{\text{lub}}) \to 0$, the maximum cell size goes to zero, and the average volume approaches the Riemann integral:

$$\overline{v} \propto \int_{\text{octree}} s^3 dV \tag{6.8}$$

which, after substitution, becomes

$$\overline{v} \propto \int_{\text{octree}} \alpha_{\text{lub}}(\vec{x}, s)^3 d\vec{x} \tag{6.9}$$

The octree is constructed so as to make α the same in each cell, to the greatest extent possible. This is the terminal occupancy criterion. Therefore, the mean of α over the octree is proportional to α_{term}. So the integrand comes out front, and what remains is a constant.

$$\overline{v} \propto \alpha_{\text{term}}^3 \tag{6.10}$$

Substituting Eq. (6.10) into Eq. (6.7) and proceeding to the small α_{term} limit (which is the large number-of-panels limit), we obtain:

$$N_L \propto \frac{1}{\alpha_{\text{term}}^3} \tag{6.11}$$

Thus, for fixed geometry and terminal occupancy, the LUB/OT method scales as:

$$N_L = \mathcal{O}\left(N_F^3\right) \tag{6.12}$$

where N_F is the number of boundary features.

6.3. Performance and Memory Consumption. Due to the very large memory consumption of our implementation, it was not possible for us to test the LUB/OT approach in a quantitatively meaningful way. Even for small problems, memory requirements quickly exceeded the capabilities of our system.

For this reason, we do not believe the LUB/OT approach to be useful by itself for finding the Implicit CPT. The much sharper bound provided by the Characteristic / Octree method (C/OT), which will be discussed in the next section, leads to a more practical direct solution. Nonetheless, some lessons learned in the LUB/OT approach will carry forward.

7. Characteristic / Octree Approach.

7.1. Theory. The C/OT approach is based directly on Mauch's C/SC algorithm; the difference is that rather than apply scan conversion (which limits applicability to test points on regular grids), we intersect the characteristic regions with the cells of an octree

If feature F_{cp} contains the closest point to a test point at $\vec{x}$, then a characteristic line of equation (2 1) passes from $\vec{x}_{cp}$ on F_{cp} to $\vec{x}$ Thus, $\vec{x}$ falls inside the characteristic region of feature F_{cp}

Suppose $\vec{x}$ is inside cell C If C has a list of all features F_k, $k = 1 \quad M$ whose characteristic regions intersect it, then only those features need to be considered when finding the closest point transform of $\vec{x}$. So our broad approach is the same as it was in the LUB/OT case. The difference is that we begin by finding the characteristic region of each boundary feature, and then build the octree in such a way that each leaf cell stores the set of features F_k whose characteristic regions intersect it. We bound the maximum number of features per cell below a constant which is proportional to $\frac{1}{\alpha_{term}}$. This process is depicted in Algorithm (3)

Algorithm 3 C/OT recursive octree construction algorithm

```
for all features F_j, j = 1  N_F do
  Compute characteristic region R_j of F_j
end for
Store all features F_j in root cell
C ← root cell
for all features F_j in C do
  if R_j intersects C then
    Add F_j to list of features in C
    if length of list > terminal occupancy then
      Divide C into eight daughter cells
      Store all features F_j associated with C in each of its daughters
      Apply this loop recursively to each daughter of C
    end if
  end if
end for
```

For a surface composed of polygons, the characteristic regions are open polyhedra. For the purposes of this algorithm, it is not necessary to construct the polyhedra explicitly; it is sufficient to find their bounding planes The process is illustrated by example in Figure (7 1).

7.2. The Characteristic Region of a Vertex. Vertex characteristic regions are denoted V in Figure 7.1

Each vertex has a nontrivial characteristic region if, and only if, the surface is locally convex (in or out) That is, the region exists if and only if the adjacent face normals all lie on one side of a plane In this case, the characteristic region bounding planes each contain the vertex and two adjacent face normals. When it exists, the characteristic region of a vertex is convex.

7.3. The Characteristic Region of an Edge. Edge characteristic regions are denoted E in Figure 7 1

Each boundary edge has a nontrivial characteristic region if, and only if, the surface is not locally flat–that is, iff its adjacent edge normals are not parallel The

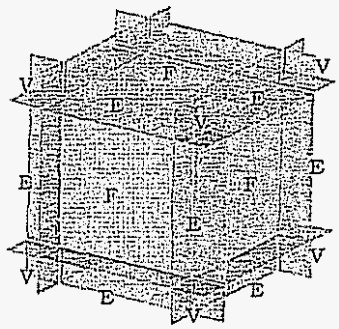

FIG 7 1 *Illustration: characteristic regions outside a cube*

characteristic region is a wedge bounded by four planes: two planes which contain the edge and an adjacent face normal, and two planes perpendicular to the edge which contain its two endpoints. For oriented surfaces which are locally convex, the wedge points away from the boundary; for those which are locally concave, the wedge points into the boundary The characteristic region of an edge is also convex

7.4. **The Characteristic Region of a Face.** The outward-facing face characteristic regions are denoted F in Figure 7 1; inward-facing ones are not shown

The characteristic region of each face is the prism whose bounding planes contain each of its adjacent edges and whose normals lie in the plane of the face For the purposes of this algorithm, we divide the region into two parts separated by the face plane. Thus, for oriented boundaries, one of the regions is outward-facing and the other is inward-facing. If a face is convex then its characteristic region is also convex.

7.5. **Analysis.** The C/OT algorithm finds the Implicit CPT in linear time once the octree is built, since the work for each test point is bounded by a constant.

Analysis of the cost of octree construction parallels that for the LUB algorithm exactly, except that area fraction is now proportional to the square of cell length:

$$\alpha_{\text{cot}}(\vec{x}, s) = a_1(\vec{x})s^2 + \mathcal{O}(s^3) \tag{7 1}$$

Carrying this change through the same reasoning presented in Section (6.2), we conclude that for the C/OT method:

$$N_L = \mathcal{O}\left(N_F^{\frac{3}{2}}\right) \tag{7.2}$$

where N_F is the number of boundary features and N_L gives the number of leaves in the octree.

7.6. **Performance and Memory Consumption.** The C/OT routines were tested on a set of triangulated tori like the one shown in Figure (7 2), with different numbers of surface triangles but otherwise identical. The octree size (given as the number of leaf cells, a measure of the amount of memory consumed) does seem to follow a $N_F^{\frac{3}{2}}$ law (Figure 7 3) This scaling also seems to be the dominant factor in octree construction time

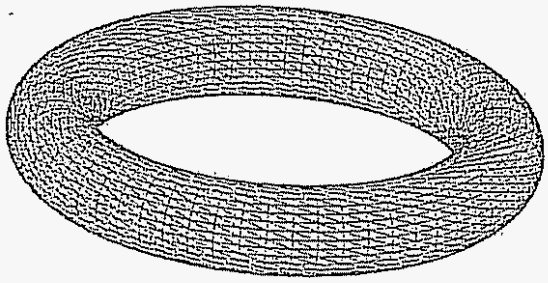

FIG 7.2. *Triangulated torus, typical of those tested*

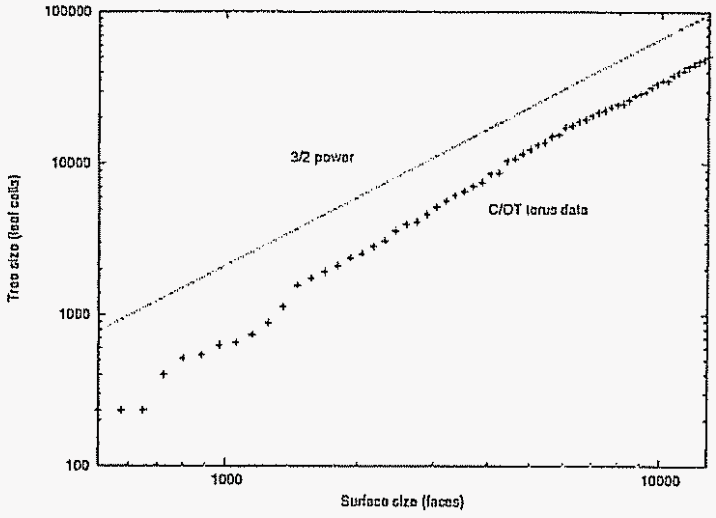

FIG 7.3 *Memory use of the C/OT octree as a function of torus surface discretization*

Scaling measurements for the C/OT method were found to be sensitive to the manner of surface refinement. Refining in only the circumferential direction, for example (which changes triangle aspect ratios) resulted in a slightly different power law. The results shown in Fig. (7.3) were obtained by refining in both directions simultaneously.

8. Combining the Two Approaches. Because the least upper bound and characteristic region criteria are fundamentally different, they can be combined in a useful way. For example, if surface distances beyond some cutoff are not needed for a particular problem, or if an approximate solution would be satisfactory beyond some minimum distance, then the LUB criterion gives a methodical way to eliminate features from consideration during C/OT octree construction.

If, in a given problem, the distance cutoff decreases proportionally to the maximum surface polygon size, then memory scaling can be improved beyond the $\frac{3}{2}$ law. Furthermore, for topologically complicated boundaries, such as those comprised of many simple surfaces whose characteristic regions overlap, applying the LUB cutoff could substantially decrease the unspecified constant multiplying the scaling power

law

9. Future Work. Both algorithms presented are linear in the number of test points. In memory consumption and setup time, however, the LUB/OT and C/OT algorithms respectively scale with the cube and three-halves power of the number of surface features. To the author's knowledge, the C/OT algorithm scales better in memory and setup time than any other known linear-time algorithm for the exact Implicit CPT. However, better performance should still be possible.

It is clearly possible to achieve better (even linear) memory/setup scaling if one is willing to accept an approximate solution over at least some of the test point domain. Supplementing the C/OT approach with LUB-like limits is an obvious starting point, and has been implemented to some degree by P. Chatelain, one of the author's colleagues. There is room for a great deal of improvement in this area however.

Even for exact solutions, though, it may be possible to do better. One property which has not yet been exploited is surface continuity. Under C/OT, features included in a leaf cell are not arranged in any particular order, despite the fact that they may be physically situated in one or more topologically connected sets. It may be possible to achieve log-linear or better memory scaling by storing the perimeters of these sets—rather than their constituent features—in octree cells. In this case, the process of finding which characteristic region includes a certain test point would be performed by, for example, bisection.

10. Acknowledgments. The author gratefully acknowledges the assistance of P. Chatelain in writing certain LUB/OT routines, and of Prof. A. Leonard for helpful suggestions and guidance.

This research was supported in part by Department of Energy contract DE-AC03-98EE50506

11. References.

REFERENCES

[1] Kim, S. An o(n) level-set method for eikonal equations. *Siam Journal on Scientific Computing*, 22(6):2178–2193, 2001.

[2] Mauch, S. *Efficient Algorithms for Solving Static Hamilton-Jacobi Equations*. PhD thesis, California Institute of Technology, 2003.

[3] Osher, S. and J. A. Sethian. Fronts propagating with curvature-dependent speed: Algorithms based on hamilton-jacobi formulations. *Journal of Computational Physics*, 79:12–48, 1988.

[4] Sethian, J. A. A fast marching level set method for monotonically advancing fronts. *Proceedings of the National Academy of Sciences*, 93:1591–1595, 1996.

[5] Sethian, J. A. Fast marching methods. *Siam Review*, 41(2):199–235, 1999.

[6] Sethian, J. A. and A. M. Popovici. Three dimensional traveltime computation using the fast marching method. *Geophysics*, 64:516–523, 1999.

[7] Tsitsiklis, J. N. Efficient algorithms for globally optimal trajectories. *IEEE Transactions on Automatic Control*, 40(9):1528–1538, 1995.

[8] Vidale, J. E. Finite-difference calculation of traveltimes in three dimensions. *Geophysics*, 55(5):521–526, 1990.

Reconnection of Colliding Vortex Rings ATTACHMENT NO 4

Philippe Chatelain, Demosthenes Kivotides, and Anthony Leonard
Graduate Aeronautical Laboratories, California Institute of Technology, Pasadena, California 91125
(Received 3 September 2002; revised manuscript received 16 December 2002; published 6 February 2003)

We investigate numerically the Navier-Stokes dynamics of reconnecting vortex rings at small Reynolds number for a variety of configurations We find that reconnections are dissipative due to the smoothing of vorticity gradients at reconnection kinks and to the formation of secondary structures of stretched antiparallel vorticity which transfer kinetic energy to small scales where it is subsequently dissipated efficiently. In addition, the relaxation of the reconnection kinks excites Kelvin waves which due to strong damping are of low wave number and affect directly only large scale properties of the flow

DOI: 10.1103/PhysRevLett.90.054501 PACS numbers: 47.32.Cc, 47.27.Eq

In flow phenomena as diverse as quantum [1], magnetic [2], and incompressible [3] fluids, it is useful to study the physics of turbulence by modeling the system as a collection of tubular flux loops which in the case of vortical fields are called vortex filaments. An intrinsic property of such highly structured systems is their ability to dynamically change their topology via reconnection mechanisms. Does this change in topology affect in turn properties of fluid turbulence such as intermittency and scalar mixing (which depend directly on the structure of the flow) or the dynamics of energy in wave number space? Or is it the case that reconnection events are not generic and thus have no direct impact on the mean properties of turbulent flows? The aim of this Letter is to address these issues by fully resolving the Navier-Stokes dynamics of interacting vortex rings for three simple geometries having great potential for illuminating the physics of reconnection. Although the flows considered are not strictly turbulent, the hope is that in a future structural approach to the problem of turbulence a significant part of the flow complexity could be traced back to the physics of similar vortex interactions.

Incompressible vortex reconnections have an extensive bibliography (for a review of the work up to 1994, see [4,5]). In [6,7] reconnections of vortex tubes were considered with an emphasis on the possibility of singularity formation as $\mathrm{Re} \to \infty$. In [8] the strong interactions between vortex rings were computed with the interest in developing numerical methods and turbulence models rather than in focusing on the physics of reconnection. In [9] it is discussed how a linked vortex configuration could be achieved starting from an unlinked initial state, and in [10] it is considered how the mixing of a nondiffusing passive scalar is affected during vortex ring collision. The reconnection of two approaching (but not colliding) vortex rings was studied experimentally in [11] and theoretically in [12]. This Letter extends these studies by considering generic vortex configurations and by capturing more features of vortex reconnections in a turbulent flow.

We solve the Navier-Stokes equations for an unbounded three-dimensional incompressible viscous flow. We employ the vorticity formulation:

$$\left(\frac{\partial}{\partial t} + u \cdot \nabla\right)\omega = (\nabla u) \cdot \omega + \nu \nabla^2 \omega, \tag{1}$$

$$\nabla \cdot u = 0, \tag{2}$$

where u is the velocity and ω is the vorticity. We use a vortex particle method [13]. In this method, the vorticity is discretized with Lagrangian elements. These elements which carry a vector-valued Gaussian distribution of vorticity are convected and stretched by the local velocity obtained by the Biot-Savart law. The complexity of the velocity computation is normally $\mathcal{O}(N^2)$ with N being the number of particles; we have used a multipole algorithm that reduces this complexity to $\mathcal{O}(N \log(N))$. Viscous diffusion is handled by the particle strength exchange scheme.

We calculate the global kinetic energy E and enstrophy Ω defined as

$$E = \frac{1}{2}\int u \cdot u dx, \tag{3}$$

$$\Omega = \int \omega \cdot \omega dx \tag{4}$$

For unbounded flows, the relation between kinetic energy and enstrophy is

$$\frac{d}{dt}E = -\nu\Omega. \tag{5}$$

We also compute the evolution of the spectrum of the kinetic energy $E(k)$ which, in terms of the Fourier transform of vorticity $\hat{\omega} = [1/(2\pi)^{3/2}] \int \omega(r) e^{-ir\,k}\, dr$, is defined as

$$E(k) = \frac{1}{2}(2\pi)^3 \int_{|k|=k} \hat{\omega} \cdot \hat{\omega}^* d\Omega_k, \tag{6}$$

 0031-9007/03/90(5)/054501(4)$20.00

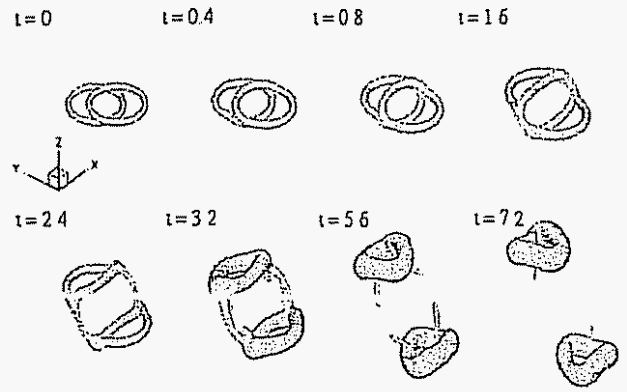

FIG. 1. Vortex rings in an offset collision: contours of vorticity; from $t = 0$ to 2.4, the contour is $\omega = 0.15\omega_{\max}^{t=0}$; for $t > 2.4$, it is $\omega = 0.025\,\omega_{\max}^{t=0}$.

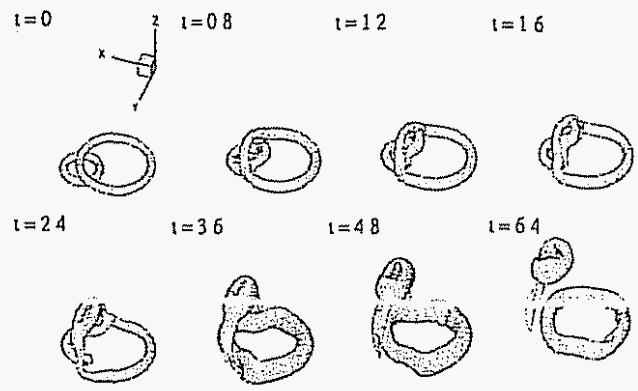

FIG. 2. Vortex rings of different radii: contours of vorticity; from $t = 0$ to 2.4, the contour is $\omega = 0.15\omega_{\max}^{t=0}$; for $t > 2.4$, it is $\omega = 0.05\omega_{\max}^{t=0}$.

where $d\Omega_k$ denotes $\sin\theta_k d\theta_k d\phi_k$, the solid angle element in spherical coordinates. The calculation of the spectrum requires a double summation over the vortex elements which results to $\mathcal{O}(N^2)$ complexity. Because of this, the calculation of the spectrum is much more costly than the solution of the Biot-Savart law. Since the number of particles grows substantially during our simulations, from around $N = 5 \times 10^4$ at $t = 0$ to 8×10^5 in the end, our computational resources did not allow us to compute the spectra for all times.

All calculations were done with the same Reynolds number: $\mathrm{Re} = \frac{\Gamma}{\nu} = 250$ where Γ is the circulation of one ring and ν is the kinematic viscosity. This small value of the Re was dictated by the computational cost and the need for well-resolved reconnection regions. All the rings have the same initial Γ. All of our conclusions are conditioned upon the small value of the Reynolds number, as well as, on the common initial circulation and should not be extrapolated uncritically to other settings. The initial vorticity distribution in the cross section of every ring is Gaussian with a cutoff

$$\omega_\theta = \frac{\Gamma}{2\pi\sigma^2} e^{[(-r^2)/(2\sigma^2)]}, \tag{7}$$

where r is the distance to the core center, σ is the core radius, and ω_θ is the azimuthal vorticity. We chose $\sigma = 0.05R$ (where R is the radius of the ring), to ensure that the rings are still thin when reconnections occur. Our results were made dimensionless in the following manner: $t = (\Gamma t'/R^2)$, $x = (x'/R)$, and $\omega = [(R^2\omega')/\Gamma]$, where t', x', and ω' are dimensional.

We studied three configurations. In the first case (Fig. 1), the initial rings are placed at a distance of $R/4$ apart in the z direction, offset by R along the y axis and they move in opposite directions along the z axis. In the second case (Fig. 2), two rings of different radii (R and $R/2$) and of initial separation $R/4$ are moving in the same direction along the z axis, with the center of the small ring in a collision course with the circumference of the large one. The small ring has a larger self-induced velocity and catches up with the large ring. Finally, in the third case (Fig. 3), the two rings are linked at 90° a ring going through the other in its center. One is moving in the positive z direction; the other, in the positive y direction.

All three evolutions lead to ring reconnection (Fig. 1–3) and have common features. The latter will be discussed here in the context of the first configuration observing that the phenomena are the same for the other two cases. The spectrum at $t = 0$ (Fig. 4) has the characteristic oscillations of the spectrum of isolated vortex rings and a cutoff at the scale of ring core radius $\sigma = 0.05$, $k = 20$. Our results (Fig. 1 and 5) suggest that (approximately) the reconnection starts around $t = 0.6$ and ends around $t = 1.75$ with a duration $\Delta t_r = 1.15$. Specifically, as the rings approach each other, they stretch and deform near the collision points so that their respective vorticities become locally antiparallel. The two ends of this stretching region eventually become reconnection kinks in which (in the absence of singularities) the strong vorticity gradients are smoothed out by diffusion. This is

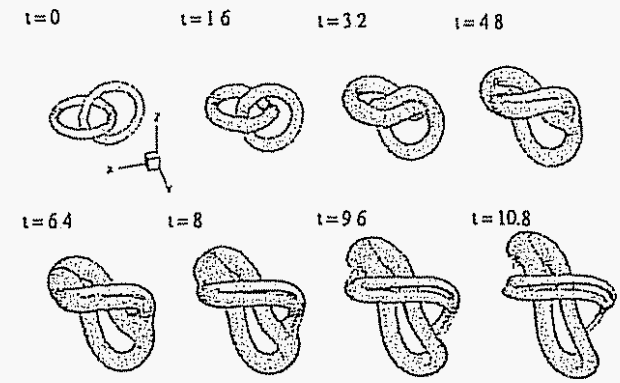

FIG. 3. Linked vortex rings: contours of vorticity; $\omega = 0.025\omega_{\max}^{t=0}$.

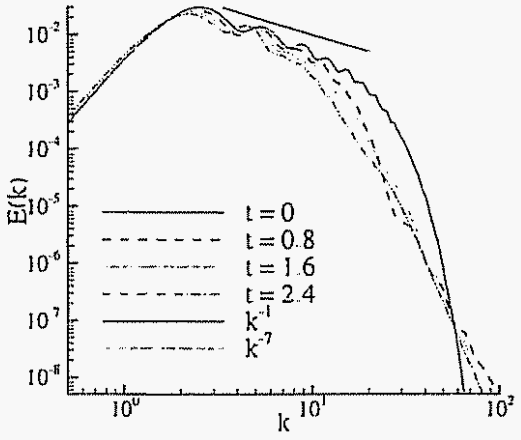

FIG. 4. Vortex rings in an offset collision: evolution of the energy spectrum

also seen in the graphs of the global quantities (Fig. 5) where the beginning of the reconnection process corresponds to a hump in the graph of Ω and to a steepening of the slope of $E(t)$ between $t = 0.6$ and $t = 1.4$. Our calculation predicts that (due to diffusion) the filament core radius increases from the value $\sigma_0 = 0.05R$ initially to the value $\sigma_r = 0.12R$ at the reconnection. Using this latter value we calculate the viscous time scale $t_\nu = \sigma_r^2/\nu = 0.36$. Scaling the convective ring velocity with $\Gamma/4\pi R$ we estimate the time needed for a ring to traverse σ_r: $t_c = 4\pi R\sigma_r/\Gamma = 1.5$. These times are of the same order as Δt_r and so it looks that both viscous and convective phenomena participate in the reconnection physics. The present relation between t_ν and Δt_r is different from the one in [11] where the viscous scale was reported to be much larger than the duration of reconnection. However, in [11] the Reynolds number was 1600. The conclusion that the reconnection duration is inversely proportional to the Reynolds number and thus to the circulation of the vortices is plausible (also in agreement with [6,14]), but it is subject to the condition in [11] that the rings are merely touching themselves rather than colliding.

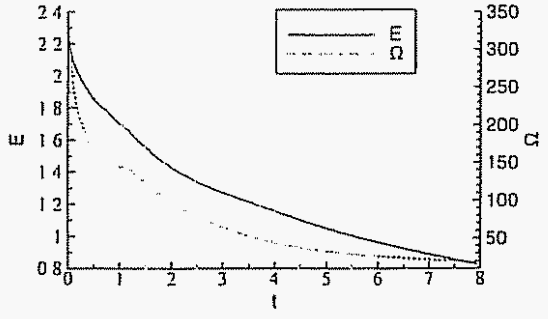

FIG. 5. Vortex rings in an offset collision: kinetic energy and enstrophy

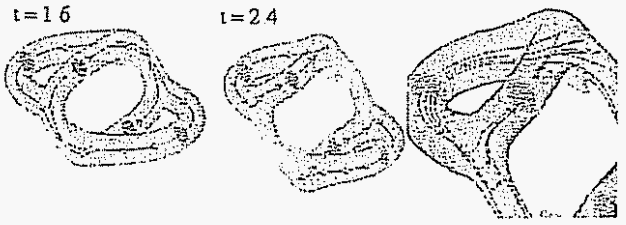

FIG. 6. Vortex rings in an offset collision: contour of vorticity and vortex lines at $t = 1.6$ and 2.4; the transparent contour is $\omega = 0.025\omega_{\max}^{t=0}$; the vortex lines in (a) and (b) were chosen to pass through the vortex core center (the maximum value of ω) at a location away from the reconnection kinks; in (c), a few neighboring lines are also shown for $t = 2.4$

After some time (Fig. 6), we can say that two new rings are formed. The pairs of filaments between the reconnection regions are stretched further as the new rings move apart from each other ($t = 1.6$ to 5.6). These stretched vorticity structures are responsible for a continued transfer of energy to the smallest scales until these structures are dissipated away. This conclusion is supported by the results of Fig. 4 where it is shown that the high wave number cutoff of the spectrum becomes a nonexponential one (although it remains still very steep) and that between $t = 0.8$ and 2.4 there is a significant decay of the energy spectrum for $k < 20$ but little change for $k > 20$. This last observation indicates that in the small scales of motion an approximate balance between energy transfer from large scales due to stretching and local energy dissipation due to diffusion is attained (temporarily). This conclusion is also consistent with the vorticity structure shown in Fig. 7.

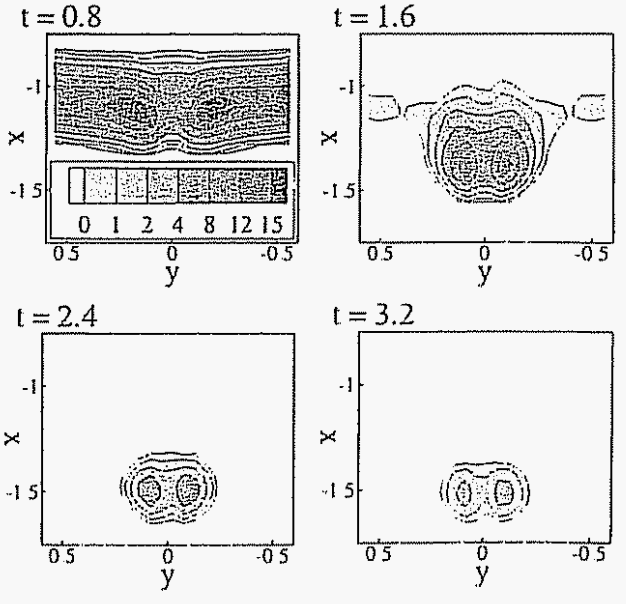

FIG. 7. Vortex rings in an offset collision: contours of vorticity magnitude in the plane $z = 0$ from $t = 0.8$ to 3.2

where it is observed that between $t = 0.8$ and $t = 2.4$ (the time of the last spectrum calculation), the vorticity magnitude in the secondary structures (where the global maximum of vorticity resides) stops increasing and in fact it decays slightly.

It is conceivable that for Reynolds numbers higher than 250 an intermediate scaling range (that is in between the k^{-1} and k^{-7} regimes) could appear with an inertial type of scaling. It is also expected that with increasing Reynolds number the hump observed in the global enstrophy during the reconnection could become more pronounced and (according to the previous discussion) shorter in duration.

In conclusion, we studied three generic vortex ring configurations and we found that in all cases the rings reconnect. This suggests that reconnection is a common phenomenon in vortex filament encounters and perhaps also in turbulent flows. In addition, we observe an intensification of dissipation which is local in time and could be a mechanism contributing to turbulence intermittency. A by-product of reconnection is the formation of stretched structures with antiparallel vorticity which transfer energy to the smallest scales where it is rapidly dissipated. Without this energy redistribution in wave number space the decay of global kinetic energy would have been slower. This important effect depends directly on the details of the initial vortex configuration (compare with experiments in [11]). The observed intensification of small scale motions hints to an enhancement of small scale mixing of passive scalars with $Sc \geq 1$. The excited Kelvin waves represent a fast mechanism for energy transfer, but the small Reynolds number of our calculations is not suitable for understanding their full importance. In particular, they are confined to low wave numbers in opposition to the Kelvin waves observed in reconnections in quantum fluids [15]. This is because quantum filaments are inviscid and have a very thin core ($\sigma \sim 0.1$ nm) so that high wave number Kelvin waves propagate without damping even for rings with small circulation.

Besides illuminating important physics, the present work will guide future introduction of phenomenological reconnection models into vortex filament computational methods. In this way, the applicability of the latter methods will be extended to flows with complex vorticity configurations.

This research was partially supported by the Office of Naval Research and the Department of Energy.

[1] D. Kivotides, J. C. Vassilicos, D. C. Samuels, and C. F. Barenghi, Europhys. Lett. 57, 845 (2002).
[2] M. Christensson and M. Hindmarsh, Phys. Rev. D 60, 063001 (1999).
[3] A. Leonard, Annu. Rev. Fluid Mech. 17, 523 (1985).
[4] S. Kida and M. Takaoka, Annu. Rev. Fluid Mech. 26, 169 (1994).
[5] R. M. Kerr and F. Hussain, Physica (Amsterdam) 37D, 474 (1989).
[6] M. J. Shelley, D. I. Meiron, and S. A. Orszag, J. Fluid Mech. 246, 613 (1993).
[7] A. Pumir and R. M. Kerr, Phys. Rev. Lett. 58, 1636 (1987).
[8] G. S. Winckelmans, Annual Research Briefs, CTR Stanford, 1995.
[9] H. Aref and I. Zawadzki, Nature (London) 354, 50 (1991).
[10] I. Zawadzki and H. Aref, Phys. Fluids A 3, 1405 (1991).
[11] P. R. Schatzle, Ph.D. thesis, California Institute of Technology, 1987.
[12] W. T. Ashurst and D. I. Meiron, Phys. Rev. Lett. 58, 1632 (1987).
[13] G.-H. Cottet and P. Koumoutsakos, *Vortex Methods, Theory and Practice* (Cambridge University Press, Cambridge, 2000).
[14] J. F. Garten, J. Werne, D. C. Fritts, and S. Arendt, J. Fluid Mech. 426, 1 (2001).
[15] D. Kivotides, J. C. Vassilicos, D. C. Samuels, and C. F. Barenghi, Phys. Rev. Lett. 86, 3080 (2001).

Quantized Turbulence Physics

ATTACHMENT NO. 5

Demosthenes Kivotides and Anthony Leonard

Graduate Aeronautical Laboratories, California Institute of Technology, Pasadena, California 91125, USA

(Received 22 January 2003; published 13 June 2003)

We elaborate the physics of systems of unconstrained, reconnecting vortex filaments with dynamic finite cores of uniform ("quantized") circulation interacting via Biot-Savart and viscous forces. The phenomenology of this purely structured turbulent system includes an inertial range with Kolmogorov's $k^{-5/3}$ scaling for the energy spectrum, as well as Kolmogorov's linear in r scaling for the third order longitudinal structure function.

DOI: 10.1103/PhysRevLett.90.234503 PACS numbers: 47.27.Ak, 47.27.Gs, 47.32.Cc

The contribution of coherent structures to the statistics of turbulent flow comprises a central problem in turbulence physics. Adopting a vorticity representation of fluid flow, one can define coherent structures to be vorticity patterns (e.g., Burgers's vortices) characterized by a number of parameters (e.g., the core radius to length ratio in case of a filament). In order for such patterns to persist in time their interactions should only cause their transition from one characteristic parameter range to another without simultaneous change of their mathematical definition. Examples of such structures are described in [1]. In this Letter we develop a novel turbulence model in order to address the following question: is there a kind of low dimensional coherent structure capable of representing the dynamically important vorticity field as a collection of its manifestations?

Our approach to the question above is inspired from previous efforts to quantize classical turbulence [2] and is motivated by drawing an analogy with quantum fluids [3]. In particular, starting from the Gross-Pitaevskii model of superfluids and using the Madelung transformation the superfluid dynamics reduce to the inviscid Euler equation, with the additional constraint that the vorticity in the flow must be exclusively in the form of vortex filaments with quantized circulation [4]. This extra constraint is a pure quantum mechanical effect. Although in classical fluids such quantization constraints are absent, the following questions are legitimate: How useful would it be (in turbulence theory) to imagine a Navier-Stokes fluid with its circulation quantized in the same manner as in superfluids? Can one construct a Navier-Stokes analog of the Euler superfluid vortices? In this Letter we respond to the questions above by formulating a heuristic quantization of the Navier-Stokes equation. We propose a turbulence model that depicts unconstrained, reconnecting vortex filaments with dynamic finite cores of uniform (quantized) circulation, interacting via inertial and viscous forces. This formulation is much more complicated than previously suggested vortex models of inertial range and fine scale turbulence [5–9]. These had to assume a specific vortex structure of unknown stability analysis and had to ignore the strong interactions between the vortices, as well as their reconnections. These simplifications are in oblique contrast to the complexity of turbulence, and there is little hope to expect that statistical mechanics obtained from such models could unlock essential turbulence physics. Thus, this Letter extends the previous studies by avoiding many of their simplifications.

If r_i is the three dimensional representation of the centerline curve of filament i then the vortex motion is described by

$$\frac{dr_i}{dt} = V(r_i(t), t), \tag{1}$$

where $V(r_i(t), t)$ is the Biot-Savart velocity:

$$V(x, t) = -\frac{1}{4\pi}\int \frac{(x - x') \times \omega(x')dx'}{|x - x'|^3} \tag{2}$$

with $\omega(x')$ the vorticity vector. In the quantum Euler case the vorticity $\omega(x')$ is a delta function along the curve of the filament C_i since the superfluid vortices have (at hydrodynamic scales) infinitesimal core sizes. However, in the classical Navier-Stokes case the vortices have dynamic, finite cores, and the vorticity is distributed. This results in a more complex vorticity representation [10]:

$$\omega(x', t) = \sum_i \Gamma \int_{C_i} \frac{1}{\sigma_i(s, t)^3}\zeta\left(\frac{|x' - r_i(s, t)|}{\sigma_i(s, t)}\right) \times \left(\frac{\partial r_i}{\partial s} + \frac{x' - r_i(s, t)}{\sigma_i(s, t)}\frac{\partial \sigma_i}{\partial s}\right)ds, \tag{3}$$

where $\sigma_i(s)$ is the local core radius of filament i and the smoothing kernel ζ describes the way vorticity spreads around the core centerline. The calculations are done with the high order algebraic kernel of [11]. Γ is the circulation strength attributed to all filaments and is the model's analog of the quantum of circulation. The formula shows that the vorticity field has two constituents. The first term of the sum inside the integral sign models the vorticity component along the direction of the filament tangent $\frac{\partial r_i}{\partial s}$. This is the only component present in quantum vortices (without the smoothing effect of ζ). The second term

 0031-9007/03/90(23)/234503(4)$20.00

models the vorticity component along the direction $x - r_i(s)$ and is induced by the change of $\sigma_i(s)$ along the filaments.

In the numerical calculations each filament is divided into a number of finite segments using a set of discretization points s^j, where $j = 1, N$ and s is the arclength parametrization. The time integration is done with a low storage, third order accurate Runge-Kutta method [12]. Both filament stretching due to the Biot-Savart velocity field and viscous action change σ_i. The former effect has been taken into account by imposing for every discretization point s^j the conservation of vortex tube volume:

$$\frac{d}{dt}(\pi\sigma_i^2(s^j)|x(s^j) - x(s^{j+1})|) = 0, \tag{4}$$

where s^{j+1} is the immediate neighbor of point s^j. The viscous effect is handled by the core-spreading method [13]:

$$\frac{d\sigma_i^2}{dt} = 2\gamma\nu, \tag{5}$$

where ν is the kinematic viscocity and γ is a factor depending on the particular kernel ζ employed and equal to $\gamma_a = 2.205$ for our choice of kernel. When two filaments approach closer than a fraction of their corresponding core radii, they reconnect. The details of the algorithm can be found in [14] where it was shown to predict adequately the changes in topology, the excitation and propagation of Kelvin waves, the viscous decay of kinetic energy, and the helicity dynamics. An important consequence of circulation quantization is a great simplification in reconnection physics. Reconnections between vortex rings of variable circulation are much more difficult to model efficiently. Periodicity was enforced with the minimum image method [15]. In the absence of a proper mathematical analysis of the error committed with the latter method we have done computational experiments with a simple system which did not show significant velocity deviations from exact reference velocity profiles.

The initial condition of the calculations done with the proposed model consists of 192 vortex rings in a periodic box. The radii and orientations of the rings are chosen using sequences of random numbers. The Reynolds number has the value $\mathrm{Re} = \frac{\Gamma}{\nu} = 5000$ where Γ is the circulation of the rings and ν is the kinematic viscosity. The results are made dimensionless in the following manner: $t = \frac{\Gamma t'}{R^2}$, $x = \frac{x'}{R}$, $\omega = \frac{R^2\omega'}{\Gamma}$, where t', x', ω' are dimensional and R is a reference initial vortex-ring radius. We have chosen $\Gamma = 1$ and $R = 1$; the box size is $l_b = 2.041$. Using the initial value of the turbulence intensity $u = \sqrt{2E/3} = 3.87$ (with u_i the velocity fluctuations and $E = \frac{1}{2}\sum_{i=1}^{3}\langle u_i u_i\rangle$ the turbulence kinetic energy) as a scale for the velocity of convective motions and the size of the largest resolvable eddies (equal to half the box size) as a scale for the length of the convective motions, we find the inertial time scale $t_c = 0.26$. For comparison the numerical solution ends at $t_e = 0.14$.

Figure 1 shows that the artificially ordered initial condition evolves (mainly because of reconnections) into a complex tangle. The final reconnection number exceeds 9000.

Figure 2 presents the energy spectra at two different times $t = 0.09$ and $t_e = 0.14$. They lead to the same conclusions, although due to turbulence decay the earlier spectrum is characterized by higher energy values. Notice that the initial condition corresponds to a nonphysical tangle state and only at $t \approx 0.05$ (when an almost linear decay sets in) is the tangle complex enough to be realistic. At $t_e = 0.14$ the minimum tube radius in the system is located at $k_h = 14$ and the maximum (tube radius) at $k_l = 8.25$. Here $k = \frac{1}{l}$ without 2π factors. We estimated the average dissipation $\langle\epsilon\rangle = \frac{dE}{dt}$ by equating it to the almost constant turbulent energy decay rate (Fig. 3)

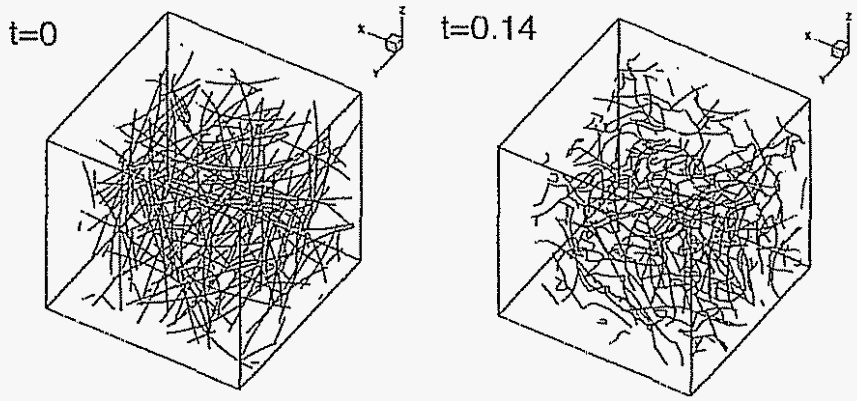

FIG. 1. Vortex filament core centerlines at initial and stoppage times. For clarity, only one-eighth of the computational box is shown.

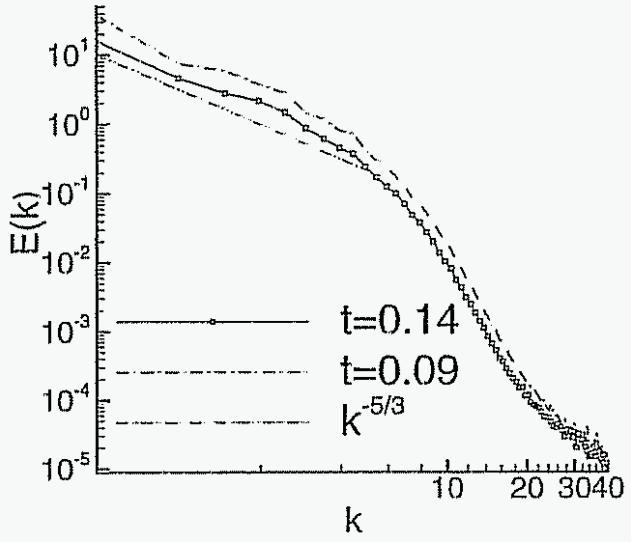

FIG. 2. Velocity spectra at $t = 0.09$ and $t_e = 0.14$.

in the time interval $t = 0.07$ to $t = 0.14$ and found $\langle\epsilon\rangle = 42$. Direct calculation using the ϵ definition is not appropriate since the major contribution to ϵ comes from the reconnection model and not from the resolved flow scales. Assuming the formula $\langle\epsilon\rangle = \frac{15\nu u^2}{\lambda^2}$ (with λ the Taylor scale) of locally isotropic turbulence to be useful in the present context, we find the Taylor wave number $k_\lambda = 37$ and the Taylor scale Reynolds number $\mathrm{Re}_\lambda = 427$. The Kolmogorov microscale is much smaller than the minimum core size and is not resolved. The $k < k_l$ part of the spectrum corresponds to the inertial range of turbulence where vortex stretching is dominant. At $k \approx k_l$ viscous effects become important and cause a sharp cutoff observed between $k \approx k_l$ and $k \approx k_\eta$. There is also evidence that at $k \approx k_\lambda$ energy tends to pile up at subcore wave numbers.

The fully resolved calculations of [16,17] depicted vortex stretching at subcore length scales during reconnections. It was shown in [14] that the intensity of this stretching process is only partially captured by the employed reconnection model, and therefore the small scale flow structure is not predicted with great accuracy. However, assuming that the physics of the inertial range depend mainly on the effective removal of kinetic energy at the smallest wave numbers and not on their detailed structure, this should not present a problem since our model incorporates such an effective dissipation. As Fig. 2 indicates, the inertial range spectrum scales like $k^{-5/3}$ and this provides clear evidence that stretching effects in turbulent vortex tangles can help explain Kolmogorov scalings in accord with a line of thought initiated in [18].

In Fig. 3 we observe a direct correlation between the reconnection rate and the (turbulent) energy decay rate. This is also consistent with the findings of [16], showing intensification of dissipation during reconnections. The results hint at a possible mechanism of dissipation intermittency in real turbulence since reconnection processes occupy at any instant only a portion of the fluid volume.

In Fig. 4 the third order longitudinal structure function is shown. The latter is defined as

$$S_3^{\parallel} = \left\langle \left\{ [u(x+r) - u(x)] \cdot \frac{r}{r} \right\}^3 \right\rangle, \qquad (6)$$

and it is negative. We have first computed the $S_3^{\parallel}$ values along each of the three Cartesian directions and then we averaged. The directional sets of data were not identical

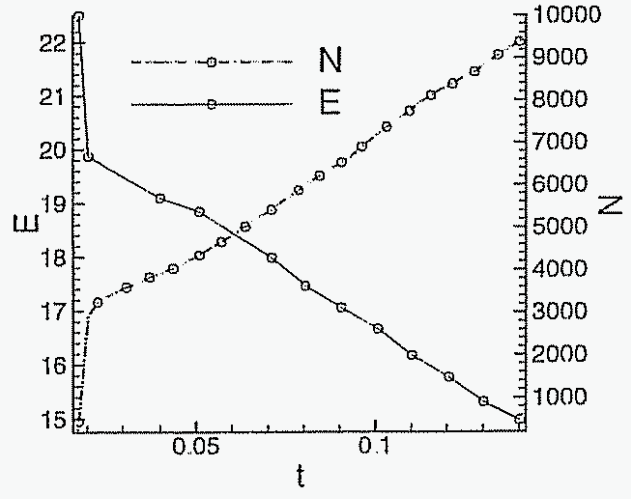

FIG. 3. Evolution of turbulent energy E and of reconnection number N

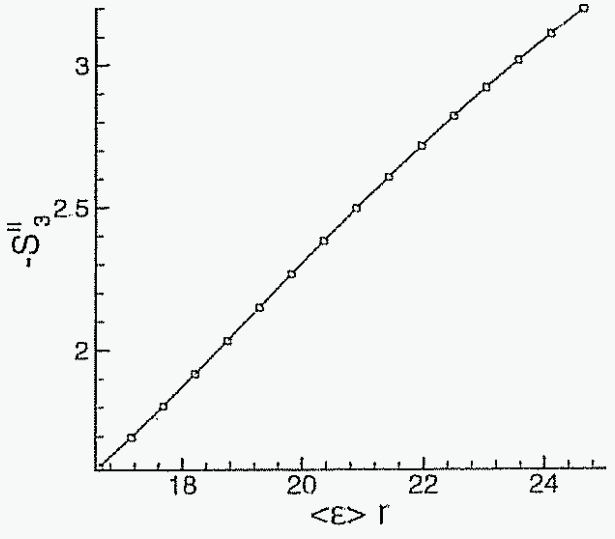

FIG 4. Third order velocity structure function at stoppage time $t_e = 0.14$; the actual r interval is [0.4, 0.6]

and the present turbulence is certainly not isotropic. The results indicate that (as in real turbulent flows) $S_3^{\parallel}$ is nonvanishing. In addition, $S_3^{\parallel} \propto r$ in a subinterval of the $k^{-5/3}$ range. This scaling behavior was apparent in all directions although its extent was varying. The slope, however, in Fig. 4 differs significantly from the Kolmogorov slope $-\frac{4}{5}\langle\epsilon\rangle$ valid for globally isotropic turbulence and calculated using the $\langle\epsilon\rangle = 42$ value. Possible reasons for this could be turbulence unsteadiness and anisotropy, a small extent of the inertial range which is not asymptotically distant from the viscous regime, as well as limitations of the present model of fully developed Navier-Stokes turbulence. In this context it is worth noticing that in the grid generated turbulence experiment of [19] with the $\mathrm{Re}_\lambda \approx 450$ similar to ours, there was also almost no range with the slope $-\frac{4}{5}\langle\epsilon\rangle$ at all.

In conclusion, we have established a schoinoidal (from the Greek $\sigma\chi o\iota\nu o\epsilon\iota\delta\eta\varsigma$ meaning ropelike, stringy) kind of turbulence. In doing this we have ignored the incoherent background vorticity of real turbulence and consequently the interaction between the latter and the vortex filaments. In this milieu, it is important that the system exhibits the Kolmogorov $k^{-5/3}$ scaling, as well as the Kolomogorov $S_3^{\parallel} \propto r$ prediction, despite the turbulence being highly intermittent and anisotropic. These do not necessarily mean that stretched line vortices are the sole factor of Kolmogorov phenomenology. The latter preassumes (among other equally plausible alternatives) that real turbulence is solely composed of linear coherent structures (as is the case of quantum turbulence) or that filamentary structures dominate an apparently incoherent background. Arguments against the latter can be found in [20]. The existence of different turbulence species all with the same statistical phenomenology but different deterministic structures should not be excluded. In this milieu, the study of hybrid systems of filament, sheet, and volume vorticity is important. In the related area of quantum fluids the results help to understand the k^{-1} [3] scaling of superfluid turbulence by noting that vortex stretching, a necessary (in this case) factor of Kolmogorov scaling is missing in the coreless quantum vortex tangles.

This research was partially supported by the Office of Naval Research and the Department of Energy.

[1] K. Horiuti, Phys. Fluids 13, 3756 (2001).
[2] K. Kondo, RAAG Memoirs 2, 71 (1958).
[3] D. Kivotides, J. C. Vassilicos, D. C. Samuels, and C. F. Barenghi, Europhys. Lett. 57, 845 (2002).
[4] *Quantized Vortex Dynamics and Superfluid Turbulence*, edited by C. F. Barenghi, R. J. Donnelly, and W. F. Vinen (Springer-Verlag, Berlin, 2001).
[5] D. I. Pullin and P. Saffman, Annu. Rev. Fluid Mech. 30, 31 (1998).
[6] N. Hatakeyama and T. Kambe, Phys. Rev. Lett. 79, 1257 (1997).
[7] D. Boyer and J. C. Elicer-Cortes, J. Phys. A 33, 6859 (2000).
[8] D. I. Pullin and T. S. Lundgren, Phys. Fluids 13, 2553 (2001).
[9] A. J. Chorin, *Vorticity and Turbulence* (Springer-Verlag, Berlin, 1994).
[10] A. Leonard, Phys. Fluids 6, 765 (1994).
[11] G. S. Winckelmans and A. Leonard, J. Comput. Phys. 109, 247 (1993).
[12] P. Orlandi, *Fluid Flow Phenomena—A Numerical Toolkit* (Kluwer Academic Publishers, Amsterdam, 1999).
[13] A. Leonard, Annu. Rev. Fluid Mech. 17, 523 (1985).
[14] D. Kivotides and A. Leonard (to be published).
[15] P. Susanne and P. Gibbon, *Many-Body Tree Methods in Physics* (Cambridge University Press, Cambridge, U.K., 1996).
[16] P. Chatelain, D. Kivotides, and A. Leonard, Phys. Rev. Lett. 90, 054501 (2003).
[17] M. J. Shelley, D. I. Meiron, and S. A. Orszag, J. Fluid Mech. 246, 613 (1993).
[18] G. I. Taylor, Proc. R. Soc. London A 164, 15 (1938).
[19] L. Mydlarski and Z. Warhaft, J. Fluid Mech. 320, 331 (1996).
[20] A. Tsinober, *An Informal Introduction to Turbulence* (Kluwer Academic Publishers, Amsterdam, 2001).

ATTACHMENT NO. 6

Available online at www.sciencedirect.com
SCIENCE DIRECT®
PHYSICS LETTERS A
Physics Letters A 318 (2003) 574–578
www.elsevier.com/locate/pla

Geometry of turbulent tangles of material lines

Demosthenes Kivotides

Graduate Aeronautical Laboratories, California Institute of Technology, Pasadena CA 91125, USA

Received 12 August 2003; received in revised form 18 September 2003; accepted 28 September 2003

Communicated by A.R. Bishop

Abstract

We show that a tangle of material lines in a purely structured, decaying turbulent flow presents flat scalings for the curvature and torsion spectra corresponding to both the inertial and viscous ranges in the energy spectrum and that it acquires a fractal dimension close to 2 resembling a material sheet.

PACS: 47.27.Ak; 47.27.Gs; 47.32.Cc

Keywords: Mixing; Turbulence; Vortices

The study of non-local turbulence characteristics requires the investigation of extended material objects like lines and surfaces since extended objects encode efficiently the effects of spatial correlations in the turbulent velocity field. The geometry of material lines is important in understanding the mixing properties of turbulence. Large scale geometrical variations of a material interface are major contributors to concentration transport and small scale corrugations lead to fractal interface dimensions which characterize the degree of mixing. The discovery of fractal interface dimensions and the self-similarity of geometry in the appropriate range of scales that they imply, as well as, the discovery of universal power law regimes in the curvature, torsion or Lagrangian velocity spectra simplify physical interscale arguments and the accounting of multiscale turbulence effects. Their importance for the geometry is similar to that of the Kolmogorov scalings for the velocity field.

In [1–3] the curvature of material lines in laminar and steady (in the Eulerian picture), chaotic flows was studied. It was verified that compression of material elements results in line folding and curvature generation. Data for curvature probability density functions indicated that the latter might be independent of the flow details. At sufficiently long times the mean curvature attained constant values with superimposed fine fluctuations. In [4] the correlation between curvature and stretching along material lines was studied for a laminar cellular flow. A power law relation between stretching and curvature along sharp bends was found. In [5] the fractal dimension of a material line distorted by the laminar flow of a blinking vortex with no boundaries (introduced in [6]), was calculated with the box counting algorithm and was found to be bounded from above by the value 2. Due to the simplicity of the underlying flows, these studies do

E-mail address: demos@galcit.caltech.edu (D. Kivotides).

0375-9601/$ – see front matter
doi:10.1016/j.physleta.2003.09.068

not provide information about material line dynamics in fully developed turbulence. In [7] the distortion of a material line by a stationary isotropic incompressible turbulent flow was studied. Emphasis was given on stretching phenomena rather than on geometrical features. In [5] the box counting algorithm was used to measure the dimension of a material line deformed by a two-dimensional, Gaussian, prescribed velocity field. It was concluded that the embedded line failed to become fractal. In this Letter we employ a model of a three-dimensional, fully structured turbulent flow introduced in [8] in order to study geometrical properties of a tangle of closed material lines. The turbulence model consists of unconstrained, reconnecting vortex filaments with dynamic finite cores of uniform circulation, interacting via inertial and viscous forces. It obeys the Kolmogorov scalings for the second and third order structure functions and it is endorsed further by the findings of [9]. We show that a tangle of material lines in a purely structured, decaying turbulent flow presents flat scalings for the curvature and torsion spectra corresponding to both the inertial and viscous ranges in the energy spectrum and that it acquires a fractal dimension close to 2 resembling a material sheet.

We compute the dynamics employing a numerical method described in detail in [8]. If r_v is the three-dimensional representation of the centre-line curve of filament v and r_m is the representation of the curve of material line m then the vortex and material motions are described by

$$\frac{dr_v}{dt} = V\big(r_v(t), t\big) = V_v, \tag{1}$$

$$\frac{dr_m}{dt} = V\big(r_m(t), t\big) = V_m, \tag{2}$$

where V_v and V_m are the Biot–Savart velocities:

$$V(x,t) = -\frac{1}{4\pi}\int \frac{(x-x')\times\omega(x')\,dx'}{|x-x'|^3} \tag{3}$$

with $\omega(x')$ the vorticity vector. The employed $\omega(x')$ formula takes into account the finite core of the filaments, as well as, variations of the latter along the vortices. The viscous effect is handled by the core-spreading scheme of [10]. When two filaments approach closer than a fraction of their corresponding core radii, they reconnect according to the method of [11]. We have implemented periodic boundary conditions by introducing image vortices thus augmenting the computational complexity. Numerical experiments determined the minimum width of the box extension (where the image vortices are located) to be $0.3l_b$, where l_b is the size of the box. Then the deviations of numerical values from exact ones were indiscernible.

We calculate the fractal dimension of the material tangle employing the box counting method of [12]. The algorithm computes $N(\delta)$, the minimum number of boxes of size δ needed to cover all points produced by the discretization of material lines. This is done for a range of box sizes. In the limit of very small δ values the slope of the curve $N(\delta)$ becomes zero since then the box size is smaller than the discretization distance between the material points and $N(\delta)$ is equal to the actual number of points that make up the material system. The box size is increased until δ is comparable to the size of the calculation box. For such δ values $N(\delta)$ exhibits a step like behaviour. Using these data we construct a log–log graph of $N(\delta)$ versus δ. If a fractal dimension exists then for an adequately large range of δ values, a slope should be visible on the graph defining the fractal dimension D:

$$\ln\left(\frac{N(\delta)}{N(\delta_{\min})}\right) = -D\ln\left(\frac{\delta}{\delta_{\min}}\right). \tag{4}$$

We compute the curvature C and the torsion T along the closed material lines using second order accurate, periodic, cubic spline interpolation. In this way, we define three functions of the arclength ξ for curvature, torsion and velocity V_m. The latter is obtained directly from the Biot–Savart law. Employing one-dimensional Fourier transforms we calculate their spectra defined as

$$\frac{1}{2}\int X(\xi)\cdot X(\xi)\,d\xi = \int_0^\infty E_X(k)\,dk, \tag{5}$$

where the dummy variable X stands for C, T or V_m and k denotes wavenumber. The present methodology is similar to that employed in [13]. It essentially calculates statistics by ensemble averaging treating each material loop as a single realization of the statistical system.

The Reynolds number has the value $Re = \frac{\Gamma}{\nu} = 5000$, where Γ is the vortex circulation and ν is the kinematic viscosity. The Taylor scale based Reynolds number is $Re_\lambda = 427$. The box size is $l_b = 2.041$

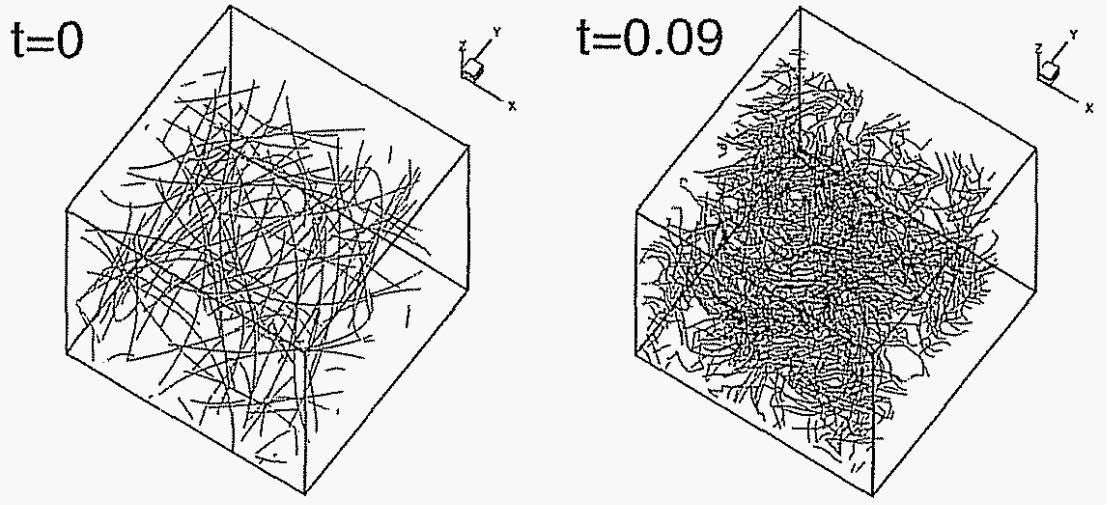

Fig 1 Material lines tangle at initial and stoppage times To serve clarity, only one eighth of the computational box is shown

These values and the vortex positions are chosen to be the same as in [8] so that the dynamics of the flow are familiar. The initial conditions include 192 randomly placed vortex rings (Fig. 1 of [8]) and an equal number of material rings (Fig. 1). The length of the latter is $L^0 = 869.91$ and it is discretized into $N^0 = 28940$ material points. As it is observed in [8] the calculation presents an initial transient which corresponds to a period of intense reconnection rate and very fast energy decay. This transient ends at around $t = 0.05$ where a decaying turbulence state appears with an almost constant dissipation rate $\langle\epsilon\rangle \approx 42$. Since this transient is an artifact of the initial conditions, we have chosen to report our findings after this transient has ceased. The results are made dimensionless in the following manner: $t = \frac{\Gamma t'}{R^2}$, $x = \frac{x'}{R}$, $\omega = \frac{R^2\omega'}{\Gamma}$ where t', x', ω' are dimensional and R is a reference initial vortex-ring radius. We have chosen $\Gamma = 1$ and $R = 1$. Using the initial value of the turbulence intensity $u = \sqrt{\frac{2}{3}E} = 3.87$ (with u_i the velocity fluctuations and $E = \frac{1}{2}\sum_{i=1}^{3}\langle u_i u_i\rangle$ the turbulence kinetic energy) as a scale for the velocity of convective motions and the size of the largest resolvable eddies (equal to half the box size) as a scale for the length of the convective motions, we find the inertial time scale $t_c = 0.26$. Therefore, the numerical solution stoppage time of $t_e = 0.09$ is of the same order as the large eddy turnover time which represents the largest correlation time in fully developed turbulence

In Figs. 1 and 2 it is observed that due to turbulence action the length of the material system grows rapidly. Also observed in Fig. 2 is that the tangle has a fractal dimension $D = 1.97$ over a significant range of scales at stoppage time. At the same time, its length is $L^e = 2857.82$ ($L^e/L^0 \approx 3.3$) and it is discretized into $N^e = 69375$ material points. L^e exceeds by a factor 455 the lengthiest of the initial material loops. In addition, the average discretization length on the lines is $\Delta s = 0.04$ and the average interline spacing is $l_m = \sqrt{l_b^3/L^e} = 0.055$. In [14] a monotonic increase in the fractal dimension of a tangle of quantum line vortices was found. Instead, the present investigation indicates a possible saturation of the material tangle dimension to a value slightly smaller than 2 or in other words the system of lines tends to become a material sheet. This comparison points to the different physics of material and vortex lines but also to a possible effect of viscous forces and turbulence decay since in [14] the system was conservative. The present turbulence is three-dimensional, dynamic and has non-Gaussian features (non-zero third order structure function). Despite these, by applying the box counting method to a single material line of length $L_s^e = 21.08$ and $N_s^e = 514$ number of points (compared to the initial values of $L_s^0 = 6.27$ and of $N_s^0 = 209$), it was found that the latter failed to become fractal as it was also reported in [5] for a two-dimensional, Gaussian, kinematic turbulence. This indicates that the fractal

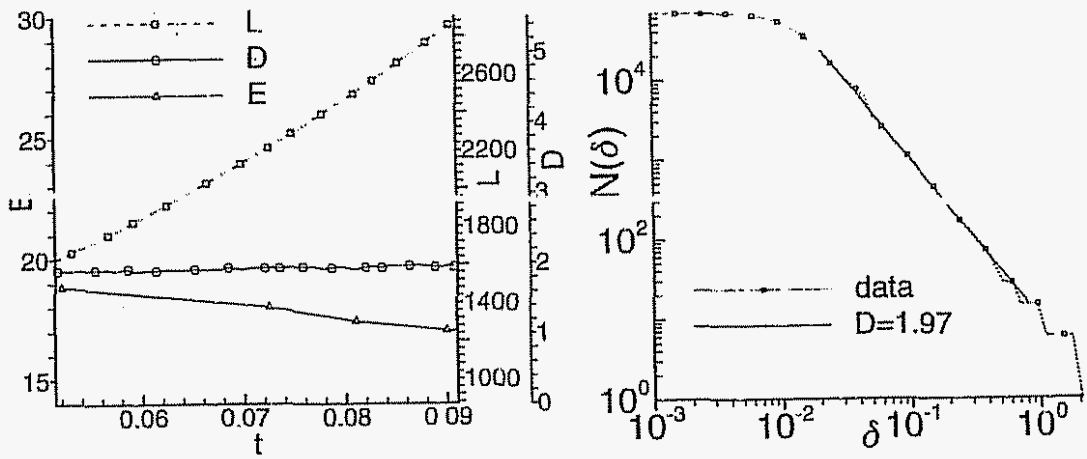

Fig. 2. Left: evolutions of turbulent kinetic energy E, material lines length L and material tangle fractal dimension D with time. Right: number of boxes N versus box size δ for the determination of the fractal dimension at stoppage time.

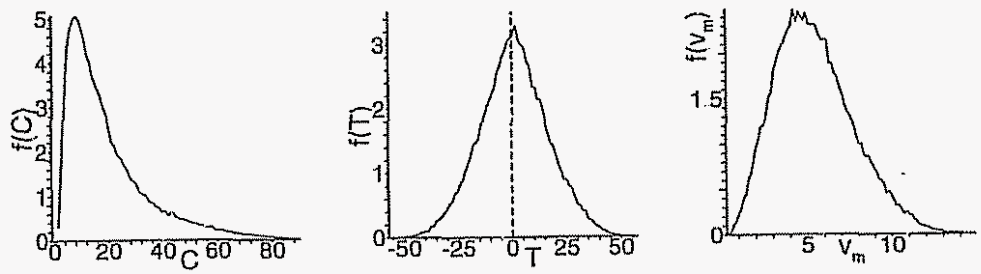

Fig. 3. Histograms of curvature C, torsion T and length of Lagrangian velocity $v_m = \|V_m\|$ at stoppage time. The frequencies are shown divided by 10^3. The number of sample points is approximately 7×10^4.

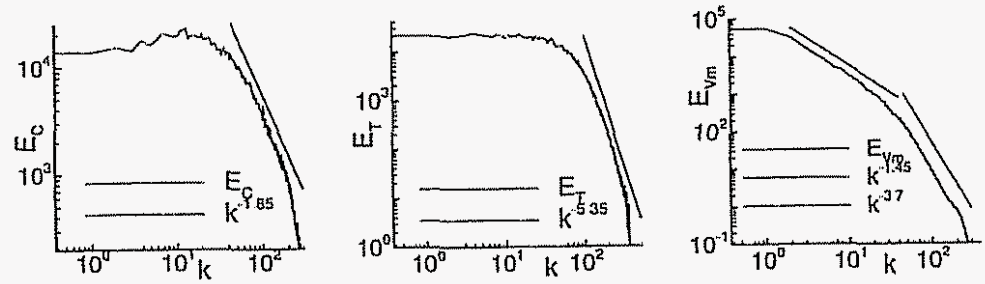

Fig. 4. Spectra of curvature E_C, torsion E_T and Lagrangian velocity E_{V_m}.

dimension observed in Fig. 2 is due to the existence of many material loops.

In Fig. 3 the histograms for curvature, torsion and Lagrangian velocity length are shown. These quantities exhibit different behaviour. Torsion's histogram is approximately symmetric around 0. In contrast to curvature it does not present long tails. The Lagrangian velocity histogram presents a flatter peak than the other two. These observations are in agreement with the spectra of the same quantities seen in Fig. 4. The torsion spectrum is flat for a wide range of scales and then presents a decay regime with a large scaling exponent. In comparison, the curvature spectrum possesses the same structure but the absolute value of the decay regime exponent is much smaller. The latter indicates that (relative to torsion) high curvature values are more energetic. This concurs with the tail observed in the histogram of curvature. The physical

values of torsion and curvature exhibit a spiky profile along the material lines which is consistent with their flat spectrum at low wavenumbers. The Lagrangian velocity spectrum presents also two discernible scaling regimes.

By comparing the three geometric spectra with the energy spectrum in [8], we observe that their low wavenumber scaling regimes terminate at approximately $k = 40$ and that they correspond to both the inertial and viscous regimes of the latter. In addition, the apparent cut-off in the geometric spectra is shifted by approximately a decade toward the high wavenumbers compared to the cut-off in the energy spectrum.

The current turbulence model is inspired by previous DNS studies of homogeneous, isotropic turbulence [9,15] that suggest the existence of coherent vorticity in the form of vortex tubes over all scales of motion. The model was shown to reproduce key Navier–Stokes dynamics and kinematics [8,16].

However, it is not certain that the present results coincide with the phenomenology of vortex tubes in actual turbulence. This is because the latter tubes interact with the incoherent bath of turbulent vorticity (inside which they reside) and as a consequence their behaviour is modified. One way of addressing this issue is by noticing that in [17] it was found that the coherent tubes of the flow contained 73% of the total flow entrophy and that the non-recognizable background vorticity contained the rest 27%. Therefore, it is reasonable to expect that various physical aspects (like the ones investigated here) might be mostly determined by the interactions between the coherent vortex structures (which are fully captured in our calculation) rather than by the interactions between the tubes and the unorganized vorticity or the pure effect of the latter. Certainly, this is the case for key quantities like energy spectra and vorticity pdf's as shown in [17]. In the same work (Figs. 1 and 4), it was also remarked that the coherent vorticity is nearly indistinguishable from the total one.

Admittedly, the above arguments are heuristic and only a future calculation of the same problem with DNS (accompanied by careful comparison of the two sets of results), could lead to definite conclusions.

Acknowledgements

This research was partially supported by the Office of Naval Research and the Department of Energy.

References

[1] D. Hobbs, F.J. Muzzio, Phys. Fluids 10 (1998) 1942
[2] M.M. Alvarez, M.J. Muzzio, S. Cerbelli, A. Adrover, M. Giona, Phys. Rev. Lett. 81 (1998) 3395
[3] S. Cerbelli, J.M. Zalc, F.J. Muzzio, Chem. Eng. Sci. 55 (2000) 363
[4] J.-L. Thiffeault, nlin.CD/0204069.
[5] J.C.H. Fung, J.C. Vassilicos, Phys. Fluids A 11 (1991) 2725
[6] H. Aref, J. Fluid Mech. 143 (1984) 1.
[7] S. Kida, S. Goto, Phys. Fluids 14 (2002) 352
[8] D. Kivotides, A. Leonard, Phys. Rev. Lett. 90 (2003) 234503.
[9] M. Farge, G. Pellegrino, K. Schneider, Phys. Rev. Lett. 87 (2001) 054501
[10] A. Leonard, K. Chua, Physica D 37 (1989) 490
[11] D. Kivotides, A. Leonard, Europhys. Lett. 63 (2003) 354.
[12] J.C. Vassilicos, J.G. Brasseur, Phys. Rev. E 54 (1996) 467
[13] D. Kivotides, J.C. Vassilicos, D.C. Samuels, C.F. Barenghi, Phys. Rev. Lett. 86 (2001) 3080
[14] D. Kivotides, C.F. Barenghi, D.C. Samuels, Phys. Rev. Lett. 87 (2001) 155301
[15] A. Vincent, M. Meneguzzi, J. Fluid Mech. 225 (1991) 1
[16] D. Kivotides, A. Leonard, Europhys. Lett., submitted for publication
[17] M. Farge, K. Schneider, G. Pellegrino, Adv. Turbulence 8 (2000) 797